Doctoral thesis

Evolutional process of subvolcanic hydrothermal system recorded in volcanic products
—Case studies on Tokachidake, Ontake, Azuma-Jododaira volcanoes in Japan—

火山噴出物に記録された活火山直下の熱水系の進化過程
—北海道十勝岳火山，木曽御嶽火山，福島吾妻-浄土平火山での事例研究—

Takumi Imura

Student ID：6517101

Graduate School of International Resource Sciences

Department of Geosciences, Geotechnology, and Materials Engineering for Resources

Akita University

March 2020

Abstract

This study aims to elucidate the evolutional process of the complex interaction between magma and hydrothermal system, focusing on the ash petrology of non-juvenile eruption products in geologic successions from multiple volcanoes. Petrological observation of individual ash grains was carried out for the following cases: (1) Holocene volcanic products from Tokachidake volcano (4.7ka, 3.3ka , and 1926AD) (Chapter 1); (2) volcanic ash from the 2014 hydrothermal eruption of Ontake volcano (Chapter 2); (3) Holocene volcanic tephra layers around 1331AD from Azuma-Jododaira volcano (Chapter 3). As a result, the conclusive remarks below were obtained.

(1) Holocene volcanic products from Tokachidake volcano (4.7ka, 3.3ka, and 1926AD) (Chapter 1): Each sample of ash grains underwent alteration to various degrees from unaltered to intensely altered. Alteration was categorized into silica type (only silcia), alunite type (silica+alunite±kaolin group mineral), and kaolin type (silica+kaolin group mineral). All of the altered ash grains are derived from the acidic alteration zone in subvolcanic hydrothermal system of Tokachidake. The hydrothermal alteration was caused by the acid-sulfate-chloride hydrothermal fluid formed by volcanic vapor that separated from the intruded magma. The rock textures of the weakly altered ash grains were formed by acidic hydrothermal fluid-rock interaction at open-flow through-system. The reaction process is explained by that a large amount of acidic hydrothermal fluid passes through and reacts with the rocks. The brief, incomplete, acidic hydrothermal alteration was caused by the Tokachidake subvolcanic hydrothermal system temporally formed with a magma intrusion.

(2) Volcanic ash from the 2014 hydrothermal eruption of Ontake volcano (Chapter 2): The petrographical and mineralogical study of ash grains from the 2014 Ontake volcano hydrothermal eruption resulted in the discovery of previously undescribed minerals in an active volcano. Aluminum-phosphate-sulfates (APS) minerals (woodhouseite), Zn-sulfide, and monazite were found in this ash grains. The discovery of woodhouseite in the volcanic ash of the Ontake 2014 hydrothermal eruption represents the first reported presence of these minerals within an active volcano. Furthermore, two types of woodhouseite were observed: zoned alunite-woodhouseite-APS and micro-

wormy vein woodhouseite-APS. The genetic environment of APS minerals is proposed to be highly acidic hydrothermal fluids existing beneath the volcanic summit, formed by condensation with magmatic volatiles exsolved from the magma chamber underneath Ontake volcano. Under these conditions, an advanced argillic alteration assemblage formed, consisting of silica, pyrophyllite, alunite, and kaolinite/dickite, plus APS, among other minerals. Further detailed studies might prove that the presence of APS at Ontake is not an exception, but likely commonplace among such active volcanoes. These characteristics are an obvious similarity with the epithermal-porphyry environments.

(3) Holocene volcanic tephra layers around 1331AD from Azuma-Jododaira volcano (Chapter 3): This study found eight tephra layers below, L1-1, L1-2, L2, L3, L4, L5, L6 and L7 from bottom to top. L1-1 and L1-2 were corelated with Az-OA unit (1331AD eruption), and L3 and L4 are corresponded layers from 1711AD eruption. For all samples from the eight layers, XRD and microscopic observation (binocular-stereoscopic microscope and SEM-EDS) had clarified the tendency of componentry change. L1-1, L1-2, L5, L7 are characterized by the X-ray peak of both 14Å-smectite and 7Å-kaolin or either of them, and by abundance of ash grains categorized into partly altered volcanic rock (PAVR), massive altered rock (MAR), and dense volcanic rock (DVR). While, L2, L3, L4, L6 are characterized by the X-ray peak of intense igneous minerals (plagioclase and pyroxene) with the disappearance (or decrease) of 14Å-smectite and 7Å-kaolin, and by abundance of unaltered ash grains as dense volcanic rock (DVR) and vesicular volcanic rock (VVR). Alterations in all samples are classified into acidic to neutral hydrothermal alterations, which are silica type (silica+titanium oxide±pyrite), pyrophyllite type (silica+pyrophyllite±alunite), kaolin type (silica+kaolin mineral±alunite), alunite type (silica+alunite), mica-chlorite type (silica+illite+sericite±chlorite±biotite), chlorite type (silica+chlorite±epidote) and mica-K-feldspar type (silica+chlorite+bioite+K-feldspar). Only L1-1 and L1-2 samples contain altered ash grains of all sets of the above alterations. Other samples than L1-1 and L1-2 indicated alterations of silica, alunite, kaolin, and pyrophyllite types with minor mica-chlorite type. Furthermore, some samples richly contain VVR-andesitic scoria or scoriaceous fragment (especially in L2), DVR-blocky highly crystalline andesitic lava and DVR-blocky holocrystalline andesitic rock (L4, L5, and L6). These ash grains (VVR-

scoria) are possible to be an essential juvenile material. From these componentry trends, Jododaira volcano of Azuma volcano group seems to repeat the hydrothermal eruption derived from a well-developed subvolcanic hydrothermal system (L1-1, L3, L5, and L7) or the magmatic hydrothermal eruption with fragmentation of the hydrothermal alteration zone and an intruded magma (L1-2, L2, and L6).

From these observations, this study defines three types of subvolcanic hydrothermal systems within active volcanoes: Tokachidake-type, Ontake-type, and Azuma-Jododaira-Type. Tokachidake type of subvolcanic hydrothermal system are directly driven by a magma intrusion, which accompanies the chemical and physical modification of the hydrothermal system. Ontake type is a well-developed and mature subvolcanic hydrothermal system similar to the epithermal-porphyry system. Finally, Azuma-Jododaira type is a subvolcanic hydrothermal system with repetitions of magmatic and non-juvenile eruptions. The above three types could be considered as the evolutional series of a subvolcanic hydrothermal system, corresponding to the very-early stage of the epithermal-porphyry system. Through initial (Tokachidake-type) and middle (Azuma-Jododaira type) stages, with various degrees of magma intrusion or eruption, the subvolcanic hydrothermal system evolves into the stable stage defined as Ontake-type during the ore-forming process in volcano.

—Outline—

Introduction

Many cases of explosive eruptions at active volcanoes are accompanied by the emission of various non-juvenile lithic fragments (e.g. Barberi et al., 1991; Mastin, 1995; Browne, and Lawless, 2001). The lithic fragments consist mainly of pre-existing rocks in the volcanic edifice, such as cognates (lava or scoriaceous or pumiceous rocks) and accidental materials (basement metamorphic rocks or altered rocks formed by hydrothermal alteration, diagenesis, and weathering) (e.g. Heiken and Wohletz, 1985; Fujinawa et al., 2008). Their rock types and the proportions of non-juveniles fragments can differ in each volcano or each volcanic succession corresponding to an single eruption, because of the physicochemical conditions of the eruptions. This study uses the terminology of "non-juvenile eruption" as a general term for such explosive eruptions carrying those non-juvenile fragments.

At active volcanoes in a subduction zone, non-juvenile eruptions are frequent occurred and sometimes bring hydrothermally altered material to the surface (Fig. 1). Such hydrothermally altered materials in these volcanic products are probably derived from the rocks of the hydrothermal alteration zone within the subvolcanic hydrothermal system (Ossaka, 1982; Ossaka and Hirabayashi, 1981; Hedenquist and Henley, 1985; Taguchi et al., 1996; Browne and Lawless, 2001; Ossaka, 2003; Ohba and Kitade, 2005; Ohba et al., 2007; John et al., 2008; Miyagi et al., 2010; Ohba, 2011; Minami et al., 2016). In this case, the hydrothermal altered lithic fragments record their formation processes as their rock texture formed by the subvolcanic hydrothermal system (Ohba and Kitade, 2005; Minami et al., 2016; Imura et al., 2019a, 2019b). However, very few studies focused on the characteristics of non-juvenile eruption, and the genetic relationship between non-juvenile eruptions and subvolcanic hydrothermal systems is still unclear.

Recent studies have estimated the origin and the environmental conditions of some non-juvenile eruptions based on petrological characteristics of their products (Ohba and Kitade, 2005; Minami et al., 2016). Ohba and Kitade (2005) determined the alteration mineral assemblages of volcanic ash samples from eight volcanoes in Tohoku district, Japan. According to their results, the volcanic ash grains bearing pyrophyllite could correlate to the pyrophyllite alteration zone within the geothermal area. Minami et al.

(2016) discovered that each altered ash grain that had undergone acidic to neutral alteration occurs in the 2014AD Ontake non-juvenile eruption ejecta. Their petrographical characteristics were correlated with each of the hydrothermal alteration zonation in the epithermal porphyry ore system (Minami, et al., 2016). Those results point out the one possibility that the alteration zonation depending on the spatial distribution of hydrothermal fluid exists also within the volcanic edifice. For some cases of the active volcanos which have a well-developed hydrothermal system, their subvolcanic hydrothermal systems might have their conditions to form the alteration zonation similar to the one from the epithermal-porphyry ore system.

Development of such alteration zonation similar to the epithermal-porphyry ore system is not necessarily typical in actual active volcanic systems. As examples from the active volcanoes with a frequent magmatic eruption and a magma intrusion, these subvolcanic hydrothermal systems should be thermochemically unstable and modified due to the changes of their environmental conditions with every event of the magmatic eruptions (Ohba, 2011; Imura et al., 2019a). Ohba (2011) considered the following environmental effects of a magma intrusion to the subvolcanic hydrothermal system and the alteration zonation: (1) pre-existing alteration zone disappears and is overlaid by an igneous rock body newly formed by a magma intrusion. (2) the chemical composition of a hydrothermal fluid (system) should be different between active and quiescent periods. Increase of volcanic fluids flux with ascending an intruded magma contributes to change the compositions, while the hydrothermal fluid during the quiescent period is affected dominantly from meteoric water. (3) during magma intrusion, the thermal conditions inside the volcanic edifice drastically change, and the hydrothermal system also changes accordingly. Therefore, the petrological and mineralogical characteristics of the altered products in such volcanoes are considered to reflect the effects of (1) to (3). In this case, such characters are likely to be essentially different from the one at volcanoes where have the zoned-hydrothermal alteration correlating to the epithermal-porphyry system.

For the above-mentioned volcanoes, which have subvolcanic hydrothermal systems, their activity trends, eruption styles, and mature levels of the hydrothermal system should be various, as shown even in a few case studies. Such characteristics are

also recorded as the petrology of their volcanic products with their compilated layers, and each volcano. Therefore, this study aims to elucidate the evolutional process of the complex interaction between magma and hydrothermal system, focusing on the ash petrology of non-juvenile eruption products in geologic successions. This research selects the multiple cases of objective volcanoes where repeated non-juvenile eruptions and Holocene geologic successions of such eruptions are well exposed (Fig. 2). Followings are the objectives of the study: (1) Holocene volcanic products from Tokachidake volcano (4.7ka, 3.3ka (Fujiwara et al., 2007, 2009), and 1926AD (Uesawa, 2014)) (Chapter 1); (2) volcanic ash from the 2014 hydrothermal eruption of Ontake volcano (Minami et al., 2016) (Chapter 2); (3) Holocene volcanic tephra layers around 1331AD from Azuma-Jododaira volcano (Yamamoto, 2005) (Chapter 3). Based on the comparison between three cases, this study aims to establish a comprehensive evolutional model of the subvolcanic hydrothermal system.

Chapter 1: Holocene volcanic products at Tokachidake volcano

Study background

This chapter focuses on the Tokachidake volcano as a case study of the subvolcanic hydrothermal system directly related to a magma intrusion (published in Imura et al. 2019a). At Tokachidake volcano, geothermal activity is manifested as a discharge of fumarolic gas and hot spring water, and also as non-juvenile eruptions (e.g., 4.7ka, 3.3ka, 1926AD) with repeated emission of hydrothermally altered material (e.g. NEDO, 1990; Uesawa, 2008, 2014; Takahashi et al., 2015). This indicates that the subvolcanic hydrothermal system is well developed in this volcano. Three magmatic eruptions have occurred during the 20th century (1926AD, 1962AD, and 1988-89AD). At every period of these magmatic eruptions, the change of ground temperature at the vents from 100 to 500 °C was detected with infrared radiometer and thermal infrared image device [URL1]. This activity trend is much different from Ontake volcano where these parameters are constant and stable [URL2]. The increase of the ground temperature also appeared even during the 2004 small non-juvenile eruption [URL1]. These surface phenomena clearly show that the eruptions at Tokachidake volcano frequently are accompanied by some precursors from a magma intrusion. These points suggest that the Tokachidake case is appropriate for this study to understand the magma-hydrothermal system interaction. In this study, petrographical and mineralogical observation has been done for altered material-bearing products in the 4.7ka, 3.3ka, and 1926 AD (Fujiwara et al. 2007, 2009; Uesawa, 2008, 2014).

Geological backgrounds

Tokachidake is a basaltic to andesitic stratovolcano located in the south-eastern part of Daisetsu-Tokachi volcanic chain in central Hokkaido (Katsui and Takahashi, 1960; Takahashi, 1960). This volcano overlies basement rocks composed of Pliocene volcanic rocks, Late Pliocene rhyolitic Biei Pyroclastic Flow Deposits (about 1.9 Ma), and Early Pleistocene rhyolitic Tokachi Pyroclastic Flow Deposits (1.1 Ma to 1.2 Ma) (Katsui et al. 1963; Ikeda and Murayama, 1983). The eruptive history of this volcano is

divided into three stages, Older (1 Ma to 500 ka), Middle (300 to 60-50 ka) and Younger (after 60-50 ka), based on radiometric ages along with the distribution of eruption centers and petrological features of erupted rocks (Katsui et al. 1963a; Ishizuka et al. 2010). Furthermore, the Younger stage is subdivided into two substages, the Y-1 (several 10 ka to 10 ka) and Y-2 (after 10 ka) (Ishizuka et al. 2010). The volcanic activity at these younger stages is mainly eruption of basaltic to andesitic lavas with pyroclasts (Fujiwara et al. 2007, 2009; Ishizuka et al. 2010). At Y-2 stage, some volcanic products contain accidental fragments with juveniles, as exemplified by the 4.7 ka Ground Crater pyroclastic flow deposits, the 3.3ka Ground Crater pyroclastic flow deposit and the 1926 AD lahar deposits (Fujiwara et al. 2007, 2009; Uesawa, 2008, 2014) (Fig. 3a-3c). The following section briefly describes their stratigraphy, distribution and lithofacies of these Holocene deposits.

4.7 ka and 3.3 ka Ground Crater pyroclastic flow deposits

Fujiwara et al. (2007, 2009) geologically and petrologically described 4.7 ka and 3.3 ka Ground Crater pyroclastic flow deposits as below (Fig. 3a, 3c). The 4.7 ka pyroclastic flow deposit (Gfl-0) is characterized by massive, poorly sorted lapplli and bombs with a yellowish-brown to yellowish-white ash matrix. This pyroclastic deposit overlies the lahar deposit A2 and is overlain by the Shirogane mudflow deposit (Sm). Their components are unaltered pumice and scoria, while accidental fragments make up approximately 50 vol. % of the ash matrix. The later 3.3 ka pyroclastic scoria flow deposit, overlying Sm, is divided into two units, Gfl-1 and Gfl-2. Gfl-2 contains abundant scoria, whereas Gfl-1 includes also pumice and banded pumice. Gfl-1 is a single pyroclastic flow deposit with reddish to yellowish-brown ash matrix, while Gfl-2 consists of multiple flow units mainly with dark brown ash matrix. Gfl-1 is rich in accidental fragments ca. 80 wt.% in the matrix, but for the Gfl-2 the abundance is less than 40 wt. %.

1926 AD lahar deposit

In 1926AD, an eruption accompanied with a lahar occurred from the Central Crater (Fig. 3a, 3b). This lahar named Taisho-Deiryu (大正泥流) is well known as an example of a snowmelt type volcanic mudflow which had caused catastrophic damage to Biei between Kami-Furano town (Tada and Tsuya, 1927). The 1926AD lahar deposit,

covering the Central Crater Cone lava, is characterized by extremely poorly sorted block and lapilli with altered ash matrix (Katsui et al. 1963; Ishikawa et al. 1971). Uesawa (2008, 2014) classified the 1926AD lahar deposit into three distinctive units, debris-avalanche deposit with light grey to blueish grey sandy matrix (Unit A), hydrothermal surge deposit with purple-grey to blueish grey sandy matrix (Unit B), debris-avalanche deposit with yellowish-brown sandy matrix (Unit C), from oldest to youngest. These units contain hydrothermally altered lithic fragments, including whitish silicified rocks and brownish rocks affected by argillic alteration (Uesawa, 2008; Takahashi and Yahata, 2018). Tada and Tsuya (1927), and Itoh et al. (2004) suggested that the lahar was caused by snowmelt by hot debris avalanche with sector collapse of the Central Crater Cone. On the other hand, according to Uesawa (2008, 2014), the hydrothermal surge (Unit B) with hot water mainly caused snowmelt and bulldozing of older Unit A, subsequently followed by mixing of Unit A and B and flow as a violent lahar.

Sample description

Study samples were collected from every unit at the Northwestern slope of Tokachidake: Gfl-0, Gfl-1, Gfl-2, and 1926AD lahar deposit (Unit A-C) (Figs. 4a-4c, Table 1). This sample collection followed the geological description and stratigraphy done by previous studies (Fujiwara et al. 2007, 2009; Uesawa, 2008, 2014). Geological occurrence and a stratigraphic column for all unit sampled are shown in Fig. 3 and 4. All units sampled are ash matrix supported, poorly sorted pyroclastic deposits. For sampling, ash sized component (< 2mm) was collected from each of the outcropping units. In some outcrops, Gfl-2 occurs as two flow units (Gfl-2 upper and Gfl-2 lower) (Figs. 5, 6), and these were both collected. All samples are named as described in Table 1. As necessary, the above samples are expressed together with each eruption age, such as 4.7 ka-series (GFL-0), 3.3 ka-series (GFL-1, GFL-2L, GFL-2U), and 1926-series (1926-A, 1926-B,1926-C). In this study, one representative sample for each layer was analyzed in detail by the following method.

Methodology of sample analyses

The samples are very heterolithic because the pyroclastic deposits are constituted by mixtures of non-juveniles, including hydrothermally altered lithics. The lithic fragments are derived from altered and unaltered pre-existing rocks derived from each different portion. For this kind of heterogeneous mixtures of non-juveniles, textural observation of individual ash grains is useful to reveal alteration patterns and their formation process (Imura et al. 2019a). Therefore, this petrolographical observation was carried out on volcanic ash-sized grains (< 2 mm) in each sample.

For these ash grains, rock texture and mineral assemblages were carried out by a scanning electron microscope equipped with an energy dispersive spectroscope (SEM-EDS), and micro Raman spectormetry, and X-ray diffractometry (XRD) on powder bulk samples. Mineral identification is based on the XRD results, especially for very fine-grained clay minerals. However, bulk XRD analytical result does not reflect original rock texture and mineral assemblages from individual ash grains. Hence, a combination between spot analysis with SEM-EDS and bulk XRD was applied to identify mineral assemblages and rock texture of the ash grains. The petrographical observation under SEM-EDS analysis was carried out by Backscattered Electron Image (BSE). For the polymorph phased minerals, which cannot be distinguished by SEM-EDS, the in-situ identification was done by micro Raman spectrometry.

Sample preparation

Untreated ash samples were sieved into two fractions, 250 μm-1 mm (coarse) for spot chemical analyses and bulk XRD analysis, < 250 μm (fine) for bulk XRD analysis. For SEM-EDS analysis, the coarse fraction was prepared as a resin-filled polished section and carbon-coated. After SEM-EDS analysis, the polished section which had its carbon coating removed was used for analysis with micro Raman spectrometer. For bulk XRD analysis, both coarse and fine fractions are prepared as powdered samples crushed by agate mill. The powders filled in an aluminum sample holder as an unoriented sample, and the hydraulic elutriated samples (fine fraction) mounted on a glass disk as an oriented one, are analyzed with XRD.

Measurement conditions

Bulk mineral identification was made with a Multiflex; Rigaku Corp. XRD installed at Akita University, Faculty of International Resource Sciences. Measurements were carried out at a rate of 0.25° per minute from 2° to 65° using a CuKα target X-ray tube with an acceleration voltage of 30 kV and a filament current of 16 mA. For data processing, Integrated X-ray powder diffraction software (PDXL2: Rigaku Corp.) were used with the database from The International Centre for Diffraction Data (ICDD) and The Inorganic Crystal Structure Database of The Crystallographic Society of Japan. In cases when the X-ray peaks at 10 Å appeared, mica minerals or halloysite was distinguished by heating the sample at 120 °C for 90 minutes.

Semiquantitative microprobe analysis was carried out with a tungsten filament SEM-EDS (SEM: JEOL JSM-6610LV and EDS: OXFORD INCA X-act) installed at Akita University, Faculty of Education and Human Studies. The analysis was carried out at an acceleration voltage of 15 kV, a probe current of 2.2 nA, a working distance of 10 mm, and a live time of 30 s. The analytical value of major elements was obtained with an evaluation of EPMA standards (JEOL corp.), and of standard glass materials (Tokachi-Ishi obsidian) and igneous minerals which were previously analyzed by X-ray fluorescence (XRF).

Polymorphs of minerals were identified by using the micro Raman spectrometer (Renishaw inVia Reflex) coupled to a Leica DM2500M microscope with 100× long working distance lens. This system is installed at Akita University, Faculty of International Resource Sciences. For this analysis, an excitation laser source with a wavelength of 532 nm (Cobolt RL532150) was used at 150 mW laser power and 1 to 3 μm laser slit size. The spectrometer was calibrated using the Raman band of a silicon standard at 520.5 cm^{-1} by counting the spectrum within ± 1 cm^{-1} error of the standard peak. The measured Raman spectra were acquired with a duration of 1s, and simple accumulation. During this analysis, a background noise appeared because of the fluorescence at the epoxy resin filling the porous ash grains. In order to reduce the background, the analyzed points were selected from the massive-coherent areas (ca. 10μm×10μm) of minerals. Data were processed with the Wire 3.4 software package

(Renishaw). For mineral identification, the measured Raman spectra were compared with the reference data from the RRUFF project database [URL4].

Spot chemical analysis for individual ash grains by SEM-EDS

Feldspar, pyroxene, olivine, biotite, hornblende, chlorite, Fe-Ti oxide minerals, alunite, barite, apatite, and pyrite, were identified by comparison of the EDS spectrum and stoichiometric-empirical formula of each mineral. For Ca-sulfate, anhydrite or gypsum was determined with bulk XRD result.

In the case when very tiny minerals (less than several micrometers) was analyzed, the EDS spectra interfere from X-ray of adjacent mineral grains. Even though the BSE is homogeneous, some portions can include a mixture of very fine-grained minerals, causing mixed spectra from multiple minerals. These effects are very complex and problematic due to the limits of the spatial resolution of SEM-EDS. Therefore, this study evaluated the change of the EDS spectra by multiple analytical points. For example, a very fine-grained mixture of kaolin and silica will produce range of composition extending between two endmembers, pure kaolin (Si/Al = 1), and pure silica (Si/Al= ∞). Even if the Si/Al is close to 2, this case does not imply the existence of pyrophyllite. In addition, polymorph phases of silica and Fe-Ti oxide minerals are determined by the micro Raman spectrometer.

Mineral identification

The result of the bulk XRD analysis is shown in Table 2 and Fig. 7a-7c. All samples mainly contain quartz, tridymite, augite, cristobalite, plagioclase, kaolin minerals, and alunite. Although small X-ray peaks of 7Å-kaolin minerals appear in every sample, it was not possible to distinguish kaolinite, nacrite, and dickite because of their low X-ray intensities. Compared with the samples of 3.3 ka-series, the samples from 1926-series and 4.7 ka-series show high X-ray intensities for alunite and cristobalite, and low intensities for plagioclase (Fig. 7a, 7c). Only the 1926-series have the X-ray intensities of gypsum, anhydrite, jarosite, and pyrite. The peaks of gypsum dominate in the fine fraction while the peak of anhydrite is evident in the coarse fraction of 1926-series. The XRD

characteristics of 3.3 ka-series are the high X-ray intensities of quartz and two pyroxenes with the small peaks of sanidine, olivine, and mica minerals (Fig. 7b).

SEM-EDS semi-quantitative analysis specified silica minerals, pyrite, apatite, magnetite, titanomagnetite, ilmenite, alunite, anhydrite, jarosite, barite, titanium oxide, plagioclase, alkali-feldspars, two pyroxenes, olivine, biotite, hornblende, and chlorite. The Si/Al ratios changing from 1 to ∞ could indicate mixtures of silica minerals and minerals consisting of Si, Al, and O. Such minerals were identified as kaolin minerals in agreement with the bulk XRD result.

Micro Raman spectroscopy specified the following mineral phases: quartz, cristobalite and tridymite silica polymorphs, and anatase titanium oxide polymorph. From this analysis, many of the silica minerals identified with SEM-EDS were found to be quartz and cristobalite, whereas tridymite is very rare. In this paper, “silica minerals” is used to indicate the two silica phases, cristobalite and quartz.

Petrography of individual ash grain

Definition of descriptive terms

For this study, following terms are defined: “ash grain” is an individual and isolate grain of volcanic ash; “ash” is an aggregate of “ash grains.” Also, from the result of the microscopic observations, most of the ash grains are altered to various degrees. Therefore, the alteration degrees for the ash grains are defined as below. “Unaltered” ash grain is a grain consisting only of igneous minerals and volcanic glass without any alteration minerals. For example, each ash grain consisting of scoriaceous and pumiceous fragments or lava fragment or holocrystalline igneous rock fragment, was described as unaltered ash grains. These might not necessarily be a juvenile fragment. “Intensely altered” ash grain is an isolate grain consisting only of alteration minerals without any unaltered igneous minerals and volcanic glass. Finally, “weakly altered” ash grain is an individual grain with intermediate characteristics between unaltered and altered grains as defined above. Any partly altered grain is considered as “weakly altered” regardless of the ratio of unaltered and altered parts.

Classification of individual ash grains

Ash grains in the analyzed samples were divided into two group, unaltered and altered (weakly into intensely) ash grains. Besides, weakly to intensely altered ash grains are subdivided three types on the basis of the alteration mineral assemblages. Main alteration mineral assemblages in these ash grains are silica minerals only, silica minerals+alunite±kaolin minerals, and silica minerals+kaolin minerals. Therefore, the alteration types corresponding to these assemblages are defined as silica type, alunite type, and kaolin type, respectively. Any of these types frequently accompanies anatase, Fe-Ti oxide minerals, and minor pyrite. The petrography of the above ash grains, unaltered, silica type, alunite type, and kaolin type, is shown in the following sections in detail.

Unaltered ash grain

Most of this type of ash grains are igneous rock fragments consisting either of hypocrystalline-porphyritic texture or holocrystalline-equigranular texture. The ash grains with hypocrystalline-porphyritic texture are of highly-vesiculated scoria and pumice, and dense lava fragments. Phenocrysts of scoria and pumice are plagioclase (labradorite), augite, orthopyroxene and titanomagnetite. Their groundmass shows a typical hyaloophitic texture consisting of plagioclase, augite, orthopyroxene, titanomagnetite, olivine, and andesitic to dacitic glass. The groundmass texture of the ash consisting of dense lava fragments is intersertal, hyaloophitic, or hyalopilitic. Their phenocrysts are plagioclase, two-pyroxenes, olivine, and titanomagnetite. The groundmass consists of plagioclase, augite, orthopyroxene, pigeonite, hornblende, titanomagnetite, and dacitic to rhyolitic glass determined by SEM-EDS. The unaltered ash grains with holocrystalline-equigranular texture consist of mineral crystals with size of several tens of μm. The main minerals are hornblende, quartz, plagioclase, alkali feldspar (anorthoclase to sanidine), titanomagnetite, ilmenite, and rare biotite.

Silica type altered ash grains

This type of ash grains is characterized by the alteration part consisting predominantly of silica minerals. The silica minerals occur as a massive-coherent mono-crystal (“massive silica”) or a granular mixture of fine-grained crystals. In many cases, Ti-Fe oxide minerals, anatase, pyrite, and rare anhydrite occur as partial vugs infills. In

some cases, these oxides and sulfides occur as disseminated or vein minerals in the massive silica or a fine-grained mixture. Furthermore, the rock texture of the alteration part is different in various degree of silica type alteration.

Intensely altered ash grains of this type are divided into the ones consisting of massive silica with dissolution texture, and the ones with pseudomorph texture on original volcanic rocks. In the former cases, the massive silica entirely occupies the isolate ash grains which have many vugs. The vugs shaped as vein, columnar and irregular are very similar to the dissolution vugs of the dissolution silicification (dissolution texture, Fig.8a). In the latter cases, phenocrysts and groundmass minerals of original volcanic rocks have been replaced entirely by silica minerals (Fig. 8b). Silica minerals in the pseudomorphs occur a massive silica or the fine-grained silica.

For weakly altered ash grains which have large area of the alteration part, the massive silica occurs in scattered vugs and coexists with unaltered crystals of plagioclase and pyroxenes. The massive silica of the alteration part appears to have the same texture in the intensely altered grains above. For the ash grains which is occupied by unaltered volcanic rock part frequently, they show the pseudomorph texture of the original porphyritic texture replaced by the fine-grained mixture of silica minerals. Replacement alteration is disseminated in phenocrysts of plagioclase and pyroxene (Fig. 8c), and also in melt inclusions hosted pyroxene phenocrysts. Occasionally, the ash grains have the inner part consisting of unaltered porphyritic texture, and fine-grained alteration silica affecting the rims (Fig. 8d).

Alunite type altered ash grains

Ash grains categorized into this type are characterized by infill texture, whereby mixtures of minerals fill in various types of vugs. The mixtures consist mainly of silica minerals+alunite±kaolin minerals, and alunite in some cases. The occurrence of the infill textures is different in alteration degree, in terms of types of the filled vugs. As an example of the intensely altered ash grains, the mineral mixtures fill in the dissolution vugs in the massive silica part similar to the silica type. The weakly altered grains often show different infill texture which the mineral mixtures fill in the cleavage and fracture of primary igneous phenocrysts, the fractures in the unaltered groundmass glass, and

vesicles in the scoriaceous part. Furthermore, regardless of the above rock textures, the altered ash grains also contain disseminated or vein like anatase, pyrite, and Ti-Fe oxide minerals, and minor jarosite and barite with the same textures.

In most of the intensely altered ash grains, fine-grained alunite fills in dissolution vugs in the massive silica (Fig. 9a). In the cases when the interstitial materials are a mixture of silica minerals and alunite, these minerals occur as either fine grained (Fig. 9b) or coarse grained (Fig. 9c). For the latter cases, the interstitial material is sometimes anhedral alunite. Fig. 9b and 9c show each infill texture occurring in individual ash grains, accompanied by colloform silica. Also, in the intensely altered ash grains of alunite type, these are associated with replacement of the original volcanic rock texture. Their original porphyritic textures remain only as pseudomorphs of phenocrysts and groundmass. In this case, the pseudomorphs mostly consist of the replaced mineral mixtures of fine-grained silica minerals+alunite±kaolin minerals. However, the pseudomorphs only of phenocrysts sometimes show the replacement into the mixtures of silica minerals+kaolin minerals (Fig. 9d).

In the weakly altered ash grains, the occurrence of alteration minerals varies depending on the occupation of alteration part. Most of the ash grains predominately with the alteration part are accompanied by fine-crystal aggregates of silica minerals+alunite±kaolin, coexisting with unaltered volcanic rock parts (Fig. 9e). For some of them with the massive silica part, the dissolution vugs in the massive silica are filled with fine-grained crystal aggregates of silica mineral + alunite + kaolin mineral. This type of infill texture is much similar to that of intensely altered ash grains. The ash grains, predominantly with unaltered volcanic rock part, also show their infill texture. However, the vugs or fractures in the grains are incompletely filled. For example, although fine crystal aggregates of silica mineral, alunite, and kaolin mineral incompletely fill the vesicles in scoria, their groundmass hyaloophitic texture remains unaltered (Fig. 9f).

Kaolin type alteration ash grain

This type of ash grains is characterized by the altered part consisting of silica mineral+kaolin mineral without alunite. Other than the main alteration minerals, veined

anatase, Ti-Fe oxide minerals and rare chlorite occur in this type. Only this type of ash grains contains an unaltered part consisting of the igneous rocks with holocrystalline-equigranular texture. As in the case of the other two types, alteration varies in intensity.

Both the intensely and weakly altered ash grains have either a massive-fine-grained crystal aggregate or a replacement texture of the original porphyritic texture. The former ash grains consist of a fine-grained crystal aggregate of silica mineral+kaolin mineral (Fig. 10a). Some of them show colloform texture with layered silica mineral and kaolin minerals. The weakly altered ash grains which have the above textures and the massive, granular parts, most are occupied by the alteration part (Fig. 10b). In the latter case of the grains with the replacement texture, silica mineral+kaolin mineral aggregate replaces either of the holocrystalline-equigranular texture or the porphyritic texture of original igneous rocks and forms their pseudomorphs. The original igneous rocks above remain as the unaltered part of the weakly altered ash grains (e.g., holocrystalline-equigranular textured igneous rock, Fig. 10c), which is similar to that from unaltered ash grains. Some of the grains consisting mainly of porphyritic-volcanic rocks are only altered in their marginal parts (Fig. 10d). In other cases, the alteration minerals cover on the inside wall of scoria vesicles. This characteristic is similar to the incomplete infill texture (Fig. 9f) occurring in the alunite type alteration.

Componentry proportion of each type for all samples from every unit

The above ash classification was applied to the ash grains of the samples from each unit. The proportion of the classified ash grains was determined based on the petrographical observation for 21 to 63 randomly selected grains from each sample (Fig. 11). All samples mainly consist of the weakly altered ash grains which underwent silica type and alunite type alterations. In particular, the samples from 4.7 ka-series and 1926-series are characterized by a large proportion of silica type and alunite type altered ash grains, and by few unaltered ash grains. Although the alunite-type altered ash grains are dominant in the 4.7 ka-series samples, the 1926-series samples predominantly contain the ash grains categorized into the silica type in addition to the alunite type.

In contrast to the samples from the 4.7 ka-series and the 1926- series, the 3.3 ka-series samples are characterized by a large proportion of unaltered ash grains, and by the

existence of kaolin type altered ash grains. For the 3.3 ka-series samples, the componentry proportion of the ash grains is slightly different in each unit. GFL-1 and GFL-2L contain abundant weakly to intensely altered ash grains classified on kaolin type, while the unaltered ash grains are dominant in GFL-U. Furthermore, the unaltered ash grains contained in GFL-2L and GFL-2U are fragments of porphyritic-textured scoria and lava and holocrystalline-equigranular textured igneous rocks. Whereas, GFL-1 contains lava fragments or scoria as unaltered ash grains.

Discussion

Chemical condition of hydrothermal fluid inferred from alteration mineral assemblages and alteration petrology

Altered ash grains described in this study were probably derived from a subvolcanic hydrothermal system in which acidic hydrothermal fluid circulates and convects. For all samples from every unit, the altered ash grains consist mainly of silica minerals, kaolin minerals and alunite as the main alteration components. The existence of these alteration mineral assemblages is typical in the acidic alteration zone, such as the silicification zone and the advanced-argillic alteration zone (Hayashi 1973; Ossaka and Hirabayashi,1981; Ossaka, 1982, 2003; Hedenquist et al., 2000; Sillitoe,2010). Besides, dissolution texture with massive, vuggy silica (e.g., Fig. 8a), replacement and pseudomorph texture (e.g., Fig. 8b, 8d), and infill texture (Figs. 7a, 7c, and 7f) were observed in many altered ash grains. During alteration by acidic hydrothermal fluid, the fluids leach most of the cations from rocks, with exception of Si and Ti, which are immobile are remain as silica minerals and titanium oxide minerals (Nogami and Yoshida, 1993, 1995; Kikawata et al., 2000). The acidic hydrothermal fluid-rock interaction results also in the pseudomorphic replacement of primary minerals through precipitation of the alteration minerals (Stoffregen, 1987; Hedenquist et al., 2000). Therefore, the petrographic characteristics observed in all samples are consistent with the occurrence of the hydrothermally altered rocks. These points strongly suggest that most of the altered ash grains observed in this study derived from acidic alteration zones of the subvolcanic-acidic hydrothermal system of Tokachidake volcano.

The dissolution vugs and the pseudomorphs characteristic of silica type (Fig. 8a, 8b) also occur in alunite type and kaolin type alterations. Especially for the alunite type, the dissolution vugs in massive silica are filled with an anhedral-single crystal of alunite or a fine-grained crystal aggregate of silica minerals+alunite. This infill texture of alunite might be formed by the precipitation from the sulfuric-acid hydrothermal fluid flowing into the dissolution cavities. In this case, the silica type and alunite type alterations are possibly formed by a continuous series of acidic alterations. Although the kaolin type alteration might have proceeded with the dissolution silicification such as the silica type, the continuous relation with the alunite type alteration is unclear.

Colloform texture also occurs in the altered ash grains (Fig. 10b). This textures in the case of several acidic alteration zones are interpreted to be formed by precipitation of colloidal to meta-colloidal minerals from over-saturated hydrothermal fluid with rapid cooling or sudden boiling (e.g., Fournier, 1985; Dong et al., 1995). The colloform texture observed in this study is a compilation consisting of layers of silica minerals and kaolin minerals in the kaolin type grains. Such texture supposes to be the product that Si and Al-rich acidic fluids through leaching from the rocks had been at the conditions to precipitate the silica minerals and kaolin minerals repeatedly.

The following sections focus on fluid chemistry of the acid hydrothermal fluid related to the above hydrothermal alteration. Generally, the mixing process between meteoric-ground water and volcanic vapors has a significant role to form this type of acidic hydrothermal fluid in an active volcano. According to the experimental studies summarized in Giggenbach (1997), the hydration of sulfur dioxide (SO_2) and hydrogen chloride (HCl) in the volcanic vapor produces sulfuric acid and hydrochloric acid respectively, which form an acid-sulfate-chloride hydrothermal fluid. This acid hydrothermal fluid differentiates due to vapor-liquid separation and precipitation of sulfur-bearing minerals (mainly sulfates). As a result, sulfate ions (SO_4^{2-}) are produced from the gas phase, while the differentiated residual liquid forms chloride-acid hydrothermal water (Giggenbach, 1997). Therefore, the alunite type ash grains might be a reaction product by the interaction between the original igneous rocks and the acid-sulfate-chloride fluid (or acid-sulfate fluid), as suggested from abundant alunite in the ash

grains. This point indicates that such acid hydrothermal fluids were also the reactant for the silica type alteration, forming a continuous series with the alunite type alteration.

Since the kaolin-type alteration ash grains lack alunite, this type of alteration derives from different conditions and situations from the other two types. The petrographic characteristics of the kaolin type ash grains show that the kaolin minerals crystallized with dissolution silicification by acid-sulfate (or -chloride) hydrothermal fluid. However, the lack of sulfate suggests that the concentration of SO_4^{-2} in the hydrothermal reactant fluid was unable to precipitate the sulfate minerals. As one of the reactant fluids to satisfy these conditions, acid-chloride hydrothermal fluid might be reasonable, which has high leaching ability while low concentration of SO_4^{-2}. Furthermore, the kaolin type altered ash grains sometimes occur as partly altered grain of the holocrystalline-equigranular igneous rocks, while the other altered types do not occur in such rocks. Such differences in the original rocks might reflect differences in the origin of each type of hydrothermal alterations.

Reaction process estimated from petrography of weakly altered ash

All samples dominantly contain weakly altered ash grains with each type of alteration, which remain porphyritic textures containing the volcanic glass from the original volcanic rock. In this case, the alteration part develops from the surface of ash grains to a depth of several μm to 150 μm, and the unaltered volcanic glass is presented in the inner part (Fig. 8d, 10d). This texture indicates that the hydrothermal alteration proceeded from the fluid-rock interface to a depth of up to about 150 μm, and the reaction did not go further. This petrographic characteristics are completely consistent with the experimental study on the open-fluid-through system of Hara and Tsuchiya (2006, 2009). The summarized results given by Hara and Tsuchiya (2006, 2009) are below: (1) the reaction between hydrothermal fluid and rock proceeds from the fluid-rock interface toward the interior of rock sample. (2) a surface layer forms at the surface of a rock sample during fluid-rock interaction. The surface layer consists of a boundary layer convecting the reactant fluid, and the altered rock part proceeding cation leaching by the fluid. The inner part, distant from the altered rock part, is not altered. In the case of the weakly altered ash grains in Tokachidake, the acidic alteration consisting of silica minerals,

alunite, and kaolin minerals might correspond to the surface layer described by Hara and Tsuchiya (2006, 2009). Besides, the dissolution texture, the pseudomorph texture, and the infill texture of alunite might also correspond to the altered rock part described by Hara and Tsuchiya (2006, 2009). In an open-flow-through system, such acidic alteration mineral assemblages should be stable at very high F/R (fluid per rock) ratio (Reed, 1997). Therefore, the above conditions and situations can be explained by a reaction process whereby a large amount of acidic hydrothermal fluid passes through and reacts with the rocks.

According to the experimental study of Nogami and Yoshida (1993), several tens μm sized powder of volcanic rock are completely silicified in a few days when reacted with an acidic solution at 160 °C. Although this reacting duration cannot simply apply for the Tokachidake case, the rough comparison between the two cases help understanding the rock texture of the Tokachidake ash grains. In both cases, the sizes or the scale of the altered portions are not far different, and both cases show that the alteration develops with a thickness or a distance of several tens μm. Also, the temperature conditions of Nogami and Yoshida (1993) are much lower than the conditions (100 to 500 °C [URL1]) under the Tokachidake vent. These points suggest that the duration of fluid-rock interaction of Tokachidake might be the same as in the experiments of Nogami and Yoshida (1993) or shorter with much higher temperature. At least, such brief, incomplete interaction (alteration) is an essential factor to form the weakly altered ash grains, in addition to the reaction process discussed in the previous paragraph.

Subvolcanic hydrothermal system of Tokachidake volcano

Tokachidake volcano had repeated the volcanic eruptions accompanied by magma intrusion (Fujiwara et al., 2007, 2009; Ishizuka et al., 2010) [URL1]. Before and after such eruptions, the number of volcanic earthquakes and tremors often increases with raising average temperature in the crater [URL1]. In particular, during the 1989 magmatic eruption, the crater temperature temporarily increased to approximately 600 °C, and subsequently decreased rapidly. Moreover, the chemical composition of the hot spring water at Fukiage hot spring changed prominently during the 1989AD eruption. This change implies that the hot spa water was affected by the injection of NaCl rich water

separated as magmatic fluid from the 1989AD intruded magma (Takahashi et al., 2015). During the 1985AD and 2004AD non-juvenile (or phreatic) eruptions, the average temperature in the crater rose to approximately 500 °C, and the number of volcanic earthquakes and tremors increased. The crater temperature rise, volcanic earthquake, and tremor increase, and the chemical composition change of hot spring water might have been the precursory surface phenomena reflecting the changes caused by a magma intrusion to shallower portion. Indeed, a magma intrusion possibly occurs under the vent area during these eruptions, regardless of the eruption styles even of the non-juvenile type.

High-temperature volcanic vapors separated from the intruded magma rise into the shallow aquifer, and the acidic and high-temperature hydrothermal system develops in the shallow area. Such a process is possible to be strongly affected by volcanic vapors. These processes can explain that the ash grains in the Tokachidake samples record the hydrothermal alteration by the acidic hydrothermal fluid affected by the volcanic vapors. Furthermore, as discussed in the previous sections, the rock textures of the weakly altered ash grains are the products formed by the brief, incomplete, hydrothermal fluid-rock interaction. Assuming that acidic alteration occurred temporarily during magma intrusion, this instant fluid-rock interaction is reasonably consistent with those volcano monitoring results such as short-term crater temperature rises, volcanic earthquakes, and tremors. At such time, the physicochemical conditions of the subvolcanic hydrothermal system would have changed significantly in a relatively short period from that of the quiescence.

Summary and conclusions

From the petrological observations of individual volcanic ash grains in the Tokachidake Holocene products of the 4.7 ka eruption, 3.3 ka eruption, and 1926AD eruptions, the following conclusions were obtained.

1. Each sample consists of ash grains altered to various degrees from unaltered to intensely altered. All types of the altered ash grains are derived from the acidic alteration zone in the subvolcanic hydrothermal system of Tokachidake. The hydrothermal

alteration was affected by the acid-sulfate-chloride hydrothermal fluid formed by the volcanic vapor separated from the intruded magma.

2. The rock textures of the weakly altered ash grains were formed by the acidic hydrothermal fluid-rock interaction closer to open-flow through-system. The reaction process is explained by a large amount of acidic hydrothermal fluid passing through and reacting with the rocks. Furthermore, the reacting duration was brief.

3. The brief, incomplete, acidic hydrothermal alteration was caused by the Tokachidake subvolcanic hydrothermal system temporally formed with a magma intrusion.

Chapter 2: Volcanic ash from the 2014 hydrothermal eruption of Ontake volcano

Study background

Ontake volcano is considered to have a developed subvolcanic hydrothermal system correlated with the epithermal-porphyry environment (Minami et al., 2016; Imura et al., 2019b). In contrast to the Tokachidake case, Ontake volcano had repeated non-juvenile eruptions (1979AD, 2004AD, and 2014AD) which were accompanied without the evident precursory signs and with the emission of hydrothermally altered rock and a limited amount of hot-muddy water [URL5]. These points suggest that the Ontake is an appropriate case to understand the magma-hydrothermal system interaction dominated by an active hydrothermal system. Primarily, this chapter documents on the results of petrographic observation on the 2014AD Ontake eruption product, published in Imura et al. (2019b) and Minami et al. (2016).

Focused introduction

Aluminum-phosphate-sulfates minerals (APS) are isostructural with the alunite-jarosite family, within the alunite supergroup. Their chemical formula is generally expressed as $AB_3(XO_4)_2(OH)_6$, where A is a large cation (Na, K, Ag, H_3O, NH_4, Pb, Ca, Ba, Sr, REE) in 12-fold coordination, B is occupied by cations of the elements Al, Fe, Cu, or Zn in octahedral coordination, and X is dominated by S, P, or As (Scott, 1987a, 1987b; Stoffregene and Alpers, 1987; Smith et al., 1998)[URL6]. This supergroup includes the alunite group (sulfate), beudantite group (phosphate-sulfate), plumbogummite group (phosphate) and dussertite group (arsenate) (Scott, 1987a, 1987b; Mills et al., 2009; Bayliss, et al., 2010). The natural APS minerals form complex solid solutions (s.s.) consisting of various endmembers within these groups (Dill, 2001) (Table 3). Chemical compositions of their s.s. reflect varying Eh, fO_2, pH, and activity physicochemical conditions of crystallization within metamorphic, igneous (both plutonic and volcanic), and sedimentary settings (Dill, 2008; Heald et al., 1987; Stoffregen and Cygan, 1990; Stoffregen and Rye, 1994; Beaifort et al., 2005; Gaboreau, et al., 2005, 2007).

APS minerals hosted in igneous rocks typically occur as a result of secondary alteration, whether hydrothermal or with supergene (weathering) in epithermal and

porphyry ore systems. Occurrences of APS have been reported in numerous previous studies of ore deposits applying a variety of analytical methods including host-rock petrography, fluid-inclusion geothermometry, and stable isotopic analysis. According to these studies, APS are present in hydrothermally altered volcanic rocks that are altered to advanced argillic and silicic alteration assemblages (Aoki et al., 1993; Arribas, et al., 1995; Hedenquist et al., 1994; Matsubara et al., 1998; Dill et al., 1995, 1997, 2000; Ando et al., 2005; Hedenquist et al., 2017). In these cases, euhedral, commonly bladed, hydrothermal alunite often shows a core of APS with crandallite-woodhouseite-svanbergite (Table 3) compositions (Aoki et al., 1993; Arribas, et al., 1995; Hedenquist et al., 1994; Matsubara et al., 1998; Dill et al., 1995, 1997, 2000; Ando et al., 2005; Hedenquist et al., 2017). APS are detected also along the contact between alkaline-igneous rocks and arigillitic country-rocks, coexisting with cement phased minerals (Calcium Silicate Hydrate (CSH), Calcium Aluminum Silicate Hydrate (CASH)) (Stoppa et al., 2010; Stoppa and Schiazza, 2014). Fluid inclusion microthermometry and stable isotopic geothermometry indicate formation temperatures between 200 °C and 350 °C (e.g., Arribas et al., 1995; Hedenquist et al., 1994; Hedenquist et al., 2017). Hydrogen, oxygen, and sulfur isotopic studies from APS and associated sulfates and sulfides show that the precipitation of APS is related to mixtures of S-rich magmatic volatiles, hydrothermal fluids, and meteoric groundwaters (Aoki et al., 1993; Arribas, et al., 1995; Hedenquist et al., 1994; Ando et al., 2005; Hedenquist et al., 2017).

Given the similarity in geologic setting, APS minerals should also occur in altered rocks associated with active volcanoes. Samples from some active volcanoes are indeed rich in hydrothermal alunite (Takano and Watanuki, 1990; Tomita et al., 1994; Ohba and Kitade, 2005; Minami et al., 2016). These products have been interpreted to be derived from sulfuric acid-rich subvolcanic hydrothermal systems. APS from an active volcano will help understand subvolcanic hydrothermal processes, providing a mineralogical record of the pre-eruptive physicochemical conditions within the subvolcanic hydrothermal system. However, occurrences of APS in active volcanic systems have not been reported. This study aims to document the presence of APS mineral in volcanic products from active volcanoes by examining samples of alunite-bearing altered rock from the 2014 hydrothermal eruption of Ontake volcano in central Japan

(Minami et al., 2016).

Geological backgrounds

Geological setting

Ontake volcano (3,067 masl), located in central Japan (Fig. 12), is a stratovolcano consisting of basalt, andesite, and dacite lava and pyroclastic rocks. This volcano overlies basement rocks composed of Jurassic to Paleogene rhyolitic to rhyodacitic volcanic and marine sedimentary rocks (Yamada and Kobayashi, 1988; Takeuchi et al., 1998). Older volcanic activity at Ontake (200-300 ka) formed an early edifice by effusion of basaltic and andesitic lava with minor dacite (Yamada and Kobayashi, 1988). The younger activity (< 80 ka) that formed the current edifice is subdivided into an early (78－39 ka) explosive stage of rhyolitic to dacitic magma and a younger (< ~10 ka) stage of effusive andesite lava (Takeuchi et al., 1988; Matsumoto and Kobayashi, 1995, 1999; Kioka et al., 1998). The summit area around Kengamine peak (Fig. 12) is composed of the young andesite lava (Yamada and Kobayashi, 1988).

During the Holocene, non-juvenile eruptions have occurred more frequently at Ontake volcano than magmatic eruptions. The frequency of the non-juvenile eruptions has been estimated to be ~0.6/ky, double that of the magmatic eruptions (Oikawa, et al., 2014. 2015). Before the 2014 eruption, three non-juvenile eruptions were witnessed in 1979, 1991, and 2007 (JMA, 1991; Nakamichi et al., 2009; Oikawa et al., 2014), suggesting a higher frequency than 0.6/ky. Geothermal manifestations have developed on the southwestern flank of Kengamine cone for at least the last 250 years (Oikawa, 2008). Hydrothermally altered rocks were exposed in the same area prior to the 2014 eruption.

Volcanic ash from the 2014 hydrothermal eruption

The eruption on 27th September 2014 took place on the southwestern flank of Kengamine peak. This eruption ejected approximately one million tonnes of volcanic ash, an estimated volume similar to that of the 1979 eruption (Takarada et al., 2016). The Volcanic Explosivity Index (VEI) of the 2014 eruption was two [URL5][URL7]. The volcanic ash draped the surface of the summit area and the eastern flank (Maeno et al.,

2016; Oikawa, et al., 2016) [URL2] [URL5]. Geophysical studies reported precursory seismicity linked to the eruption (Kato et al., 2015; Maeda et al., 2015; Ogiso et al., 2015).

The ash of the 2014 eruption is composed of abundant altered lithic fragments and minor unaltered volcanic rock fragments (Miyagi et al., 2014). Based on the study of individual ash particles, Minami et al. (2016) classified the alteration into five types: silica–pyrite, silica+pyrite±alunite±kaolin, silica+pyrophyllite+pyrite, silica+muscovite±chlorite, and silica+K-feldspar±albite±garnet±biotite. These results indicate that the ash grains were derived from an active subvolcanic magmatic-hydrothermal system existing under the crater and consisting of silicic, advanced argillic, phyllic, and potassic alteration zones. Minami et al. (2016) interpreted these zones as comparable to the alteration zones in a porphyry copper system (Fig.13) (Silitoe, 2010). Another study on the volcanic products reported a sulfur isotopic equilibrium temperature of ca. 286 °C, based on the assumption of equilibrium between sulfate (gypsum and anhydrite) and pyrite (Ikehata and Maruoka, 2016). These results clearly show that the 2014 eruption was a hydrothermal eruption (Browne and Lawless, 2001) driven by a convecting hot water or steam-dominated hydrothermal system. In this paper we use the term “hydrothermal eruption” (Browne and Lawless, 2001) to best describe the 2014 Ontake eruption.

Methodology

For this study we used an ash sample documented in Minami et al. (2016). The sample was collected four days after the eruption, at a roadside point (35°54’29.00” N, 137°34’06.23” E) 8 km northeast from the vent (Fig. 12). The sample consists mainly of fine (< 250 μm) ash. A relatively coarse fraction (70 - 125 μm) obtained by sieving was prepared for a polished section using epoxy resin. The polished section was observed with a JEOL JSM-6610LV scanning electron microscope (SEM) coupled with an Oxford Instruments energy dispersive X-ray spectrometer (EDS) at Akita University and a JEOL JSM-7100F field emission (FE) SEM and Oxford Instruments EDS at Hokkaido University. Grain morphological, textural, and petrographic observations were made using backscattered electron images (BEI). Qualitative and semi-quantitative chemical

analyses were obtained using the EDS spectra. The analytical instrumental conditions were: 15 kV acceleration voltage, probe current of 2.2 nA (SEM-EDS) and 0.5 nA (FE-SEM-EDS), 10 mm working distance, and a 20 second live time.

Mineral identification

Semi-quantitative chemical analyses by EDS were carried out to identify APS minerals. APS minerals are defined by the stoichiometric formula (Na, K, Ag, H_3O, NH_4, Pb, Ca, Ba, Sr, REE) (Al, Fe, Cu, and Zn)$_3$ ((S, P, As) O_4) $(OH)_6$ (Scott, 1987a, 1987b; Stoffregene and Alpers, 1987; Smith et al., 1998)[URL6]. Crystals with spectra consisting of O, S, P, Ca, and Al were identified as APS minerals (Fig. 14). In this paper, we use the general name of "APS" to express the designate s.s. between endmember compositions listed in Table 3. For example, the APS crystals consisting mainly of P, S, Ca are denoted by "woodhouseite-APS" (woodhouseite composition-rich APS). Alunite crystals with spectra consisting of O, S, Al, Na, K, and Ca were distinguished from APS (Figs. 14 and 15). In many cases, these alunite crystals consist of Na-Ca-K in various proportion. We simply express the alunite as the designate s.s. of Na, K, and Ca endmembers (Table 3). For example, Na-K rich alunite is expressed as "Na-K-alunite".

For the mineral identification, we basically followed the results of the XRD, and SEM-EDS analyses done by Minami et al. (2016) (Table 4). In addition to the previous result, Zn-bearing mineral, monazite, alkali feldspars in this samples were identified also from the EDS spectrum and stoichiometric-empirical formula of each mineral. Si-Al clay minerals were identified as pyrophyllite and kaolin minerals, based on the change of Si/Al ratio from the spot chemical analysis. However, the EDS analysis cannot identify the polymorphs, such as silica minerals (quartz-cristobalite-tridymite) and titanium oxide minerals (rutile-anatase-brookite). Furthermore, kaolin group minerals cannot be subdivided into nacrite, kaolinite, and dickite. Therefore, we use the inclusive terms: silica mineral, titanium oxide and kaolin mineral.

Classification of ash grains related to APS minerals

APS minerals were observed in the volcanic ash grains altered to advanced argillic and silicic assemblages (Minami et al., 2016). The main types of ash grain bearing

the APS are divided into three types based on their mineral assemblages and rock textures. Even though these types were not reported as APS and alunite bearing ash grains (Minami et al., 2016), this study found both sulfates also in those types (Imura, et al., 2019). The following description for the three types is from the observation of Minami et al. (2016) (Fig. 16a-16f).

Silica mineral+pyrite

This type was described and defined by Minami et al. (2016) as residual silicified alteration (RA). This association consists dominantly of silica mineral, subordinate pyrite, and minor rutile. Grains of this association are abundant in the ash. They appear opaque white under a binocular microscope. This association includes various textures: pseudomorphic replacement of original volcanic rock textures (Fig. 16b), colloform texture, and mosaic texture. The grains are composed of silica minerals, minor pyrite, and rutile. The pseudomorphic textured grains preserve the original volcanic rock textures, although the original minerals have been completely replaced, mostly by silica mineral. The grains are rich in voids that are spherical, tabular, veinlet, and irregular in shape. The voids range from submicron to hundreds of μm in size, and small voids often form spongy textures. Pyrite crystals frequently fill the voids and the cleavage of the pseudomorphs of phenocrysts (Figs. 16b, 16c). The pores in the highly porous grains are spherical, tabular, vein-like, and irregular in shape and range from several hundred to just a few micrometers (Fig. 16c). The spherical pores are larger than the other types and have diameters of several hundred μm. Tabular-shaped pores typically range from few μm to few tens of μm. The grains with colloform texture consist of micron-width wavy bright bands and darker matrix on BEI (Fig. 16d). The colloform grains contain void veins and irregular-shaped pores (Dong et al. 1995; Fig. 16d). Mosaic-textured grains consist of tens-μm-sized equant interlocking quartz crystals. The crystalline rock fragments contain pores ranging from submicron to tens of μm.

Silica mineral+pyrite ± alunite ± kaolin minerals

This type was described and defined by Minami et al. (2016) as advanced argillic alteration (AA). The association of silica mineral+pyrite ± alunite ± kaolin minerals is the most common of the ash grains. Grains with this assemblage appear as opaque white-

colored or opaque gray-colored under a binocular microscope. The original minerals have been entirely replaced by silica mineral, alunite, kaolin-group mineral, rutile, and pyrite through hydrothermal alteration. The grains are classified into three types according to textures: pseudomorphic volcanic texture, fine-grained texture, and coarse mosaic texture. Grains with pseudomorphic volcanic texture are rich in vugs and preserve textures of the original volcanic rocks that are porphyritic, hyaloophitic, or hyalopilitic. Some vugs are rectangular, indicating that the original crystals had been dissolved during alteration, although some crystals have been replaced by silica mineral or kaolin (Fig. 16e). Other vugs are spherical, vein-like, and irregular in shape, ranging from a few to several hundred μm. Pyrite and alunite crystals fill some of the vugs and cleavages of the pseudomorphic crystals. Grains with fine-grained texture show no sign of original rock texture but merely consist of fine-grained crystals. These grains are rich in μm-size vugs that are spherical or irregular and contain densely distributed submicron vugs forming a spongy texture. The coarse mosaic texture consists of tens- to μm-sized equant silica, euhedral to anhedral alunite, and intercrystalline voids. Flaky or massive crystals of alunite fill some of the voids.

Silica minerals+pyrophyllite+pyrite

This type was described and defined by Minami et al. (2016) as advanced argillic alteration (AA). The association of silica minerals, pyrophyllite, and pyrite is common, occurring as opaque gray-colored or transparent grains. The original texture is completely lost, and the original minerals have been replaced by silica mineral, pyrophyllite, pyrite, and minor rutile. Some grains comprise anhedral silica crystals and fine-grained matrix of pyrophyllite (Fig. 16f). The silica mineral grains range from 1 to 100 μm in size. Some silica grains contain abundant micron-sized spherical pores. The matrix pyrophyllite occurs as an aggregate of fine flaky crystals or very fine spongy texture dotted with euhedral pyrite crystals. The very fine matrix contains irregular shaped voids. Some pyrophyllite-bearing grains consist solely of very fine-grained pyrophyllite with such voids.

Occurrence of APS minerals

The mineral assemblage, alteration type, and occurrence of the woodhouseite-APS in the ash grains studied is summarized in Table 5. Woodhouseite-APS crystals commonly occur as cores of euhedral alunite crystals. Two crystal textures were observed: zoned alunite-woodhouseite-APS and micro-wormy vein woodhouseite-APS. The former is more abundant in the examined altered ash grains (Table 5).

Zoned alunite-woodhouseite-APS: This type of occurrence is characterized by compositionally zoned alunite crystals. In BSE, the crystal consists of a bright core and a dark rim. As shown in Fig. 17 (the EDS elemental intensity profile corresponds to the scan line in the BSE image), the X-ray counts per second (cps) for Ca and P Kα1 peaks are high in the core and low in the rim, whereas those for S, Na, and K show an inverse relationship. This profile indicates that the woodhouseite-APS component (Ca-P and low S) is more abundant in the core than in the rim, which has an alunite composition. Most alunite rims were found to have chemical compositions close to Na-K-alunite.

Zoned alunite-woodhouseite-APS appears in a variety of occurrences within ash grains classified as advanced argillically- or residual/vuggy silica-altered, according to Minami et al. (2016). In one type of occurrence, individual zoned alunite-woodhouseite-APS crystals typically range between 10 and 50 micrometers in size (Fig. 18a, 18b, Table 5). Within these zoned alunite-woodhouseite-APS crystals, an internally homogenous core of woodhouseite-APS, which in many cases shows a texture suggesting partial dissolution, is surrounded by concentric polygons of woodhouseite-APS and, further out, by euhedral alunite (Fig. 18b). A fine mixture of silica mineral(s) and pyrophyllite fill the interstitial spaces.

Zoned alunite-woodhouseite-APS is also observed in irregular aggregates of coarse alunite crystals (Fig. 18c, 18d). In this case, woodhouseite-APS occur as what appear to be partially dissolved, often fibrous, clusters within the surrounding alunite, which is typically concentrically zoned. Within the alunite surrounding the woodhouseite-APS, the inner rims have a chemical composition closer to K-alunite and the outer rims are closer to Na-Ca-alunite.

Another type of occurrence of zoned alunite-woodhouseite-APS is shown in Fig. 18e and 18f. The ash grain comprises a massive silicified part and irregular or vein-like

open spaces or vugs, which are partially filled with an aggregate of zoned alunite-woodhouseite-APS. Similar to those described previously, the alunite crystals contain woodhouseite cores. The crystals are smaller (submicron to ca. 10 μm) than the other two types (Fig. 18f).

Micro-wormy vein woodhouseite-APS: In this type of occurrence, the APS mineral forms a homogeneous single-phase in microveinlets reminiscent of the wormy texture used to describe intergrowths between quartz and advanced argillic alteration minerals, such as pyrophyllite, dickite or alunite, in porphyry copper systems of the Cajamarca region of northern Peru (c.f. Gustafson et al., 2004). At Ontake a similar texture is observed in mineral mixtures of silica and woodhousite-APS or kaolinite/dickite (Fig. 19a, 19b). The typical size of the wormy-veins is less than 10 μm in width (Fig. 19b). The micro wormy-vein woodhousite-APS texture occurs as an intricate network of silica and woodhouseite-APS with silica occasionally crosscutting the woodhousite-APS.

Other remarks than APS

Zn-sulfide mineral (possibly sphalerite) also occurs as a component of this ash sample, mainly in the altered lithic ash grain. The Zn-sulfide crystals are several tens of μm in size and are subhedral to anhedral (Fig. 20a-20c). They are typically contained in the AA ash grains with silica+alunite+pyrophyllite+pyrite assemblage (Fig. 20a), and the ones with very fine-grained silica+kaolin+gypsum (Fig. 20b). In some cases, the Zn-sulfide crystals occur as isolated free crystals (Fig. 20c). However, Zn-sulfide-bearing ash grains are rare in this sample, compared with the abundant pyrite and gypsum.

Ash grains consisting of unaltered holocrystalline-igneous rock also occur in this sample. They form holocrystalline-equigranular texture composed of the mineral assemblages of silica+orthopyroxene+augite+biotite+ilmenite+alkali feldspars (sanidine to anorthoclase)+monazite with no glassy materials (Fig. 21). The componential mineral crystals are all anhedral, and especially massive Orthopyroxene is a part of subophitic texture seemed like intestinal material. For the monazite crystals, their EDS spectrum clearly shows the X-ray intensities of P, La, Ce, Nd. The average chemical composition of the entire grain is closer to andesitic composition. These points possibly indicate that

the ash grain derived from fragmentation of deep portion consisting of the hypabyssal or plutonic andesitic body.

Discussion

Subvolcanic hydrothermal system similar to high-sulfidation epithermal-porphyry system

Non-juvenile eruptions, including phreatic (or hydrothermal) and phreatomagmatic (or magmatic-hydrothermal) (Browne and Lawless, 2001) frequently bring to the surface altered lithic fragments from sub-volcanic hydrothermal systems (e.g., Hedenquist and Richard, 1985; Ohba and Kitade, 2005; Ohba et al., 2007; John et al., 2007). The woodhouseite-APS-bearing ash erupted from the September 2014 hydrothermal eruption of Ontake volcano is derived from pre-existing altered rocks under the Kengamine summit crater (Fig. 22). These rocks formed in the sub-volcanic environment within an active magmatic-hydrothermal system. The ash grains containing APS minerals consist mainly of hydrothermal minerals, including silica, pyrophyllite, kaolinite/dickite, and alunite. The stability temperature conditions of the mineral assemblages in that style of hydrothermal environment range between ~150 and 350 °C under highly acidic conditions (Hayashi, 1973; Brown, 1978). This temperature range is consistent with the temperature of 286 °C determined by sulfur isotopic fractionation between sulfate and sulfide minerals in volcanic products also from the Ontake 2014 eruption (Ikehata and Maruoka, 2016). These genetic conditions indicate a magmatic volatile-rich hydrothermal environment, which is directly comparable with that observed in the early alteration stage of high-sulfidation epithermal ore Au-Cu-Ag-As deposits (Arribas, 1995) and the advanced argillic alteration lithocaps above porphyry copper deposits (e.g., Hedenquist et al., 1998; Silitoe, 2010l; Hedenquist et al., 2017). This genetic linkage is also implied from the existence of the Zn-sulfide bearing ash grain in this sample. This point might confirm the genetic association proposed among porphyry coppers deposits, some epithermal deposits, and hydrothermal systems within the core of active volcanoes in magmatic arcs (Hedenquist and Lowenstern, 1994). Furthermore, the Ontake eruption derived from the various portions of the volcanic edifice in terms of depth, wide, and alteration, even accompanying with the hypabyssal or plutonic igneous

rock body other than the fresh volcanic rocks.

The occurrences described here of both zoned alunite-woodhouseite-APS, and micro-wormy vein woodhouseite-APS are similar to hydrothermal APS and alunite from epithermal-porphyry ore systems (Hedenquist et al., 1994; Matsubara et al., 1998; Ando and Tsutsumi, 2005). For example, both at the Rodalquilar gold-alunite epithermal deposit in Spain (Arribas et al., 1995) and the world-class Far Southeast (FSE) porphyry Cu-Au-Ag deposit in the Philippines (Hedenquist et al., 2017), euhedral-bladed hydrothermal alunite contains identical cores of APS minerals (Fig. 23a, 23b). Similarly, hydrothermal APS has also been observed as a monomineralic vein (Aoki et al., 1993) comparable to the micro-wormy vein woodhouseite-APS at Ontake volcano. Although those two types found by this study show different textures, both types formed under similar genetic conditions within subvolcanic advanced argillic and silicic alteration zones (Minami, et al., 2016).

Process of the 2014 eruption

The monitoring of volcanic earthquakes and tremors around the 2014 eruption shows the following characteristics. (1) Micro seismicity increased beginning around two weeks before the eruption, and subsequently, the shallow volcano-tectonic earthquake (VT) sharply again increased less than 10 min again before the eruption (e.g., Kato et al., 2015). (2) The hypocenter of the VT events was concentratedly located 2-3 km below the summit (e.g., Kato et al., 2015; Maeda et al., 2015; Ogiso et al., 2015). The local subsidence as deflation also occurred shallow (~500 m beneath the vents) (Narita and Murakami, 2018) and deep (~3-6 km beneath the vents) (Murase et al., 2016; Narita et al., 2019) determined by grand deformation analysis from In SAR and GNSS data.

These results are consistent with the material source model of Minami et al. (2016), implying that the reservoir of hydrothermal fluid related to the eruption can be located around 2-3 km beneath the vents. The hydrothermal fluid should be at hydrothermal temperature (ca. 200-300 °C) suggested from mineralogical and sulfur isotopic studies (Minami et al., 2016; Ikehata et al., 2016; Imura et al., 2019b). Furthermore, the ground temperature at Ohtaki vent area near the top of summit had been almost constant around 100 °C during 1970AD to 2015AD [URL2]. Those points do not

significantly show affection of magma or magmatic vapors to the hydrothermal system beneath the Ontake at least in 2014AD eruption. In the case the well-developed hydrothermal system are present in the edifice, there should be the portion showing the vertical temperature distribution almost constant at 200-300 °C by fluid convection in scale of 2-3km depth, which is similar to the case of geothermal system (ex. Kakkonda geothermal area reported by Ikeuchi et al., 1998; Muraoka et al., 1997). Therefore, for the 2014AD eruption as explosion of the hydrothermal system, the fluid expansion by depressurization of the hydrothermal fluid (200-300 °C) might be one of considerable factors.

Here this study shows one idea to explain the 2014 eruption process below. (1) The VT increase of two weeks before the eruption might have formed open cracks wall rocks of the hydrothermal system. Trigger of the VT event was unclear, which had been caused by weather rise of magma and magmatic vapor or tectonic earthquake of fault. (2) Hydrothermal fluid or hydrothermal gas rose up to the shallow portion through the open cracks developed by hydraulic fracturing (e.g., local subsidence). (3) Hydrothermal fluid moved to shallower with decompression during the hydraulic fracturing and reached critical condition for flashing (the VT increase 10 min before the eruption). These three steps might be consistent with the deep and shallow deflation source.

Summary and conclusions

The petrographical and mineralogical study of ash grains from the 2014 Ontake volcano hydrothermal eruption resulted in the following conclusions.

1. APS minerals such as woodhouseite, Zn-sulfide, and monazite occur also in active volcanoes. The discovery of woodhouseite in the volcanic ash of the Ontake 2014 hydrothermal eruption represents the first reported presence of these minerals within an active volcano. This is an obvious similarity with the epithermal-porphyry environments.

2. Two types of woodhouseite were observed: zoned alunite-woodhouseite-APS and micro-wormy vein woodhouseite-APS. The genetic environment of APS minerals is proposed to be highly acidic hydrothermal fluids existing beneath the volcanic summit, formed by condensation with magmatic and/or ground waters of magmatic volatiles exsolved from the magma chamber underneath Ontake volcano. Under these conditions,

an advanced argillic alteration assemblage formed, consisting of silica, pyrophyllite, alunite, and kaolinite/dickite, plus APS, among other minerals.

3. Further detailed studies might prove that the presence of APS at Ontake is not an exception, but rather commonplace among such active volcanoes.

Chapter 3: Holocene volcanic tephra layers around 1331AD from Azuma-Jododaira volcano

Study background

This chapter aims to elucidate the evolutional process and the repeating styles of the complex interaction between magma and hydrothermal system, focusing on the ash petrology for volcanic successions. This study focuses on the case of Holocene volcanic tephra layers erupted around 1331AD from Jododaira volcano of Azuma volcanic groups, Fukushima, central Japan (Yamamoto, 2005). The Jododaira volcano had experienced explosive eruptions since the formation at Azuma-Kofuji around 6 ka. After that, the repetitions of small-magmatic and non-juvenile eruptions formed the volcanic successions named as "Azuma-Jododaira product" (Yamamoto, 2005). The products consist basically of tephra layers of the vulcanian or non-juvenile eruptions (Yamamoto, 2005). In this study, a petrologic observation was carried out, on each volcanic succession around 1331AD Az-OA non-juvenile eruption tephra layer of Azuma-Jododaira volcanic products.

Geological background

Azuma volcano—Jododaira volcano

Azuma volcano is a basaltic andesitic to andesitic parasite volcano group, located in western part of Fukushima city, Fukushima prefecture, central Japan (Fig. 24). This volcano overlays the basements composed of Cretaceous hornblende-biotite granodiorite, and middle to late Miocene dacitic tuff breccias, belonging to the Hibara Formation, Yuzuritoge Formation, Itaya Formation, and Yokomuki Formation (NEDO, 1991; Kubo et al., 2003; Furukawa, et al., 2018; Matsumoto et al., 2018). The volcanic edifice consists of andesitic cones named as Nakadaiten, Higashidaiten, Nishidaiten, Nishiazumayama, Nakaazumayama, Higashiazumayama, Azuma-kofuji, Issaikyoyama, Takayama, and much older andesitic edifices where have already been dissected (Fujinawa amd Kamoshida, 1999).

At Azuma volcano, effusions of andesitic lava flows had been dominant as the volcanic activity until the formation of Azuma-kofuji pyroclastic cone. Matsumoto et al. (2018) carried out K-Ar dating for the above lavas. According to Matsumoto et al. (2018), the parasitic edifices comprised of Azuma volcano are divided into twelve units listed below (Fig. 25a, 25b): Shio-no-gawa volcano (1200 to 1000 ka), Takakura-Yama volcano (900 to 740 ka), Naka-Daiten and Higashi-Daiten volcanoes (700 to 510 ka), Nishi-Daiten and Nishi-Azuma-Yama volcanoes (420 to 370 ka) including Tengu-Iwa volcano, Naka-Azuma-Yama volcano (370 to 240 ka), Eboshiyama volcano (200 to 30 ka) including Higashi-Azuma-Yama and Taka-yama volcanoes, and Issaikyo-yama volcano (520 to 170 ka) with basaltic Mae-Daiten volcano. After the activity of Issaikyo-yama stage, the eruptive center was moved onto Jododaira volcano (6.7ka to present day) (Yamamoto, 2005).

Yamamoto (2005) discovered twelve tephra layers (Azuma-Jododaira product) distributed between Jododaira to Iwodaira and northwestern to southeastern slopes of Issaikyoyama. Based on the tephra stratigraphy and carbon dating on the soil, “Jododaira volcano” was defined with the Azuma-Jododaira product during the last 7,000 years (Yamamoto, 2005; Matsumoto et al., 2018; Furukawa et al., 2018). According to Yamamoto (2005), repetition between vulcanian and non-juvenile eruptions formed the craters and pyroclastic cones, Goshikinuma, Ooana, Okenuma, Azuma-Kofuji (c.a. 6.7 ka) (Fig. 26a, 26b). During this explosive activity in 7 ka, the chemical compositions of these magmatic products are all calc-alkaline andesite mixed between shallow felsic and deep mafic endmembers (Ban et al., 2013, 2016). The current active area is around Oana crater (Fig. 28) which are manifested as fumaroles, and as several times of small non-juvenile eruptions (JMA, 2013) [URL8]. The eruptions in historical times had occurred at the Oana crater (1331AD, 1711AD, 1950AD, and 1977AD), and at the Tsubakurosawa craters (1893-1895AD).

Azuma-Jododaira products (Yamamoto, 2005)

The following descriptions based on Yamamoto (2005). Azuma-Jododaira products consist of twelve tephra layers deposited by eruptions of the Jododaira volcano after 7 ka. The tephra layers distribute along Jododaira to Iwodaira and northwestern to

southeastern slopes of Issaikyoyama. These twelve tephra layers can be divided by the intervening soils, and subdivided into the five layers of andesitic vulcanian ash (Okenuma unit: Az-OK, Goshikinuma unit: Az-GS, Kofuji unit: Az-KF, Issaikyo unit: Az-IS, Oana unit: Az-OA) and the seven layers of non-juvenile eruption ash (Jododaira phreatic unit 1 to 7: Az-JP1 to 7)) (Fig. 26b). The deposition dating is based on carbon dating for the intervening soils and stratigraphic correlation. Az-OA in the stratigraphy of Yamamoto is correlated with the 1331AD Oana non-juvenile eruption, based on the carbon dating results and the description from historical documents (Yamamoto, 2005). As mentioned, this study focuses on the tephra layers around the Az-OA tephra (1331AD) which has been well dated.

Az-OA consists of two parts showing different colors. The central main part is the whitish ash layer with clay-sized ash matrix. The clay-rich ash layers are overlain by the uppermost part of the bluish-grey ash layer with fine sand-sized ash matrix. In the uppermost layer, andesitic blocky ballistics with sizes of several meters occur and are associated with sag structures with impact crater (Fig. 27). Therefore, the uppermost layer might derive from a vulcanian eruption with juvenile material, in contrast to the main part, which was non-juvenile eruption. The vulcanian products in the uppermost part contain 80~90% of andesitic volcanic rock fragments which consist of poorly vesiculated black groundmass and phenocrysts of plagioclase, augite, orthopyroxene, and rare olivine. After Az-OA layer, several layers of the non-juvenile eruption products bearing altered lithic fragments overlaid on the Az-OA with boundaries of intervening soils. For some of them, the continuity as a layer is not well determined.

Sample collection and description

Geological observation on the tephra layers, including Az-OA, was conducted along Iwodaira to the Kamoshika-zaka slope (Fig. 28), based on their stratigraphy established by Yamamoto (2005). In study, eight ash layers with the intervening black to brown soils were defined at Loc. 1, which are L1-1, L1-2, L2 to L7 from bottom to top (Fig. 29). These eight ash layers are laterally continuous because they were also found at Loc. 2 and Loc. 3. In this study, L1-1 and L1-2 were distinguished as Az-OA of

Yamamoto (2005), determined by similar characteristics of their stratigraphic relations, colors, and sedimentary facies. Although the JP7 of the latest eruption ash layer in Yamamoto (2005) should be any one of the six layers after L1-1 and L1-2, the correlation and the correspondence are still unclear. This study used the samples collected from L1-1 to L7 at Loc. 1 (Table 6) because of the presence of layer Az-OA, which has been well dated.

This study also found out the eight layers older than L1-1 (Az-OA) at Loc. 2 below, La to Lc, Ld-1 to Ld-3, Le, and Lf from top to bottom (Fig. 29). Some of them are also laterally continuous and occur in the lower part of the outcrop at Loc. 3. However, the correlation between these layers and the stratigraphy of Yamamoto (2005) is still unclear. Geological description for ash layers after Az-OA is presented below (Figs. 29, 30, and 32).

- L1-1 and L1-2 (series of Az-OA (1331AD)): L1-1 is a well-sorted pyroclastic deposit supported by the fine-sand sized ash matrix with pale grey to white color. This layer is directly overlain by L1-2 with a wavy boundary, and they show the structure of mantle bedding. L1-2 is a well-sorted pyroclastic deposit supported by fine-sand sized ash matrix with blue grey color. These two products are fallout tephra. Closer to the Oana crater (along the trail to Issaikyoyama), their stratigraphic relation clearly appears with L1-1 covered by L1-2, and the L1-2 becomes a coarser pyroclastic deposit consisting of andesitic ballistic bombs with sizes of several tens centimeters to several meters (Fig. 27) (also described in Yamamoto, 2005). At some places, the uppermost of L1-2 lacks from the stratigraphic relations (e.g. Loc. 2 and Loc. 3), while the L1-1 widely distributes also at the other outcrops. These facieses characteristics correlate with the description of Az-OA in Yamamoto (2005).
- L2: This layer is a well-sorted pyroclastic deposit supported by the clay-sized ash matrix with white color. L2 covers on L1-1 and L1-2 indirectly with the intervening soil, showing mantle bedding. This deposit is also fallout tephra. Although the thickness of this layer is thin, the continuity as a geologic layer is well in Loc. 1 and Loc. 3.

- L3 and L4 (series of one eruption?): L3 is a well-sorted pyroclastic deposit supported by the fine-sand sized ash matrix with blue grey color. This layer covers indirectly on L2 with an intervening soil, and both are overlain directly by L4. L4 is a well-sorted pyroclastic deposit supported by the fine-sand sized ash matrix with grey to dark grey color. The two layers are continuous between Loc. 1 and Loc. 3. Furthermore, they also show mantle bedding and are fallout tephra. The boundary between L3 and L4 does not shows a time gap of their deposition due to lack of intervening soil. These two layers are possibly correlated with JP7 unit in the stratigraphy established by Yamamoto (2005).
- L5: This layer is a well-sorted pyroclastic deposit, closely-clast supported by the coarse-sand sized ash with the blue-grey colored finer ash matrix. L5 shows mantle bedding and a bit unclear normal grading and characterizes as fallout tephra. This product indirectly overlies the L4 with the intervening soil and are well continuous as a geologic layer.
- L6: This layer is a well-sorted pyroclastic deposit supported by the fine sand-sized ash matrix with white blue grey color. L6 overlies L5 indirectly with the intervene soil, showing mantle bedding. This deposit is also fallout tephra. Although the layer also appears at Loc. 3, it might have been affected by reworking and weathering.
- L7: This layer is a well-sorted pyroclastic deposit supported by fine sand-sized ash matrix with light grey to white color. L7 overlies L6 indirectly with intervening soil, showing mantle bedding. This deposit is also fallout tephra. Although the layer also appears at Loc. 3, it might have been affected by reworking and weathering. At Loc. 1, L7 is covered by the poorly sorted-white pyroclastic deposit with erosion surface at the uppermost. This unknown layer might be part of the products in the 1893-1895AD Tsubakurosawa crater eruption.

Geological description older than Az-OA (only description is shown here) (Figs. 29, 31, and 32)

- La: This layer is a poorly-sorted pyroclastic deposit supported by the fine sand-sized ash matrix with yellowish white color (Loc. 2). La contains whitish to yellowish brown lithics lapilli and bombs. This layer indirectly underlays L1-1 with the intervening soil, and also indirectly overlies Lb with the intervening soil. This deposit

shows mantle bedding, and sag structure by the bombs into the deposit, which is typical of fallout tephra in proximal facies. Although lithofacies change to a well-sorted pyroclastic deposit with the fine sand-sized ash matrix, the stratigraphically corresponding layer occurs also at Loc. 3.

- Lb: This layer is a poorly-sorted pyroclastic deposit supported by the fine sand-sized ash matrix with yellowish white color (Loc. 2). La contains whitish to yellowish brown lapilli to bombs and black scorieceous fragments. This layer indirectly overlies uppermost of Lc with the intervene soil. This deposit shows mantle bedding, and sag structure by the bombs into the deposit, which is typical of fallout tephra in proximal facies. Although lithofacies change to a well-sorted pyroclastic deposit with the fine sand-sized ash matrix, the stratigraphically corresponding layer occurs also at Loc. 3, as same with La.
- Lc: This layer is a well-sorted pyroclastic deposit, closely-clast supported by lapilli fragments with the yellowish white colored finer ash matrix. Lc contains whitish to yellowish brown lapilli to bomb and black scorieceous fragments. This layer directly overlies uppermost of Ld-1 with sag structure by the bombs into Ld-1. This deposit shows also clear normal-coarse tail grading, and, which is typical of fallout tephra in proximal facies. The Lc layer only occurs at Loc. 2.
- Ld-1, Ld-2, Ld-3: These layers commonly show weakly to clear low-angled cross bedding and divided by each different color while any intervening soil does not occur in their boundaries. The stratigraphic relation is Ld-1, Ld-2, and Ld-3 from uppermost to bottom. Ld-1 is a poorly sorted pyroclastic deposit supported by the consolidate- fine-sand sized ash matrix with red color (oxidized), accompanying with clear low-angled cross bedding. Ld-2 is a poorly sorted pyroclastic deposit supported by the consolidate- fine-sand sized ash matrix with pale grey to white, accompanying with weakly low-angled cross bedding. Ld-3 is a poorly sorted pyroclastic deposit supported by the consolidate- fine-sand sized ash matrix with grey to blue grey color. Each layer might show the characteristics of low-dense pyroclastic density current similar to pyroclastic surge. The corresponding layers occur at Loc. 3 due to their color and the stratigraphic relations.

- Le: This layer is a well-sorted massive pyroclastic deposit supported by the fine sand-sized ash matrix with white light grey to dark grey color. Le directly underlays the lowermost of Ld-3 and also overlies Lf.
- Le: This layer is a well-sorted pyroclastic deposit supported by the fine sand-sized ash matrix with white yellowish-brown color, accompanying with normal-coarse tail grading. The lowermost of Le is not exposure.

Methodology of sample analyses

For these ash grains in the samples from L1-1, L1-2, L2, L3, L4, L5, L6, and L7 at Loc.1 (Table 6), rock texture and mineral assemblages are studied by a binocular-stereomicroscope, semi-quantitative analyses (a scanning electron microscope equipped with energy dispersive spectroscopy (SEM-EDS) and powder bulk analysis (X-ray diffractometry (XRD)). Mineral identification is based on XRD, especially for very fine-grained clay minerals. However, bulk XRD does not give information on the original rock texture and mineral assemblages from individual ash grains. Hence, a combination between spot analysis with SEM-EDS and bulk XRD was applied for mineral assemblages and rock texture of the ash grains. The petrographical observation under SEM-EDS analysis was carried out by Backscattered Electron Image (BSE).

Untreated ash samples were sieved into two fractions, 250 μm-1 mm (coarse), < 250 μm (fine). For SEM-EDS analysis, the coarse fraction was prepared as a resin-filled and carbon-coated polished grain mounts. For XRD analysis, the untreated bulk sample and fine fraction are powdered by agate mill.

Bulk mineral identification was used with the XRD (Rigaku Corp. Multiflex) installed at Akita University, Faculty of International Resource Sciences. Measurements were carried out at a rate of 0.25° per minute from 2° to 65° using a CuKα target X-ray tube with an acceleration voltage of 30 kV and a filament current of 16 mA. For data processing, Integrated X-ray powder diffraction software (PDXL2: Rigaku Corp.) were used with the database from The International Centre for Diffraction Data (ICDD) and The Inorganic Crystal Structure Database of The Crystallographic Society of Japan. In

the case the X-ray peaks at 14Å appeared, whether chlorite or smectite was determined by adding ethylene glycol in the sample.

Semiquantitative microprobe analysis was carried out with a tungsten filament SEM-EDS (JEOL JSM-6610LV and OXFORD INCA X-act) installed at Akita University, Faculty of Education and Human Studies. The analysis was carried out at an acceleration voltage of 15 kV, a probe current of 2.2 nA, a working distance of 10 mm, and a live time of 30 s. The analytical value of major elements was obtained with an evaluation of EPMA standards (JEOL corp.), and of standard glass materials (Tokachi-Ishi obsidian) and igneous minerals which are already analyzed by X-ray fluorescence (XRF).

Remarks for spot chemical analysis for individual ash grains

Mineral identification with semiquantitative analysis by SEM-EDS was done following the methodology of Chapter 1 and Imura et al. (2019a) as below. Minerals were identified from the EDS spectrum and stoichiometric-empirical formula of each mineral. The polymorph minerals such as silica and titanium oxides are not distinguished by SEM-EDS.

In case very tiny minerals (less than several micrometers) are analyzed, the EDS spectra are affected by X-ray of adjacent mineral grains. Even when the BSE is homogeneous, some grains can contain very fine-grained minerals. These effects are very complex and problematic due to the limits of the spatial resolution of SEM-EDS. Therefore, this study evaluated the change of the EDS spectrums by multiple analytical points.

XRD mineral identification

The result of the bulk XRD analysis is shown in Table 7 and Fig. 33. All samples mainly contain quartz, tridymite, augite, cristobalite, plagioclase and alunite with their specified X-ray intensities. X-ray peaks of 7 Å-kaolin minerals appeared at almost all samples and could not be subdivided into kaolinite, nacrite, and dickite because of their small X-ray intensities. For the samples which show the 14 Å X-ray peak, the peaks were from smectite due to the X-ray peak movement to 18 Å or disappearance after the ethylene

glycol treatment. Although any results of fine fraction show almost the same patterns of the X-ray intensities with the one from the bulk, the peaks of 14 Å-smectite, 7 Å-kaolin minerals and alunite are more relatively intense in the fine fraction, accompanied with the weakened X-ray intensities of pyroxene and plagioclase. This point suggests that the 14 Å-smectite, 7 Å-kaolin minerals and alunite are mainly contained as very fine particles with clays in these samples, compared with pyroxene and plagioclase consisting of the lithic ash.

The X-ray peaks of 14 Å-smectite and 7 Å-kaolin minerals appeared in almost all samples. For the samples from L1-1, L1-2, L5, and L6, they are characterized by the high-X-ray intensities of quartz and cristobalite. In contrast with these samples, L2 and L7 are characterized by high-X-ray intensities of cristobalite with tridymite and quartz. However, the samples from L3 and L4 do not have the X-ray intensities of 14 Å-smectite and 7 Å-kaolin minerals while they are characterized by the peaks of the 8 Å-amphibole group minerals. Besides, the intense peaks of plagioclase, cristobalite, tridymite appeared in L3 and L4.

Componentry analysis on ash samples

Classification of ash grains under a binocular-stereomicroscope

Petrographic observation under a binocular-stereomicroscope was conducted to describe, color, morphology, rock texture of ash grains of all samples. The observed ash grains were roughly classified into five types: dense-volcanic rock (DVR), vesicular-volcanic rock (VVR), massive-altered rock (MAR), partly altered volcanic rock (PAVR), and fragmented crystals (CF) (Fig. 34). The definitions are below.

- Dense-volcanic rock type (DVR): the ash grain clearly shows porphyritic texture consisting of phenocrysts of plagioclase and pyroxenes, and poorly vesicular groundmass (Fig. 34a to 34c). Some of them have a highly crystalline porphyritic texture closer to holocrystalline (Fig. 34b). Their typical color is dark grey to pale grey and sometimes is oxidized reddish brown. Their surface morphology is dominantly blocky-polygonal, and sometimes their corner is abraded into subangular. In many cases, their phenocrysts in the isolated ash grains are ruptured and divided by their polygonal-smooth surface. This type of ash grains are likely a cognate

material as non-juvenile fragment. Although they are not necessarily fresh-unaltered volcanic rock fragments, the alteration part consisting of very-fine grained minerals is not seen under a binocular-stereo microscope (Fig. 34a to 34c).

- Vesicular-volcanic rock type (VVR): the ash grain clearly shows porphyritic texture consisting of phenocrysts of plagioclase and pyroxenes, and well-vesicular groundmass. Their typical color is dark grey to brown grey. Their surface morphology is blocky-polygonal to cuspate-irregular, and sometimes their corner is abraded into subangular to subrounded (Fig. 34d). Although they are not necessarily fresh volcanic rock fragments, the alteration part consisting of very-fine grained minerals is be seen under a binocular-stereomicroscope. Furthermore, this type is also not necessarily a juvenile material.
- Massive-altered rock type (MAR): the ash grain mainly consists of a massive aggregate of very-fine grained crystals and lack of porphyritic-volcanic rock texture (Fig. 34e). Their typical color is light grey to yellowish-brown. Their surface morphology is blocky-polygonal to round. They are non-juvenile lithic fragments.
- Partly altered volcanic rock type (PAVR): the ash grain mainly consists of a massive aggregate of very-fine grained crystals and the part of porphyritic-volcanic rock texture similar to DVR or VVR (Fig. 34f). The typical color of the altered part is light grey to yellowish-brown, while the fresh part is dark grey to pale grey. The ratio of fresh and altered parts in the ash grain is variable. Sometimes the lath-shaped plagioclase phenocryst only remained, while entire of ash grains consist of the massive aggregate of fine-grained crystals. Their surface morphology is blocky-polygonal to cuspate-irregular. They are non-juvenile lithic fragments.
- Fragmented crystals (CF): this type is crystal fragments typically observed in a pyroclastic deposit. The fragments are mainly plagioclase, orthopyroxene, and augite, which are broken into anhedral to synhdedral fragments.

Componentry trends of categorized ash grains under a stereoscopic binocular microscope

Individual ash grains in the samples from each unit were categorized with the above ash classification based on the observation with a binocular stereo microscope (Figs. 35 to 42). The componentry proportion of the classified ash grains was determined on the basis of counting the randomly selected 400 to 800 grains from each sample (Fig.

43). All samples mainly consist of altered ash grains categorized into MAR and PAVR. From L1-1 through L1-2, the ratio of DVR increases from approximately 10 to 30 %, which is consistent with the changes of eruption styles from non-juvenile to vulcanian eruptions described in Yamamoto (2005). They are rich in MAR and PVAR with several tens % of DVR, which is almost the same pattern with L2 and L7. In comparison with that, L3 to L4 contains volcanic rock fragments of DVR and VVR much more than L1-1, L1-2, and L7. The changes of both samples are distinctive, which is consistent with that only these show the X-ray intensities of 8Å-amphibole group mineral (Fig. 33, Table 7). Especially, the ratio of VVR in the L4 sample is the highest values in all samples (c.a. 10%) while the ratio in almost all samples is less than 5 %. The samples of L5 and L6 also contain DVR and VVR almost closer to 50 %.

Petrographic observation based on spot-chemical analysis with SEM-EDS

The detailed petrographic observation under the back-scatter electron image (BEI) with SEM-EDS was carried out to describe their altered or volcanic rock textures, alteration mineral assemblages, and occurrences. SEM-EDS semi-quantitative analysis specified the following minerals, silica, pyrite, apatite, magnetite, titanomagnetite, ilmenite, alunite, barite, titanium oxide, plagioclase, alkali-feldspars (sanidine and anorthoclase), potassium-feldspar, two-pyroxenes, biotite, sericite, illite, chlorite, kaolin, pyrophyllite, vermiculite. In many cases observed on altered ash grains, silica, sericite, illite, chlorite, kaolin, and pyrophyllite form a fine-grained crystal aggregate consisting of any or some of these minerals. For the crystal aggregates, each mineral was specified by an evaluation of the spot-EDS spectrum by the multiple-analyzed points, compared with a stoichiometric-empirical formula of each mineral respectively. During the observation, this study also faced to both cases of the Si/Al ratios from 1 to ∞ or from 1.5 to 2 (with small Kα X-ray intensity of Mg) by every EDS analyzed points. Each of these cases implies a mixture of silica+kaolin or silica+pyrophyllite, respectively. Therefore, the Si-Al-K mica clays, pyrophyllite, and chlorite were identified in ash grains from some samples using by SEM-EDS, even though the X-ray peaks of these minerals have not appeared in the bulk-powder XRD result (Fig. 33, Table 7).

Based on their alteration mineral assemblages in individual altered ash grains, the alteration types in samples are classified into six below, silica+titanium oxide±pyrite (silica type), silica+pyrophyllite±alunite (pyrophyllite type), silica+kaolin mineral±alunite (kaolin type alteration), silica+alunite (sil+alu, alunite type), silica+illite+sericite±chrolite±biotite (mica-chlorite type), silica+chlorite±epidote (chlorite type) and silica+chrolite+biotite+K-feldspar (mica-K-feldspar type). For altered ash grains, this study uses anyone or several types of the above alteration types to describe (Table 8). The following subsections show the componentry description already done by Imura et al. (2018) which analyzed for the samples of Horikoshi (2017MS) corresponding to this study.

1331AD Az-OA units: L1-1 to L1-2

The sample of L1-1 is characterized by a variety of such altered ash grains (Table 8). As shown in the observation result of a binocular-stereomicroscope, this sample from the L1-1 layer contains much of altered ash grains such as whitish to yellowish grey MAR and PAVR (Figs. 35, 36 and 43). The sample of L1-2 contains almost same components of L1-1 above. However, the grey to brown DVR ratio increases more than L1-2.

Most of the altered ash grains are the fragments of a massive-dissolution silicified rock (silica and alunite types) or an aggregate of fine-grained minerals (kaolin and pyrophyllite types). For the former ones, the massive silicified rocks show typical dissolution texture (similar to the case of Imura et al., 2019a) consisting of massive-homogeneous silica with irregular to rectangular shaped vugs (silica type) (Fig. 44a). These vugs are sometimes filled by pyrite or TiO_2 minerals or fine-grained alunite (alunite type) (Fig. 44b). The latter ones classified into kaolin and pyrophyllite types occur as a fine-grained crystal aggregate in the ash grains. Such alteration types sometimes coexist with the isolated ash grains of silica type, and or the unaltered volcanic rocks as DVR (Fig. 44c). Furthermore, the altered ash grains classified into mica-chlorite (Fig. 45a) and mica-K-feldspar (Fig. 45b) types occur as a complete altered rock (MAR) without any volcanic rock texture. In some cases, the crystal aggregates of these types (silica+chlorite) interstitially fill blanks between the crystals of euhedral coarse silica (Fig. 45c).

Although both samples of L1-1 and L1-2 abundantly contain PAVR ash grains, this trend is clearer in L1-2. These ash grains consist of the remained highly-crystalline-andesitic rock (DVR) coexisted with any of the above alteration parts. Part of DVR in single ash grains typically show coherent-porphyritic texture consisting of phenocrysts of two-pyroxene and plagioclase and groundmass. Their groundmass texture is dyctytaxitic to intersertal texture, accompanying with the mineral assemblage of silica (igneous quartz)+alkali-felspar (anorthoclase to sanidine)+plagioclase+two-pyroxene±a few of rhyolitic to dacitic glass. These ash grains commonly show holocrystalline-intersertal texture without groundmass glass. Sometimes VVR-scoriaceous volcanic rock fragment occurs in both samples. However, they have been already altered into kaolin or pyrophyllite type alterations.

L2

The sample of L2 is characterized by a presence of VVR or VVR origin PAVR (Table 8, Figs. 37 and 43). They are mostly brown to brownish colored, andesitic scoria, or scoriaceous fragment with highly vesiculated and glassy to hyaloophtic porphyritic texture. Although much of them are already hydrothermally altered (alunite, kaolin) or weathered (Fig. 46a), the unaltered one is also observed in ash scale (Fig. 46b, 46c). They contain phenocrysts of augite+orthopyroxene+pigeonite±olivine, and groundmass of plagioclase+augite+pigeonite+andesitic glass. Sometimes the scoriaceous ash grains have rhyolitic glass inclusion in single grain (Figs. 46d and 47). Also, unaltered rhyolitic glass shard (around SiO_2 75%) occurs in this sample (Fig. 46e, 46f). DVR in these samples are coherent-andesitic lava fragments with lower to moderately vesiculated and highly crystalline. They contain phenocrysts of augite+orthopyroxene+plagioclase and groundmass of plagioclase+two-pyroxene±a few of rhyolitic to dacitic glass. Several of these ash grains show holocrystalline-intersertal texture with a groundmass of igneous quartz+alkali-felspar (anorthoclase to sanidine)+plagioclase+two-pyroxene.

The dominant alteration types in this sample are silica type typically accompanying a massive silica crystal with many vugs (dissolution texture). These vugs are sometimes filled by TiO_2 minerals or fine-grained alunite (alunite type). The above DVR has an alteration part with an aggregate of fine-grained minerals (kaolin and

pyrophyllite types). Rarely, the altered ash classified into mica-chlorite type occurs in this sample.

JP7 unit: L3 to L4

L3 and L4 are commonly characterized by their componentry changes in each sample. The sample of L3 contains MAR and PAVR as 50%, while the sample of L4 contains DVR and VVR approximately as 70% (Table 8, Fig. 43). Especially, brown to brownish colored, andesitic scoria, or scoriaceous fragment (same as L2) are obviously contained in L4 (Figs. 38 and 39). However, the rock types forming the ash grains have not significantly changed between both samples.

Most of DVR in these samples is grey to light grey, blocky, coherent-andesitic lava fragments with poor to moderate vesiculation and various crystallinity. Probably, their all phenocryst assemblage is commonly of augite+orthopyroxene+plagioclase (mostly ruptured), while it is still unclear because of pyroclastic ash grain. Their groundmass texture varietizes as hyaloohtic to hyalopillitic, dyctytaxtic to intersertal, and holocrystalline-intersertal with changes of crystallinity. Hyaloohtic to hyalopillitic textured lava fragments consist of plagioclase+augite+orthopyroxene+titanomagnetite+dacitic to rhyolitic glass, which is moderately or highly vesiculated (Fig. 48a, 48b). With increase of crystallinity and decrease of vesiculation, dyctytaxtic to intersertal lava fragment mainly consist of plagioclase+augite+orthopyroxene+titanomagnetite+quartz+dacitic to rhyolitic glass. Alkali-feldspars (sanidine to anorthoclase) are sometimes contained in these lava fragments, still coexisting with rhyolitic groundmass glass. Finally, holocrystalline-intersertal lava (intrusive?) is almost same as the one which described in previous sections (L1-1, L1-2, and L2) (Fig. 48c). In terms of presence of olivine phenocryst, the other DVR is distinctive from the above grey DVR ash grains. This DVR is black, blocky, coherent-andesitic lava fragments with poor to moderate vesiculation and high crystallinity (Fig. 48d, 48e). The olivine-two pyroxene andesitic lava groundmass shows hyalopillitc to intersertal texture consisting of plagioclase+augite+orthopyroxene±pigeonite+titanomagnetite+quartz+rhyolitic glass. These grey and black DVR ash grains are more abundant in L4 than L3. The glassy, scoria

or scoriaceous fragment is almost too weathered to observe them, comparing with the unaltered one in L2.

The alteration types and their patterns are almost similar to L2. MAR and PAVR with Silica type alteration typically occur as a massive silica crystal with many vugs (dissolution texture). These vugs are sometimes filled by TiO_2 minerals or fine-grained alunite (alunite type). Aggregate of alunite crystals also occurs as alunite type. The above DVR and VVR-scoriaceous fragments have alteration part with an aggregate of fine-grained minerals (kaolin and pyrophyllite types).

L5

L5 is distinctively characterized by much abundance of MAR and PAVR (Table 8, Fig. 43). Porous scoria and scoriaceous fragment in L2 to L4 have not appear in this sample (Fig. 40). The dominant alteration types in this sample is kaolin type which occurs as MAR of a massive aggregate of fine-grained silica+kaolin crystals (Fig. 49a). The ash grains with pyrophyllite type alteration also occurs similar like kaolin types. Silica type altered ash grains also occur as a massive silica crystal with many vugs and well developed pseudomorphs of igeneous minerals (dissolution texture) (Fig. 49b, 49c). These vugs are sometimes filled by TiO_2 minerals or fine-grained alunite (alunite type) (Fig. 49c). The above DVR have alteration part with an aggregate of fine-grained minerals (kaolin and pyrophyllite types). Rarely, the altered ash classified into mica-chlorite type occurs in this sample (Fig. 49d). Although a few of ash grains showing the highly crystalline andesitic rock is contained, most of them are PAVR with kaolin type alteration (Fig. 49e, 49f). Sometimes black colored DVR similar to L4 occurs in L5, while they lack olivine phenocryst.

L6

The sample of L6 is characterized by abundance of DVR and VVR-scoria or scoriaceous fragment with monotone alteration types similar to L2 to L4 (Table 8, Figs. 41 and 43). DVR in these samples are brownish grey to black, blocky, coherent-andesitic lava fragments with lower to moderately vesiculated and highly crystalline. They contain phenocrysts of augite+orthopyroxene+plagioclase and hyaloohtic to intersertal groundmass of plagioclase+two-pyroxene±a few of rhyolitic glass (Fig. 50a). Sometimes

black colored DVR similar to that in L4 occurs also in L6, while they do not have olivine phenocryst. VVR are mostly transparent to light brownish grey, irregular to cuspate, andesitic scoria or scoriaceous fragment with highly vesiculated and glassy porphyritic texture (Fig. 50b, 50c). They contain phenocrysts of augite+orthopyroxene+plagioclase, and hyaloophtic groundmass of plagioclase+augite+orthopyroxene±pigeonite±quartz+andesitic glass. Sometimes they accompany with weathered part.

The dominant alteration types in this sample is kaolin type which occurs as a massive aggregate of fine-grained silica+kaolin. Silica type alteration also occurs as a massive silica crystal with many vugs (dissolution texture). These vugs are sometimes filled by TiO_2 minerals or fine-grained alunite (alunite type). The above DVR and VVR have alteration part with an aggregate of fine-grained minerals (kaolin and pyrophyllite types). Although a few of ash grains showing the holocrystalline-intersertal andesitic rock is contained, most of them are PAVR with kaolin type alteration (Fig. 50d).

L7

L7 is distinctively characterized by much abundance of MAR and PAVR (Figs. 42 and 43). Most of the ash grains are completely altered into any of silica, kaolin alunite, and pyrophyllite types without original texture of igneous rocks (Table. 8). The dominant alteration types in this sample is kaolin type which occurs as MAR of a massive aggregate of fine-grained silica+kaolin crystals (Fig. 51a). The ash grains with pyrophyllite type alteration also occurs similar like kaolin types. Silica type alteration also occurs as a massive silica crystal with many vugs (dissolution texture). These vugs are sometimes filled by TiO_2 minerals or fine-grained alunite (alunite type) (Fig. 51b). The above DVR have alteration part with an aggregate of fine-grained minerals (kaolin and pyrophyllite types). Rarely, the altered ash classified into mica-chlorite type occurs in this sample (Fig. 51c). Although a few of ash grains showing the holocrystalline-intersertal andesitic rock is contained, most of them are PAVR with kaolin type alteration or weathering (FeOH-AlOH minerals and vermiculite) (Fig. 51d).

Discussion

Fluid chemistry of hydrothermal fluid inferred from altered ash grains

Altered ash grains in this case study were probably derived from the subvolcanic hydrothermal system at which acidic hydrothermal fluid circulates and convects. For the ash grains of silica, alunite, kaolin, and pyrophyllite types, each of alteration mineral assemblages is typical in the acidic alteration zone likewise a silicification zone and the advanced-argillic alteration zone (Hayashi 1973; Ossaka and Hirabayashi,1981; Ossaka, 1982, 2003; Hedenquist et al., 2000; Sillitoe,2010). Besides, their alteration rock textures such as dissolution texture with a massive, porous silica, replacement and pseudomorph texture (e.g., Figs. 36a, 36d), and infill texture (e.g. Fig. 36b) were also the petrographical characteristics derived from the acidic-hydrothermal alteration of subvolcanic hydrothermal system (Imura et al., 2019a). In the case of acidic-alteration in the subvolcanic hydrothermal system, hydration of magmatic vapor (CO_2, SO_2, and H_2S) separated from a magma body plays a significant role to form strongly-acid hydrothermal fluid at high temperature, acid-sulfate-chloride water or acid-sulfate water (Giggenbach, 1977). From petrographic observation, those types sometimes show coexistence each other in the individual ash grain, indicating that the chemical conditions of such reactant fluid were changed repeatedly. Basically, all samples were mainly derived from such alteration area in subvolcanic hydrothermal system. In addition, the temperature of volcanic gas suddenly increased into 400-500 °C (1979AD reported by Ozawa et al., 1981: 2008-2016AD reported by Shinohara and Kazahaya, 2016), and the isotope ratios of δD and $\delta^{18}O$ show a mixture of magmatic gas and meteoric water (Shinohara and Kazahaya, 2016; Yaguchi et al., 2017). These points indicate that the current subvolcanic hydrothermal system is being affected and driven by magmatic gas separated from shallow intruded magma beneath the Oana crater. Then, the shallower hydrothermal fluid mixed with the magmatic gas might keep strongly acid to form the above acidically and hydrothermally altered volcanic products.

The P-T conditions might have been different from the state before 1331AD. The other alterations of mica-chlorite and mica-K-feldspar types were also derived from the hydrothermal alteration zone of the subvolcanic hydrothermal system. However, conditions of the reaction fluid to form such alteration types are different from the above

acidic alteration types. In the typical case of geothermal or epithermal-porphyry systems, their potassic or sericitic alteration are formed at the existence of a neutral-hydrothermal fluid rich in alkaline elements (Hayashi 1973; Ossaka and Hirabayashi, 1981; Ossaka, 1982, 2003; Hedenquist et al., 2000; Sillitoe, 2010). Furthermore, in the open-through rock alteration system, the F/R ratio (fluid per rock mass ratio) is necessary to be very low for the crystallization of chlorite and K-feldspar, while the high F/R can form alunite, quartz, and kaolin (Reed, 1997). In contrast with the acidic-alterations of silica, alunite kaolin, and pyrophyllite types, the neutral-hydrothermal alterations of mica-chlorite and mica-K-feldspar types were possibly different alteration zones of the subvolcanic hydrothermal system in terms of fluid chemistry and their location or depth. In addition, these neutral alteration types only occur in L1-1 and L1-2 (Az-OA) which contain also acidic alteration types (Table 8). The reality suggests that the alteration area formed by the subvolcanic hydrothermal system might have been various at 1331AD Az-OA eruption.

Origin of volcanic rock fragments

Samples from all units widely contain DVR. Most of the DVR ash grains are possible to be a cognate material of two pyroxenes andesitic lava because they are fragmented with a blocky polygonal surface, even though they are unaltered. Assumed that all layers were brought from anywhere around the Oaana crater in the Jododaira area (currently active), these cognates could be the fragments derived from the lava flows distributed around there. Their candidate units are Issaikyoyama products (520 to 170 ka, phenocrysts of olivine+augite+orthopyroxene+plagioclase) (Frukawa et al., 2018; Mastumoto et al., 2018) or Vulcanian pyroclasts of 1331AD eruption (augite+orthopyroxene+plagioclase+small amount of olivine) (Ban et al., 2013). Furthermore, olivine-augite-orthopyroxene andesite also occurs in L2, L3, and L4, which might be different magmatic fragments from the two-pyroxene andesite above. Especially, olivine-augite-orthopyroxene andesitic scoria or scoria fragments in L2 might be a juvenile material related to the eruption. In L3 and L4, the olivine-augite-orthopyroxene andesite occurs as blocky, moderately crystalline lava fragments, and they might be a cognate derived from olivine bearing andesitic lava around Jododaira area (Issaikyoyama

lava?). However, samples of L3 and L4 also contain many scoria or scoria fragments even weathered, and these are possible to be an essential material.

The extremely high crystalline-andesitic lithic fragments commonly apper in all samples. Mainly, they are abundant in L1-1, L1-2, and L4. Their groundmass mineral assemblage and the almost-holocrystalline rock texture not necessarily show a rapid-cooling at the subaerial condition. No andesitic rocks consisting of plus alkali-feldspar+quartz are correlated with any lava units around the Jododaira area. The Holocene magma feeding system produces andesitic volcanic products formed by magma mixing between two endmembers: 50.00 % SiO_2 mafic magma 20-47 km below and 65.50 % SiO_2 felsic magma chamber shallower than 4 km (Ban et al., 2013, 2016). The holocrystalline andesitic fragments might be the shallow felsic intrusive body corresponding to the felsic magma chamber assumed by Ban et al. (2016). Furthermore, the ash grains of the extremely high crystalline-andesitic fragments sometimes partly altered with the acidic-hydrothermal alterations classified into silica, alunite, kaolin, and pyrophyllite types. It suggests that the original rock body of the extremely high crystalline-andesitic fragments partly caused such hydrothermal alteration.

Evolutional shifts of subvolcanic hydrothermal system of Jododaira volcano and eruption styles after 1331AD (Az OA) eruption

The evolutional change of Jododaira subvolcanic hydrothermal system was revealed on the basis of this study results above (summarized in Fig. 52). Here this study explains each state at those eruptions derived from the subvolcanic hydrothermal system. This section assumed that each eruption vent supplying the materials are around several 100 meters area of Oana crater to Jododaira area.

Sample from L1-1 layer corresponding to Az-OA 1331AD eruption contains the variously altered ash grains. All six alterations of silica, alunite, kaolin, mica-chlorite, and mica-K-feldspar types were derived from each of alteration zones corresponded to each of different hydrothermal fluids and different portions of the subvolcanic hydrothermal system. Such componentry patterns are consistent with the case of the Ontake 2014AD hydrothermal eruption (Minami, et al., 2016; Imura et al., 2019b). Probably, L1-1 of Az-OA was brought by the hydrothermal eruption (Browne and Lawless, 2001) derived from

the Jododaira-subvolcanic hydrothermal system where the alteration zonation between the acidic to neutral hydrothermal alteration. Subsequently, L1-2 corresponding to the uppermost of Az-OA was deposited by vulcanian eruption richly brought non-juvenile fragments between cognates and altered lithics. At this time, the 1331AD intruded magma might have formed the hypabyssal-holocrystalline andesitic plug.

From Az-OA, alteration types contained in L2 became monotone which is only acidic alterations (Table). Furthermore, this L2 layer contains much of scoria and scoriaceous fragments (sometimes weathered) as juveniles. The componentry patterns indicated that the L2 was brought by magmatic hydrothermal eruption (Browne and Lawless, 2001) driven by andesitic vesiculated magma and acidic hydrothermal system. At L2 eruption, the magma intrusion at 1331AD Az-OA vulcanian eruption had been modified hydrothermal alteration area from acidic-neutral alterations to monotone-acidic alteration, similar to the case of Tokachidake chapter (Imura et al., 2019a).

At L3-L4 stage (17711AD?), the eruption products were mostly derived from fragmentation of the hypabyssal-holocrystalline andesitic plug, and the cognate lava flows distributed surficial area. However, the scoria or scoriaceous frgments similar to L2 even almost all weathered are contained in these samples. Hence, the L3 and L4 eruption styles are also reasonable to be magmatic-hydrothermal eruption. Furthermore, hydrothermally altered MAR ash grains and PAVR ash grains relatively are abundant in L3 more than L4. Therefore, these points suggest that the series of the eruptions commenced from magmatic-hydrothermal eruption fragmented mainly in the acidic hydrothermal alteration area. The series of componentry change is very similar to the case of L1-1 and L1-2 Az-OA eruption, and it might reflect the contineous change of eruption styles from hydrothermal (or small magmatic hydrothermal) to magmatic (magmatic hydrothermal or vulcanian).

From the continuous scoria output eruption (L2 to L4), the componentry patterns of L5 was changed into lithic rich (PAVR, MAVR and DVR). Although small amount of highly crystalline andesitic rock fragments, most of the components are altered into silica, kaolin, pyrophyllite, alunite, and minor of chlorite-mica types. Therefore, juveniles such as L2 to L4 are not contained in L5, and the suitable eruption style might be hydrothermal

eruption (Browne and Lawless, 2001) derived from fragmentation of the above alteration area.

L6 sample contains much of DVR and small amount of scoria or scoriaceous fragments. From alteration types of L5, L6 lacks chlorite-mica type and richly contained silca and kaolin types. Even though the juveniles are contained as small amount of VVR, the suitable eruption style might be the cognate rich vulcanin eruption because of abundance of DVR-blocky andesitic lava fragments. Since 1771AD L3-L4, very small input of magma intrusion is possible to occur in L6 eruption.

Finally, the componentry patterns of L7 was very altered lithic rich (PAVR, MAVR) with quite small amount of DVR and VVR. Most of the components are altered into silica, kaolin, pyrophyllite, alunite, and minor of chlorite-mica types, and sometimes these types accompanies vermiculite, and AlOH-FeOH minerals. Therefore, the suitable eruption style might be hydrothermal eruption (Browne and Lawless, 2001) derived from fragmentation of the above alteration area and the surficial weathered zone.

Summary and conclusions

From the petrological observations of individual volcanic ash grains in the Azuma-Jododaira product, the following conclusions were obtained.

1. In contrast with the geological survey result of Yamamoto (2005), this study found out the eight tephra layers below, L1-1, L1-2, L2, L3, L4, L5, L6 and L7 from bottom to uppermost. L1-1 and L1-2 were corelated with Az-OA unit (Yamamoto, 2005). The other layers were newly defined by this study.

2. XRD for powder ash samples and binocular-stereomicroscope observation on ash grains roughly clarified the tendency of componentry change. L1-1, L1-2, L2, L5 to L7 are characterized by the X-ray peak of 14 Å-smectite and 7 Å-kaolin, and by abundance of altered ash grains of MAR and PAVR. While, L3 and L4 are characterized by the X-ray peak of 8Å-amphibole group mineral with the disappearance of 14 Å-smectite and 7 Å-kaolin, and by abundance of unaltered ash grains of DVR (and VVR).

3. Eruptions involving magma (L1-2, L2, L3, L4, L6) and almost hydrothermal eruption (L1-1, L5, L7) occurred during last several hundred years after the 1331AD Az-OA eruption. Although the above changes in the XRD results and the componetry patterns show response to the eruptions, not necessalily implyng that the influence of magma intrusion to shallower subvolcanic hydrothermal system is as large as Tokachidake case.

Discussion using case studies of Tokachidake, Ontake, Azuma-Jododaira volcanoes

Genetic classification of subvolcanic hydrothermal systems with magma-hydrothermal system interaction

Ash petrology including alteration petrology by this study succeeded to elucidate the process of magma-hydrothermal system interaction recorded as rock texture of individual ash grains (Chapter 1 to 3, Minami et al., 2016; Imura et al., 2019a, 2019b). Based on the above results, this study figured out the differences of subvolcanic hydrothermal systems for three case, (1) Holocene volcanic products from Tokachidake volcano; (2) volcanic ash from the 2014 hydrothermal eruption of Ontake volcano; (3) Holocene volcanic tephra layers around 1331AD from Azuma-Jododaira volcano. For each case, this study newly defined the classification of subvolcanic hydrothermal system based on their magma-hydrothermal system interactions which are different each other. The following subsections explain the definitions, Tokachidake type, Ontake type, and Azuma-Jododaira type.

Tokachidake-type subvolcanic hydrothermal system: This uses the definiton "Tokachidake type" for such subvolcanic hydrothermal system directly driven by supply of magmatic vapor from a magma intrusion. Every sample from the 4.7 ka, 3.3ka, and 1926AD products commonly contain ash grains partly altered by acidic hydrothermal alteration. Most of them were formed by the brief, incomplete, acid-hydrothermal fluid-rock interaction closer to the open-flow through system. These characteristics reflect the drastic changes of physiochemical-conditions of the Tokachidake subvolcanic hydrothermal system, accompanying a magma intrusion (ex. 1926AD, 1962AD, and 1988-89AD). However, more frequent magma eruptions and magma intrusion to shallower depth, should keep the inside of the summit dry and extremely high temperature. In this case far from Tokachidake-type, the subvolcanic hydrothermal system might disappear or change to the vapor-dominant system.

Ontake-type subvolcanic hydrothermal system: This uses the definition "Ontake type" for a well-developed and mature subvolcanic hydrothermal system similar to the epithermal-porphyry system. This ash samples petrologically and mineralogically correlate with the alteration zonation at advanced argillic alteration to potassic alteration of the epithermal-

porphyry system. Furthermore, the existence of aluminum-phosphate-sulfates, Zn-sulfide (sphalerite), and monazite are also consistent with the correlation results. In the case, hydrothermal eruptions at such volcanoes mainly occur during the last several thousand years, without disturb of subvolcanic hydrothermal system by a frequent magma intrusion or eruption and addition of magmatic materials (mostly magmatic vapor).

Azuma-type subvolcanic hydrothermal system: This study defines "Azuma-Jododaira type" for the subvolcanic hydrothermal system with repetitions of magmatic and non-juvenile eruptions (hydrothermal or steam-blast). A complex magma-hydrothermal system interaction occurs at Jododaira volcano of the Azuma volcano group, accompanying with repetition of small magmatic and non-juvenile eruptions during the last several hundred years. This point is consistent with the rise and fall of the X-ray intensities of 14Å-smectite and 7Å-kaolin, and the changes of alteration patterns in the ash components. At the stage dominantly with the hydrothermal eruption, the subvolcanic hydrothermal system with alteration zonation similar to the Ontake type (before Az-OA). The non-juvenile eruptions derived from the well-developed subvolcanic hydrothermal system repeatedly occur at this volcano. However, the subvolcanic hydrothermal system sometimes is affected by small magma eruption induced by a magma intrusion and is slightly modified and got back a similar stage before Az-OA. For this type, magmatic vapor separated from shallow intrusion sill affects to the sub volcanic hydrothermal system, as provision of magmatic materials to the shallow.

Evolutional relationship from a subvolcanic hydrothermal system (immature) to an epithermal-porphyry system (mature)

Genetic relationships between active volcanoes and hydrothermal-ore system have been pointed out by numerical studies. Volcanic fluids derived from magma play a significant role in the formation process of hydrothermal ore deposits (e.g., Hedenquist and Lowenstern, 1994; Hedenquist et al., 2000; Silitoe, 2010). Their fluid circulation system alters surrounding rocks and conveys and concentrate the precious elements leached out (Giggenbach, 1997; Reed, 1997). Therefore, the fluid circulation system to form ore-forming fluid is also possible to be in a subvolcanic hydrothermal system. Actually, the existence of magma as a source to supply such fluids has been drowned in

the geologic structure models of epithermal (Hedenquist et al., 2000) or porphyry (Silitoe, 2010) ore systems.

Ontake-type subvolcanic hydrothermal system is a case to correlate with the zoned-hydrothermal alterations in the epithermal-porphyry system, accompanying with the several similarities in mineralogy and petrology. This result does not necessarily show the evidence of the ores in the volcano because Ontake is still active. Therefore, the Ontake-type should be still in the very early stage of the epithermal-porphyry system. If this is reasonable, Tokachidake and Azuma-Jododaira types can be at much-earlier stages of the epithermal-porphyry system than Ontake type. However, Ontake type accompanying with sets of acidic to potassic alterations is correlated with the late-stage system in the evolution model of the epithermal-porphyry system (e.g., Silitoe, 2010) (Fig. 53). This discrepancy might be from the lack of a case study from the subvolcanic hydrothermal system of active volcanoes. Probably, this research results indicate that only for formation of such hydrothermal alteration area or systems does not take such log duration without enrichments of precious elements as “ore”.

In this study the evolution model of very-early stage-hydrothermal system, from immature-subvolcanic hydrothermal system through mature one, is newly established (Fig. 54). According to the evaluation of current activity of each case (chapter 1 to 3), thermal state at surface by ground temperature and volcanic gas are distinctive each other. The above types are also consistent with each eruption history in terms of frequency of magmatic or non-juvenile eruptions during last 10,000 years (Fig. 55). Each trend might reflect the difference of volcanic fluid fluxes (magma (melt+crystal), magmatic vapor, and magmatic water). In the evolution model done by this study, Tokachidake, Ontake, Azuma-Jododaira types were used for explanation at each stage during evolution between the very-early epithermal-porphyry systems.

Tokachidke-type is the subvolcanic hydrothermal system at “initial stage”. At this stage, magma behaves still active and intrudes into shallower portion, accompanying with the modification of subvolcanic hydrothermal system. At “middle stage”, the subvolcanic hydrothermal system repeats small magmatic and non-juvenile eruptions, such as Azuma-Jododaira type. During this stage, although the modification of

subvolcanic hydrothermal system probably occurs, the degree is much less than Tokachidake type and closer to Ontake type with the zoned hydrothermal alteration. At “stable stage” to prepare to form the epithermal-porphyry system, the subvolcanic hydrothermal system such as Ontake-type is active with the developed-evolved hydrothermal fluid. During this stage, hydrothermal eruption derived from the zoned hydrothermal alterations occurs and repeats in sometimes.

Summary and conclusions of entire study results

Petrological observation of individual ash grains was carried out for the following cases, (1) Holocene volcanic products from Tokachidake volcano (4.7ka, 3.3ka (Fujiwara et al., 2007, 2009), and 1926AD (Uesawa, 2014)) (Chapter 1); (2) volcanic ash from the 2014 hydrothermal eruption of Ontake volcano (Minami et al., 2016) (Chapter 2); (3) Holocene volcanic tephra layers around 1331AD from Azuma-Jododaira volcano (Yamamoto, 2005) (Chapter 3). As a result, the petrologic and mineralogic characteristics shows each of the magma-hydrothermal system interactions relating to subvolcanic hydrothermal systems.

Based on this reality, this study defines three types of subvolcanic hydrothermal systems within active volcanoes below, Tokachidake-type, Ontake-type, and Azuma-Jododaira-Type. Tokachidake type is for such subvolcanic hydrothermal system directly driven by a magma intrusion, accompanying the chemical and physical modification of subvolcanic hydrothermal system. Ontake type is for a well-developed and mature subvolcanic hydrothermal system similar to the epithermal-porphyry system. Finally, Azuma-Jododaira type is for the subvolcanic hydrothermal system with repetitions of magmatic and non-juvenile eruptions (hydrothermal or steam-blast).

The above three types can be considered as the evolutional series of subvolcanic hydrothermal system, corresponding to the very-early stage of the epithermal-porphyry system. Therefore, the evolution model of the subvolcanic hydrothermal system to the epithermal-porphyry system was newly established (Fig. 54). Though initial (Tokachidake-type) and middle stages (Azuma-Jododaira type) with various degree of

magma intrusions or eruptions, the subvolcanic hydrothermal system evolves into the stable stage like Ontake-type to proceed the ore-forming process at volcanoes.

Table 1. The list of samples analyzed.

Sample ID	Eruption Age	Geological unit	Occurrence	Number on Fig. 2(c)	Sample location	
					Lat.	Long.
1926-C	1926 AD	Unit C	debris avalanche deposit	11	43° 25' 56.0" N	142° 39' 40.9" E
1926-B	1926 AD	Unit B	hydrothermal surge deposit	14	43° 25' 57.4" N	142° 39' 57.9" E
1926-A	1926 AD	Unit A	debris avalanche deposit	16	43° 25' 50.0" N	142° 40' 16.9" E
GFL-2U	3.3 ka	Gfl-2 upper	pyroclastic flow deposit	8	43° 26' 15.1" N	142° 39' 23.1" E
GFL-2L	3.3 ka	Gfl-2 lower	pyroclastic flow deposit	2	43° 26' 17.3" N	142° 38' 45.1" E
GFL-1	3.3 ka	Gfl-1	pyroclastic flow deposit	2	43° 26' 17.3" N	142° 38' 45.1" E
GFL-0	4.7 ka	Gfl-0	pyroclastic flow deposit	1	43° 26' 36.9" N	142° 39' 02.2" E

Sample IDs are assigned after the geological units and abbreviated.

Table 2. Mineral identification by XRD

Samples		Qt	Crs	Trd	Sa	Pl	Aug	En	Ol	Mca	Mag	Ilm	Rt	Kl	Alu	Gp	Anh	Jrs	Py
1926-C	F		**	*		*	*	*						*	**	***	*	**	
	C	*	***	*	f	**	*	f					f	*	**	*	*		
1926-B	F		***	*		*	*	*						f	**	***	*		
	C	*	***			**	*	*			*		*	*	**		*		*
1926-A	F		***	*		**					*		*	*	***	*	*		f
	C	*	***			**	*	*			*			*	***		f		
GFL-2U	F	**	**	**	**	**	***	**	*		*	*			*				
	C	**	**	**	*	**	***	**	*		*	*		f	*				
GFL-2L	F	**	**	*	*	***	***	*	*	f	*	*	*	*	*				
	C	**	**	*	**	***	**	*	*			*		*	*				
GFL-1	F	**	**	*	*	***	**	**	*		*			*	**				
	C	**	**	*	*	***	**	*	*	f				*	*				
GFL-0	F	*	***	**		*	*							*	***				
	C	**	***	**		**	*					*	*	*	**				

Abbreviations; F: fine fraction (<250μm), C: coarse fraction (250μm-1mm), Qtz: quartz, Crs: cristobalite, Trd: tridymite, Sa: sanidine, Pl: plagioclase, Aug: augite, En: orthopyroxene, Ol: olivine, Mca: mica mineral, Ilm: ilmenite, Rt: rutile or anatase, Kl: kaolin group mineral, Alu: alunite, Gp: gypsum, Anh: anhydrite, Jrs: Jarosite, Mag: magnetite and Py: pyrite. The intensities of X-ray peaks in the XRD result are shown by asterisks; ***: intense, **: weak, *: minor, and f: faint.

Table 3. Each endmember composition of APS and alunite

APS endmembers		**Alunite subgroup endmembers**	
Svanbergite	$SrAl_3(PO_4)(SO_4)(OH)_6$	Alunite	$KAl_3(SO_4)_2(OH)_6$
Woodhouseite	$CaAl_3(PO_4)(SO_4)(OH)_6$	Huangite	$Ca_{0.5}Al_3(SO_4)_2(OH)_6$
Hinsdalite	$PbAl_3(PO_4)(SO_4)(OH)_6$	Natroalunite	$NaAl_3(SO_4)_2(OH)_6$
Goyazite	$SrAl_3(PO_4)(PO_3OH)(OH)_6$		
Crandallite	$CaAl_3(PO_4)(PO_3OH)(OH)_6$		
Gorceixide	$BaAl_3(PO_4)(PO_3OH)(OH)_6$		
Florencite	$CeAl_3(PO_4)_2(OH)_6$		
Alunite	$KAl_3(SO_4)_2(OH)_6$		
Huangite	$Ca_{0.5}Al_3(SO_4)_2(OH)_6$		
Natroalunite	$NaAl_3(SO_4)_2(OH)_6$		

The selected minerals in Table 1 are referred from Stoffregen and Alpers (1987), Mills et al. (2009) and Bayliss et al. (2010).

Table 4. XRD result for the volcanic ash of the 2014 eruption at Ontake volcano

Fraction	Qz	Crs	Trd	Pl	En	Mca	Sme	Prl	Kl	Py	Alu	Anh	Gp
Bulk	***	**	f	**	***	f	f	f	*	*	***	f	**
Coarse	***	***	*	**	***	f	f	f	*	***	*	f	*
Medium	***	**	f	***		f	f	f	***	**	**	***	*
Fine	***	f			f	**	**	f	***	f	***		***

Abbreviations; Bulk: untreated sample, Coarse: coarse fraction (250μm-1mm), Medium: medium fraction (125μm-70mm), Fine: fine fraction (<250μm), Qz: quartz, Crs: cristobalite, Trd: tridymite, Pl: plagioclase, En: orthopyroxene, Mca: mica mineral, Ilm: Sme: smectite group mineral, Prl: pyrophyllite, Kl: kaolin group mineral, Py: pyrite, Alu: alunite, Anh: anhydrite and Gp: gypsum. The intensities of X-ray peaks in the XRD result are shown by asterisks; ***: intense, **: weak, *: minor, and f: faint. The above results are based on Minami et al. (2016).

Table 5. Summary of petrographical observation on volcanic ash grains

Ash grain ID	Minerals in ash grains[a]							Alteration[b]	APS type[c]
	Sil	Kl	Prl	Alu	Wod	Py	Ti		
ONTK-VA-001	+			+	+	+	+	RS	ZA
ONTK-VA-002	+			+	+	+		RS	ZA
ONTK-VA-003	+	+						AA	n.d.
ONTK-VA-004				+	+			AA	ZA
ONTK-VA-005	+		+	+	+	+		AA	ZA
ONTK-VA-006	+		+	+				AA-RS	n.d.
ONTK-VA-007	+		+	+				AA-RS	n.d.
ONTK-VA-008	+		+	+				AA-RS	ZA
ONTK-VA-009	+		+	+	+			AA-RS	MW
ONTK-VA-010				+	+			AA	ZA
ONTK-VA-011				+				AA	ZA
ONTK-VA-012	+		+	+	+			AA	ZA
ONTK-VA-013	+		+	+				AA-RS	n.d.
ONTK-VA-014	+			+	+		+	RS	n.d.
ONTK-VA-015	+	+			+			AA	MW
ONTK-VA-016				+		+		AA	n.d.
ONTK-VA-017	+		+	+	+	+		AA	ZA

Presence of the minerals in volcanic ash grains are shown as: + present, and blank none

a Mineral names are abbreviated as: Sil: silica mineral, Kl: 7-Å kaolin-group mineral, Prl: pyrophyllite, Alu: alunite, Wod: woodhouseite-APS, Py: pyrite, and Ti: titanium oxide

b RA: residual silicified alteration; AA: advanced argillic alteration, these alteration types are based on the result in Minami et al. (2016).

c ZA: zoned alunite-woodhouseite-APS; MW: micro-wormy vein woodhouseite-APS

Table 6. Sample list for volcanic products at Azuma-Jododaira volcano

Sample IDs	Sample codes	Occurrence	Geological unit	Locality	
				Lat.	Long.
L1-1	AZM180908001_1	fall ash deposit	L1-1 corelated to Az-OA	37°72′794″	140°26′197″
L1-2	AZM180908001_2	fall ash deposit	L1-2 corelated to Az-OA	37°72′794″	140°26′197″
L2	AZM180908001_3	fall ash deposit	L2 defined by this study	37°72′794″	140°26′197″
L3	AZM180908001_4	fall ash deposit	L3 defined by this study	37°72′794″	140°26′197″
L4	AZM180908001_5	fall ash deposit	L4 defined by this study	37°72′794″	140°26′197″
L5	AZM180908001_6	fall ash deposit	L5 defined by this study	37°72′794″	140°26′197″
L6	AZM180908001_7	fall ash deposit	L6 defined by this study	37°72′794″	140°26′197″
L7	AZM180908001_8	fall ash deposit	L7 defined by this study	37°72′794″	140°26′197″

These above samples were collected from the single outcrop at Loc.1.

Table 7: XRD result for the samples from L1-1 to L7 at Azuma-Jododaira volcano

Sample		Qz	Crs	Trd	Sa	Pl	Aug	En	Amp	Sme	Kl	Alu	Gth
L7	bulk	**	***	**	f	**	**	**		*	*	*	
	F	*	***	**	f	*	*	*		**	*	*	
L6	bulk	***	**	*	f	**	*	*		f	f	*	
	F	***	**	*	f	**	*	*		*	*	*	
L5	bulk	***	***	*	*	*	*	**		*	*	*	
	F	***	***	*	f	*	*	f		*	*	**	
L4	bulk	*	**	**	*	***	*	*	*			**	
	F	*	**	**	*	**	*	*	*			*	
L3	bulk	*	**	**	*	***	f	f	*			**	
	F	*	**	**	*	***			*		f	**	
L2	bulk	**	***	*		**	**	**		f	f	*	**
	F	**	***	*		*	*	*		*	*	**	
L1-2	bulk	***	**	*		*	f	**		*	*	*	
	F	***	**	*		*	f	f		*	*	**	
L1-1	bulk	***	**	*		**	**	f		*	*	*	
	F	***	**	*		*	f	f		*	*	*	

Abbreviations; bulk: untreated sample, F: fine fraction (<250μm), Qz: quartz, Crs: cristobalite, Trd: tridymite, Sa: sanidine, Pl: plagioclase, Aug: augite, En: orthopyroxene, Amp: amphibole group mineral, Sme: smectite group mineral, Kl: kaolin group mineral, Alu: alunite, and Gth: goethite. The intensities of X-ray peaks in the XRD result are shown by asterisks; ***: intense, **: weak, *: minor, and f: faint.

Table 8: Summary of componentry analysis combining between a binocular stereoscopic microscope and SEM-EDS.

Samples	DVR		VVR		Alteration types in MAR and PAVR						
	LV	HCVR	Sc[*1]	Pm	Sil	Prl	Kl	Alu	Mca	Chl	K-feld
L7	*	*			*	*	**	*	*		
L6	**	*	*		*	*	*				
L5	*	*			*	*	**	*	*		
L4	**	**	**		*	*	*	*			
L3	*	*	**		*	*	*	*			
L2	**	*	**	*	**	*	**	*	*		
L1-2	**	**			*	*	**	*	*	*	
L1-1	*	*			*	**	**	*	*	*	*

Abbreviations; DVR: dense volcanic rock, LV: lava fragment. HCVR : holocrytalline volcanic rock, VVR: vesicular volcanic rock, Sc : scoria, Pm : pumice, MAR: massive altered rock, PAVR: partly altered volcanic rock, Sil : silica type, Prl : pyrophyllite type, Kl : kaolin type, Mca : mica-chlorite type, Chl : chlorite type, and K-feld : mica-K-feldspar type. The asterisks show presence of categorized ash grains as **: abundant, *: present, none: not present.

*[1] scoria or scoria fragment are mostly weathered.

Figures

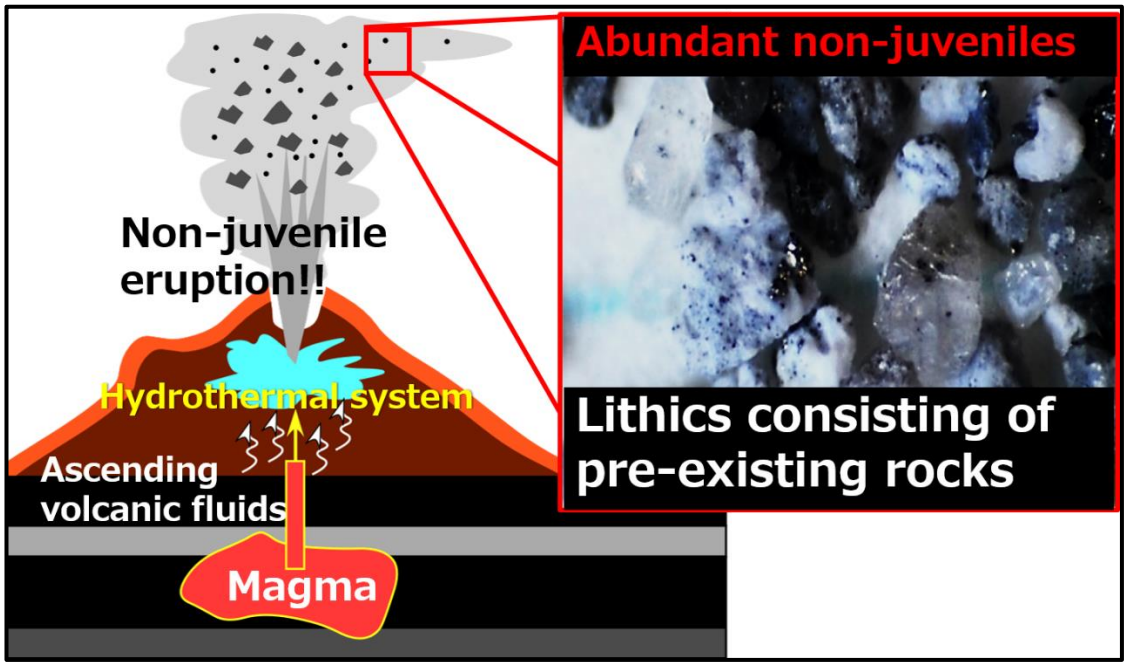

Fig. 1: Schematic relations between subvolcanic hydrothermal system and altered volcanic products

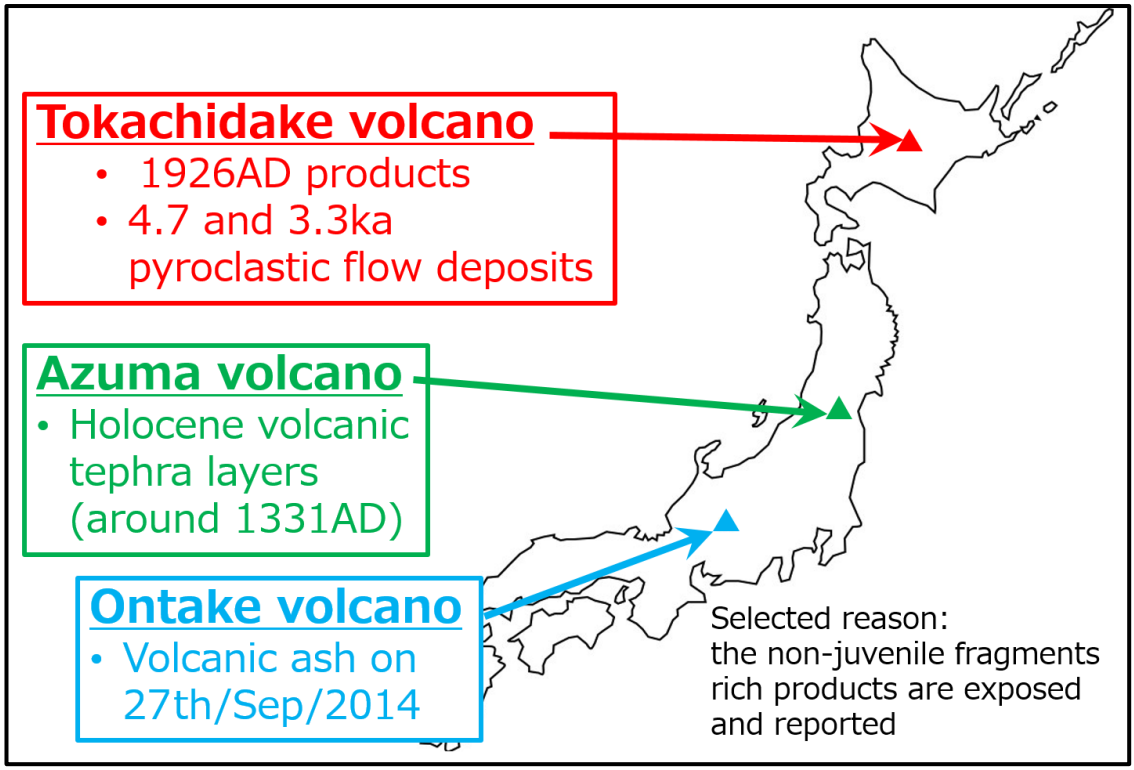

Fig. 2: Study objective products for three selected cases in Japan.

Each of them are : (1) Holocene volcanic products from Tokachidake volcano (4.7ka, 3.3ka (Fujiwara et al., 2007, 2009), and 1926AD (Uesawa, 2014)) (Chapter 1); (2) volcanic ash from the 2014 hydrothermal eruption of Ontake volcano (Minami et al., 2016) (Chapter 2); (3) Holocene volcanic tephra layers around 1331AD from Azuma-Jododaira volcano (Yamamoto, 2005) (Chapter 3).

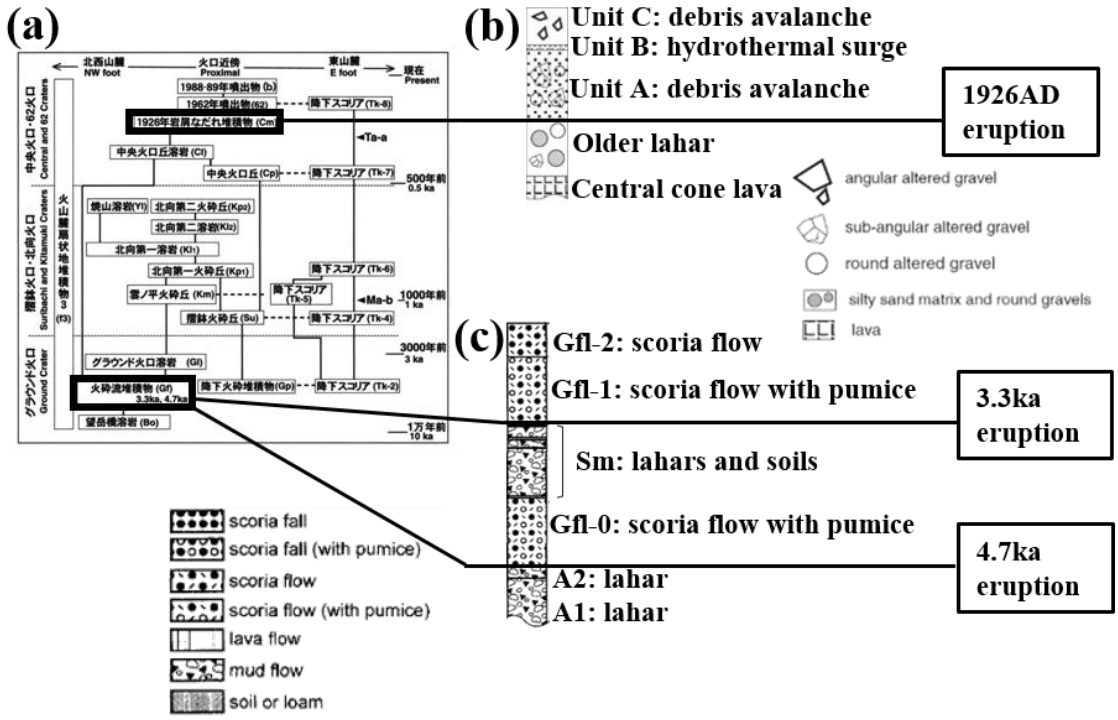

Fig. 3: Geological background of Tokachidake volcano.

(a): The volcanic history of Tokachidake volcano during Holocene (Ishizuka et al., 2010). (b): The stratigraphy of 1926AD lahar deposit (Uesawa, 2014). (c): The stratigraphy of the 3.3ka and 4.7 ka Ground Crater pyroclastic flow deposits (Fujiwara, 2009).

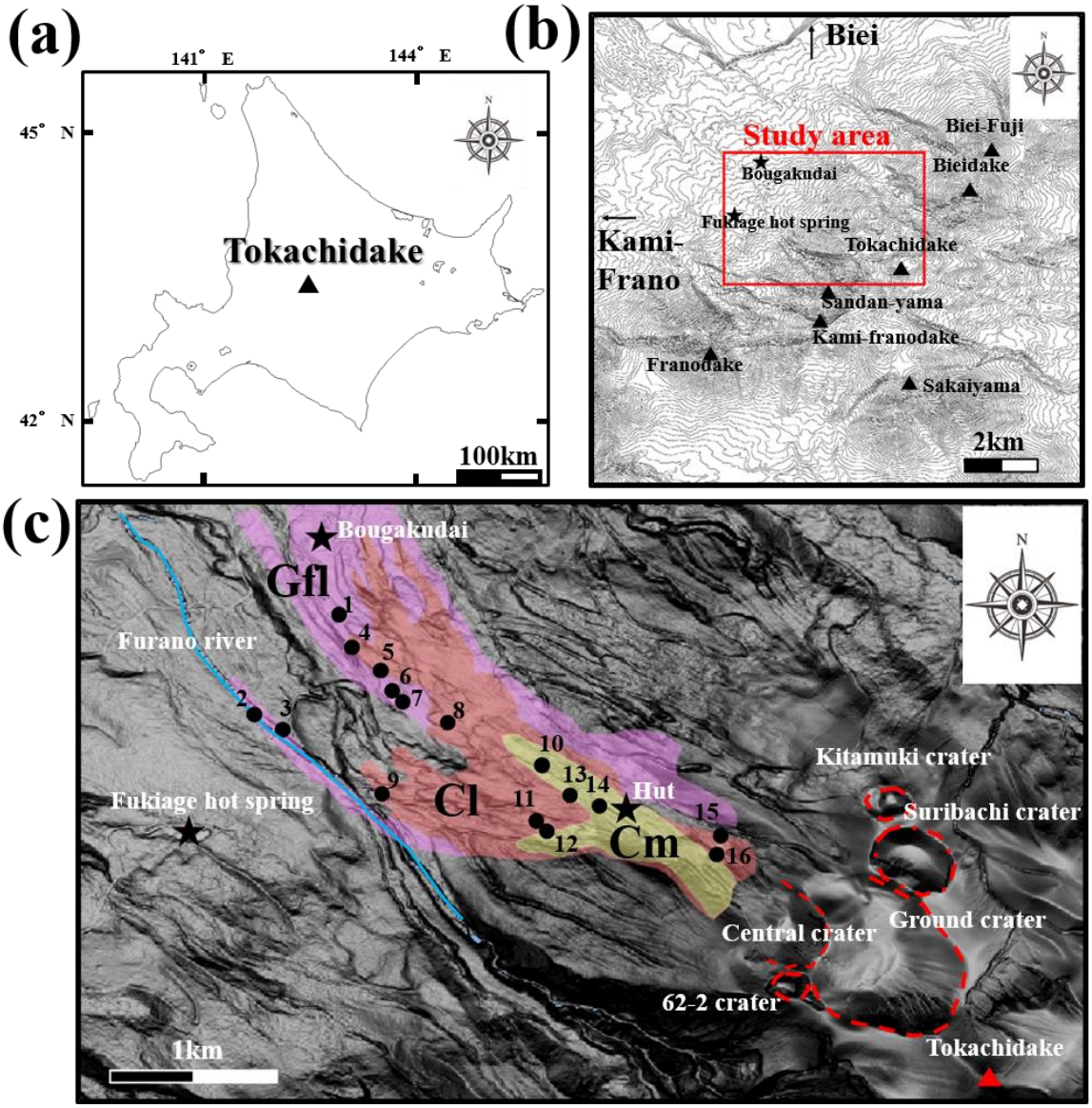

Fig. 4. Location of studied area and sampling points.

(a): Index map. (b): Map of Tokachidake and surrounding area created by using the 10m-mesh DEM from [URL3]. (c): Sampling and observation points (1-16). The map was created by using the 5m-mesh DEM data from [URL3]. The colored areas are the distributions of the products (Ishizuka et al., 2010); yellow: the 1926AD lahar deposit (Cm), orange: the 330AD lava (Cl), pink: the pyroclastic flow deposits in 3.3ka and 4.7ka (Gfl).

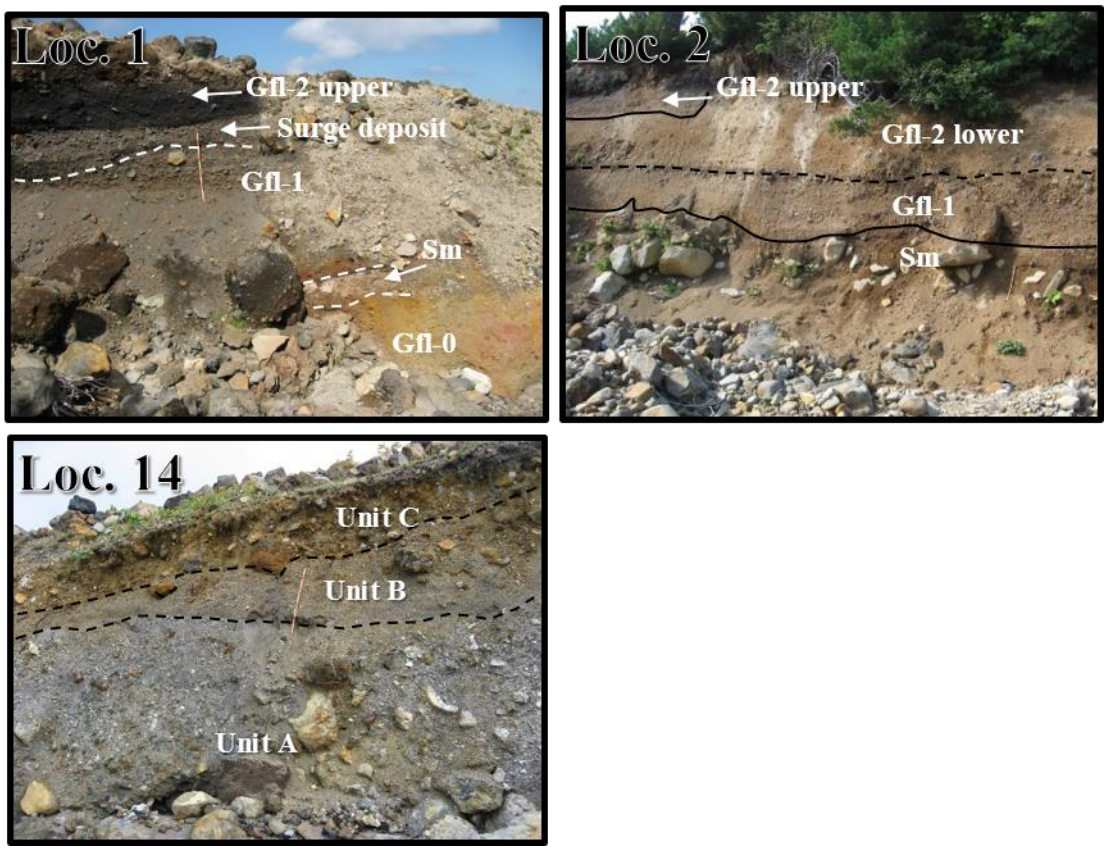

Fig. 5. Outcrops of the studied deposits of Gfl-0, Gfl-1, Gfl-2 (lower and upper), and 1926AD lahar deposits (Units A to C).

Loc.1: Occurrence of the 4.7 and 3.3 ka pyroclastic flow deposits. A lahar deposit (Shirogane lahar deposit: Sm) intercalates between the 4.7 ka deposit (Gfl-0) and the 3.3 ka deposit (Gfl-1). The Gfl-2 upper deposit consists of upper a massive part and a lower surge layer. Loc.2: The 3.3 ka pyroclastic flow deposit. Gfl-2 consists of two units (upper and lower). Loc.12: The 1926 lahar deposit consisting of three units (A, B, and C).

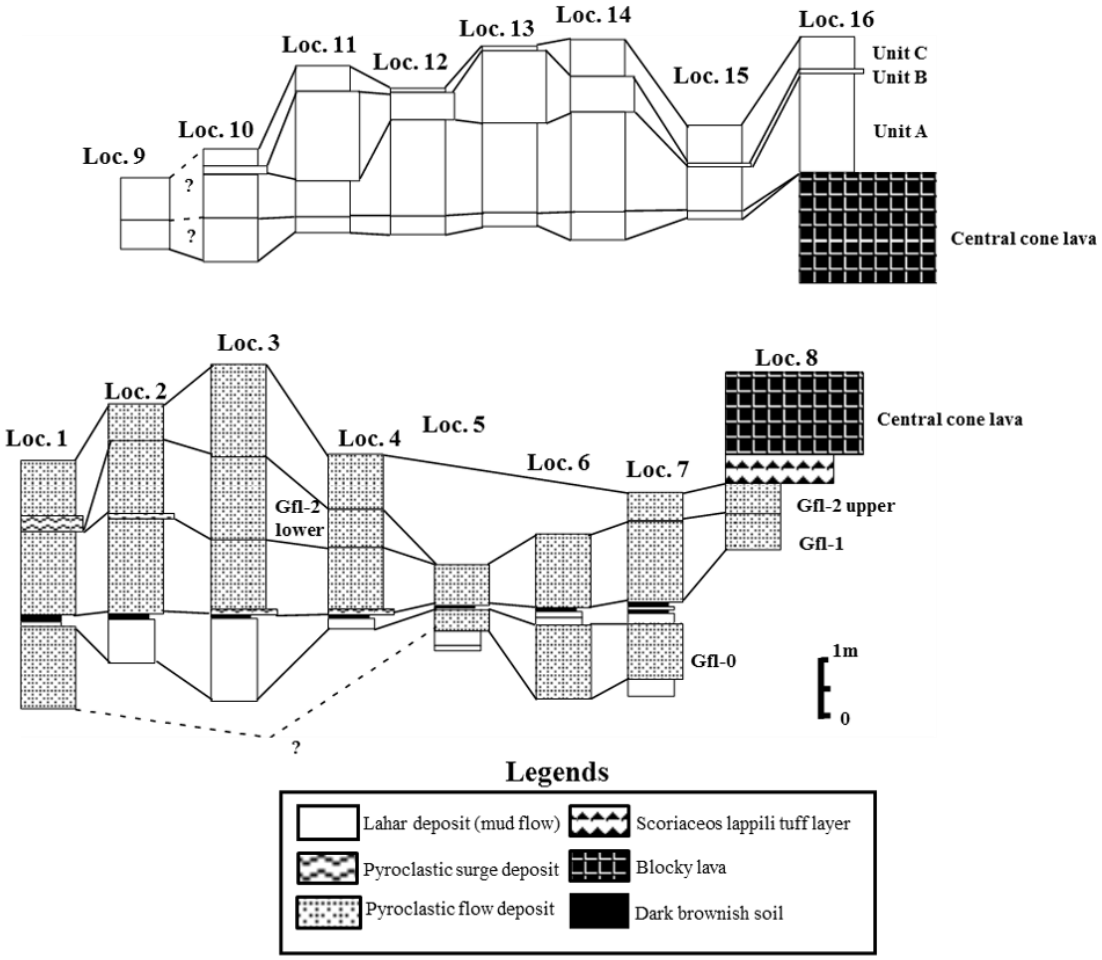

Fig. 6. Columnar sections at the sampling points on the north-eastern slope (Loc. 1 to 16 in Fig. 4c).

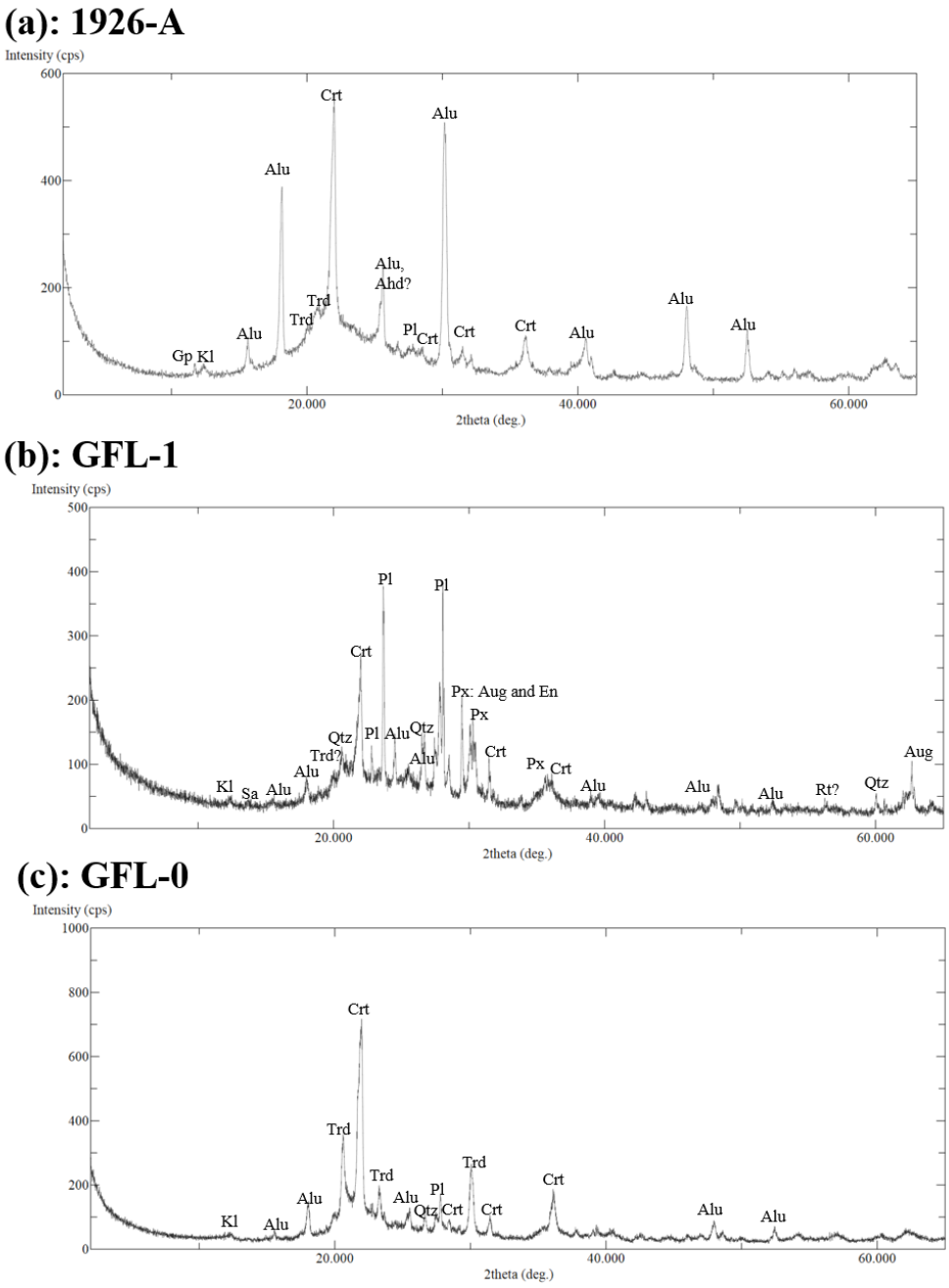

Fig. 7: Representative chart of XRD measurements for bulk ash samples (a fraction < 250μm). Abbreviations are same to Table 2.

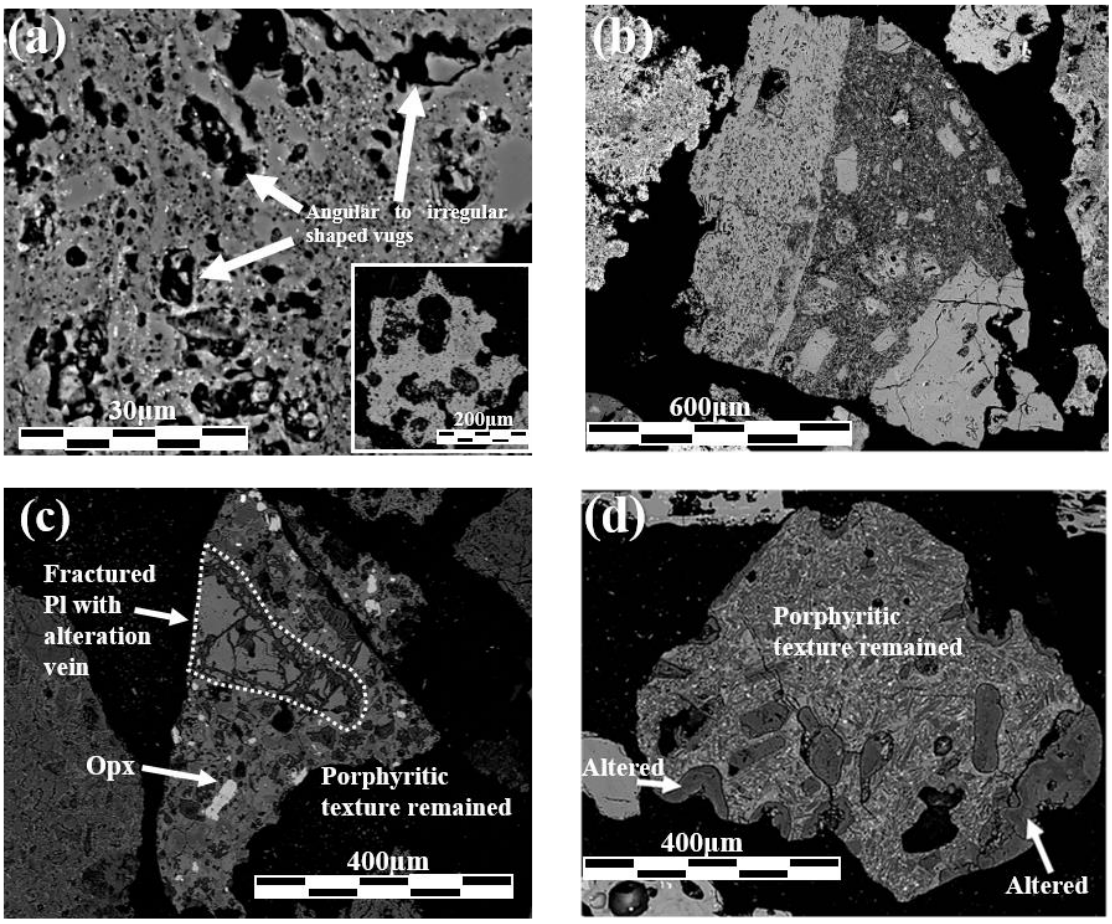

Fig. 8: Representative backscattered electron images of silica type ash grains.

(a)1926-A-004: a massive silica containing abundant vugs. This texture develops in scale of 100 nm to several 10 μm. (b)GFL-0-006: silica pseudomorphs of phenocryst and groundmass crystals. (c)1926-A-006: unaltered phenocrysts penetrated by alteration minerals veins. (d)GFL-2U-013: Partly altered porphyritic rock, remaining primary phenocryst minerals and glass-bearing groundmass.

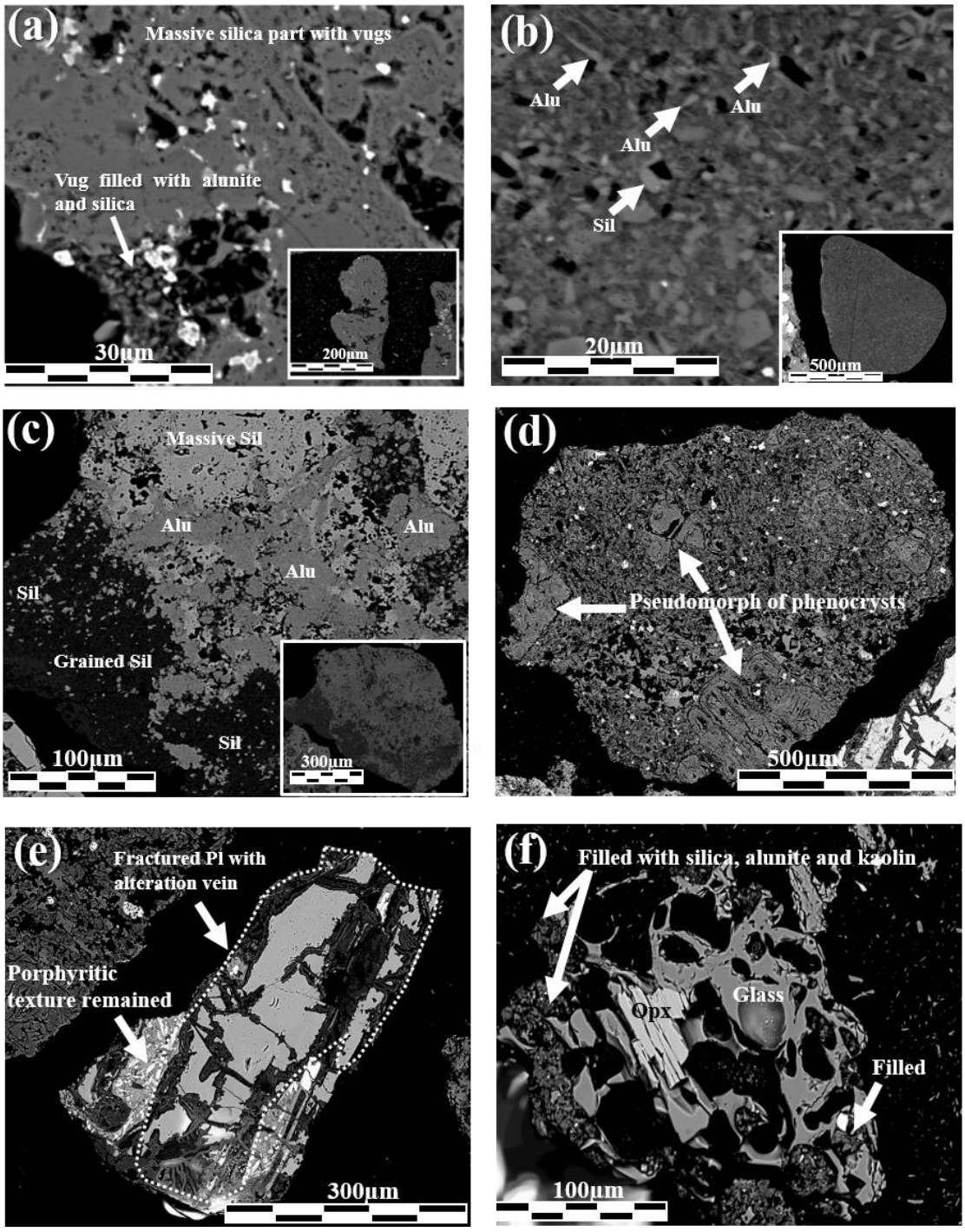

Fig. 9: Representative backscattered electron images of alunite type ash grains.

(a) GFL-2L-009: Vugs in massive silica, partly filled with fine-grained crystals of alunite and silica. (b) GFL-1-24: An ash grain composed of fine-grained crystals (<10μm) of silica mineral, alunite and kaolin mineral. (c) GFL-0-004: An aggregate of alunite crystals filling the vugs in massive silica. The alunite aggeregates consist of fine-needle shaped crystal (<10μm) and coarse-massive crystal (several 10μm). (d)

1926-A-001: Pseudomorphs of phenocryst crystals replaced by silica and kaolin minerals. The matrix part consists of crystals of silica and alunite. (e) 1926-A-002: Unaltered phenocrysts penetrated by veins composed of silica mineral, alunite, and kaolin mineral. (f) GFL-1-014: Fine-grained crystals of silica and alunite filling the bubbles in scoriaceous ash grain.

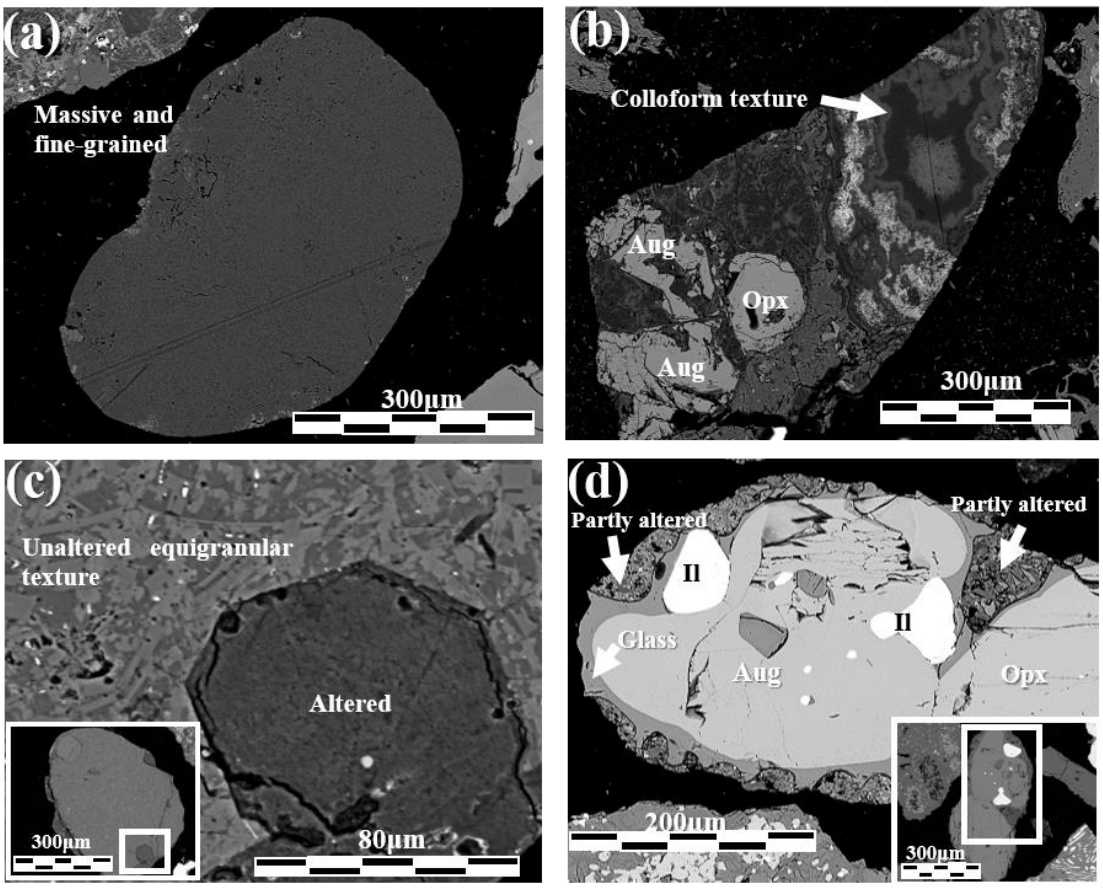

Fig. 10: Representative backscattered electron images of kaolin type ash grains.

(a)GFL-1-022: An ash grain consisting of fine-grained crystals of silica and kaolin. (b)GFL-1-013: Colloform texture consisting of layered silica and kaolin mineral, developed in the weakly altered ash grain. (c)GFL-1-042: Partly altered holocrystalline equigranular rock. Altered part consists of silica and kaolin mineral. (d)GFL-1-032: An ash grain mostly composed of unaltered volcanic rock. Silica and kaolin replace glassy groundmass partly.

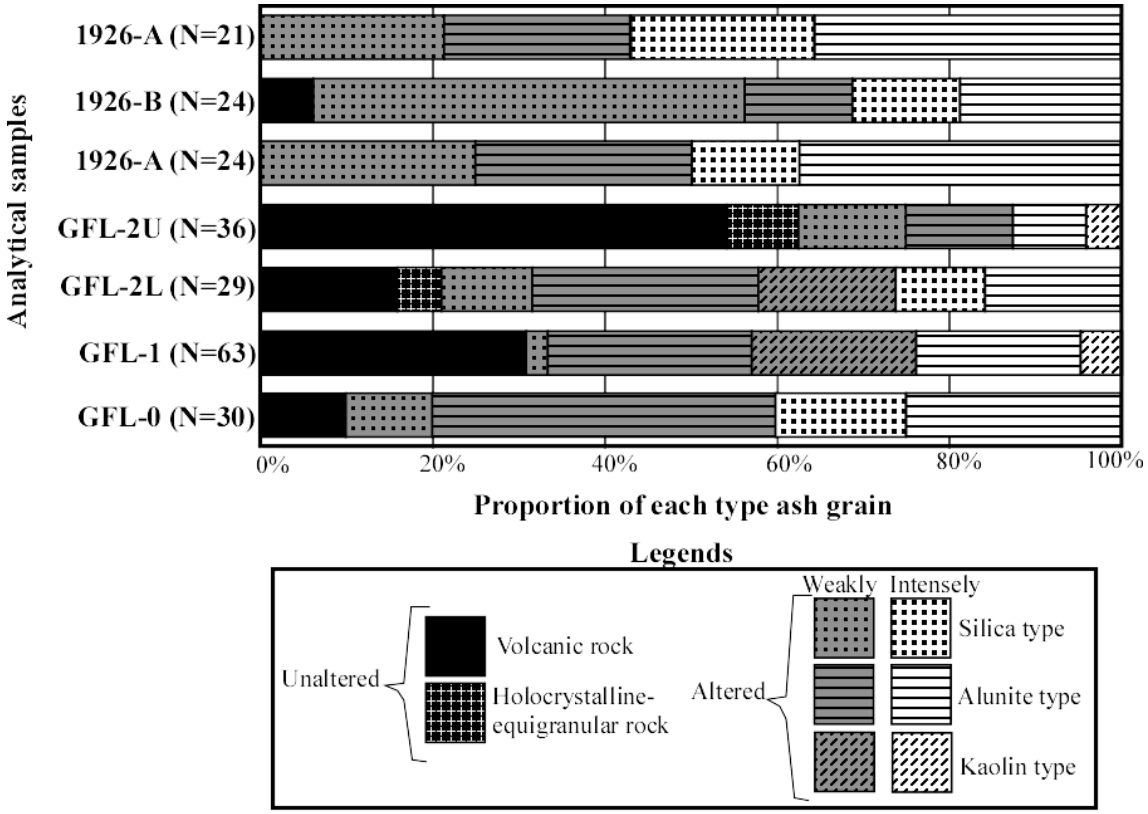

Fig. 11. Relative abundances of altered to unaltered ash grains.

The proportion is estimated by counting numbers of the ash grain types under the views of SEM-EDS.

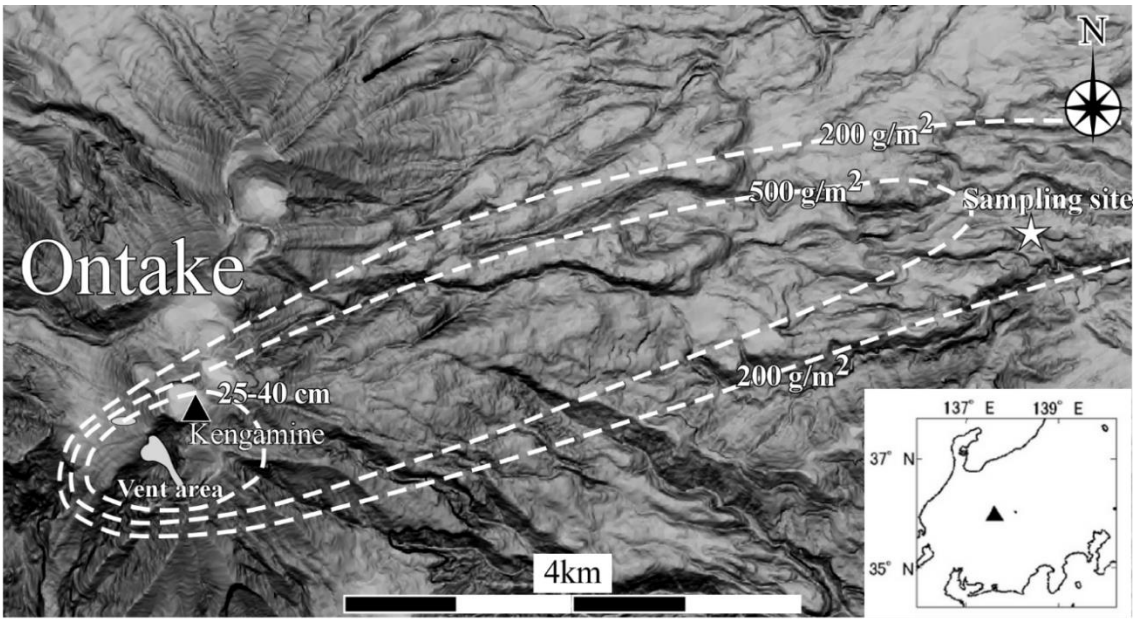

Fig. 12: Sampling location of volcanic ash from the 2014 eruption. The topographical relief map is created with Kashimir3D from the 10-m-mesh DEM data provided by the Geospatial Information Authority of Japan [URL].

Thickness and isomass contours of the volcanic ash from the 2014 eruption were referred from the results of the geological survey conducted by Earthquake Research Institute, The University of Tokyo (ERI) (2014) [URL].

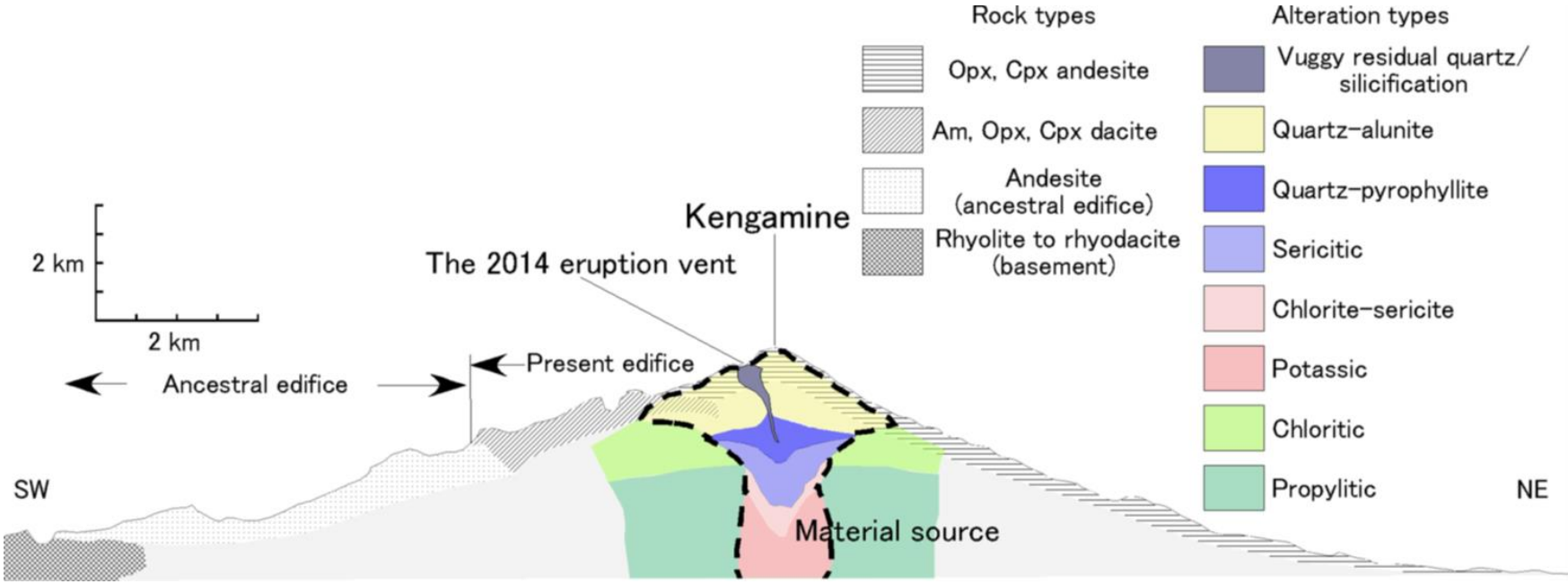

Fig. 13: Cross section of Ontake volcano (Minami et al., 2016) showing models of basement rock types, ancestral and present edifice based on Yamada and Kobayashi (1988). Alteration zones underlying the edifice are modified from Sillitoe (2010) to estimate the source depth of the volcanic ash. The dashed line indicates possible regions of the source of the volcanic ash

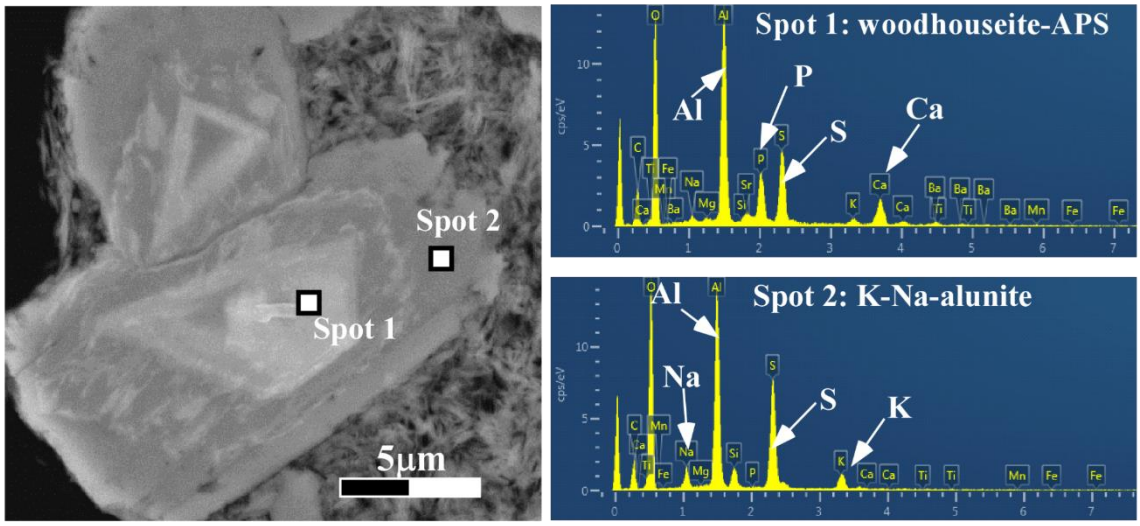

Fig. 14: Typical energy dispersive X-ray (EDS) spectrum of aluminum-phosphate-sulfates (APS) mineral occurring as a core of alunite.

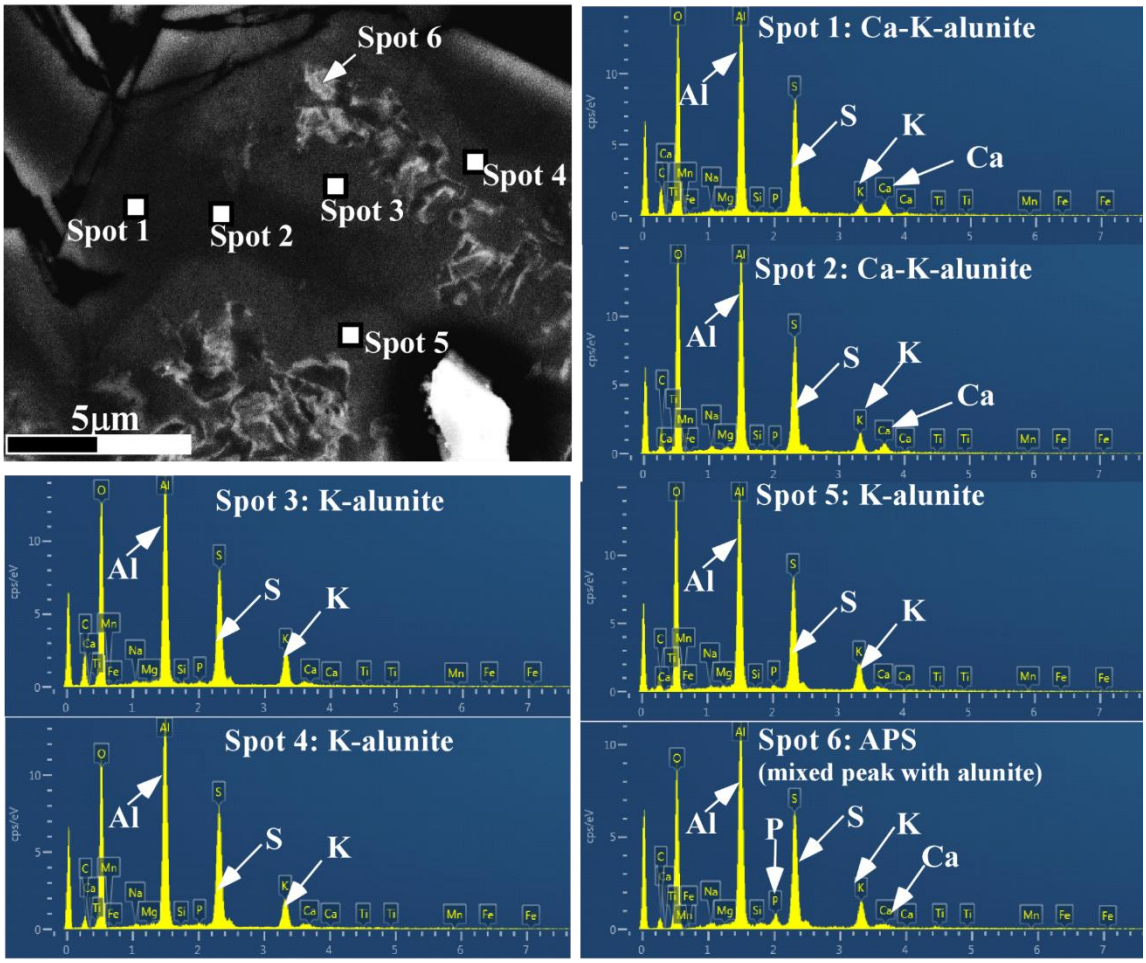

Fig. 15: Compositionally zoned alunite containing a core of a dissolved-fibrous APS mineral.

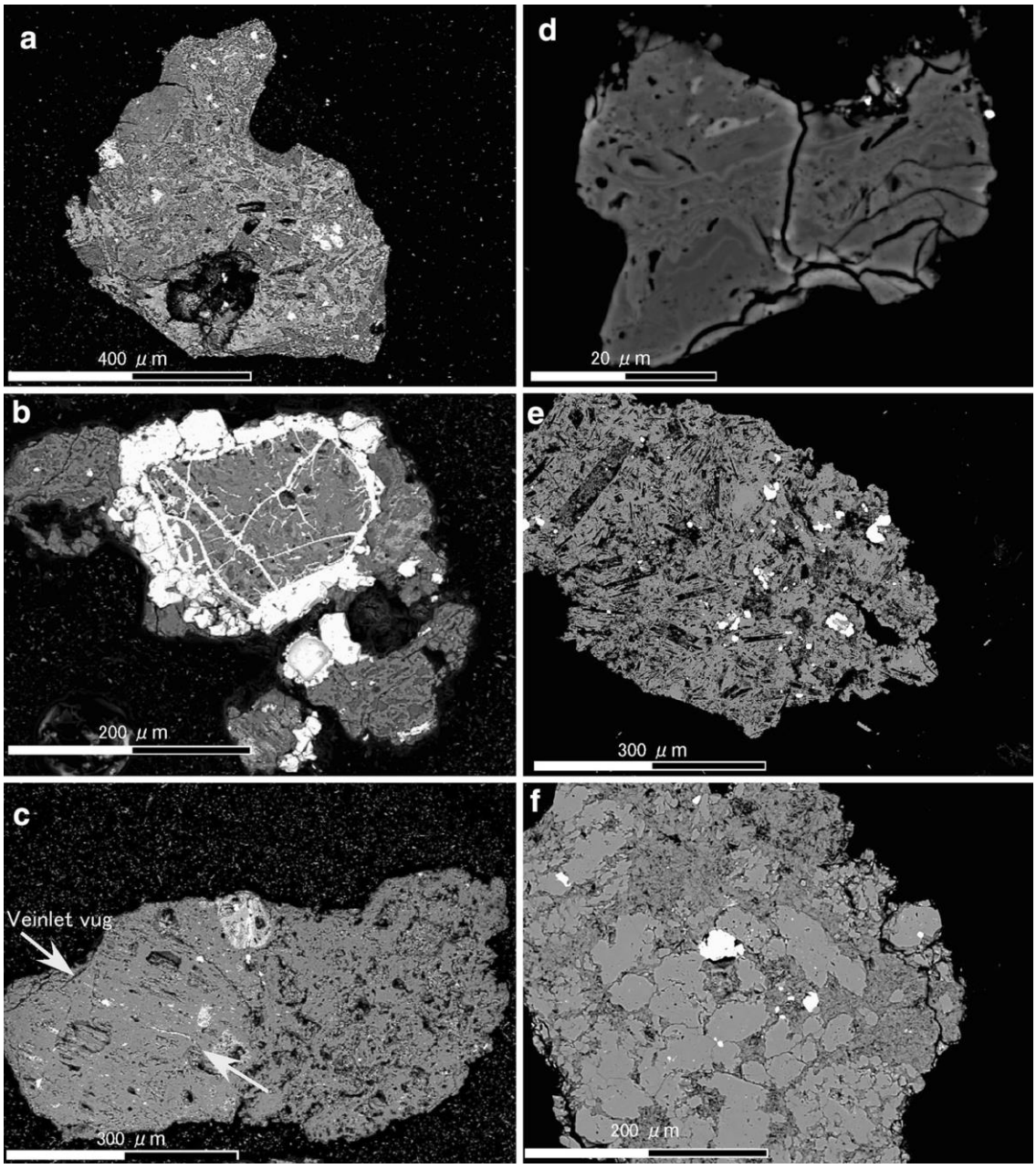

Fig. 16: BEI images of volcanic ash particles described in Minami et al. (2016).

Following captions were referred from Minami et al. (2016). a: Typical partly altered volcanic fragments in the coarse fraction containing microlites of plagioclase, anorthoclase, sanidine, and minor interstitial glass. Some of plagioclase microlites and glass were replaced by pyrite, silica mineral, kaolin-group mineral, and muscovite. b: The silica+pyrite assemblage in a grain containing darker pseudomorph in the matrix. Pyroxene phenocryst is replaced by silica mineral, and pyrite crystals fill the cleavage of the pseudomorphs. c: The right side of the grain partly retained the original vesicular texture, while the left part shows a completely deformed texture. Narrow veinlets of vug and pyrite crystals are recognized in the deformed

part (arrow). d: Grains containing silica+pyrite assemblage with colloform texture consisting of micron-width wavy bright bands and darker matrix. e: Grain consisting of silica mineral, pyrite, alunite, kaolin-group mineral, showing pseudomorphic volcanic texture. Original crystals were replaced by silica mineral or kaolin (darker) or became void. f: A silica minerals+pyrophyllite+pyrite assemblage grain comprises anhedral silica crystals (gray) and a fine-grained matrix of pyrophyllite (darker)

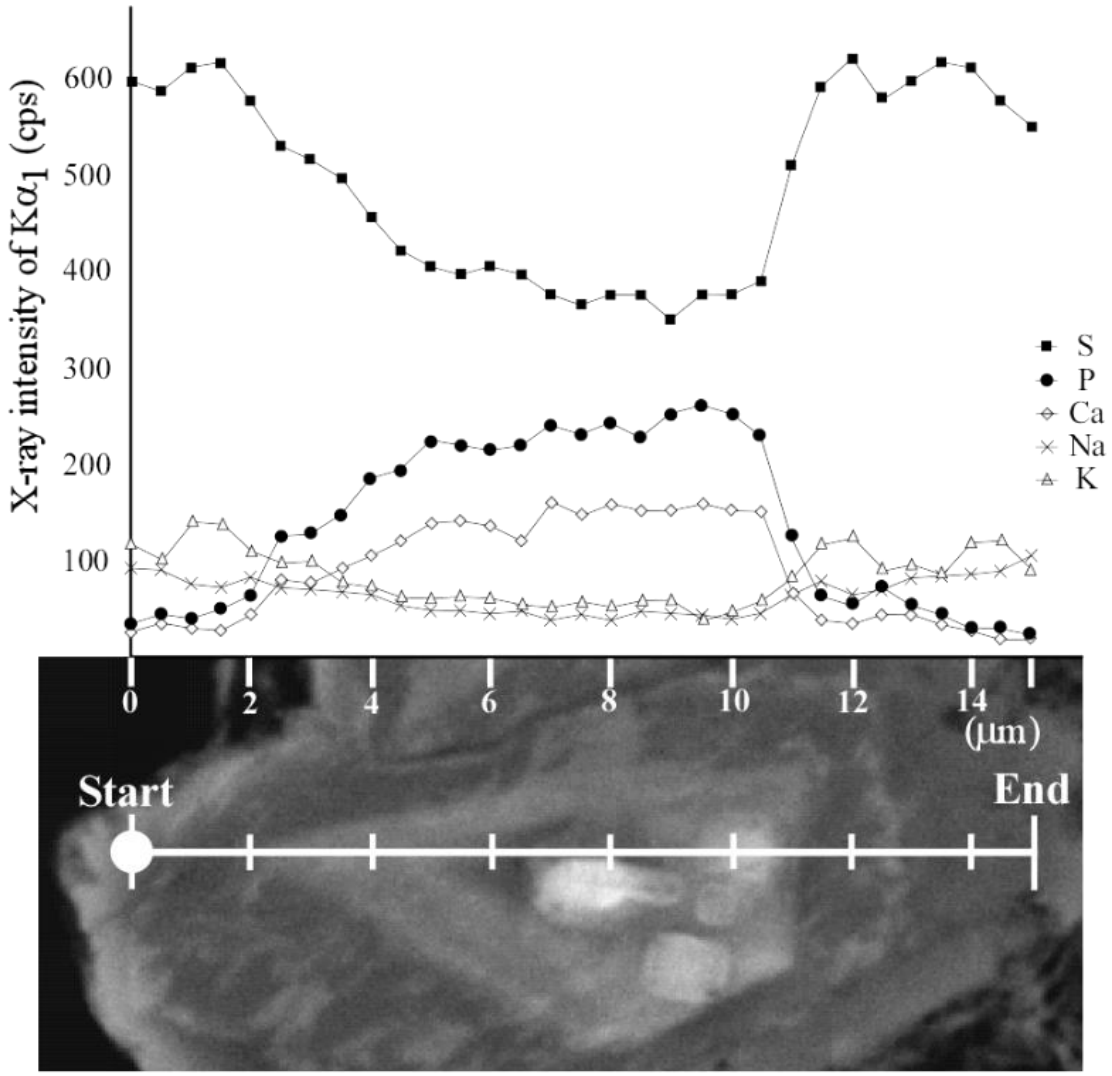

Fig. 17. EDS line scan profile with the backscattered electron images (BEI) image of the woodhouseite-bearing alunite crystal. The compositionally zoned crystal is contained in the grain of ONTK-VA-012 in Table 5 and Fig. 18b.

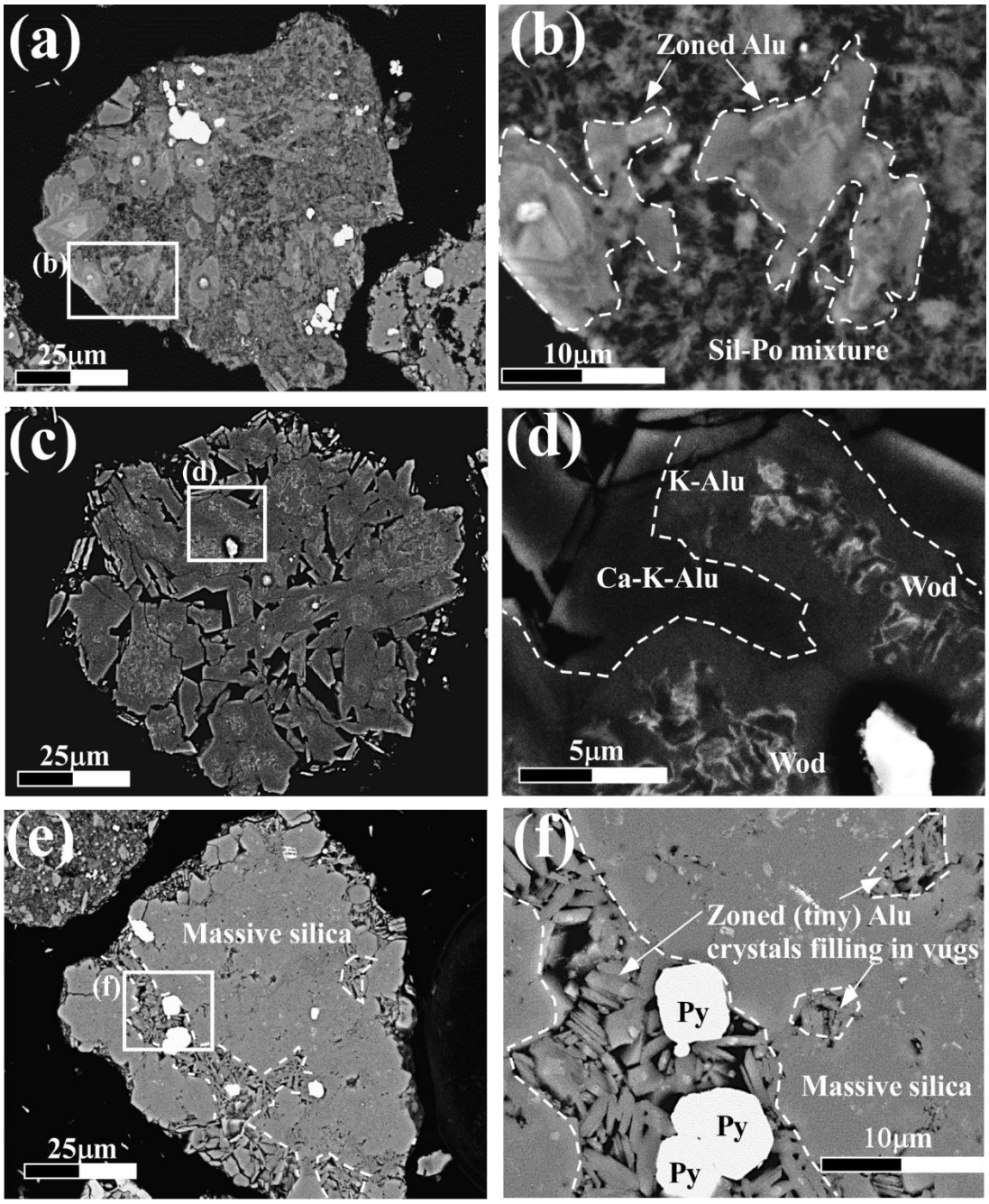

Fig. 18: Representative backscattered electron images of Zoned-alunite-woodhouseite-APS.

Each of (a), (c), and (e) shows the entire view of the ash grain, corresponding respectively to the magnified images of (b), (d), and (f). The mineral abbreviations are the same as in Table 5. (a) An aggregate of zoned-alunite crystals in the matrix of silica-pyrophyllite mixture (ONTK-VA-017 in Table 5). (b) A fine-grained silica-pyrophyllite mixture interstitially fills among the zoned alunite crystals with a woodhouseite core. (c) An aggregate of coarse zoned alunite crystals. (d) Zoned alunite containing a fibrous-woodhouseite core (ONTK-VA-004 in Table 5). The interstitial silica and Si-Al clay minerals are not accompanied with the

zoned alunite. (e) Zoned alunite filling the vugs in a massive silicified rock fragment. Irregular or vein-shaped vugs are incompletely filled with tiny zoned alunite crystals (ONTK-VA-001 in Table 5). (f) An aggregate of tiny crystals of zoned alunite in the vugs.

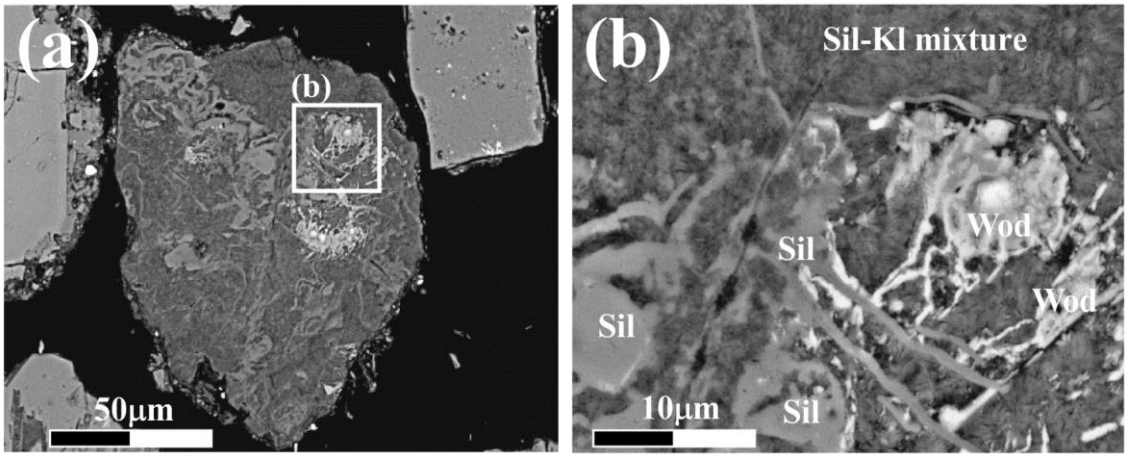

Fig. 19**:** Representative backscattered electron images of *micro-wormy vein woodhouseite-APS*.

(a): entire ash grain containing micro-wormy veins. The grain consists mainly of silica (Sil) and kaolin (Kl) minerals (ONTK-VA-015 in Table 2) (b) Micro-wormy vein APS cross-cut by siliceous micro-wormy veins in the matrix of fine-grained silica-kaolin mixtures.

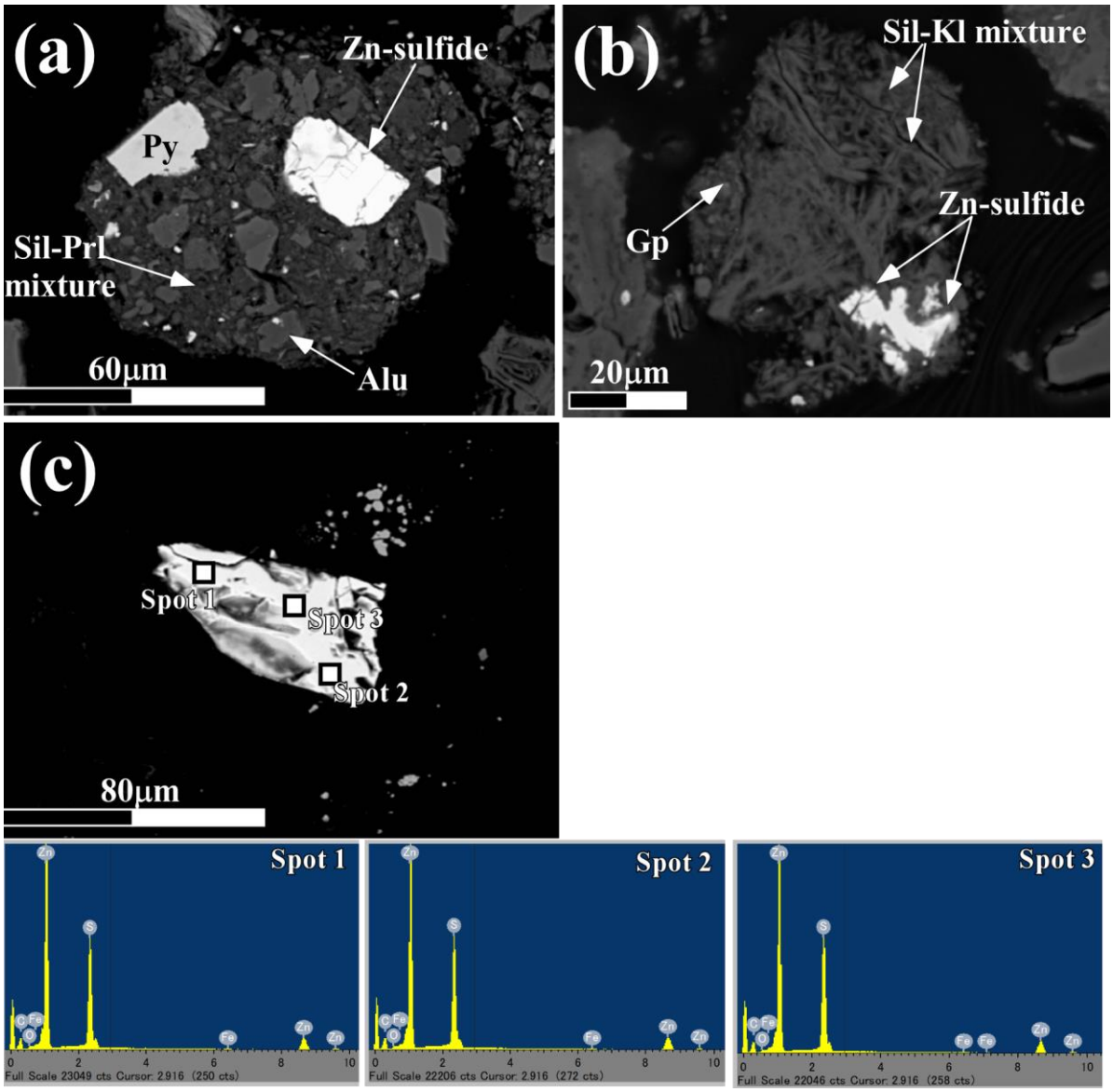

Fig. 20: Representative backscattered electron images of Zn-sulfide bearing ash grains with EDS spectrum. The mineral abbreviations are same with Table. 4 and 5. (a): The ash grain having coexistence of alunite, Zn-sulfide and pyrite crystals with interstitial Sil+Prl mixtures (ONTK-18110606). (b) The ash grain consisting of very-fine grained Sil+Kl+Gp mixtures, accompanying with Zn-sulfide (ONTK-18110605). (c) Isolate-free crystal of Zn-sulfide determined by EDS spectrum (ONTK-18110603).

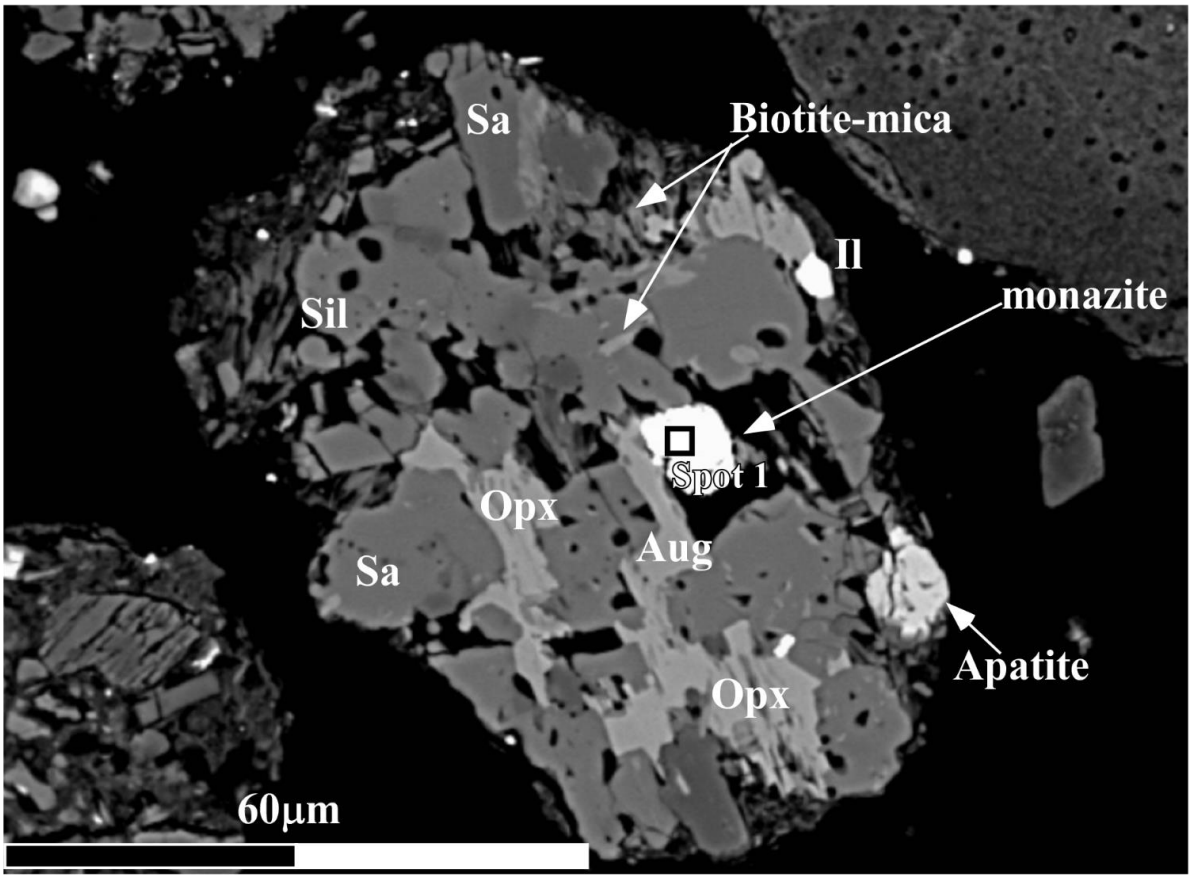

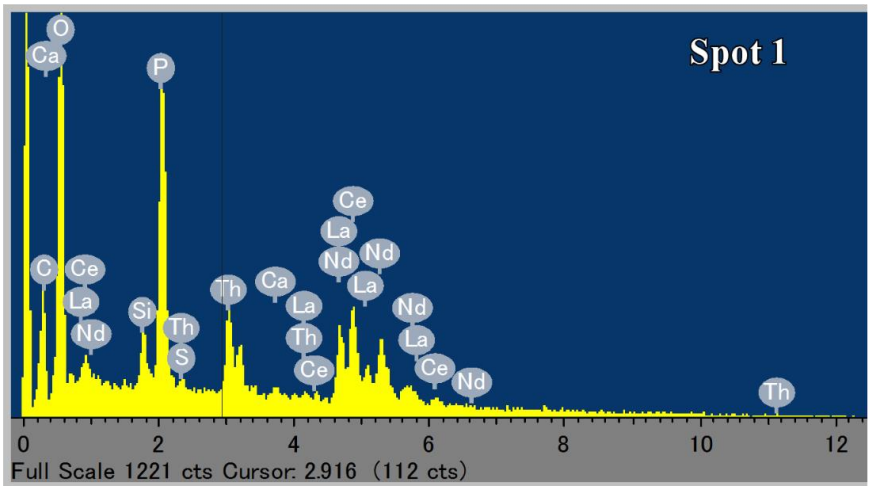

Fig. 21: Representative backscattered electron images of monazite bearing ash grains with EDS spectrum (ONTK-18110604).

The mineral abbreviations are same with Tables. 2, 4 and 5.

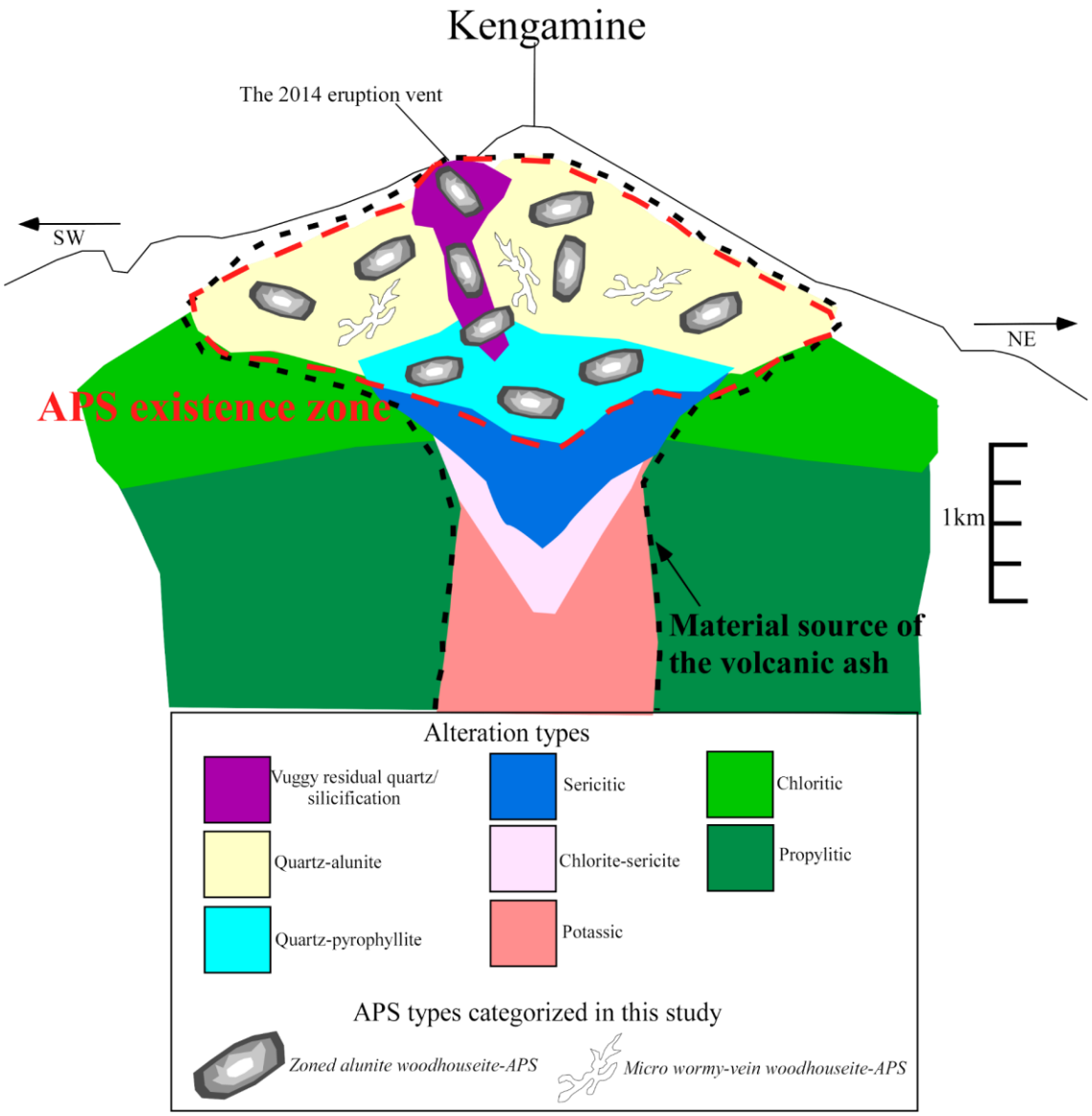

Fig. 22: APS existence zone in the material source model (alteration column) of the volcanic ash from the 2014 Ontake eruption.

This figure was created and modified from Silitoe (2010) and Minami et al. (2016). The APS existence zone surrounded by the dashed red line was based on petrography and mineralogy of the individual volcanic ash (Figs. 18 and 19). The black dotted area is whole material source of the volcanic ash (maximum depth ~2km) estimated by Minami et al. (2016).

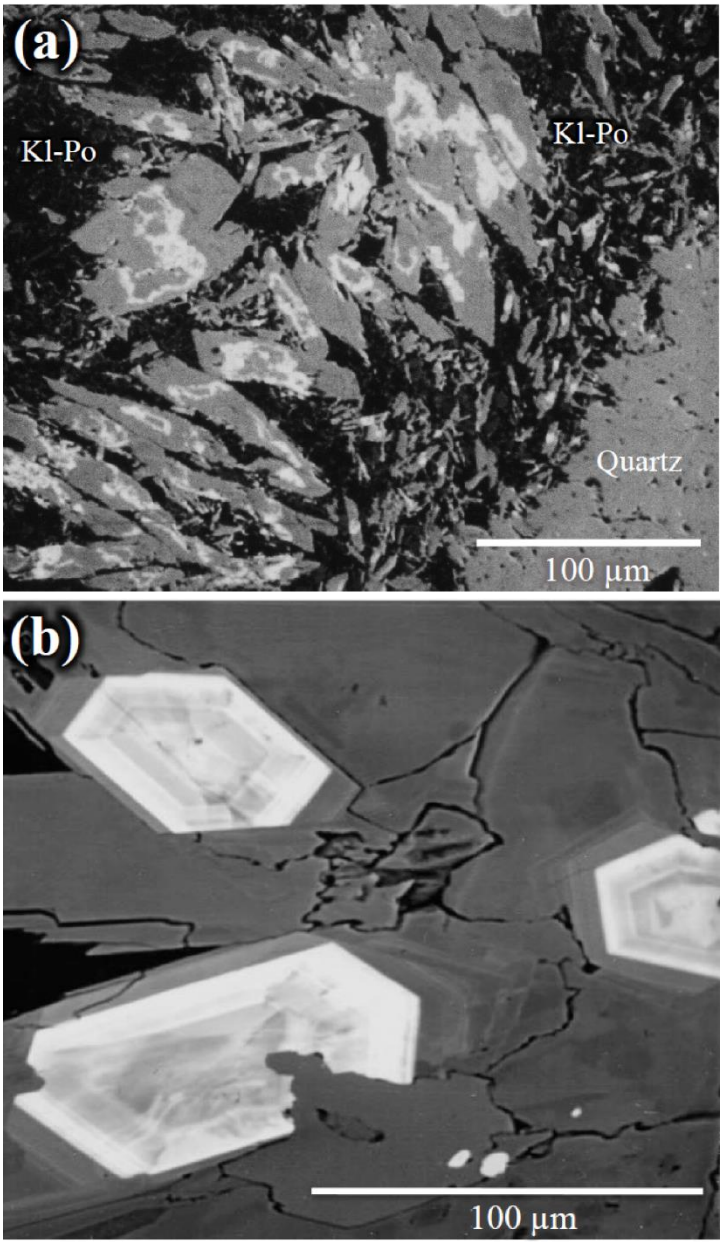

Fig. 23: APS minerals in hydrothermal ore deposit.

(a) Backscattered electron image of bladed-alunite crystals containing dissolved cores of woodhouseite-crandallite-svanbergite accompanying massive quartz within a fine-grained matrix of kaolinite-pyrophyllite (Rodalquilar gold-alunite ore deposit, Spain) (Arribas et al., 1995) [16]. (b) Backscattered electron image of alunite and APS minerals from the advanced argillic zone immediately above the Far Southeast (FSE) porphyry Cu-Au-Ag deposit, Philippines (Hedenquist, et al., 2017). These photographs are modified and referred from Arribas et al. (1995) and Hedenquist et al. (2017), respectively.

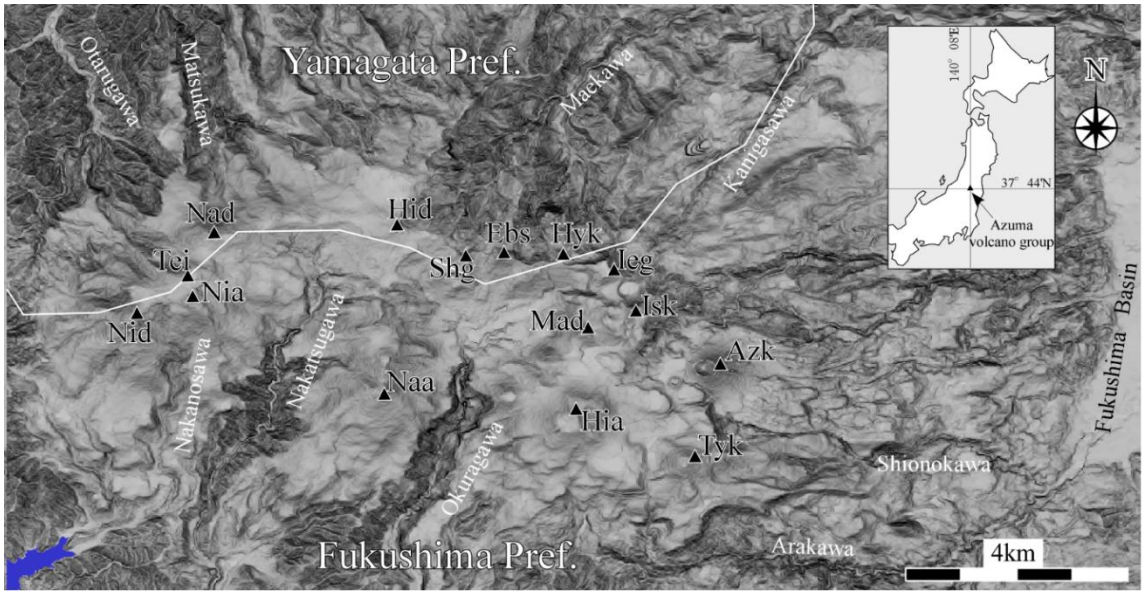

Fig. 24: Locality map around Azuma volcano group.

This map was created by using the 10m-mesh DEM from [URL3]. The peaks around Azuma volcano group are abbreviated as Azk: Azuma-kofuji, Ebs: Eboshiyama, Hia: Higashiazumayama, Hid: Higashidaiten, Hyk: Hyokko, Ieg: Iegatayama, Isk: Issaikyoyama, Mad: Maedaiten, Naa: Nakaazumayama, Nad: Nakadaiten, Nia: Nishiazumayama, Nid: Nishidaiten, Shg: Shogen-yama, Tei: Tenguiwa, and Tyk: Takayama.

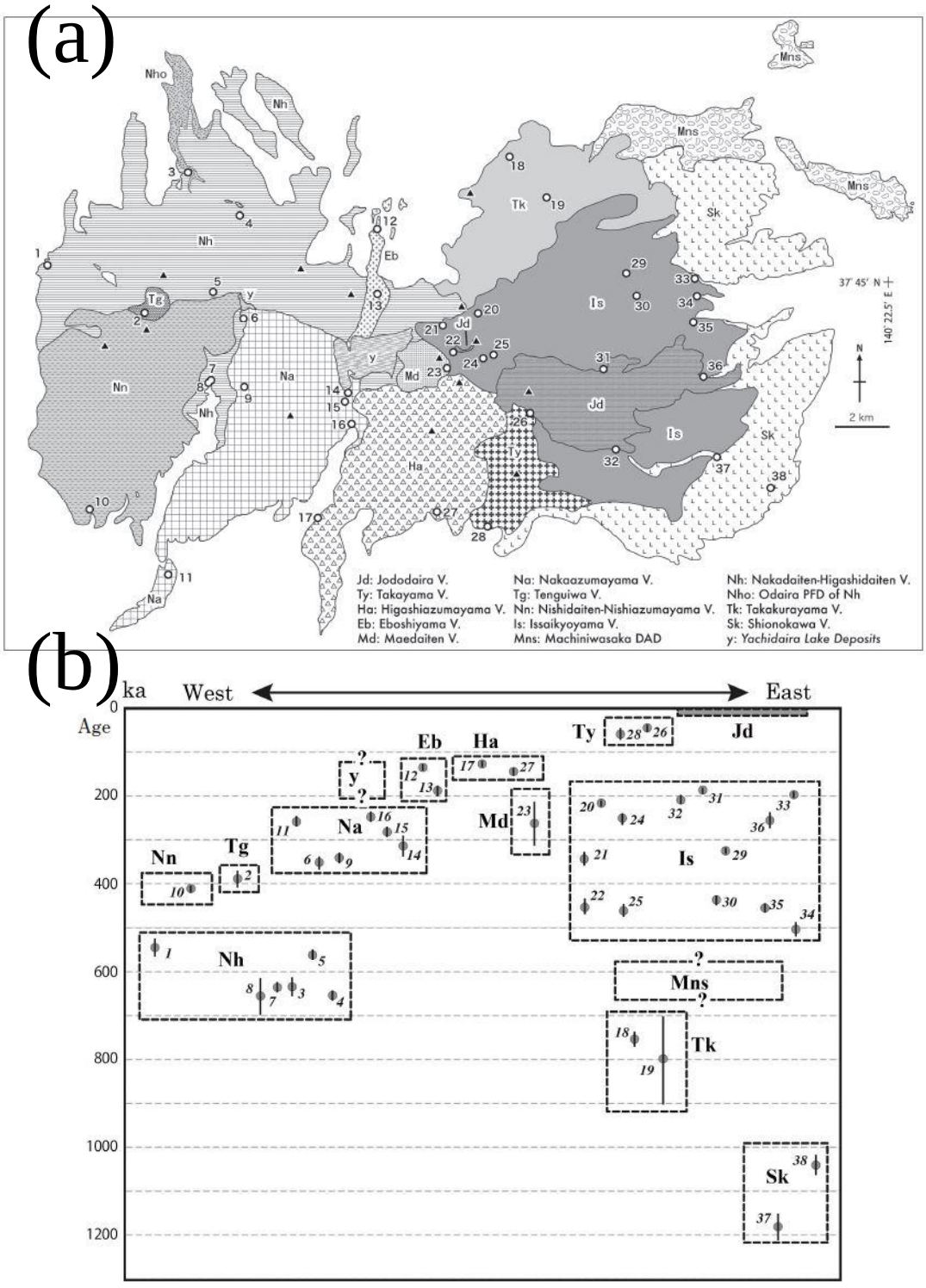

Fig. 25: Classification of volcanic products from Azuma volcano group determined by K–Ar age dating (Matsumoto et al., 2018).

(a): Geological map of Azuma Volcano based on K–Ar age data (Matsumoto et al., 2018). V.: volcanic products, PFD: pyroclastic flow deposit, DAD: debris avalanche deposit. (b): Temporal and special change

of volcanic activity of Azuma Volcano (Matsumoto et al., 2018). Abbreviations are the same with Fig. 25a. The vertical axis shows temporal change and horizontal axis shows spatial distribution from west to east. K–Ar ages are given with error bars at the 1 σ uncertainty level.

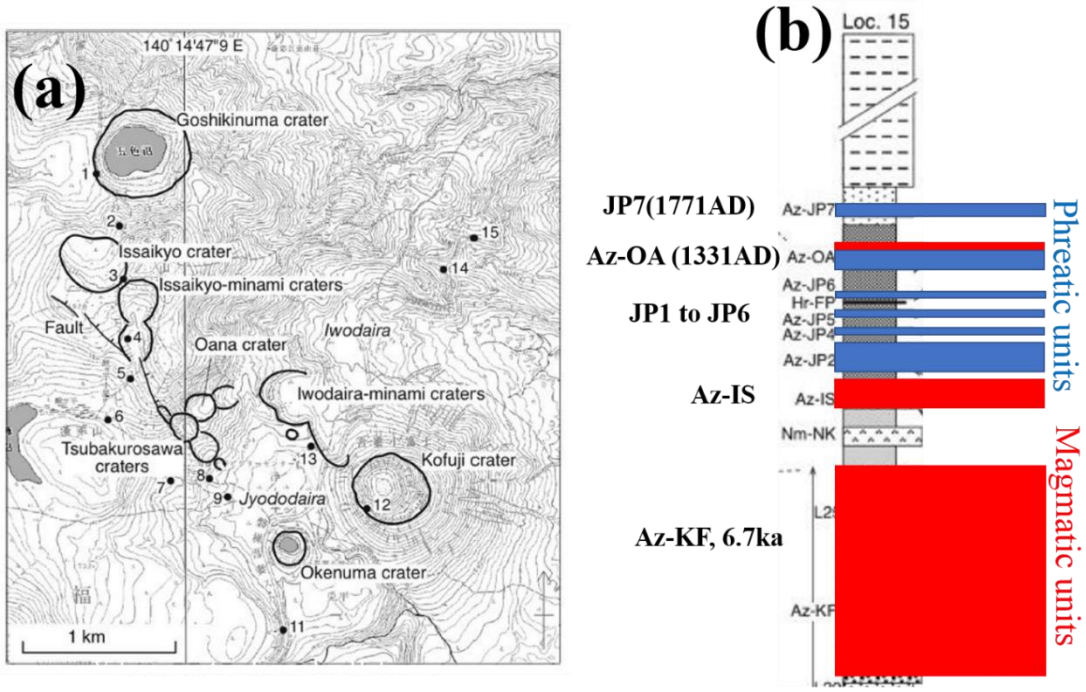

Fig. 26: Azuma-Jododaira product around Jododaira-Iwodaira defined by (Yamamoto, 2005).

(a): Volcanic craters based on geological survey on Azuma-Jododaira product (Yamamoto, 2005). Numbers and black circles show location of the tephera outcrops described in Yamamoto (2005). (b): Representative columnar section of Azuma-Jododaira product (Yamamoto, 2005).

Fig. 27: Ballistic-bread crust bombs of uppermost Az-OA, distributing along the mountain trail from Jododaira to Issaikyoyama. The location taken both photos were very near in number 9 in Fig. 26a.

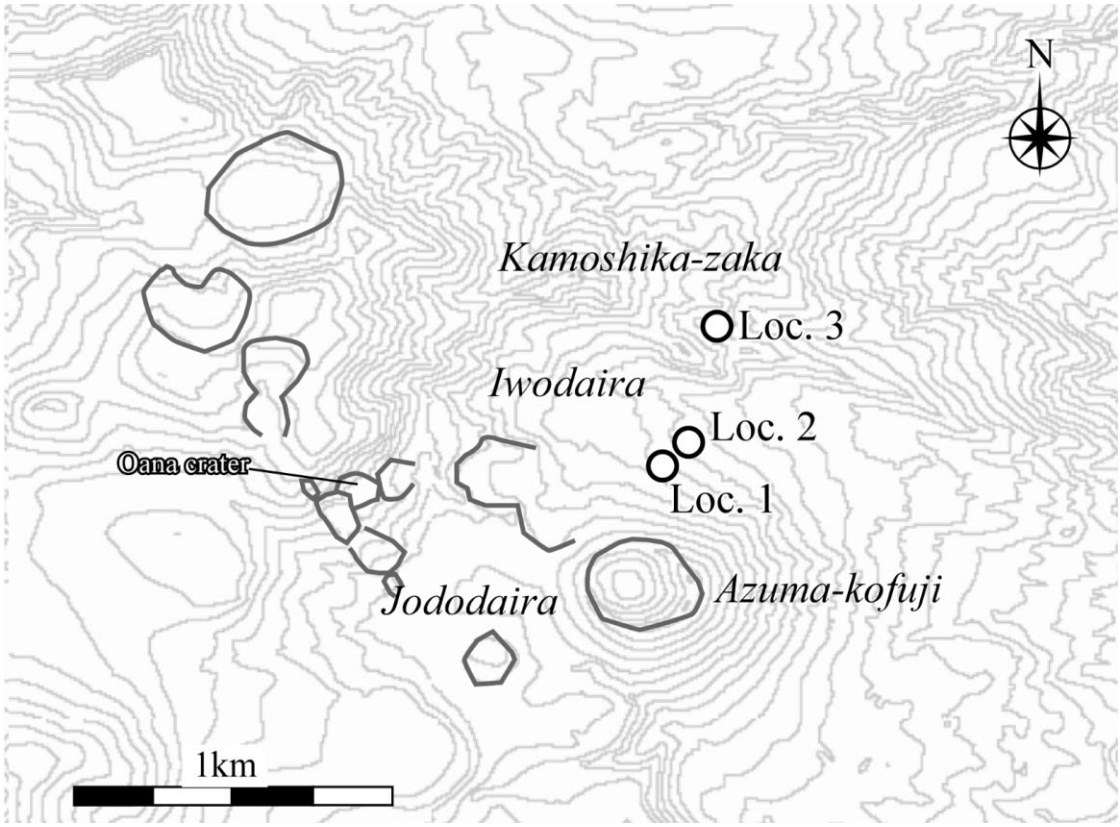

Fig. 28: Sampling location map around Jododaira to Iwodaira.

This map was created by using the 10m-mesh DEM from [URL3]. Loc. 1 to 3 with the circles are the tephra outcrops described in this study. Loc. 3 is same point with the numbers 14 and 15 reported in Yamamoto (2005). The areas surrounded by grey line show the craters defined by Yamamoto (2005).

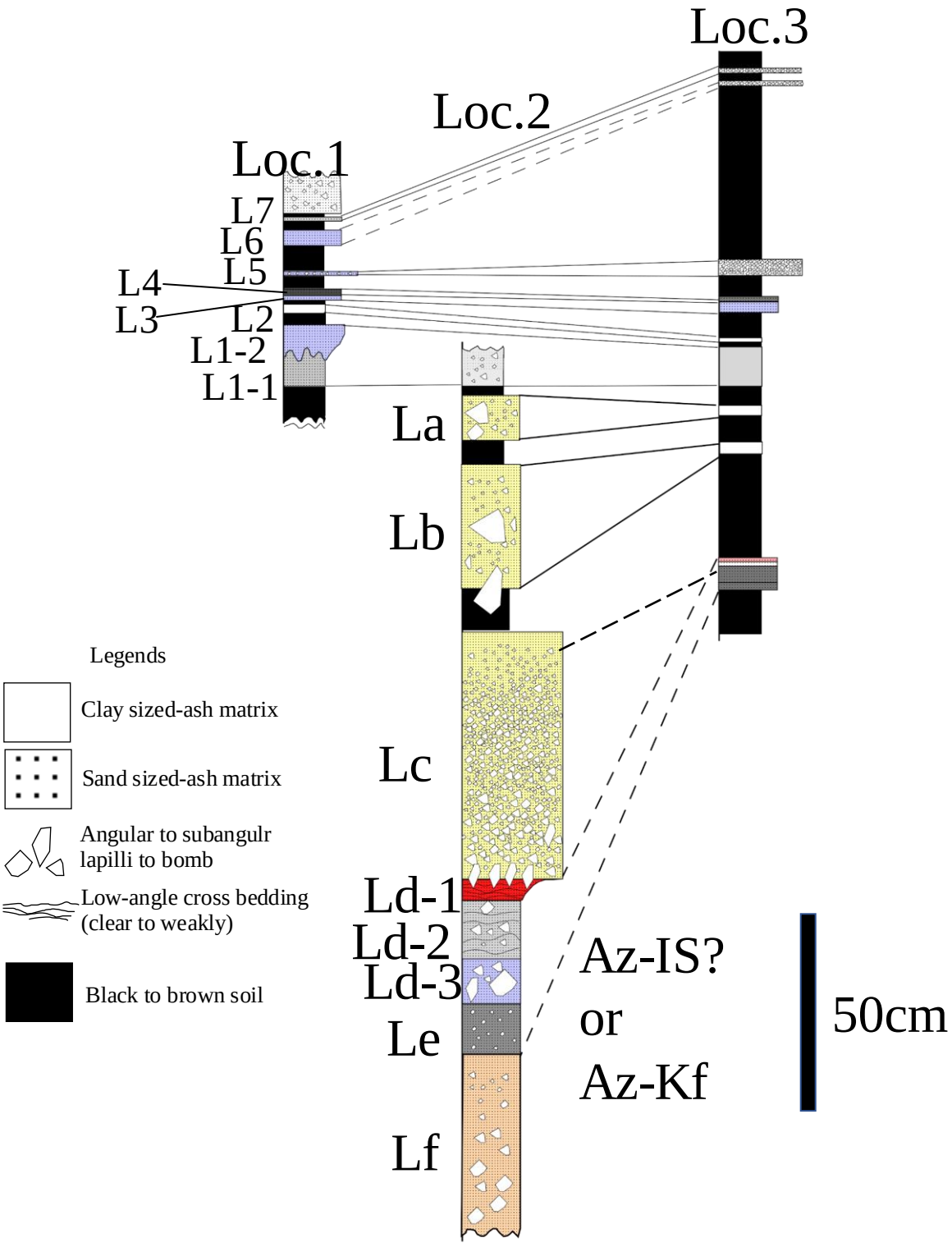

Fig. 29: Corelated columnar sections of Azuma-Jododaira product described at Loc. 1 to 3.

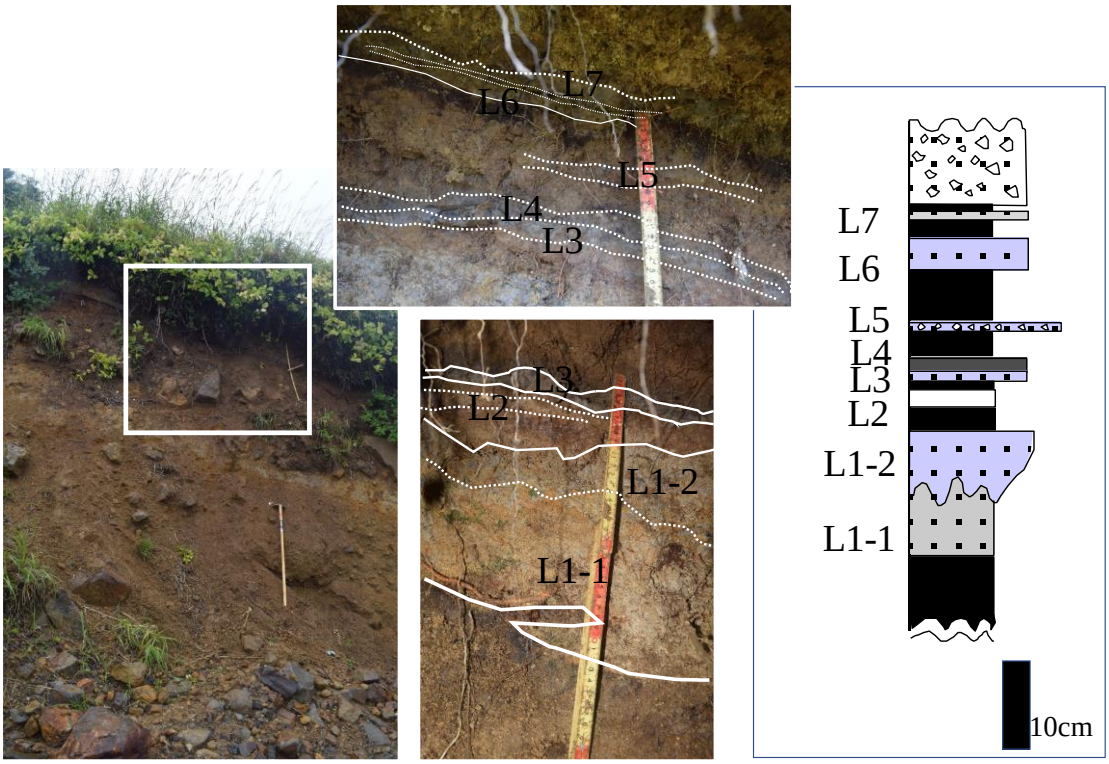

Fig. 30: Geological occurrence of L1-1 to L7 tephra layers at Loc. 1.

The rectangular area surrounded by white line is observational area in this outcrop, and the tephra layers occur as the centered both photos and the right columnar section.

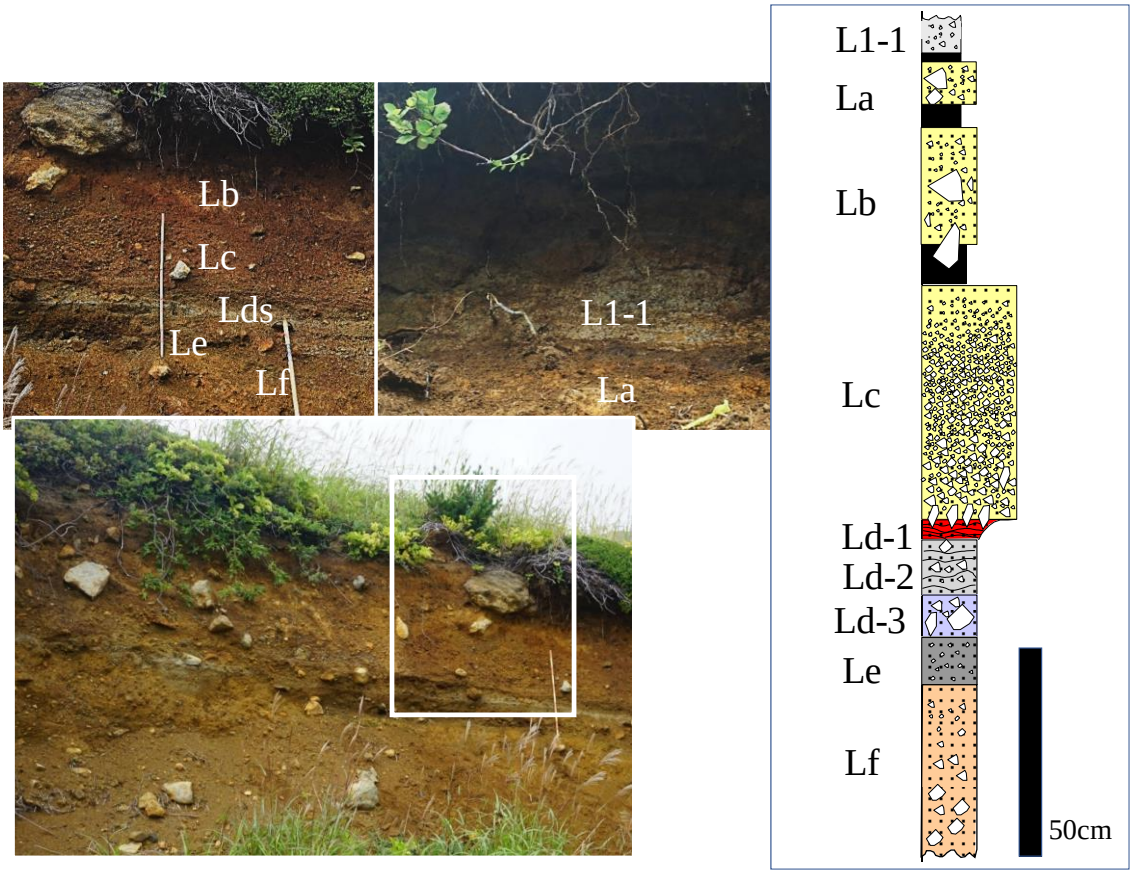

Fig. 31: Geological occurrence of tephra layers from L1-1 to Lf at Loc. 2.

The rectangular area surrounded by white line is observational area in this outcrop, and the tephra layers occur as the centered both photos and the right columnar section.

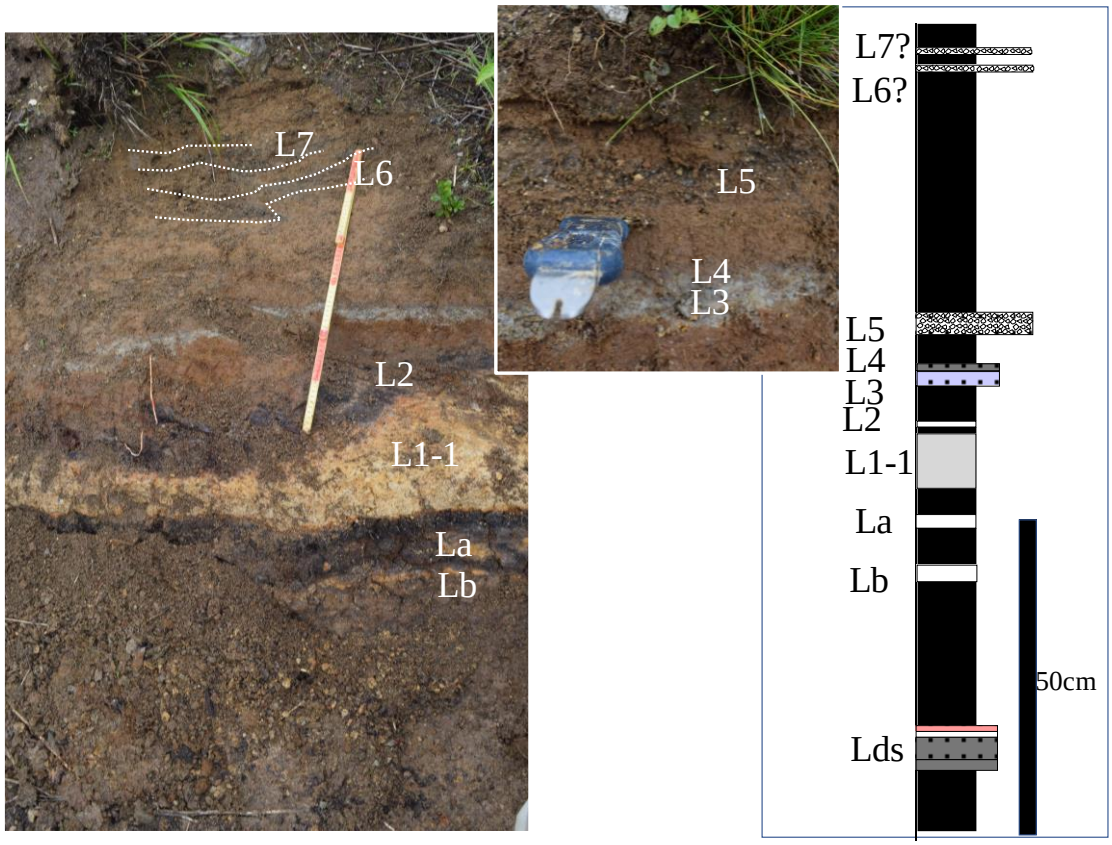

Fig. 32: Geological occurrence of tephra layers at Loc. 3 (same outcrop with 14 and 15 in Yamamoto (2005)).

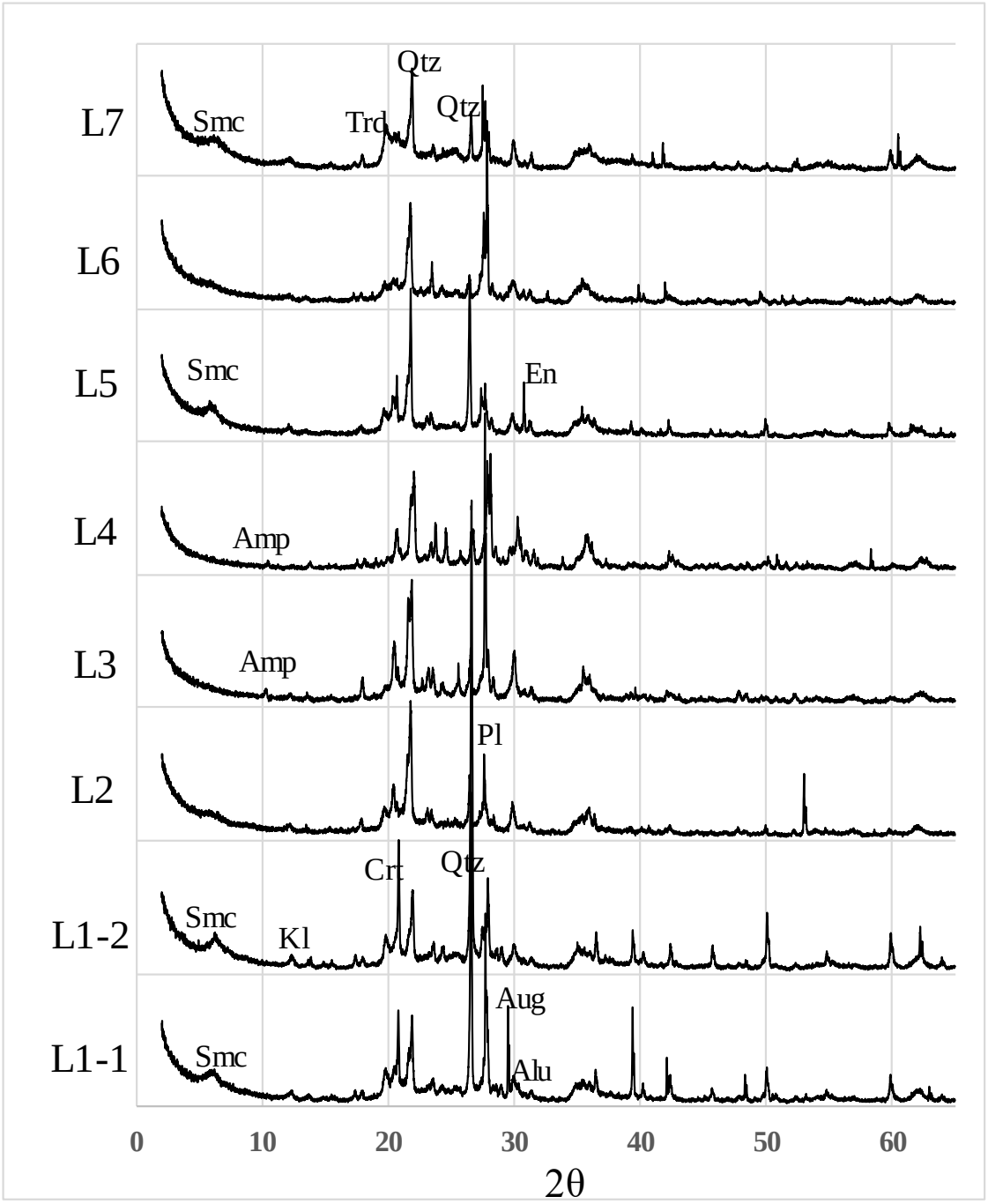

Fig. 33: XRD peak chart of samples from L1-1 to L7 (bulk).

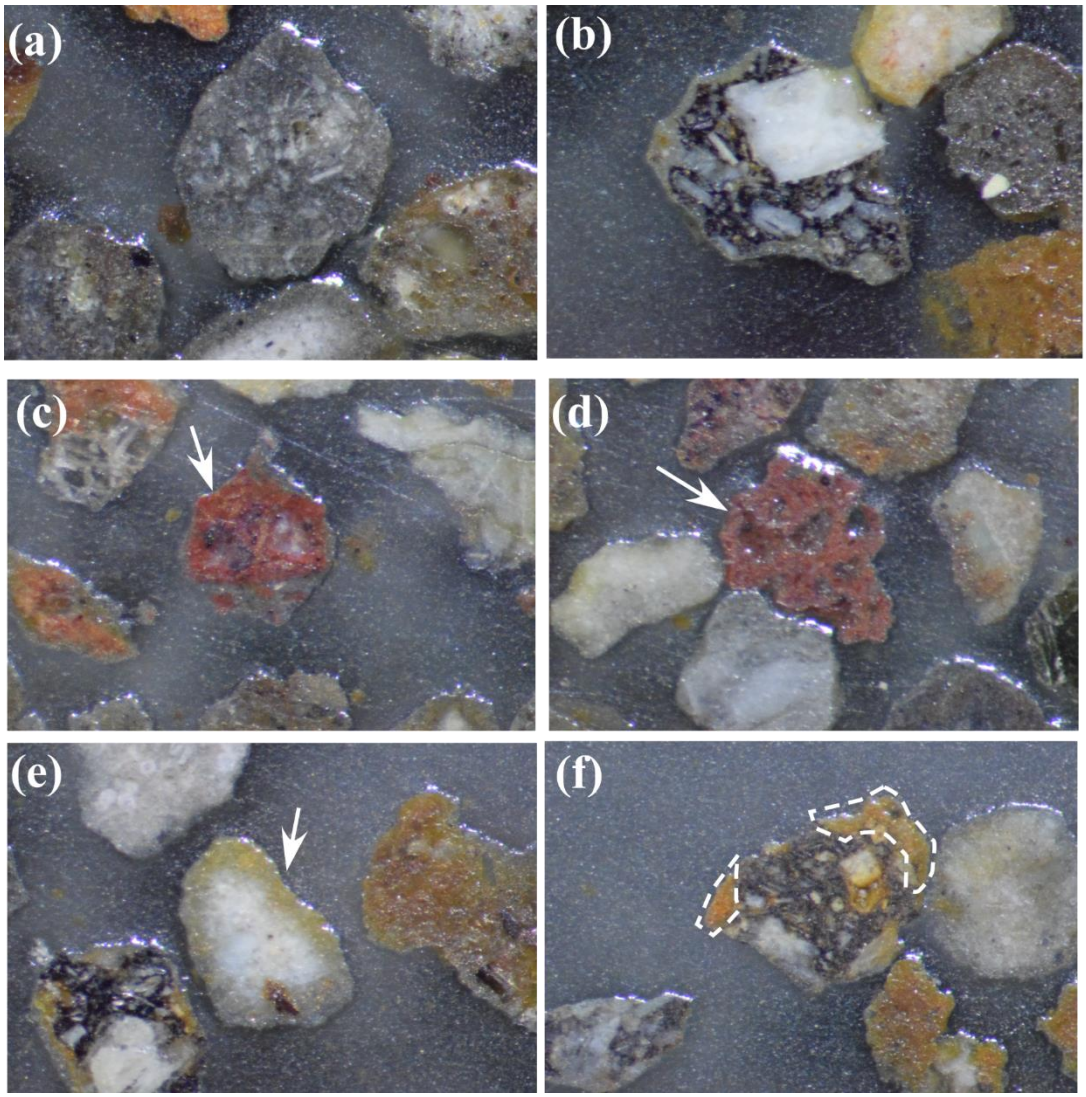

Fig. 34: Typical types of ash grains under a binocular-stereomicroscope.

(a): Grey dense volcanic rock fragment (DVR). (b): Highly crystalline grey dense volcanic rock fragment (DVR). (c): Red dense volcanic rock fragment (DVR). (d) Red, vesicular volcanic rock fragment with cuspate-irregular surface (VVR). (e): White to yellowish brown massive altered rock fragment (MAR). (f): Partly altered volcanic rock fragment (PAVR). This grain consists of grey volcanic rock part (similar to (a)) and yellowish-brown very fine-grained mineral mixture.

Fig. 35: Sample photo of mounted ash grains of L1-1.

Fig. 36: Sample photo of mounted ash grains of L1-2.

Fig. 37: Sample photo of mounted ash grains of L2.

Fig. 38: Sample photo of mounted ash grains of L3.

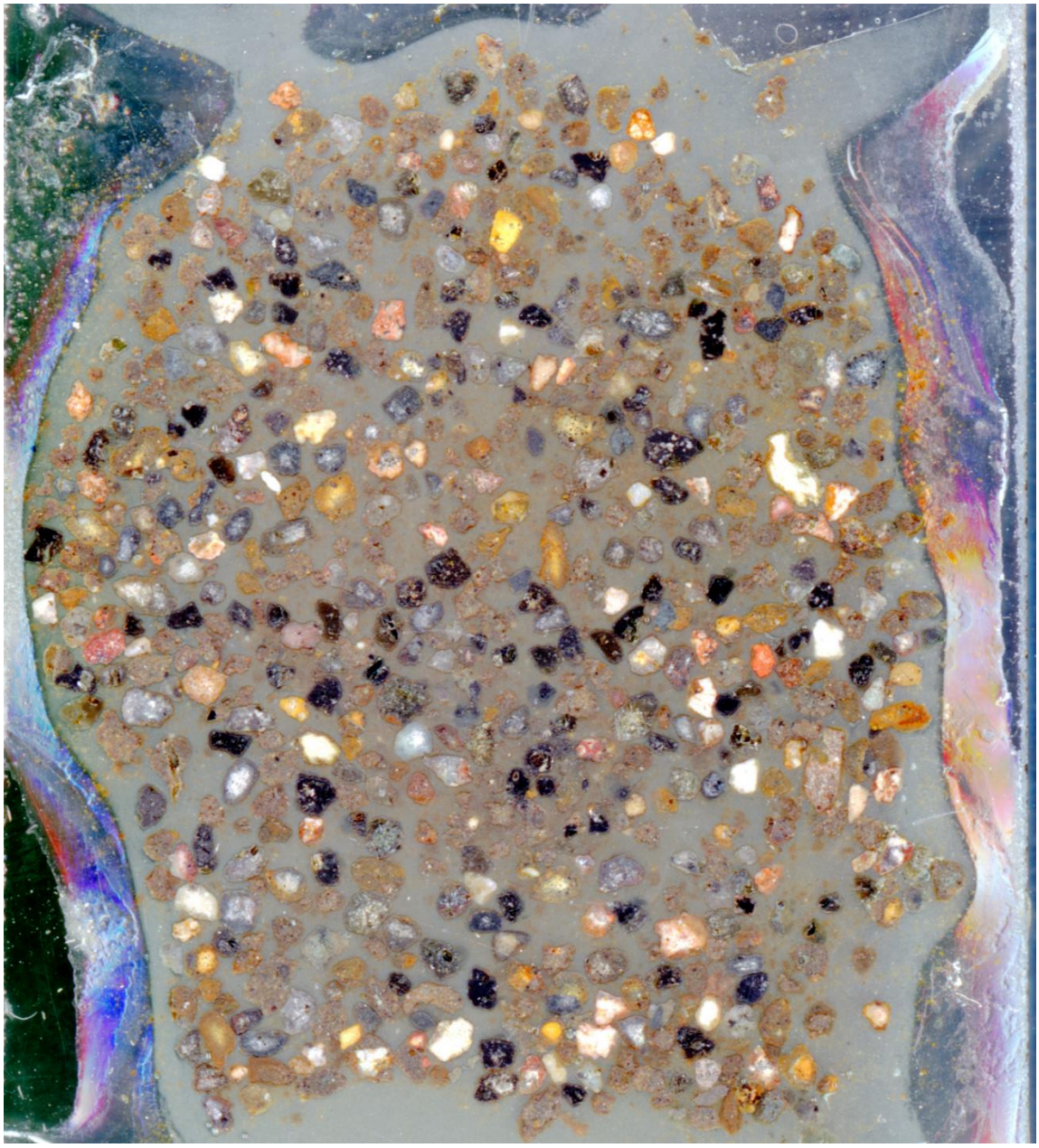

Fig. 39: Sample photo of mounted ash grains of L4.

Fig. 40: Sample photo of mounted ash grains of L5.

Fig. 41: Sample photo of mounted ash grains of L6.

Fig. 42: Sample photo of mounted ash grains of L7.

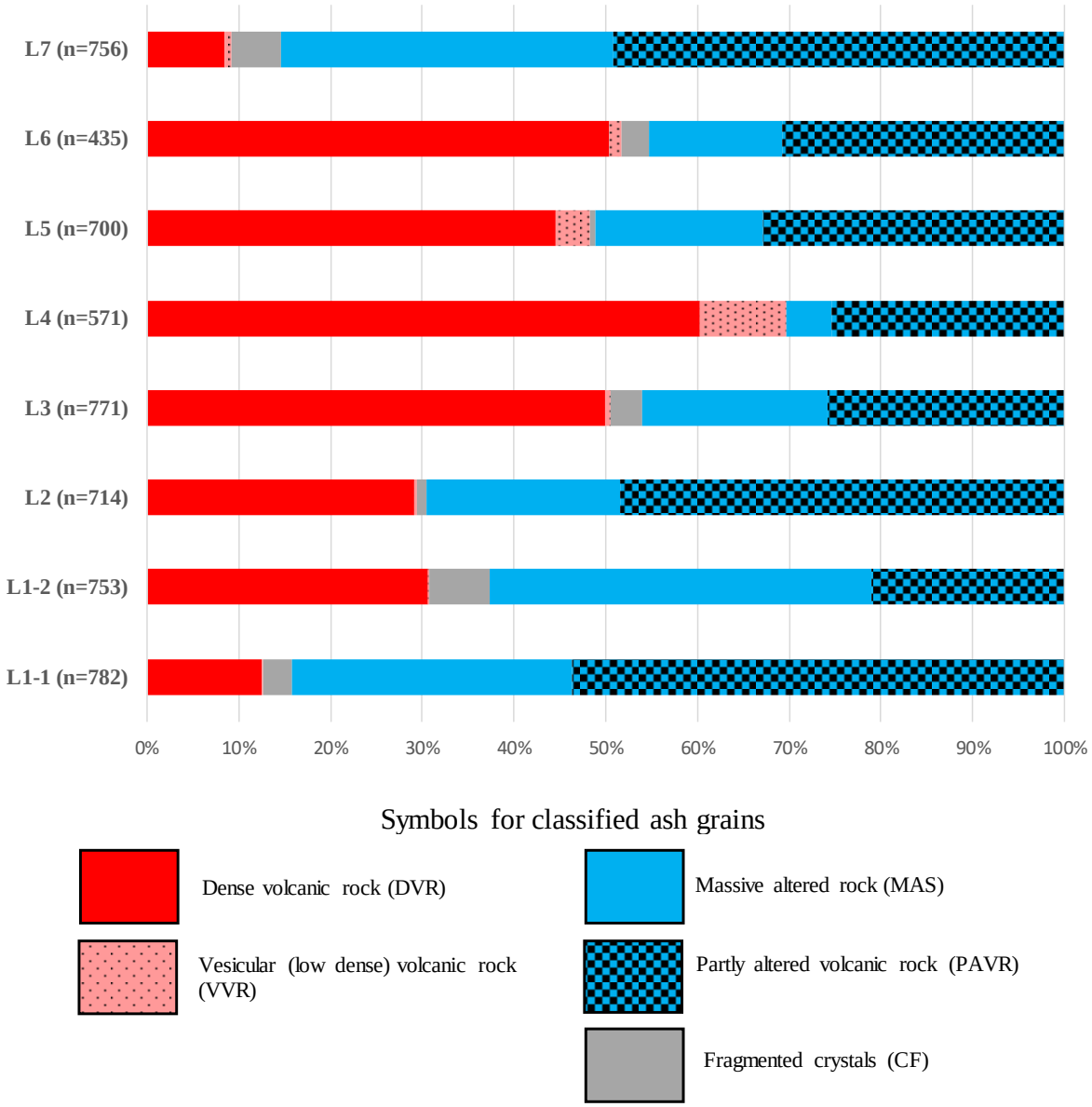

Fig. 43: Relative abundances of classified ash grains.

The proportion is estimated by counting numbers of the ash grain types under the views of a binocular-stereomicroscope.

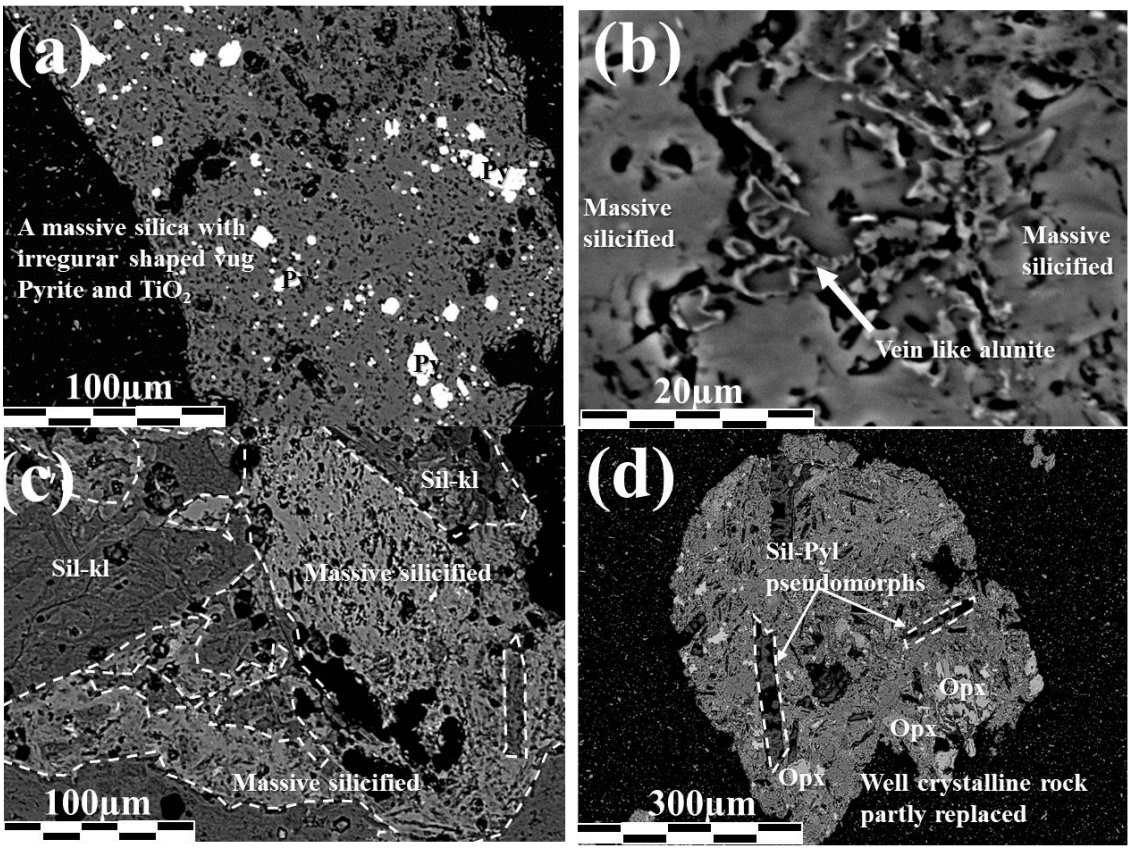

Fig. 44: BSE images of altered ash grains classified into silica, pyrophyllite, kaolin and alunite types in L1-1 (Az-OA).

(a): Silica type altered ash grains with dissolution texture (grain code: OA-003) (described in Imura et al. (2019a)). (b): Altered ash grains showing coexisting between silica and alunite type alterations (OA-009). (c): Complex altered ash grains having coexistence of silica and kaolin type alterations (OA-002). (d): Pyrophyllite type altered ash grains (partly altered) with pseudomorphic replacement texture (OA-017) (described in Imura et al. (2019a))

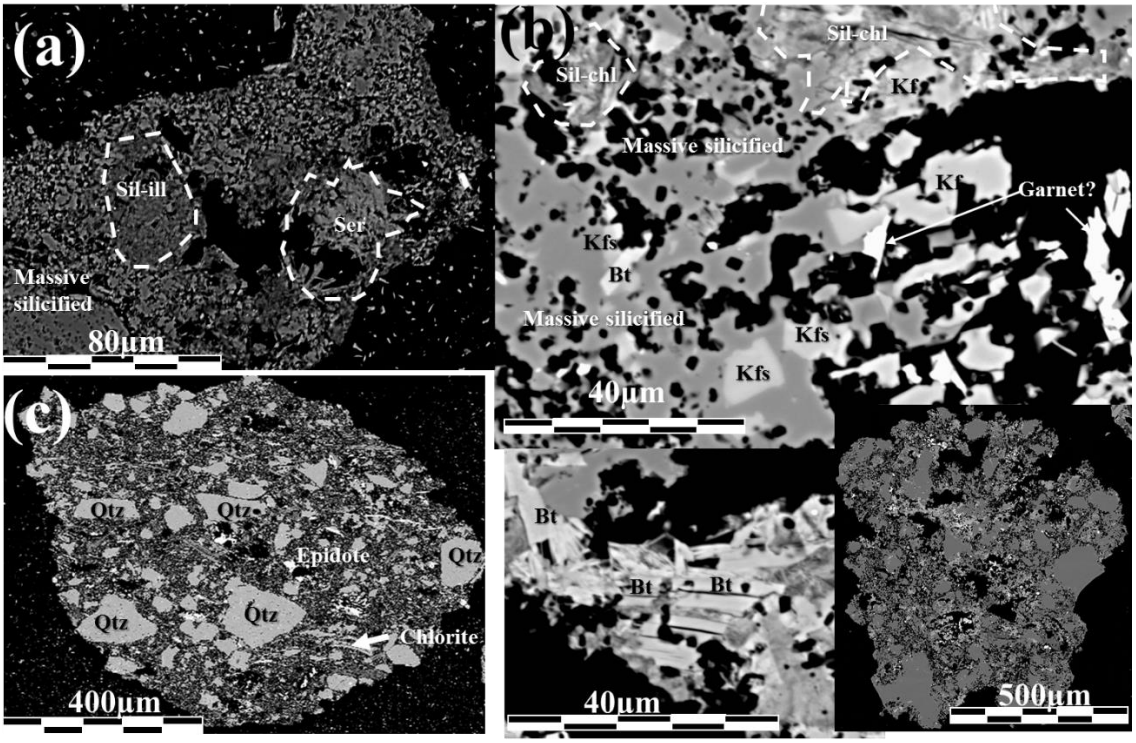

Fig. 45: BSE images of altered ash grains classified into mica-chlorite and mica-K-feldspar types in L1-1 (Az-OA).

(a): Altered ash grain having coexistence of silica and mica-chlorite types (OA-015). (b): Altered ash grain with mica-K-feldspar type (OA-042). (c): Altered ash grin classified into chlorite type (closed to mica-chlorite type?) with euhdral to synhedral coarse grained silica.

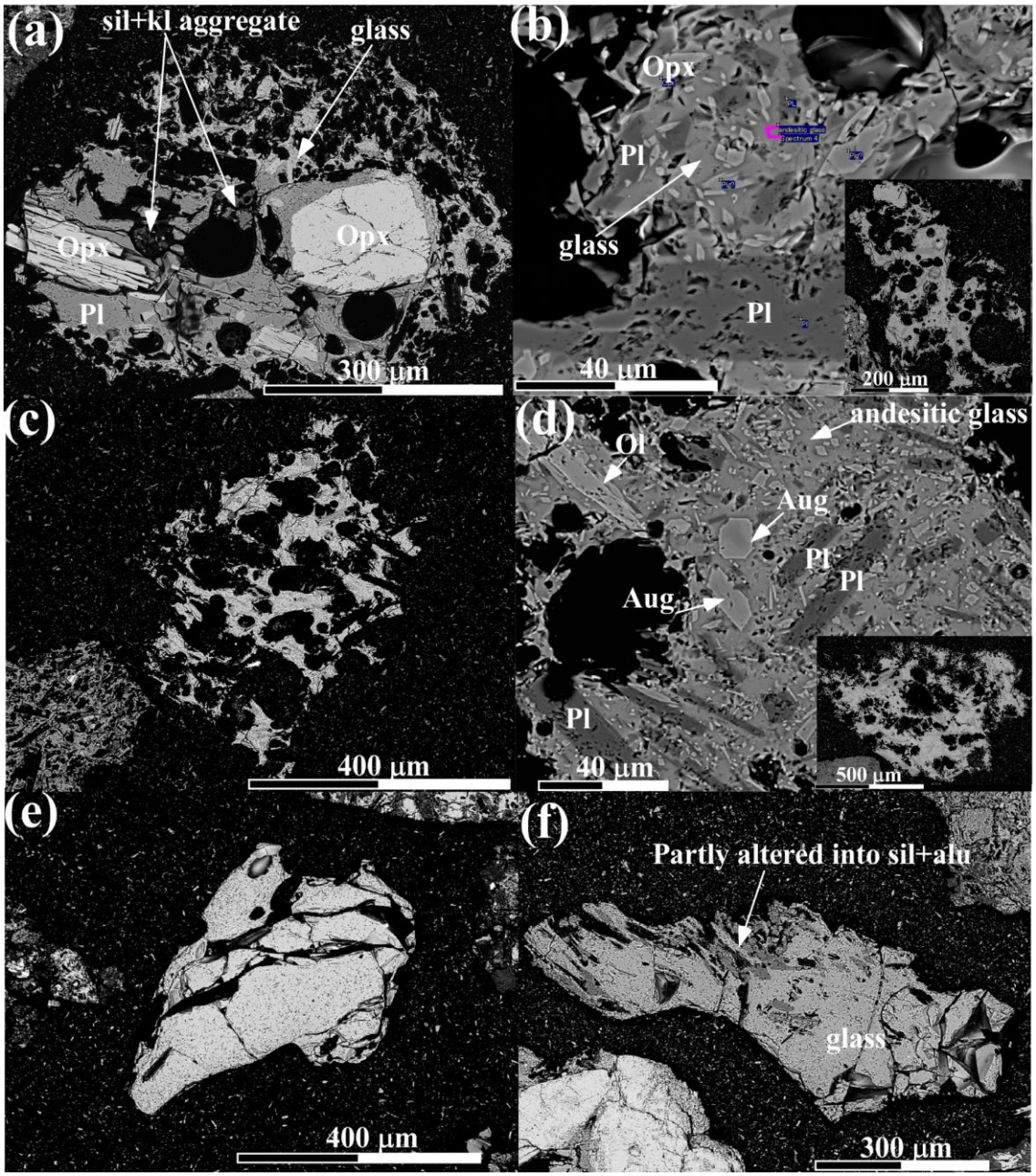

Fig. 46: BSE images of typical unaltered ash grains in L2.

(a): Brown grey andesitic scoria fragment partly kaolin type altered (L2_1). Sil+kl fine crystal aggregate fills in vesicles. (b) and (c): Brown grey andesitic scoriaceous ash grain with hyaloophitic to glassy porphyritic texture (respectively, L2_40 and L2_41). (d): Olivine microphenocryst bearing brown grey andesitic scoriaceous ash grain with hyaloophitic porphyritic texture (L2_7, detailed photo in Fig. 47). (e): Transparent rhyolitic glass shard with vesicles (L2_4). (f): Transparent rhyolitic glass fragment partly altered into alunite type.

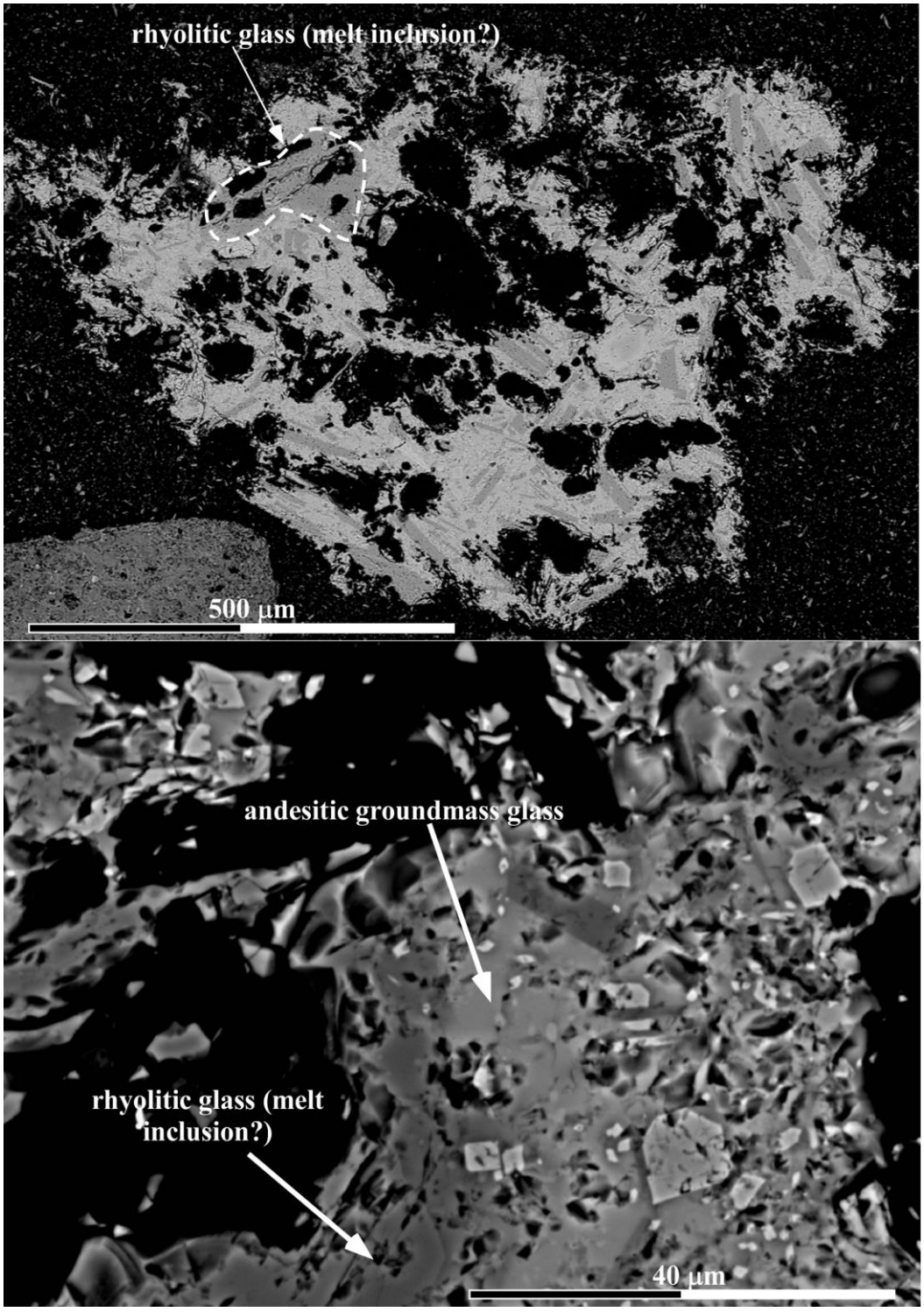

Fig. 47: BSE images of L2_7 grain containing rhyolitic melt inclusion.

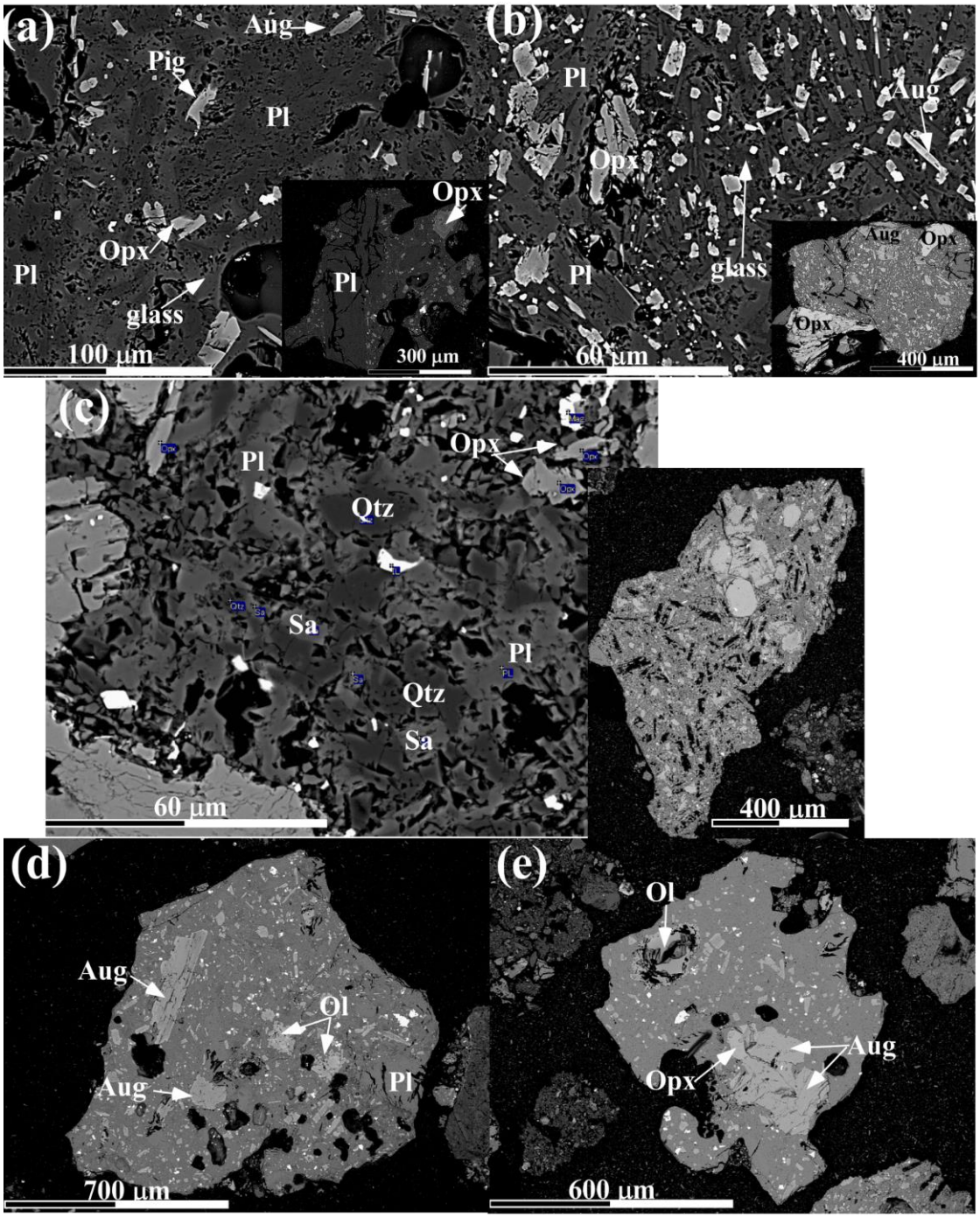

Fig. 48: BSE images of typical unaltered ash grains in L3 and L4.

(a): Black vesicular andesitic lava fragment with hyaloophitic texture (L4_6). (b) Brown grey andesitic lava fragment with dyctytaxitic to intersertal texture (L4_10). (c): Light grey holocrystalline andesitic to dacitic rock (L4_4). (d) and (e): Black olivine bearing-andesitic lava with hyaloophitic texture (respectively, L4_8 and L3_32)

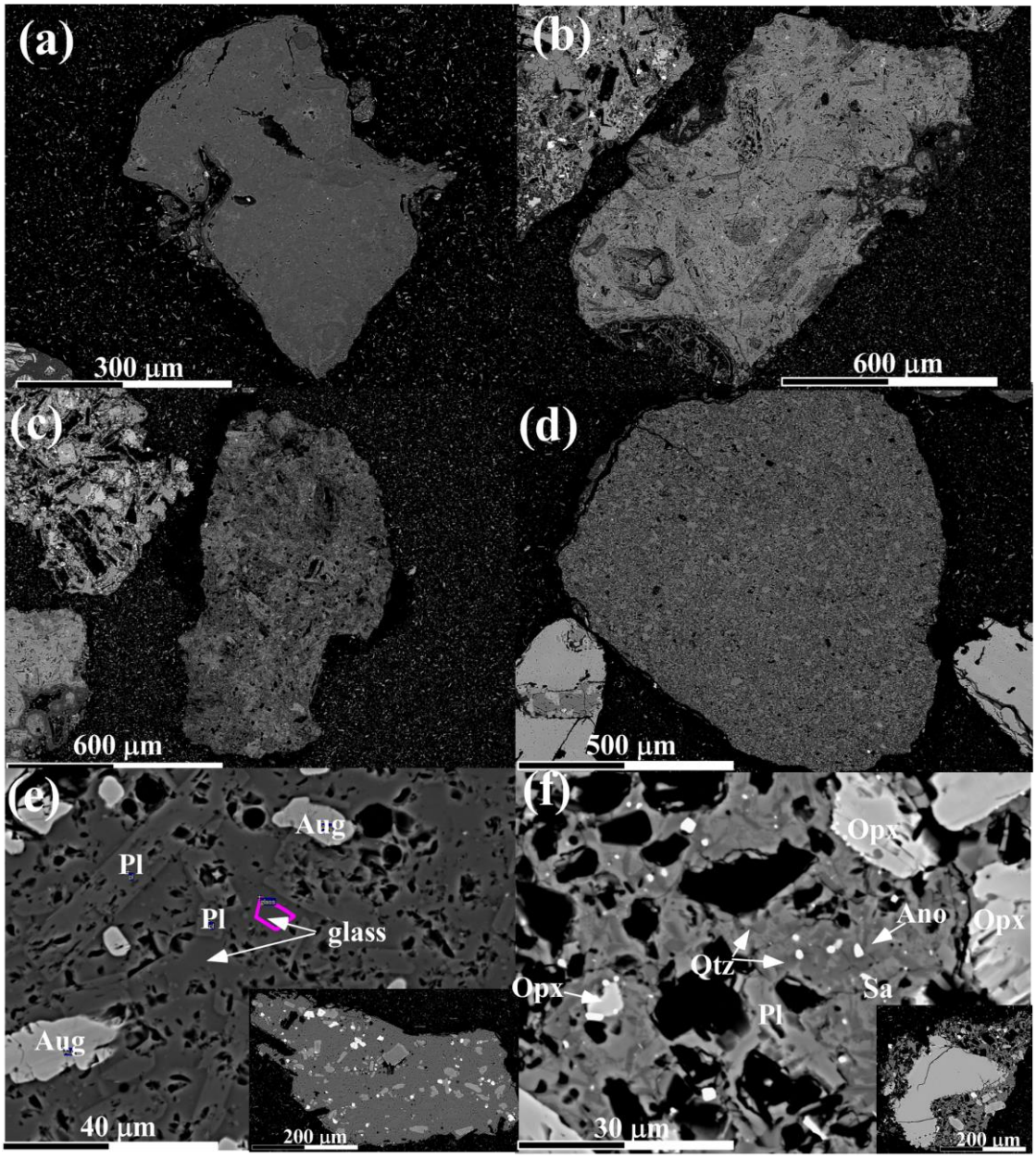

Fig. 49: BSE images of typical ash grains in L5.

(a): White ash grains of massive aggregate of silica+kaolin+alunite mixtures (L5_38). (b): Light grey ash grains completely altered into silica to alunite types with remained pseudomophs from volcanic rock (L5_16). (c): Light grey altered ash grain completely replaced by fine grained silica (silica type) (L5_17). (d): Light grey altered ash grain of massive aggregates of silica+illite (mica-chlorite type) (L5_15). (e): Brown grey andesitic lava fragment with hyaloophitic to hyalopillitic texture (L5_31). (f): Black holocrystalline andesitic rock with intersertal texture (L5_6).

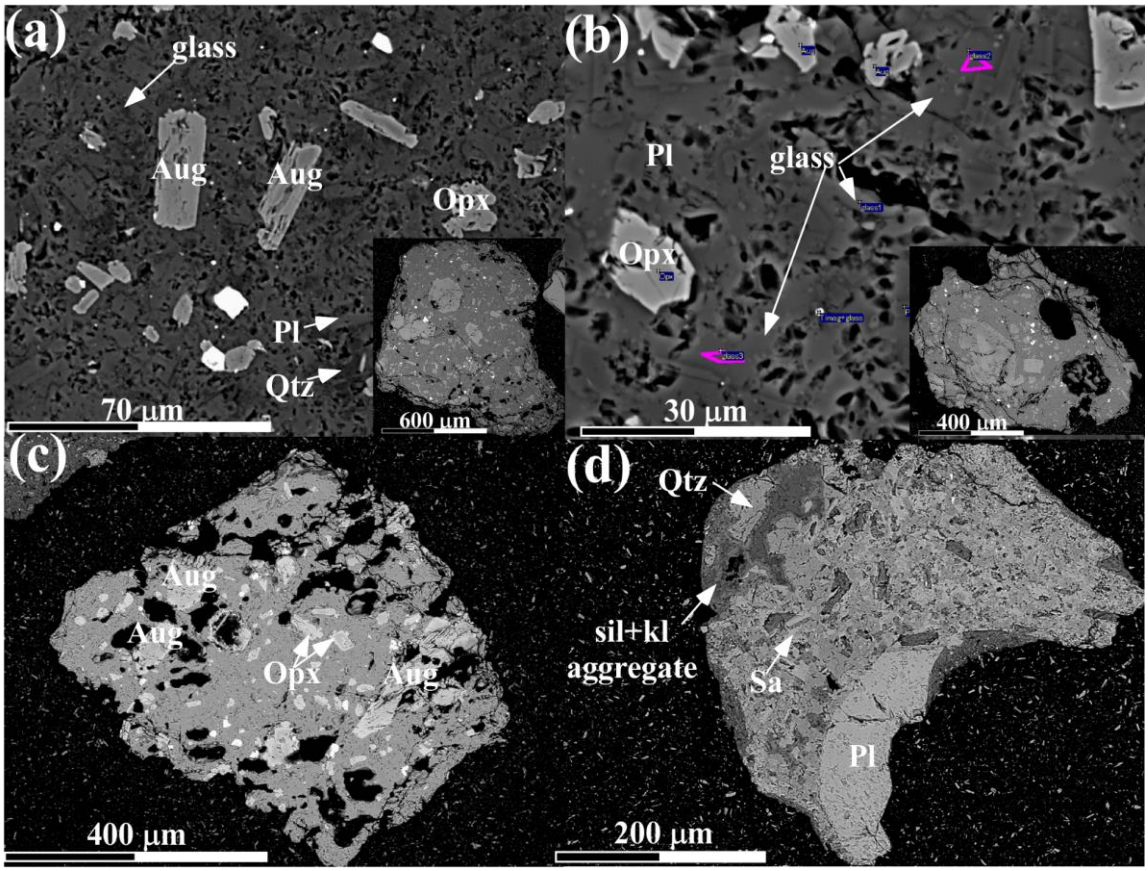

Fig. 50: BSE images of typical ash grains in L6.

(a): Black andesitic lava fragment with dyctytaxitic to intersertal texture (L6_4). (b) and (c): Translucent brown grey andesitic scoriaceous ash grains with hyaloophitic texture (respecetively, L6_12 and L6_13). (d): Brown grey holocrystalline andesitic rock partly altered into kaolin type (L6_20).)

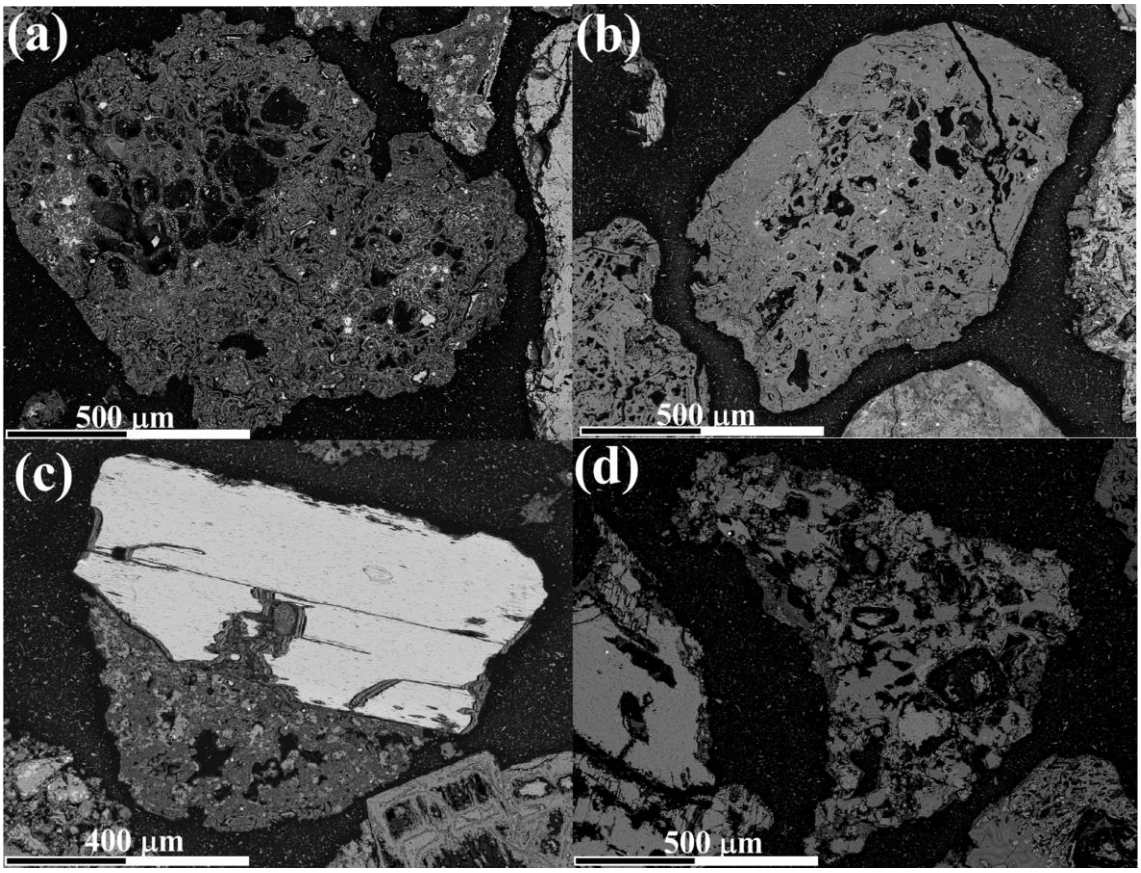

Fig. 51: BSE images of typical ash grains in L7.

(a): Yellowish brown altered volcanic rock almost replaced by silica+kaolin+alunite mixtures (kaolin type) (L7_9). (b): Yellowish white altered volcanic rock almost replaced by silica+kaolin+alunite mixtures (kaolin type) (L7_6). (c): Brown volcanic rock almost replaced by silica+illite mixtures with remained orthopyroxene phenocryst (mica-chlorite type) (L7_21). (d): Yellowish white altered volcanic rock almost replaced by silica+alunite+vermiculite mixtures (weathered?) (L7_3).

	XRD paterns	Componentry paterns	
		Alteration type	Unaltered ash
L7	14 Å sme+Qz+Trd	Acidic to Neutral	few (almost all PAVR)
L6	Pl	Acidic	50% DVR with small VVR
L5	14 Å sme+Qz	Acidic to Neutral	40% DVR
L4	8 Å Amp+Pl	Acidic	70% DVR with weathered VVR
L3	8 Å Amp+Pl+Alu	Acidic	50% DVR with weathered VVR
L2	Qz+Crs+Pl+Px	Acidic (silicification)	30% DVR+ much of weathered scoria VVR
L1-2	14 Å sme+Qz+Px	Acidic to Neutral	30~40% DVR
L1-1	14 Å sme+Qz	Acidic to Neutral (potassic?)	few (almost all PAVR)

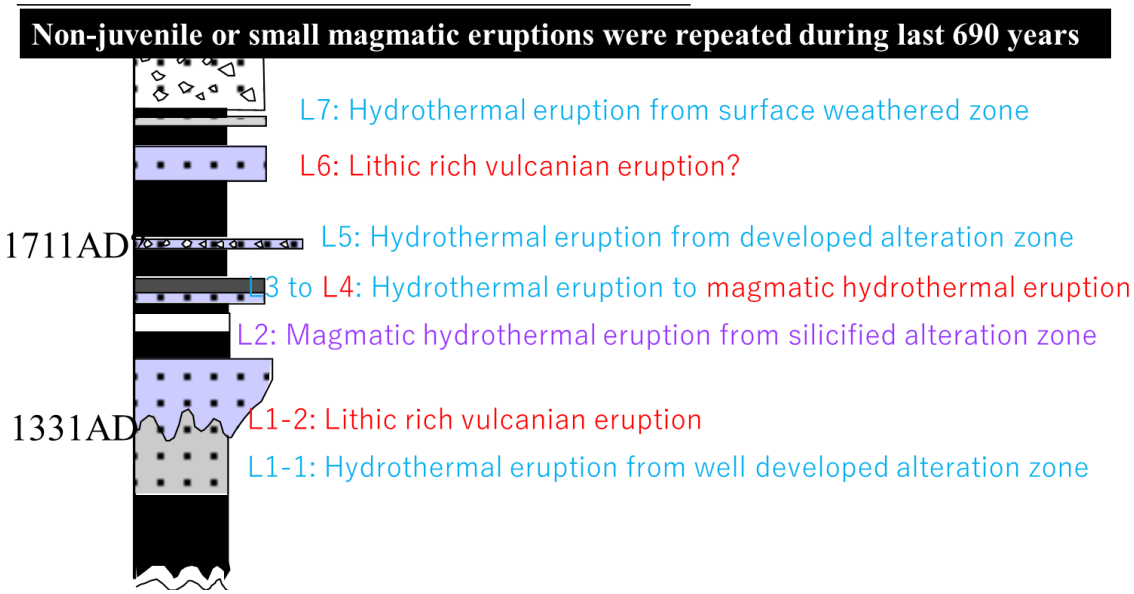

Fig. 52: Summary of analytical results.

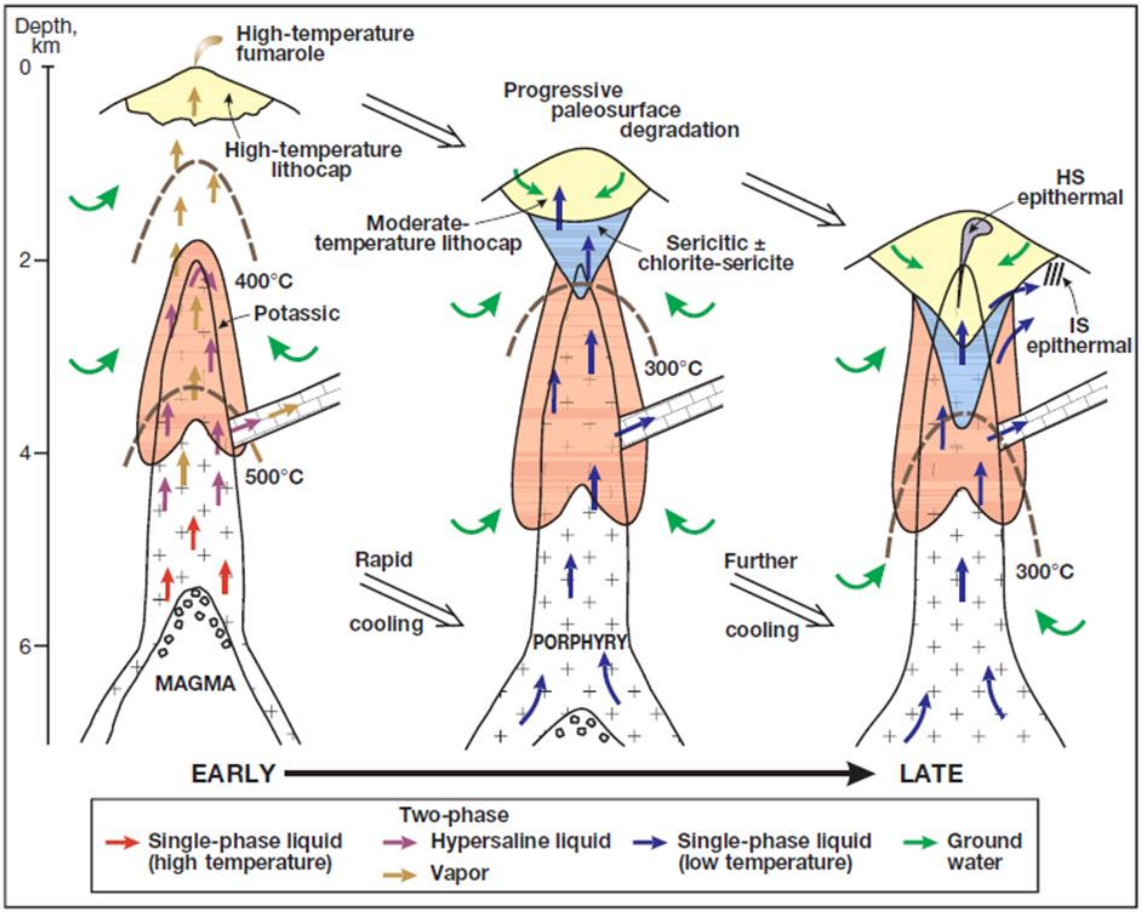

Fig. 53: Evolution of hydrothermal system to a mature epithermal-porphyry system estabiiehed by Silitoe, 2010.

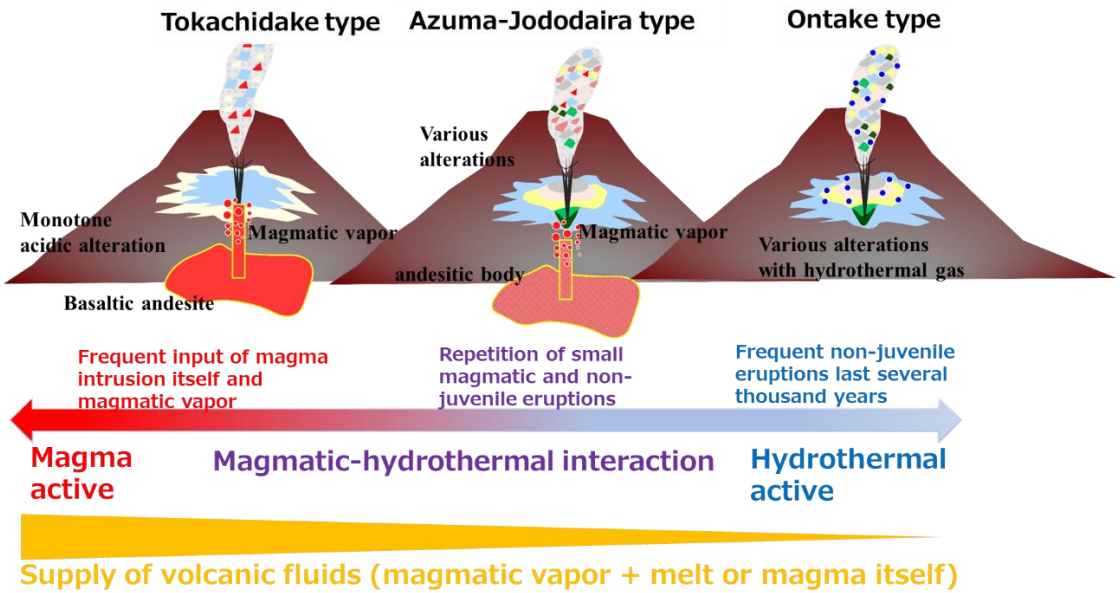

Fig. 54: Evolutional steps of subvolcanic hydrothermal system corelated with the very-early stage of epithermal-porphyry system.

From left to right with the arrow, subvolcanic hydrothermal system seems to evolve with decrease of magmatic activities.

Difference of the types depends on their activity trends?

- Tokachidake→frequent magmatic eruption/intrusion in 20th century (1926, 1962, 1988-89)
- Ontake→frequent non-juvenile (hydrothermal) eruptions during last 1000 years (1979, 1991, 2007, 2014)
- Azuma→small-magmatic (magmatic hydrothermal) eruptions during last several 100 years

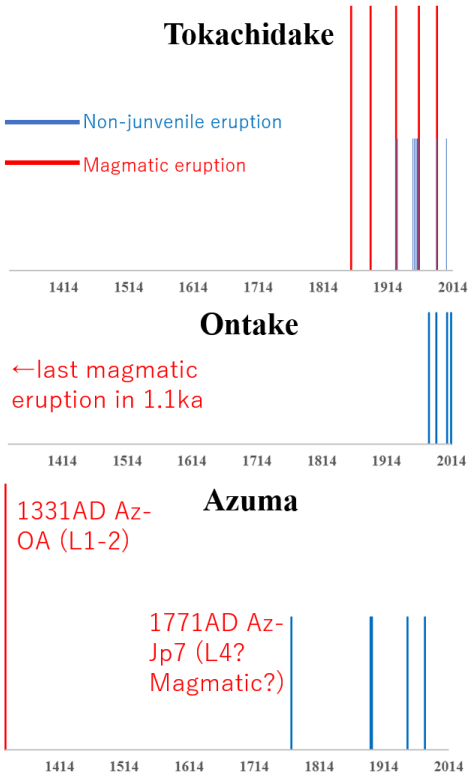

Fig. 55: Eruption timing in historical ages with red line of magmatic eruption and blue line of non-juvenile eruption (referred from JMA, 2013; [URL1]; [URL2]).

Acknowledgement

This study is a complete work of graduation thesis on the leading program “New Frontier Leaders for Rare-Metals and Resources”, Graduate School of International Resource Sciences, Akita University. The author really would like to appreciate Prof. Tsukasa Ohba for his constant supervision and high-level education technically and academically in geoscience throughout the course of this study. The author thanks to Dr. Yusuke Minami (GSJ-AIST), Prof. Antonio Arribas (University of Texas), Prof. Akira Imai (Kyushu University), Dr. Akiko Matsumoto and Prof. Mitsuhiro Nakagawa (Hokkaido University) for collaborative works during this study. The author gratefully acknowledges the discussions and significant technical support rendered by Prof. Shintaro Hayashi, Dr. Takashi Hoshide, Dr. Ryohei Takahashi, Dr. Takuya Echigo, Dr. Takeyuki Ogata, and Ms. Yumi Hayakawa. The author also thank the Higashikawa Ranger Office of the Ministry of Environment, the Urabandai Ranger Office of the Ministry of Environment, and the Fukushima Forrest Office in the Kanto Reginal Forest Office of the Ministry of Agriculture, of Forestry and Fisheries for granting permission to conduct sampling of Tokachidake volcanic rocks and Azuma-Jododaira volcanic rocks. Finally, the author would like to express his sincere for kind support from his family, friends and laboratory mates.

This research was supported by Ministry of Education, Culture, Sports, Science and Technology-Japan (MEXT) “Understanding evolutional change and detecting unnormal phenomena for subvolcanic hydrothermal system”(1003 project in 2014) (http://www.mext.go.jp/b_menu/shingi/gijyutu/gijyutu6/sonota/attach/1348197.htm), Ministry of Education, Culture, Sports, Science and Technology-Japan (MEXT) “Integrated Program for Next Generation Volcano Research and Human Resource Development”, Japan Society for the Promotion of Science (JSPS) leading program “New Frontier Leader Program for Rare-metals and Resources”, “Japan Society for the Promotion of Science Grant-in-Aid for Scientific Research(C) 17K0319”, and “Japan Society for the Promotion of Science Grant-in-Aid for Scientific Research(C) 15K01245”.

Reference

Ando, Y. and Tsutsumi, S., 2005, Acid alteration and geochemistry of alunite in the western Izu Peninsula, Shizuoka Prefecture. *Jpn. Mag. Miner. Petrol. Sci.* 34, 59—68. (in Japanese with English abstract)

Aoki, M., Comsti, E.C. and Lazo, F. B., 1993, Advanced argillic alteration and geochemistry of alunite in an evolving hydrothermal system at Baguio, Northern Luzon, Philippines. *Resour. Geol.*, 43, 155—164.

Arribas Jr., A., 1995, Characteristics of high sulfidation deposits, and their relation to magmatic fluid. In Magmas, Fluids and Ore Deposits Thompson, J. F. H., ed., *Mineralogical Society of Canada*, 23, 419—454.

Arribas Jr., A., Cunningham, C.G., Rytuba, J. J., Rye, R. O., Kelly, W. C., Podwysocki, M. H., McKee, E. H. and Tosdal, R. M., 1995, Geology, geochemistry, fluid inclusions and isotope geochemistry of the Rodalquilar gold alunite deposit, Spain. *Econ. Geol.*, 90, 795—822.

Ban, M., Matsui, R., Iwata, N., Yamamoto, T., Fujinawa, A. and Nakashima, K., 2013, Petrologic characteristics of the newest stage in Azuma volcano group, Northeast Japan. Intern. *Jour. Erupt. Hist. Info.*, Accepted Manuscript. http://ehai-www.rd.fukuoka-u.ac.jp/ijehai/files/IJEHAI_1301_Ban_et_al.pdf

Ban, M., Takebe, Y., Adachi, T., Matsui, R. and Nishi, Y., 2016, Eruption histories of Zao and Azuma volcanoes and their magma feeding systems for recent activities. *Bull. Earthq. Res. Inst. Univ. Tokyo*, 91, 25–39.

Bayliss, P. and Kolitsch, U. and Pring, A., 2010, Alunite supergroup: recommended nomenclature. *Mineral Mag*. 74, 919–927.

Barberi, F., Bertagnini, A., Landi, P. and Principe, C., 1992, A review on phreatic eruptions and their precursors. *Jour. Volcanol. Geotherm. Res*., 52, 231–246.

Beaufort, D., Patrier, P., Laverret, E., Bruneton, P. and Mondy, J., 2005, Clay Alteration Associated with Proterozoic Unconformity-Type Uranium Deposits in the East Alligator Rivers Uranium Field, Northern Territory, Australia. *Econ. Geol.* 100, 515—536. DOI: https://doi.org/10.2113/gsecongeo.100.3.515

Browne, P.R.L. 1978, Hydrothermal alteration in active geothermal fields. *Annu. Rev. Earth. Pl. Sc.* 6, 229—250.

Browne, P. R. L. and Lawless, J. V., 2001, Characteristics of hydrothermal eruptions, with examples from New Zealand and elsewhere. *Earth-Sci. Rev.*, 52, 299–331

Dill, H.G. 2001, The geology of aluminum phosphate and sulphates of the alunite group minerals: A review. *Earth-Sci. Rev.* 53, 35—93.

Dill, H.G., Fricke, A. and Hening, K.-H., 1995, The origin of Ba- and REE-bearing aluminium-phosphate-sulphate minerals from the Lohrheim kaolinitic clay deposit (Rheinisches Schiefergebirge, Germany). *Appl. Clay. Sci.*, 10, 231—245.

Dill, H.G., Bosse, H.-R., Henning, K.-H., Fricke, A. and Ahrend, H., 1997, Mineralogical and chemical variations in hypogene and supergene kaolin deposits in a mobile fold belt—the Central Andes of northwestern Peru. *Miner. Deposita*, 32, 149—163.

Dill, H. G., Bosse, H.-R. and Kassbohm, J., 2000, Mineralogical and chemical studies of volcanic-related argillaceous industrial minerals of the Central American Cordillera (western El Salvador). *Econ. Geol.* 95, 517—538.

Dong, G., Morrison, G. and Jaireth, S., 1995, Quartz texture in epithermal veins, Queensland－classification, origin and implication. *Econ. Geol.*, 90, 1841–1856.

Fujinawa, A. and Kamoshida, T., 1990, Azuma volcano. In Volcanoes in the Tohoku Region: Field Guide of Japanese Volcano 4., Takahashi, M. and Kobayashi, T. ed., Tsukijishokan, Tokyo, 89–104 (in Japanese).

Fournier, R. O., 1985, The behavior of silica in hydrothermal solution. *Rev. Econ. Geol*., 2, 45¬–62.

Fujinawa, A, Ban, M., Ohba, T., Kontani, K. and Miura, K., 2008, Characterization of low-temperature pyroclastic surges that occurred in the northeastern Japan arc during the late 19th century. *Jour. Volcanol. Geotherm. Res*., 178, 113–130.

Fujiwara, S., Nakagawa, M., Hasegawa, S. and Komatsu, D., 2007, Eruptive history of Tokachi-dake volcano during the last 3,300 years, central Hokaido, Japan. *Bull. Volcanol. Soc. Japan*, 55, 53¬64. (In Japanese with English abstract)

Fujiwara, S., Ishizuka, Y., Yamazaki, T. and Nakagawa, M., 2009, Newly found 4.7ka pyroclastic flow deposit on the Northwestern foot of Tokachi-dake volcano, central Hokkaido, Japan and reexamination of the eruptive activity during holocene. *Bull. Volcanol. Soc. Japan*, 6, 253¬262. (In Japanese with English abstract)

Furukawa, R., Nakano, S., Takahashi, Y. and Yamamoto, T., 2018, Geology of the Azuma Yama district. With Geological sheet map at 1:50,000; Geological Survey of Japan: Tsukuba, Japan. (in Japanese with English Abstract)

Gaboreau, S., Beaufort, D., Vieillard, P. and Partrier, P., 2005, Aluminum phosphate-sulfate minerals associated with Proterozoic unconformity-type uranium deposits in the East Alligator River Uranium Field, Northern Territories, Australia. *Can. Mineral.*, 43, 813—827.

Gaboreau, S., Cuney, M., Quirt, D., Beaufort, D., Patrier, P. and Mathieu, D., 2007, Significance of aluminum phosphate-sulfate minerals associated with U unconformity-type deposits: The Athabasca basin, Canada. *Am. Mineral.*, 92, 267—280.

Giggenbach, W. F., 1997, The origin and evolution of fluids in magmatic—hydrothermal systems. In Geochemistry of hydrothermal ore deposit 3rd ed., Barnes, H. L., ed., Wiley, 737–196.

Gustafson, L.B., Vidal, C.E., Pinto, R. and Noble, D.C., 2004, Porphyry-epithermal transition, Cajamarca region, Northern Peru. *Soc. Eco. Geo. Spc. Pub*. 11, 279—299.

Hayashi, M., 1973, Hydrothermal alteration in the Otake geothermal area, Kyushu. *Jour. Japan Geotherm. Energy Assoc*., 10, 9¬46. (In Japanese with English abstract)

Hara, J. and Tsuchiya, N., 2006, Evaluation on solid-liquid interface structure of altered rock based on hydrothermal flow experiments. *J. Geotherm. Res. Soc. Japan*, 28, 1, 95¬106. (In Japanese with English abstract)

Hara, J. and Tsuchiya, N., 2009, Chemical modification of pyroclastic rock by hot water: an experimental investigation of mass transport at the fluid-solid interface. *Geofluids*, 9, 24¬38.

Heald, P., Foley, N.K. and Hyaba, D.O., 1987, Comparative anatomy of volcanic-hosted epithermal deposits: acid-sulphate and adularia-sulfate types. *Econ. Geol.* 82, 11-26.

Hedenquist, J.W. and Henley, R.W., 1985, Hydrothermal eruptions in the Waiotapu geothermal system, New Zealand; their origin, associated breccias, and relation to precious metal mineralization. *Econ. Geol*., 80, 1640¬1668.

Hedenquist, J. W. and Lowenstern, J. B. 1994, The role of magmas in the formation of hydrothermal ore deposits. *Nature*, 370, 519—527.

Hedenquist, J.W., Matsuhisa, Y., Izawa, E., White, N.C., Giggenbach, W. F. and Aoki, M., 1994, Geology, geochemistry, and origin of high sulphidation Cu ― Au mineralization in the Nansatsu District, Japan. *Econ. Geol.*, 89, 1—30.

Hedenquist, J.W., Arribas Jr. A. and Reynolds, T.J., 1998, Evolution of An Intrusion-Centered Hydrothermal System: Far Southeast-Lepanto Porphyry and Epithermal Cu-Au Deposits, Philippines. *Econ. Geol*. 93, 373—404.

Hedenquist, J.W., Arribas, A. and Gonzalez-Urien, E., 2000, Exploration for epithermal gold deposits. *Rev. Econ. Geol*., 13, 245¬277.

Hedenquist, J.W., Arribas Jr., A. and Aoki, M., 2017, Zonation of sulfate and sulfide minerals and isotopic composition inc the Far Southeast Porphyry and Lepanto epithermal Cu-Au deposits, Philippines. *Resour. Geol.*, 67, 174—196.

Heiken, G. and Wohletz, K., 1985, PHREATOMAGMATIC ERUPTIONS, PHREATIC ERUPTIONS. In Volcanic Ash., Sharp, D. H., and Simmons, M. Jr., ed., Los Alamos National Laboratory: *University of California Press*, 85–142.

Horikoshi, K. 2017MS, Geological study of the eruption deposit at Jododaira, Azuma volcano, Graduation thesis of department of engineering and resource science, Akita University.

Ikeda, Y. and Mukoyama, S., 1983. Stratigraphy and correlation of the pyroclastic flow deposits in the Furano-Asahikawa area, central Hokkaido, Japan. *Jour. Geol. Soc. Japan*, 89, 163¬172. (in Japanese with English abstract).

Ikehata, K. and Maruoka, T., 2016, Sulfur isotopic characteristics of volcanic products from September 2014 Mount Ontake eruption, Japan. *Earth Planets Space*, 68:116. DOI 10.1186/s40623-016-0496-z

Ikeuchi, K., Doi, N., Sakagawa, Y., Kamenosono, H. and Uchida, T., 1998, High-temperature measurements in well WD-1a and the thermal strucuture ofthe Kakkonda geothermal system, Japan. *Geothermics*, 27, 591-607.

Imura, T., Ohba, T. and Horikoshi, K., 2018, Petrologic characteristics of non-juvenile ash in Holocene pyroclastic deposits at Azuma volcano, Fukushima, North-eastern Japan. *The Volcanol. Soc. Japan. Meet. 2018, Abstr*., 24p. (In Japanese)

Imura, T., Ohba, T. and Nakagawa, M., 2019a, Characteristics of hydrothermally altered minerals in volcanic products at Tokachidake volcano, central Hokkaido, Japan. *Jour. Geol. Soc. Japan*., 125, 3, 203–218. (In Japanese with English abstract) doi: 10.5575/geosoc.2018.0064

Imura, T., Minami, Y., Ohba, T., Matsumoto, A., Arribas, A. and Nakagawa, M., 2019b, Hydrothermal aluminum-phosphate-sulfates in ash from the 2014 hydrothermal eruption at Ontake volcano, central Honshu, Japan. *Minerals*, 9, 462; doi:10.3390/min9080462

Ishikawa, T., Yokoyama, I., Katsui, Y. and Kasahara, M., 1971, Tokachidake, Geology, Eruptive History, Recent Activity and Countermeasure for Prevention. Committee for Prevention of the Natural Disaster of Hokkaido, Sapporo, 136. (In Japanese)

Ishizuka, Y., Nakagawa, M. and Fujiwara, S., 2010, Geological Map of Tokachidake Volcano, Scale 1:30,000 and its Explanatory Text. Geol. Surv. Japan, AIST.

Itoh, H., Wakiyama, K., Yoshida, M., Nagayama, T., Harada, N. and Kusunoki, M., 2004, Mechanism of snowmelt type mudflow―Experimental approach and interpretation of 1926 mudflow of Tokachidake volcano―. *The Volcanol. Soc. Japan. Meet. 2004, Abstr*., 36. (In Japanese)

Itoh, J., Hamasaki, S. and Kawanabe, Y., 2018, Re-evaluation of explosive activities of Iwate volcano in the last 10,000 years: Spatial and temporal relationship of phreatic and magmatic explosions, Jour. Geol. Soc. Japan., 124, 4, 271–296. (In Japanese with English abstract) doi: 10.5575/geosoc.2018.0009

Japan Meteorological Agency (JMA), 1991, Volcanic Activity in Japan, during April-June 1991: Ontake volcano. *Bull. Volcanol. Soc. Japan*, 36 (3), 385. (in Japanese)

Japan Meteorological Agency (JMA), 2013, 34. Azumayama. In National Catalogue of the Active Volcanoes in Japan 4th edition 1. Hokkaido and Tohoku distirict., Japan meteorological Agency ed., *Japan Meteorological Business Support Center*, 479¬504.

John, D. A., Sisson, T. W., Breit, G. N., Rye, R. O. and Vallance, J. W., 2008, Characteristics, extent and origin of hydrothermal alteration at Mount Rainier volcano, Cascades Arc, USA: Implications for debris-flow hazards and mineral deposits. *Jour. Volcanol. Geotherm. Res*., 175, 289¬314.

Katsui, Y., Takahashi, T., 1960, A note on chemical composition of the lavas from Daisetsu-Tokachi volcanic chain. *Jour. Mineral. Petrol. Econ. Geol.*, 44, 142¬151. (In Japanese with English abstract)

Katsui, Y., Takahashi, T. and Doi, S., 1963, Explanatory Text of The Geological Map of Japan, scale 1:50,000, Tokachidake(Kusiro-1)). Geol. Surv. Hokkaido, 47.

Kato, A., Terakawa, T., Yamanaka, Y., Maeda, Y., Horikawa, S., Matsuhiro, K. and Okuda, T., 2015, Preparatory and precursory processes leadingup to the 2014 phreatic eruption of Mount Ontake, Japan. *Earth Planets Space,* 67:111. DOI 10.1186/s40623-015-0288-x

Kikawada, Y., Inoue, A., Ossaka, T., Oi, T. and Ossaka, J., 2000, Rock alteration by Kusatsu-Yubatake hot spring water. *The Jpn. Soc. hot spring sci.*, 49, 186–196. (In Japanese with English abstract)

Kioka, H., Furuyama, K., Miyake, Y., Sakai, I., Nagao, K., Ikemoto, M., Noiri, H. and Oda, K., 1998, K–Ar chronology of the Middle Pleistocene lavas at Ontake Volcano, central Japan. *Earth. Sci. (Chikyu Kagaku)*, 52, 464—474.

Kubo, K., Yanagisawa, Y., Yamamoto, T., Komazawa, M., Hiroshima, T. and Sudo, S., 2003, GELOGICAL MAP OF JAPAN 1;200,000, FUKUSHIMA. With explanatory text; Geological Survey of Japan: Tsukuba, Japan. (in Japanese with English Abstract)

Maeda, Y., Kato, A., Terakawa, T., Yamanaka, Y., Horikawa, Y., Matsuhiro, K. and Okuda, T., 2015, Source mechanism of a VLP event immediately before the 2014 eruption of Mt. Ontake, Japan. *Earth Planets Space,* 67:187. DOI 10.1186/s40623-015-0358-0

Maeno, F., Nakada, S., Oikawa, T., Yoshimoto, M., Komori, J., Ishizuka, Y., Takeshita, Y., Shimano, T., Kaneko, T. and Nagai, M., 2016, Reconstruction of a phreatic eruption on 27 September 2014 at Ontake volcano, central Japan, based on proximal pyroclastic density current and fallout deposits. *Earth Planets Space*, 68:82. DOI 10.1186/s40623-016-0449-6

Matsubara, S., Matsuyama, F., Kiyota, K. and Kato, A., 1998, Huangite from Okumanza, Gunnma Prefecture, Japan. *Mineral. Mag.*, 20, 123—135.

Matsumoto, A. and Kobayashi, T., 1995, K–Ar age determination of late Quaternary volcanic rocks using the "mass fractionation correction procedure": application to the Younger Ontake Volcano, central Japan. *Chem. Geol.* 125, 123—135.

Matsumoto, A. and Kobayashi, T., 1999, K–Ar ages of the older Ontake volcanic products, Ontake volcano, central Japan: reappraisal of the volcanic history based on the radiometric data. *Bull. Volcanol. Soc. Japan*, 44, 1—12. (in Japanese with English abstract)

Mills, S.J., Hatert, F., Nickel, E.H. and Ferraris, G., 2009, The standardisation of mineralgroup hierarchies: application to recent nomenclature proposals. *Eur. J. Mineral*, 21, 1073—1080.

Minami, Y., Imura, T., Hayashi, S. and Ohba, T., 2016, Mineralogical study on volcanic ash of the eruption on September 27, 2014 at Ontake volcano, central Japan: correlation with porphyry copper systems. *Earth Planets Space*, 68:67.

Miyagi, I., Itoh, J., Shinohara, H. and Kagoshima Observatory, JMA, 2010, Re-activation process of Showa volcanic vent at Sakura jima volcano in 2008: evidence from volcanic ash. *Bull. Volcanol. Soc. Japan*, 55, 21–39. (In Japanese with English abstract)

Miyagi, I., Geshi, N., Hamasaki, S. and Tomiya, A., 2014, Volcanic ash particles from Ontake volcano on September 2014. Abstracts of supplement: emergency academic session in the Volcanological Society of Japan 2014 fall meeting 2014, UP—15.

Muraoka, H., Uchida, T., Sasada, M., Yagi, M., Akaku, K., Sasaki, M., Yasukawa, K., Miyazaki, S., Doi, N., Saito, S., Sato, K. and Tanaka, S., 1998, Deep geothermal

resources survey program: igneous, metamorphic and hydrothermal processes in a well encountering 500 °C at 3729 m depth, Kakkonda, Japan. *Geothermics*, 27, 507–534.

Murase, M., Kimata, F., Yamanaka, Y., Horikawa, S., Matsuhiro, K., Matsushima, T., Mori, H., Ohkura, T., Yoshikawa, S., Miyajima, R., Inoue, H., Mishima, T., Sonoda, T., Uchida, K., Yamamoto, K. and Nakamichi, H., 2016, Preparatory processs preceding the 2014 eruption of Mount Ontake volcano, Japan: insights from precise leveling measurements. *Earth Planets Space*, 68:9.

Nakamichi, H., Kumagai, H., Nakano, M., Okubo, M., Kimata, F., Ito, Y. and Obara, K., 2009, Source mechanism of very-long-period event at Mt. Ontake, central Japan: response of a hydrothermal system to magma intrusion beneath the summit. *Jour. Volcanol. Geotherm. Res.*, 187, 167–177.

Narita, S. and Murakami, M., 2018, Shallow hydrothermal reservoir inferred from post-eruptive deflation at Ontake volcano as revealed by PALSSAR-2 InSAR. *Earth Planets Space*, 70:191.

Narita, S., Murakami, M. and Tanaka R., 2019, Quantitative relationship between plume emission and multiple deflations after the 2014 phreatic eruption at Ontake volcano, Japan. *Earth Planets Space*, 71:145.

New Energy and Industrial Technology Development Organization (NEDO), 1990, 1989AD Nationwide Geothermal Resources Exploration Project (3rd phase), Regional Exploration of Geothermal Fluid Circulation System, Tokachi region, *New Energy and Industrial Technology Development Organization*, 54–89. (In Japanese)

New Energy and Industrial Technology Development Organization (NEDO), 1991, Nationwide Geothermal Resources Exploration Project (3rd phase), Regional Exploration of Geothermal Fluid Circulation System, Bandai area. *New Energy and Industrial Technology Development Organization*, 80p. (In Japanese)

Nogami, K. and Yoshida, M., 1993, Leaching process of rock forming components through acidic alteration. *The Chem. Soc. Japan*, 3, 251–258. (In Japanese with English abstract)

Nogami, K. and Yoshida, M., 1995, Leaching rates of rock-forming components through acidic alteration. *Jour. Volcanol. Geotherm. Res*., 65, 289–314.

Oikawa, T., 2008, Reinvestigation of the historical eruption and fumarolic activity records at Ontake Volcano, central Japan. Misunderstanding reports about the 774 AD and 1892 AD eruptions. *Bull. Geol. Surv. Japan*, 59, 203–210.

Oikawa, T., Suzuki, Y. and Chiba, T., 2014, Eruptions of Ontake-san: history and 2014 eruption. *Kagaku*, 84, 1218—1225. (in Japanese)

Oikawa, T., Yamaoka, K., Yoshimoto, M., Nakada, S., Takeshita, Y., Maeno, F., Ishizuka, Y., Komori, J., Shimano, T. and Nakano, S., 2015, The 2014 eruption of Ontake volcano, Central Japan. *Bull. Volcanol. Soc. Japan*, 60, 411—415. (in Japanese with English explanatory text)

Oikawa, T., Yoshimoto, M., Nakada, S., Maeno, F., Komori, J., Shimano, T., Takeshita, Y., Ishizuka, Y. and Ishimine, Y., 2016, Reconstruction of the 2014 eruption sequence of Ontake Volcano from recorded images and interviews. *Earth Planets Space*, 68:79. DOI 10.1186/s40623-016-0458-5

Ogiso, M., Matsubayashi, H. and Yamamoto, T., 2015, Descent of tremor source locations before the 2014 phreatic eruption of Ontake volcano, Japan. *Earth Planets Space*, 67:206. DOI 10.1186/s40623-015-0376-y

Ohba, T., 2011, Hydrothermal mineral-bearing volcanic products: relationships with subvolcanic hydrothermal systems, and styles and patterns of their formation. *Jour. Geol. Soc. Japan*., 117, 344–356. (In Japanese with English abstract)

Ohba, T. and Kitade, Y., 2005, Subvolcanic hydrothermal systems: implication from hydrothermal minerals in hydrovolcanic ash. *Jour. Volcanol. Geotherm Res*., 145, 249–262.

Ohba, T., Taniguchi, H., Miyamoto, T., Hayashi, S. and Hasenaka, T., 2007, Mud plumbing system of an isolated phreatic eruption at Akita Yakeyama volcano, northern Honshu, *Jour. Volcanol. Geotherm. Res*., 161, 35–46.

Ossaka, J., 1982, Activity of volcanoes and clay minerals. *Jour. Clay Sci. Soc. Japan*, 22, 127–137. (In Japanese with English abstract)

Ossaka, J, 2003, Clay minerals contained in volcanic ejecta and their correlation with volcanic activities in Japan. *Bull. Volcanol. Soc. Japan*, 48, 43–61. (In Japanese with English abstract)

Ossaka, J. and Hirabayashi, J., 1981, Clay minerals in volcanic ejecta. *Mineral. Mag.*, 15, special issue, 223–228. (In Japanese with English abstract)

Ozawa, T., Kimijima, K., Tohma, Y., Ossaka, J. and Hirabayashi, J., 1981, Variation of chemical compositions of volcanic gases and hot spring waters accompanied with 1977-1979 activity at Issaikyo, volcano Azuma, Fukushima Prefecture, *Report of the Joint Geophysical and Geochemical Observations of the Azuma Volcano - October, 1979* -, 93-103. (In Japanese)

Scott, K.M., 1987a, Solid solution in, and classification of gossan-derived members of the alunite―jarosite family, Northwest Queensland, Australia. *Am. Mineral*. 72, 178—187.

Scott, K.M. 1987b, The mineralogical distribution of pathfinder elements in gossans derived from dolomitic shale-hosted Pb―Zn deposits, Northwest Queensland, Australia. *Chem. Geol,*. 164, 295—306.

Shinohara, H. and Kazahaya, R., 2016, Fumarolic activity of Azumayama volcano, Ooana crater, *The Volcanol. Soc. Japan. Meet. 2016, Abstr*., 56p. (In Japanese)

Sillitoe, R. H., 2010, Porphyry Copper Systems. *Econ Geol.*, 105, 3–41.

Smith, D.K., Roberts, A.C., Bayliss, P. and Liebau, F., 1998, A systematic approach to general and structure-type formulas for minerals and other inorganic phases. *Am Mineral.* 83, 126—132.

Stoffregen, R.E., 1987, Genesis of acid-sulfate alteration and Au―Cu―Ag mineralization at Summitville, Colorado. *Econ. Geol*., 82, 1575¬1591.

Stoffregen, R.E. and Alpers, C.N., 1987, Woodhouseite and svanbergite in hydrothermal ore deposits: products of apatite destruction during advanced argillic alteration. *Can. Mineral.*, 25, 201—211.

Stoffregen, R.E. and Cygan, G.L., 1990, An experimental study of Na-K exchange between alunite and aqueous sulfate solutions. *Am. Mineral.* 75, 209—220.

Stoffregen, R.E., Rye, R.O. and Wasserman, M.D., 1994. Experimental studies of aluntie: I 18O and D－H fractionation factors between alunite and water at 250―450°C. *Geochim. Cosmochim. Acta*, 58, 903—916.

Stoppa, F. and Schiazza, M., 2014, Extreme chemical conditions of crystallization of Umbrian Melilitolites and wealth of rare, late stage/hydrothermal minerals. *Cent. Eur. J. Geosci.*,. 6(4) 549-564. DOI: 10.2478/s13533-012-0190-zl

Stoppa, F., Scordari, F., Mesto, E., Sharygin, V.V. and Bortolozzi, G., 2010, Calcium-aluminum-silicate-hydrate "cement" phases and rare Ca-zeolite association at Colle Fabbri, Central Italy. *Open Geosci.*, 2(2):175-187.

Reed, M. H., 1997, Hydrothermal alteration and its relationship to ore fluid composition. In Geochemistry of hydrothermal ore deposit 3rd ed., Barnes, H. L., ed., Wiley, 303–365.

Tada, F. and Tsuya, H., 1927, The eruption of the Tokachidake volcano, Hokkaido, on May 24th, 1926. Bull. *Earthq. Res. I. Tokyo*, 2, 49¬84. (In Japanese with English abstract)

Taguchi, S., Itoi, R., Kai, S., Watanabe, K., Ehara, Y. and Tsutsui, T., 1996, Reports on Mechanism of Phreatic Eruption and Process of Volcanic Activity in October, 1995 at Kuju Volcano, 75¬82. (In Japanese with English abstract)

Takahashi, R., Shibata, T., Murayama, Y., Ogino, T. and Okazaki, N, 2015, Temporal changes in thermal waters related to volcanic activity of Tokachidake Volcano, Japan: implications for forecasting future eruptions. *Bull. Volcanol*., 77. 2–13.

Takahashi, R. and Yahata, M., 2018, Effects of subvolcanic hydrothermal systems on edifice collapses and phreatic eruptions at Tokachidake volcano, Japan. *Jour. Volcanol. Geotherm Res*., 352, 117–129.

Takahashi, T., 1960, Geology and petrology of the south-western part of the Daisetsu-Tokachi volcanic chain I. Geology of the Tokachi volcanic group and its volcano-tectonic structure. *Bull. Geol. Committee. Hokkaido*, 39, 7–18. (In Japanese with English abstract)

Takano, B. and Watanuki, K., 1990, Monitoring of volcanic eruptions at Yugama crater lake by aqueous sulphur oxyanions. *Jour. Volcanol. Geotherm Res*., 40, 71—87.

Takarada, S., Oikawa, T., Furukawa, R., Hoshizumi, H., Itoh, J., Geshi, N. and Miyagi, I., 2016, Estimation of total discharged mass from the phreatic eruption of Ontake Volcano, central Japan, on September 27, 2014. *Earth Planets Space,* 68:138. DOI 10.1186/s40623-016-0511-4

Takeuchi, M., Nakano, S., Harayama, S. and Otuska, T., 1998, Geology of the Kiso-Fukushima District. With geological sheet map at 1:50,000; Geological Survey of Japan: Tsukuba, Japan. (in Japanese)

Tomita, K., Kawano, M. and Kobayashi, T., 1994, Minerals in the volcanic ash erupted from Shin-dake in Kuchinoerabu Island in 1980. *Report of the Faculty of Science, Kagoshima University. Earth Sci. Biol*., 27, 1—10.

Uesawa, S., 2008, Restudy of stratigraphy and paleomagnetic characteristics of Taisho lahar deposit associated with the 1926 eruption on Tokachidake volcano, central Hokkaido, Japan. *Bull. Volcanol. Soc. Japan*, 53, 171¬191. (In Japanese with English abstract)

Uesawa, S., 2014, A study of the Taisho lahar generated by the 1926 eruption of Tokachidake Volcano, central Hokkaido, Japan, and implications for the generation of cohesive lahars. *Jour. Volcanol. Geotherm Res*., 270, 23¬34.

Yaguchi, M., Ohba T., Takagi, A. and Fukui, K., Geochemical characteristics of volcanic gases at Issaikyo, Azuma volcano, Japan, *JpGU-AGU Joint Meeting 2017, Abstr*., SVC48-P04. (In Japanese)

Yamada, N. and Kobayashi, T., 1988, Geology of the Ontakesan District. With Geological sheet map at 1:50,000; Geological Survey of Japan: Tsukuba, Japan. (in Japanese with English abstract)

Yamamoto, T., 2005, Eruptive history of Azuma volcano, NE Japan, during last 7,000 years: Stratigraphy and magma-plumbing system of the Azuma-Jododaira products. *Jour. Geol. Soc. Japan*., 111, 94–110. (In Japanese with English abstract)

[URL1] Sapporo District Meteorological Observatory, 2018, Monthly Report for Volcanic Activity of Tokachidke Volcano (August 2018), http://www.data.jma.go.jp/svd/vois/data/tokyo/STOCK/monthly_vact_doc/sapporo/16m08/108_16m08.pdf. Accessed on 8th August 2018. (In Japanese)

[URL2] Japan Meteorological Agency, 2014, Annual Report for 2014 Volcanic Activity of OntakeVolcano. http://www.data.jma.go.jp/svd/vois/data/tokyo/STOCK/monthly_vact_doc/tokyo/2014y/312_14y.pdf. Accessed on 8th August 2018. (In Japanese)

[URL3] Geographical Information Authority of Japan, 2016, Download Service of Fundamental Geospatial Data in Japan. http://fgd.gsi.go.jp/download/demsel.php. Accessed on 10th August 2016. (In Japanese)

[URL4] Lafuente, B., Downs, R. T., Yang, H. and Stone, N., 2015, The power of databases: the RRUFF project. In: Highlights in Mineralogical Crystallography, T Armbruster and R M Danisi, eds. Berlin, Germany, W. De Gruyter, pp 1-30. http://rruff.info. Accessed on 10th August 2016.

[URL5] Japan Meteorological Agency (JMA). Report of coordinating committee for prediction of volcanic eruption. 2014. Available online: http://www.data.jma.go.jp/svd/vois/data/tokyo/STOCK/kaisetsu/CCPVE/shiryo/130/130_no01.pdf (accessed on 6th July 2018) (in Japanese)

[URL6] Mindat.org. Nickel-Strunz Classification-Primary Groups 10th edition. 2019. Available online: https://www.mindat.org/strunz.php (accessed on 29th July 2019)

[URL7] Earthquake Research Institute at the University of Tokyo (ERI). Eruption of the Ontakesan, 27th September, 2014. Available online: http://www.eri.u-tokyo.ac.jp/en/2014/09/30/eruption-of-the-ontakesan-27th-september-2014/(accessed on 6th July 2018)

[URL8] Sendai District Meteorological Observatory, 2019, Monthly Report for Volcanic Activity of Azuma Volcano (August 2019), http://www.data.jma.go.jp/svd/vois/data/tokyo/STOCK/monthly_v-

act_doc/sendai/19m08/213_19m08.pdf (Accessed on 8th August 2019. (In Japanese)

Appendixes

Appendix 1: List of collected samples in Chapter 1

Appendix 2: Outcrop photos in Chapter 1

Appendix 3-1: XRD results in Chapter 1 (Bulk ash sample sieved into < 250μm)

Appendix 3-2: XRD results in Chapter 1 (Coase fraction sieved into 250μm-1mm)

Appendix 4: List of described ash grains in Chapter 1

Appendix 5: Collected sample list in Chapter 3

Appendix 6-1: XRD results in Chapter 3 (Bulk ash samples)

Appendix 6-2: XRD result in Chapter 3 (Fine fraction sieved into <250μm)

Appendix 7: List of described ash grains in Chapter 3

Appendix 8: Counted ash grains under binocular stereoscopic microscope in Chapter 3

Appendix 9: Weathered scoria or scoria fragments under binocular stereoscopic microscope in Chapter 3

Appendix 1: List of collected samples in Chapter 1

	Location					
Sample code	Number	Height(m)	Latitude	Longitude	Unit name	Occurrence
140830001_1	1	974	43° 26' 36.91" N	142° 39' 02.16" E	3.3ka Gfl-2 upper	pyroclastic flow deposit
140830001_2	1	974	43° 26' 36.91" N	142° 39' 02.16" E	3.3ka Gfl-1	pyroclastic flow deposit
140830001_3	1	974	43° 26' 36.91" N	142° 39' 02.16" E	4.7ka Gfl-0	pyroclastic flow deposit
140902001_1	2	989	43° 26' 17.26" N	142° 38' 45.14" E	3.3ka Gfl-2 lower	pyroclastic flow deposit
140902001_2	2	989	43° 26' 17.26" N	142° 38' 45.14" E	3.3ka Gfl-1	pyroclastic flow deposit
140902001_3	2	989	43° 26' 17.26" N	142° 38' 45.14" E	3.3ka Gfl-0	pyroclastic flow deposit
140902002_1	3	993	43° 26' 13.96" N	142° 38' 49.37" E	3.3ka Gfl-1	pyroclastic flow deposit
140902002_2	3	993	43° 26' 13.96" N	142° 38' 49.37" E	3.3ka Gfl-1	banded pumice
140902002_3	3	993	43° 26' 13.96" N	142° 38' 49.37" E	3.3ka Gfl-1	low vesicular scoria
140830002_1	4	1000	43° 26' 31.11" N	142° 39' 03.49" E	3.3ka Gfl-2 upper	pyroclastic flow deposit
140830002_2	4	1000	43° 26' 31.11" N	142° 39' 03.49" E	3.3ka Gfl-1	pyroclastic flow deposit
140830002_3	4	1000	43° 26' 31.11" N	142° 39' 03.49" E	3.3ka Gfl-1	pyroclastic flow deposit
140830002_4	4	1000	43° 26' 31.11" N	142° 39' 03.49" E	3.3ka Sm	mud flow deposit
140830003_1	5	1022	43° 26' 26.46" N	142° 39' 09.84" E	3.3ka Gfl-1	pyroclastic flow deposit
140830003_2	5	1022	43° 26' 26.46" N	142° 39' 09.84" E	4.7ka Gfl-0	pyroclastic flow deposit
140830003_3	5	1022	43° 26' 26.46" N	142° 39' 09.84" E	4.7ka A-2	lahar deposit
140830003_4	5	1022	43° 26' 26.46" N	142° 39' 09.84" E	4.7ka A-2	lahar deposit
140830003_5	5	1022	43° 26' 26.46" N	142° 39' 09.84" E	4.7ka A-1	lahar deposit
140831003_1	6	1040	43° 26' 21.30" N	142° 39' 12.93" E	3.3ka Gfl-1	pyroclastic flow deposit
140831003_2	6	1040	43° 26' 21.30" N	142° 39' 12.93" E	4.7ka Gfl-0	pyroclastic flow deposit
140831001_1	8	1093	43° 26' 15.07" N	142° 39' 23.10" E	3.3ka Gfl-2 upper	pyroclastic flow deposit
140831001_2	8	1093	43° 26' 15.07" N	142° 39' 23.10" E	3.3ka Gfl-2 lower	pyroclastic flow deposit
140831001_3	8	1093	43° 26' 15.07" N	142° 39' 23.10" E	3.3ka Gfl-1	pyroclastic flow deposit
140831001_4	8	1093	43° 26' 15.07" N	142° 39' 23.10" E	350 y Cl	aa lava
140828001_1	9	1095	43° 26' 01.71" N	142° 39' 10.40" E	1926y distal facies	lahar deposit
140828001_2	9	1095	43° 26' 01.71" N	142° 39' 10.40" E	overlying 1926y deposit	lahar deposit
140824001_1	10	1179	43° 26' 07.40" N	142° 39' 41.71" E	1926y unit C	debris avalanche deposit
140824001_2	10	1179	43° 26' 07.40" N	142° 39' 41.71" E	1926y unit A	debris avalanche deposit
140829002_1	11	1211	43° 25' 55.95" N	142° 39' 40.88" E	1926y unit C	debris avalanche deposit
140829002_2	11	1211	43° 25' 55.95" N	142° 39' 40.88" E	1926y unit B	hydrothermal surge deposit
140829002_3	11	1211	43° 25' 55.95" N	142° 39' 40.88" E	1926y unit A	debris avalanche deposit
140828003_1	12	1227	43° 25' 54.29" N	142° 39' 42.87" E	1926y unit B	hydrothermal surge deposit
140828003_2	12	1227	43° 25' 54.29" N	142° 39' 42.87" E	1926y unit A	debris avalanche deposit
140828003_3	12	1227	43° 25' 54.29" N	142° 39' 42.87" E	1926y unit A	debris avalanche deposit
140824002_1	13	1245	43° 26' 00.46" N	142° 39' 47.74" E	1926y unit C	debris avalanche deposit
140824002_2	13	1245	43° 26' 00.46" N	142° 39' 47.74" E	1926y unit B	hydrothermal surge deposit
140824002_3	13	1245	43° 26' 00.46" N	142° 39' 47.74" E	1926y unit A	debris avalanche deposit
140827001_1	14	1275	43° 25' 57.41" N	142° 39' 57.92" E	1926y unit C	debris avalanche deposit
140827001_2	14	1275	43° 25' 57.41" N	142° 39' 57.92" E	1926y unit B	hydrothermal surge deposit
140827001_3	14	1275	43° 25' 57.41" N	142° 39' 57.92" E	1926y unit A	debris avalanche deposit
140827002_1	15	1424	43° 25' 52.83" N	142° 40' 17.34" E	1926y unit C	debris avalanche deposit
140827002_2	15	1424	43° 25' 52.83" N	142° 40' 17.34" E	1926y unit B	hydrothermal surge deposit
140827002_3	15	1424	43° 25' 52.83" N	142° 40' 17.34" E	1926y unit A	debris avalanche deposit
140822001_1	16	1445	43° 25' 49.97" N	142° 40' 16.93" E	1926y unit C	debris avalanche deposit
140822001_2	16	1445	43° 25' 49.97" N	142° 40' 16.93" E	1926y unit C	debris avalanche deposit
140822001_3	16	1445	43° 25' 49.97" N	142° 40' 16.93" E	1926y unit B	hydrothermal surge deposit
140822001_4	16	1445	43° 25' 49.97" N	142° 40' 16.93" E	1926y unit A	debris avalanche deposit
140822001_5	16	1445	43° 25' 49.97" N	142° 40' 16.93" E	1926y unit A	debris avalanche deposit

Appendix 2: Outcrop photos in Chapter 1

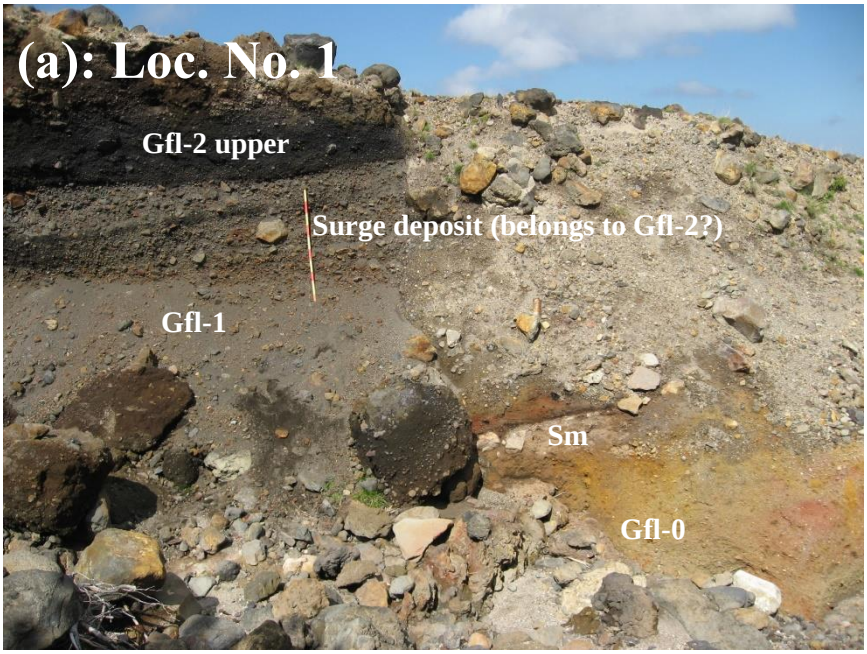

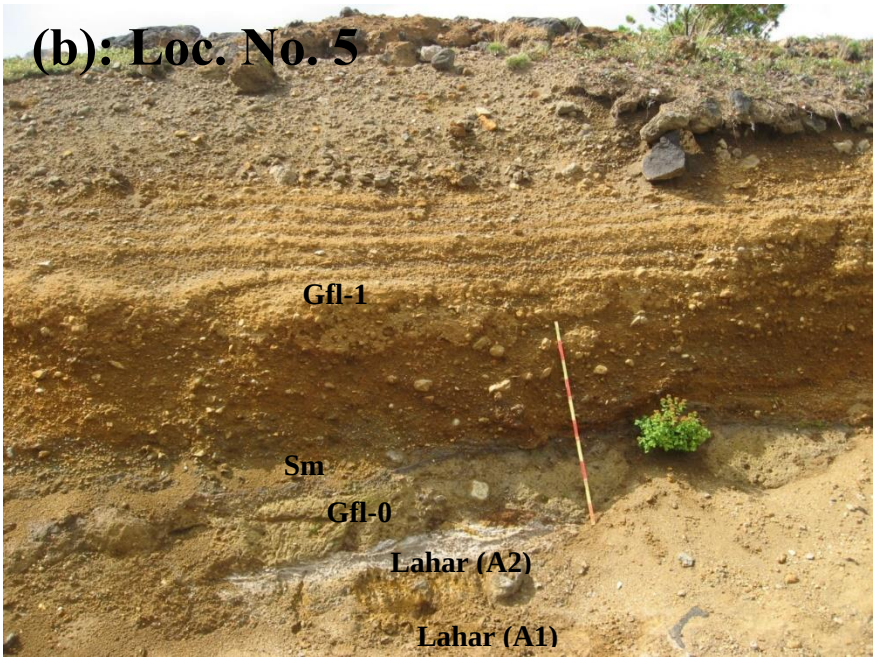

Outcrops photo for stratigraphic relationships in Gfl-0, Gfl-1, and Lahar deposits (A1 and A2). (a): Gfl-0 is covered by Sm and Gfl-1 and Gfl-2 upper. Gfl-2 lower does not expose in this outcrop. (b): Gfl-0 overlies on the older lahar deposits (A1 and A2).

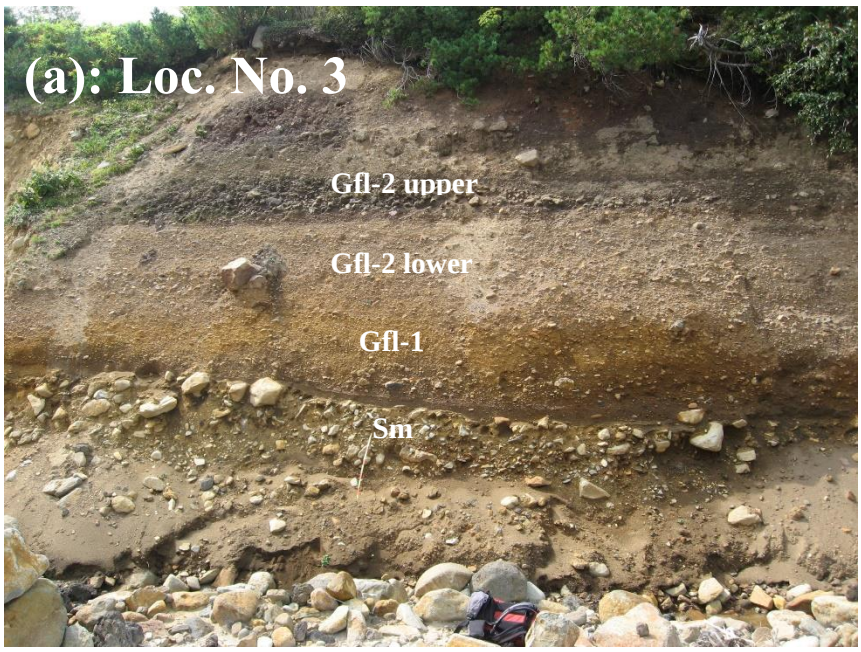

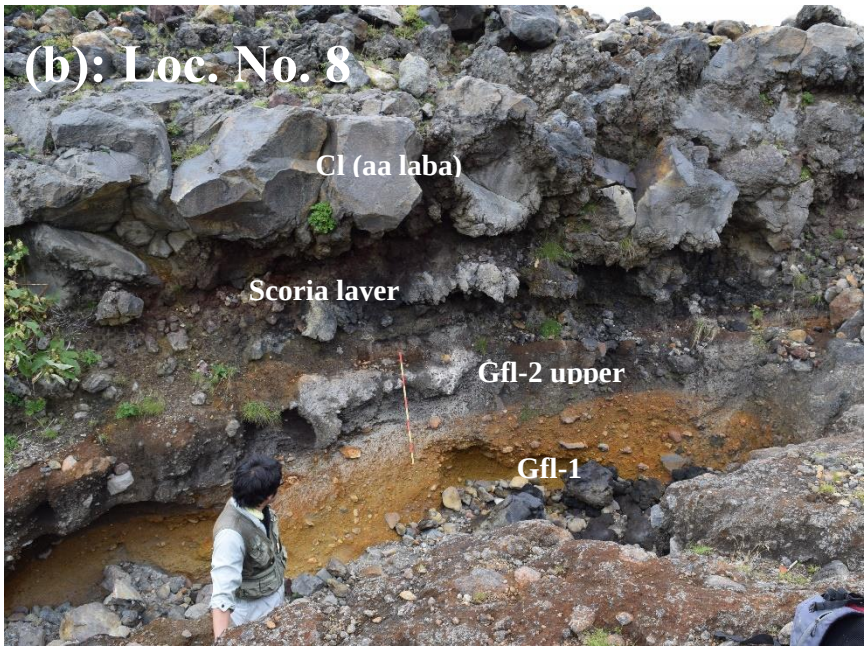

Outcrops photo for stratigraphic relationships between Gfl-1 and Gfl-2. (a): Gfl-1, Gfl-2 lower, and Gfl-2 upper expose in this outcrop along Frano-river. (b): Cl covers on Gfl-1, Gfl-2 upper and Scoria layer. There is a charcoal layer in the boundary between Gfl-2 upper and Scoria layer.

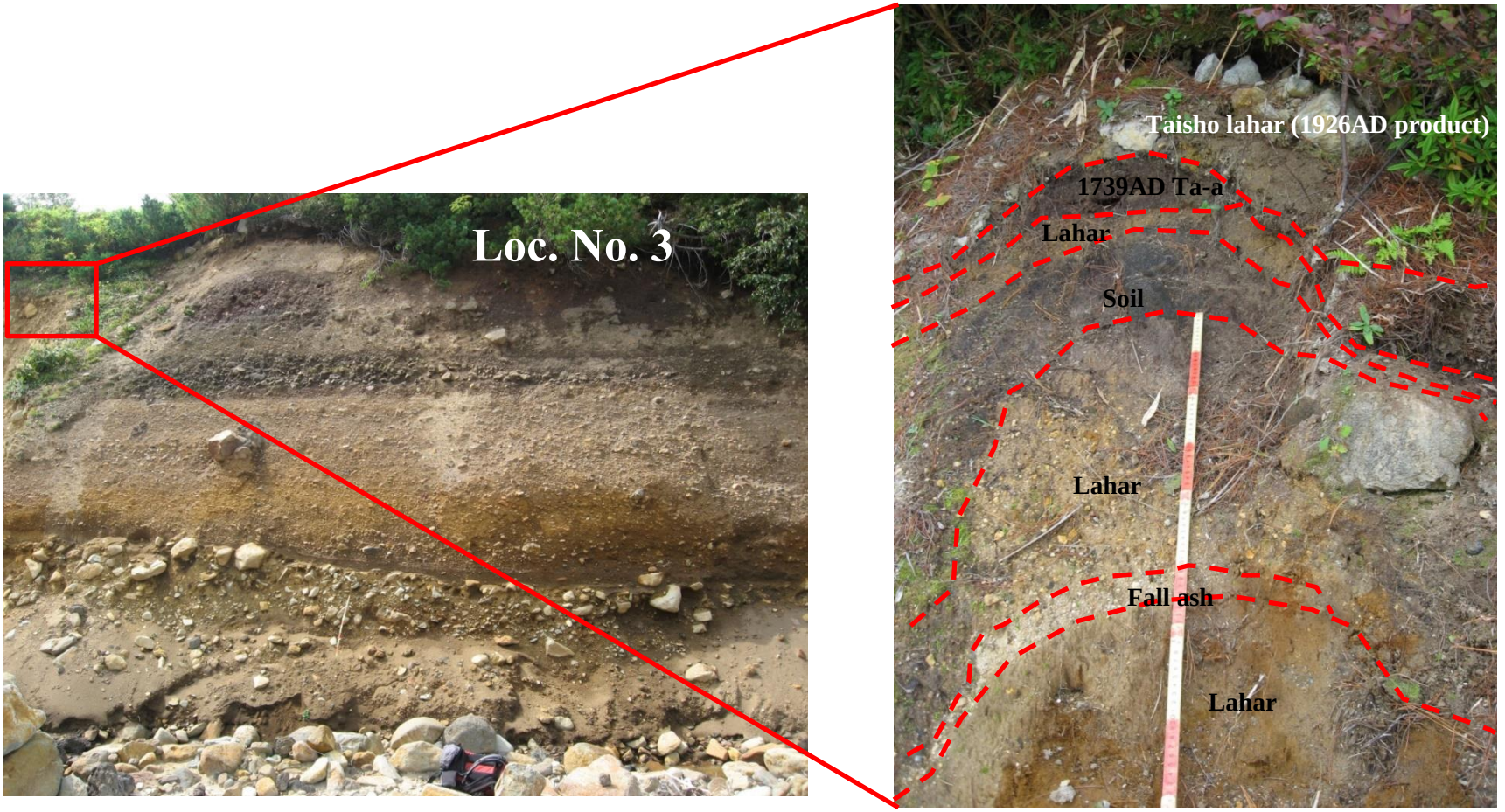

Distal facies of the 1926AD products around Location Number 3. The products occur as only one layer in this outcrop, and covers on Ta-a (Uesawa, 2008).

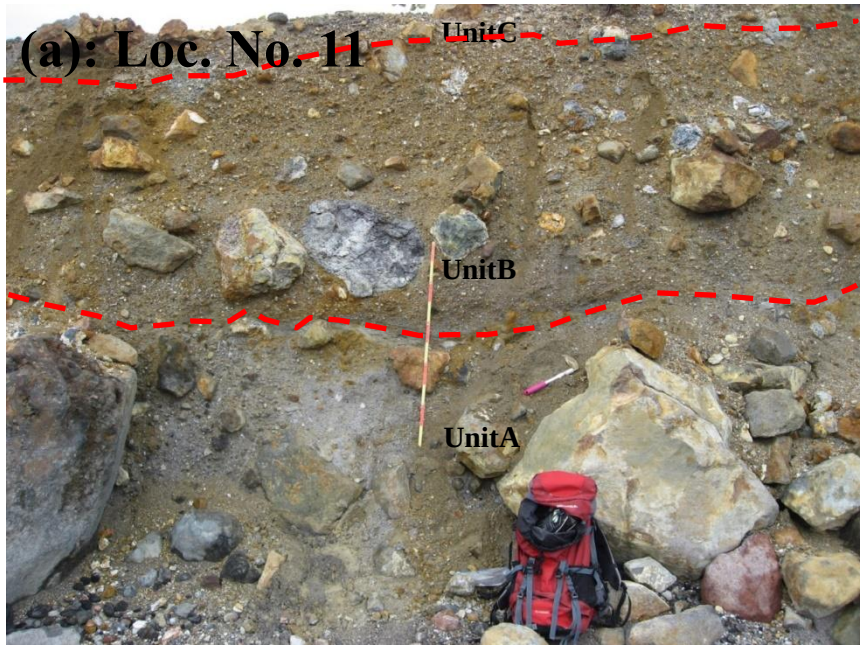

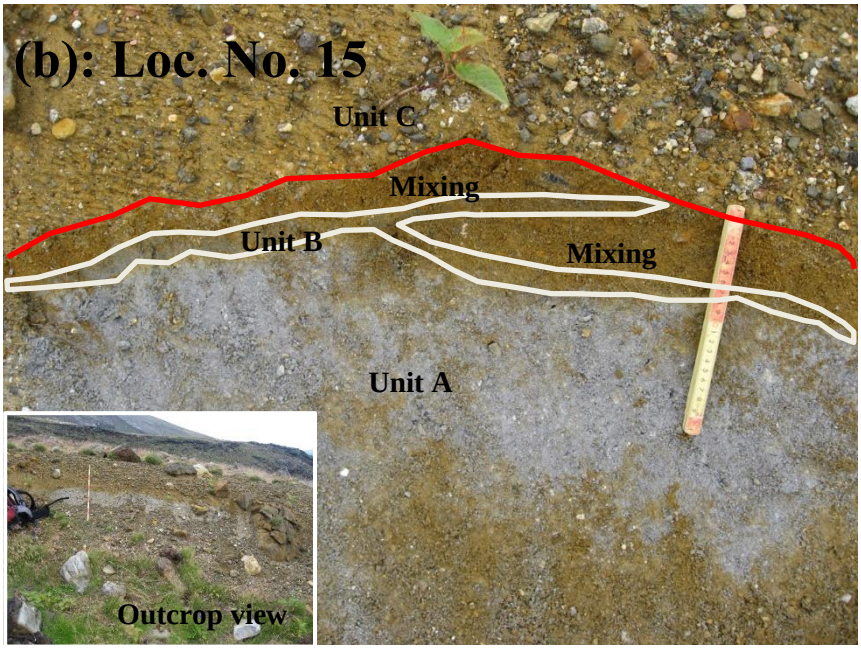

Outcrop photos for stratigraphic relationships in the 1926 AD products (Unit A to C). (a): Every boundary of Unit A to C is usually unclear. (b): Each boundary of Unit A to C in Location Number 15 around the Hut is relatively clear. Unit B connects Unit C with a mixing part consisted of therm.

Appendix 3-1: XRD results in Chapter 1 (Bulk ash sample sieved into < 250μm)

定性分析結果

基本情報

解析日	2016/05/18 22:51:34		
試料名	4.7ka PDC (Gfl-0 のサンプル)	測定日	2016/05/12 10:38:22
ファイル名	160512 gf-0 bulk.raw	測定者	User1
コメント	Ouchi_slowly		

同定された結晶相

結晶相名	化学式	FOM	相の登録手法	DB カード番号
tridymite	Si O2	0.725	ICDD (PDF-2/Release	05-001-0058
Natroalunite	Na0.58 K0.42 Al3 (S	1.192	ICDD (PDF-2/Release	01-075-1685
Cristobalite-alpha	Si O2	1.091	ICDD (PDF-2/Release	01-082-1232
sodium tecto-	Na (Al Si3 O8)	1.474	ICDD (PDF-2/Release	01-083-1610
cristobalite α HP	Si O2	1.240	ICDD (PDF-2/Release	01-082-1233
Albite, disordered	Na (Si3 Al) O8	1.457	ICDD (PDF-2/Release	00-010-0393
Quartz, low	Si O2	1.419	ICDD (PDF-2/Release	00-005-0490
Kaolinite	Al4 (O H)8 (Si4	1.668	ICDD (PDF-2/Release	01-078-2110
Illite	2 K2 O ・3 Mg O ・	1.959	ICDD (PDF-2/Release	00-002-0050
Pyrophyllite	Al (Si2 O5) (O H)	1.581	ICDD (PDF-2/Release	01-083-1805
Illite-Montmorillonite,	K - Al4 (Si Al)8 O20	3.209	ICDD (PDF-2/Release	00-007-0330
Alunite	(K0.805 Na0.132 (H2	1.106	ICDD (PDF-2/Release	01-075-9141
Augite	(Na0.09 Ca0.616)	1.496	ICDD (PDF-2/Release	01-071-1070

結晶相データパターン

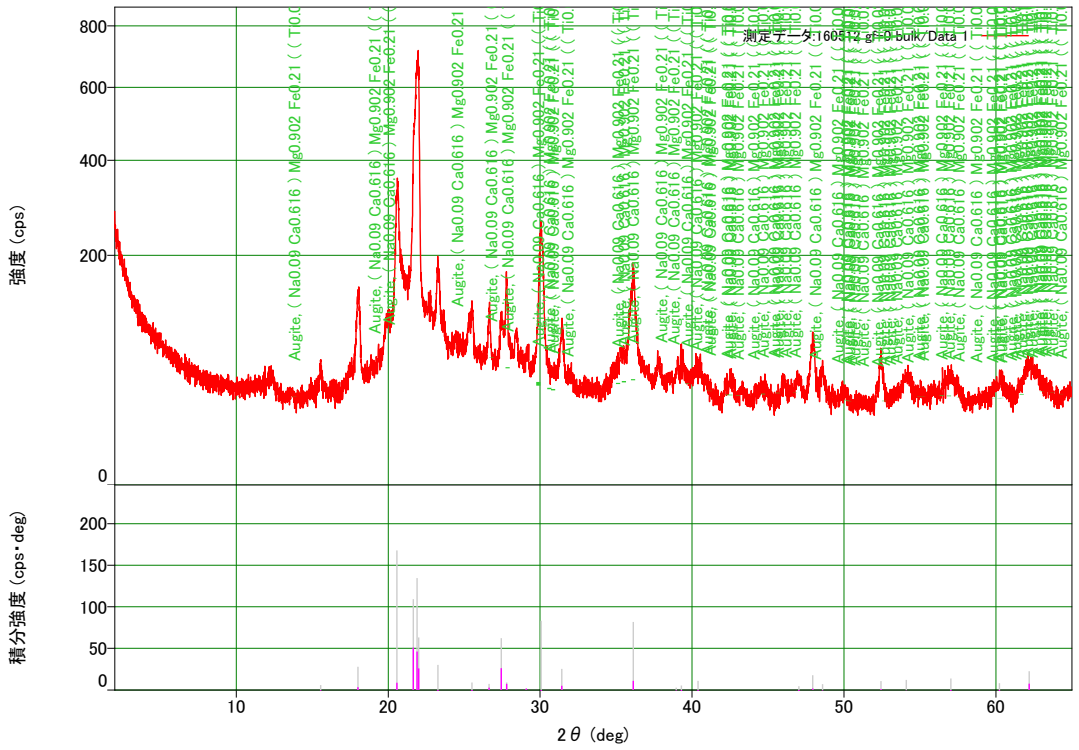

定性分析結果

基本情報

解析日	2016/05/18 22:33:54		
試料名	3.3ka PDC lower (Gfl-1 のサンプル)	測定日	2016/05/12 14:50:41
ファイル名	160512 gf-1.raw	測定者	User1
コメント	Ouchi_slowly		

同定された結晶相

結晶相名	化学式	FOM	相の登録手法	DB カード番号
Plagioclase	Ca0.68 Na0.30	1.114	ICDD (PDF-2/Release	01-083-1372
Cristobalite, syn	Si O2	1.124	ICDD (PDF-2/Release	00-039-1425
Margarite-2M1	Ca Al2 (Si2 Al2) O10	1.510	ICDD (PDF-2/Release	00-018-0276
Anatase, syn	Ti O2	2.754	ICDD (PDF-2/Release	00-021-1272
Enstatite	Mg Si O3	3.074	ICDD (PDF-2/Release	01-072-1507
Augite	Ca (Mg , Fe) Si2 O6	1.834	ICDD (PDF-2/Release	00-024-0203
Sanidine	(K , Na) (Si3 Al) O8	1.855	ICDD (PDF-2/Release	00-019-1227
Tridymite	Si O2	2.754	ICDD (PDF-2/Release	00-001-0378
Kaolinite	Al4 (O H)8 (Si4	2.721	ICDD (PDF-2/Release	01-078-2110
Quartz, low	Si O2	2.664	ICDD (PDF-2/Release	00-005-0490
Phlogopite-1M	K Mg3 (Si3 Al) O10	1.760	ICDD (PDF-2/Release	00-010-0495
Pyrophyllite	Al (Si2 O5) (O H)	2.815	ICDD (PDF-2/Release	01-083-1805
Chlorite-IIb-4	(Mg11.06 Fe0.94)	3.515	ICDD (PDF-2/Release	01-075-8291
Montmorillonite-	Na - Ca - Al - Si4 O10	3.005	ICDD (PDF-2/Release	00-007-0027
Natroalunite	Na0.58 K0.42 Al3 (S	2.870	ICDD (PDF-2/Release	01-075-1685
Alunite	K (Al3 (S O4)2 (O	2.747	ICDD (PDF-2/Release	01-071-1776

結晶相データパターン

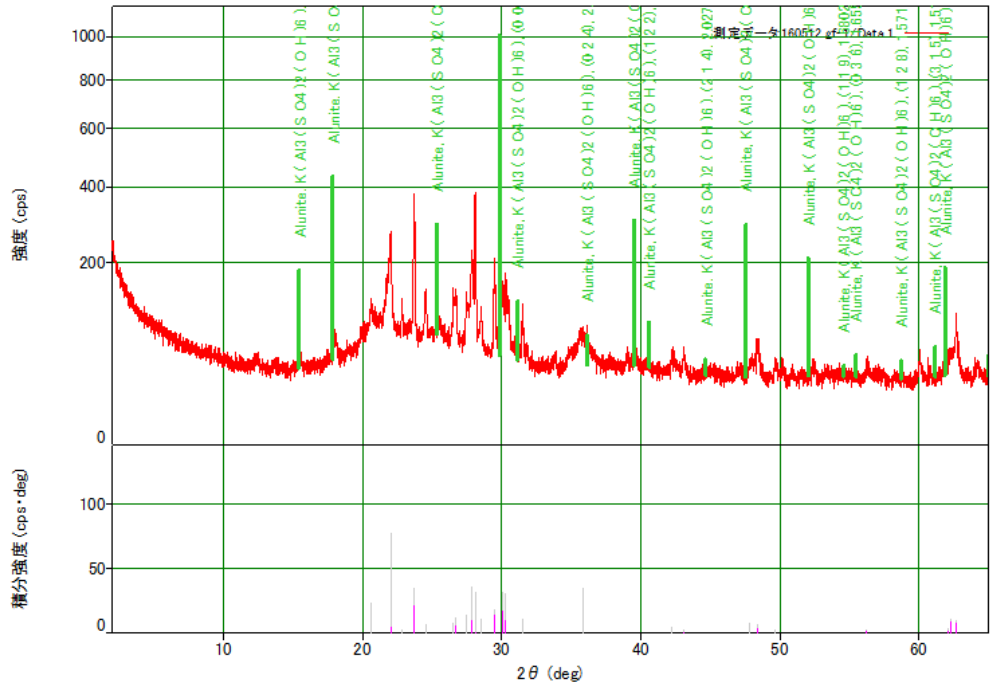

定性分析結果

基本情報

解析日	2016/05/18 23:25:05		
試料名	3.3ka PDC transfer (Gfl-2 lower のサンプル)	測定日	2016/05/12 19:02:58
ファイル名	160512 gf transfer bulk.raw	測定者	User1
コメント	Ouchi_slowly		

同定された結晶相

結晶相名	化学式	FOM	相の登録手法	DB カード番号
Anorthite, ordered	Ca Al2 Si2 O8	1.271	ICDD (PDF-2/Release	00-041-1486
cristobalite, high	Si O2	2.635	ICDD (PDF-2/Release	00-027-0605
Cristobalite-alpha	Si O2	2.596	ICDD (PDF-2/Release	01-071-6240
Dickite	Al2 Si2 O5 (O H)4	3.033	ICDD (PDF-2/Release	01-076-0632
Pyrophyllite	Al (Si2 O5) (O H)	3.033	ICDD (PDF-2/Release	01-083-1805
Sanidine	(K , Na) (Si3 Al) O8	3.048	ICDD (PDF-2/Release	00-019-1227
Enstatite, syn	Mg(Ca0.054	3.213	ICDD (PDF-2/Release	01-072-7791
Tridymite	Si O2	3.110	ICDD (PDF-2/Release	00-001-0378
Quartz, syn	Si O2	2.746	ICDD (PDF-2/Release	00-033-1161
Chlorite	Mg2 Al3 (Si3 Al) O10	3.067	ICDD (PDF-2/Release	00-013-0003
Augite	(Mg0.86 Fe.1 Al0.03	3.384	ICDD (PDF-2/Release	01-073-8528
Phlogopite-1M	K2 Mg6 (Si.75	2.821	ICDD (PDF-2/Release	01-073-0224

結晶相データパターン

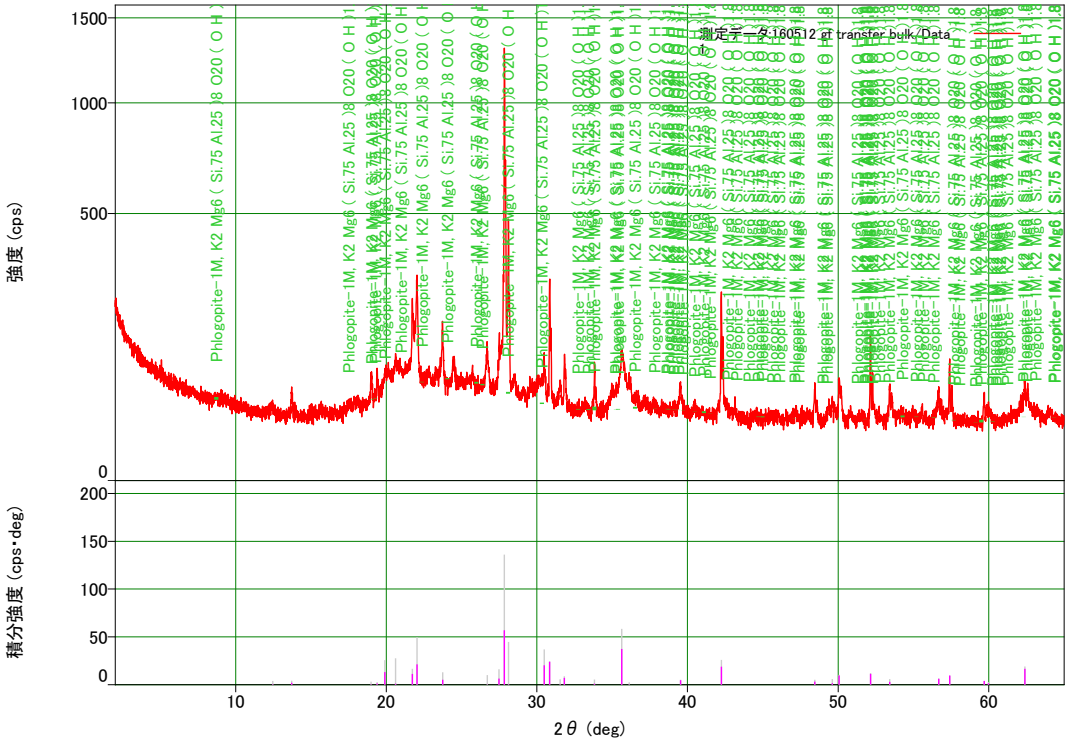

定性分析結果

基本情報

解析日	2016/05/18 23:08:23		
試料名	3.3ka PDC upper (Gfl-2 upper のサンプル)	測定日	2016/05/13 11:28:24
ファイル名	160513 gf-2 bulk unori.raw	測定者	User1
コメント	Ouchi slow sp		

同定された結晶相

結晶相名	化学式	FOM	相の登録手法	DB カード番号
Augite	Ca0.90 Mg0.71	1.629	ICDD (PDF-2/Release	01-083-2015
Plagioclase	Ca0.65 Na0.32	1.400	ICDD (PDF-2/Release	01-083-1368
Quartz	Si O2	1.495	ICDD (PDF-2/Release	01-070-8054
Cristobalite	Si O2	1.542	ICDD (PDF-2/Release	01-075-0923
Olivine, syn	Mg Fe (Si O4)	3.107	ICDD (PDF-2/Release	01-070-6485
Magnetite, titanian	Fe (Fe1.17 Ti0.54)	3.010	ICDD (PDF-2/Release	01-071-6449
Enstatite	Mg (Si O3)	3.076	ICDD (PDF-2/Release	01-073-6356
Natroalunite	Na0.58 K0.42 Al3 (S	3.091	ICDD (PDF-2/Release	01-075-1685
Alunite	(K0.805 Na0.132 (H2	3.226	ICDD (PDF-2/Release	01-075-9141
Albite	Na Al Si3 O8	3.038	ICDD (PDF-2/Release	00-001-0739
Tridymite	Si O2	3.100	ICDD (PDF-2/Release	00-001-0378
Sanidine	K0.41 Na0.56 Ca0.03	3.263	ICDD (PDF-2/Release	01-077-0982

結晶相データパターン

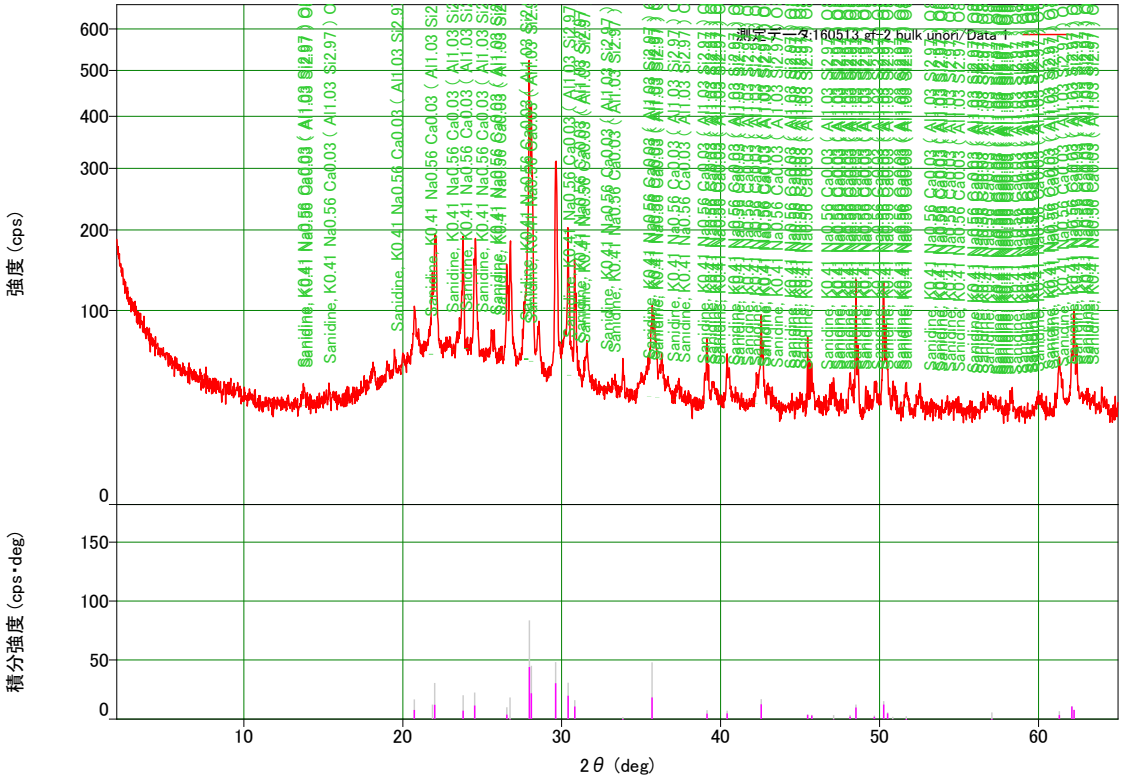

定性分析結果

基本情報

解析日	2016/05/18 21:42:49		
試料名	1926 TL unitA	測定日	2016/05/13 15:41:12
ファイル名	160513 tl-u A.bulk.raw	測定者	User1
コメント	Ouchi slow sp		

同定された結晶相

結晶相名	化学式	FOM	相の登録手法	DB カード番号
Natroalunite	Na Al3 (S O4)2 (O	0.274	ICDD (PDF-2/Release	00-014-0130
Cristobalite, syn	Si O2	0.452	ICDD (PDF-2/Release	00-011-0695
Cristobalite beta, syn	Si O2	0.498	ICDD (PDF-2/Release	01-077-8670
Albite, syn	Na (Al Si3 O8)	0.629	ICDD (PDF-2/Release	01-071-1150
Anhydrite, syn	Ca S O4	0.733	ICDD (PDF-2/Release	00-037-1496
Alunite	(K0.805 Na0.132 (H2	0.785	ICDD (PDF-2/Release	01-075-9141
Kaolinite	Al4 (O H)8 (Si4	1.231	ICDD (PDF-2/Release	01-078-2110
Gypsum, syn	Ca S O4 ･2 H2 O	0.858	ICDD (PDF-2/Release	00-033-0311
Rutile, syn	Ti O2	0.646	ICDD (PDF-2/Release	01-071-6411
Pyrite	Fe S2	0.769	ICDD (PDF-2/Release	00-042-1340
Magnetite, titanian	Fe (Fe1.04 Ti0.67)	0.876	ICDD (PDF-2/Release	01-071-6448

結晶相データパターン

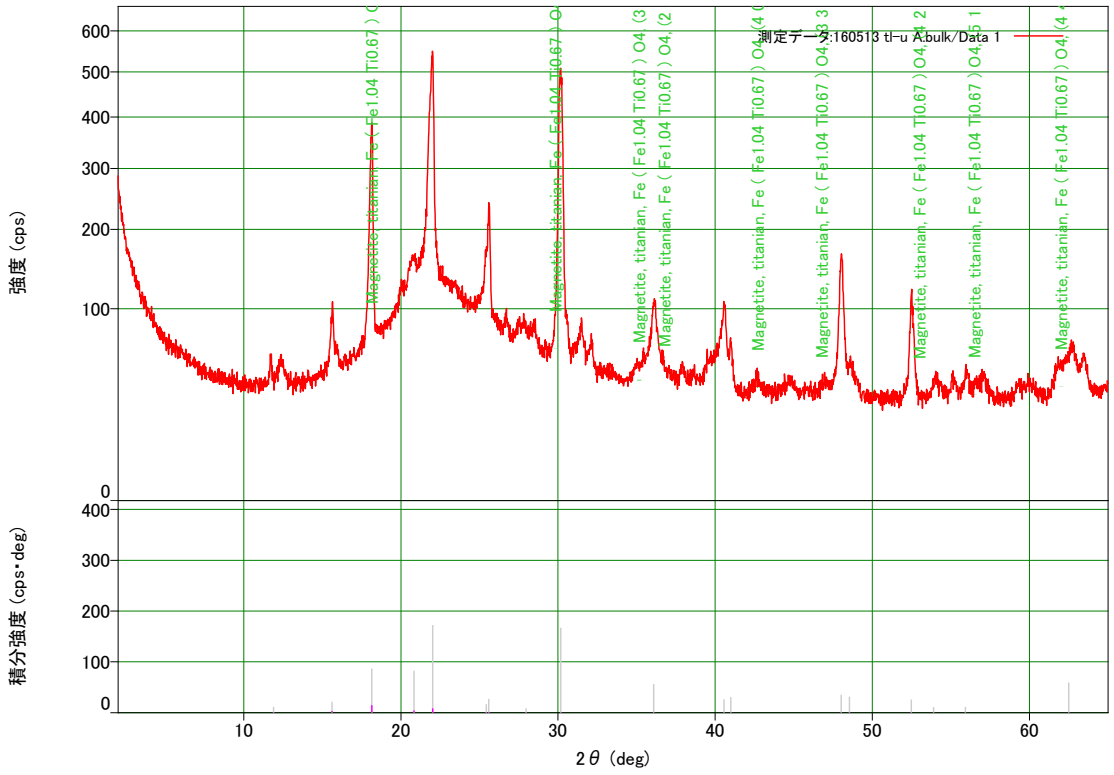

定性分析結果

基本情報

解析日	2016/05/18 21:55:05		
試料名	1926 TL unitB	測定日	2016/05/13 19:53:33
ファイル名	160513 tl-u B.bulk.raw	測定者	User1
コメント	Ouchi slow sp		

同定された結晶相

結晶相名	化学式	FOM	相の登録手法	DB カード番号
Natroalunite	Na Al3 (S O4)2 (O	0.707	ICDD (PDF-2/Release	00-014-0130
Cristobalite	Si O2	0.602	ICDD (PDF-2/Release	01-075-0923
gypsum low, calcium	Ca (S O4) (H2 O)2	0.992	ICDD (PDF-2/Release	01-070-7009
Anhydrite	Ca (S O4)	1.733	ICDD (PDF-2/Release	01-080-6363
Alunite	(K0.805 Na0.132 (H2	1.735	ICDD (PDF-2/Release	01-075-9141
Albite, ordered	Na Al Si3 O8	1.461	ICDD (PDF-2/Release	00-009-0466

結晶相データパターン

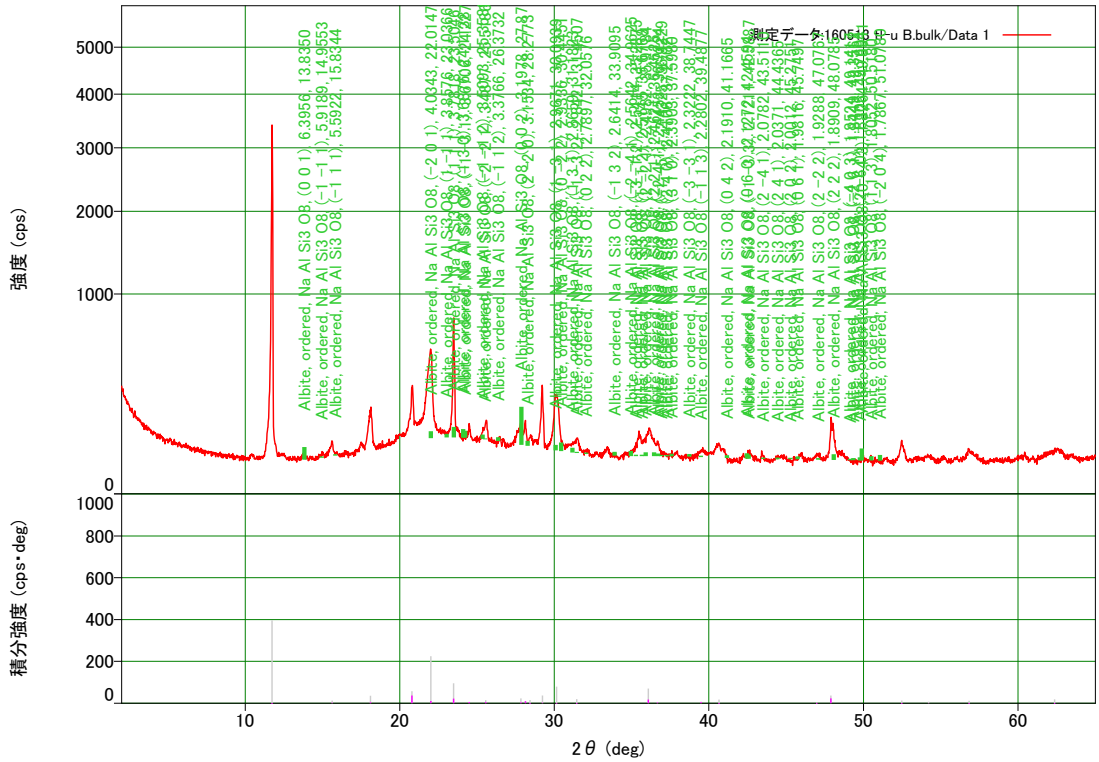

定性分析結果

基本情報

解析日	2016/05/18 22:07:04		
試料名	1926 TL unitC	測定日	2016/05/14 00:05:54
ファイル名	160513 tl-u C unori bulk.raw	測定者	User1
コメント	Ouchi slow sp		

同定された結晶相

結晶相名	化学式	FOM	相の登録手法	DB カード番号
Alunite	(K0.805 Na0.132 (H2	0.463	ICDD (PDF-2/Release	01-075-9141
Jarosite, sodian, syn	(K0.52 Na0.46) Fe3	0.575	ICDD (PDF-2/Release	01-076-7598
Cristobalite low, syn	Si O2	0.650	ICDD (PDF-2/Release	01-077-1317
Gypsum, syn	Ca (S O4) (H2 O)2	0.799	ICDD (PDF-2/Release	01-071-2701
Tridymite, syn	Si O2	1.630	ICDD (PDF-2/Release	01-074-8988
Anorthite	Ca (Al2 Si2 O8)	1.632	ICDD (PDF-2/Release	01-075-1587
Kaolinite 1A	Al2 Si2 O5 (O H)4	1.396	ICDD (PDF-2/Release	01-075-1593
Natroalunite	Na0.58 K0.42 Al3 (S	0.487	ICDD (PDF-2/Release	01-075-1685
Albite, syn	Na (Al Si3 O8)	0.654	ICDD (PDF-2/Release	01-071-1150
Anhydrite	Ca (S O4)	1.316	ICDD (PDF-2/Release	01-080-6360
Augite	(Mg0.9 Fe0.06 Al0.02	0.694	ICDD (PDF-2/Release	01-073-8529
Enstatite, ferroan	(Ca.069 Mg1.490	0.860	ICDD (PDF-2/Release	01-071-0720

結晶相データパターン

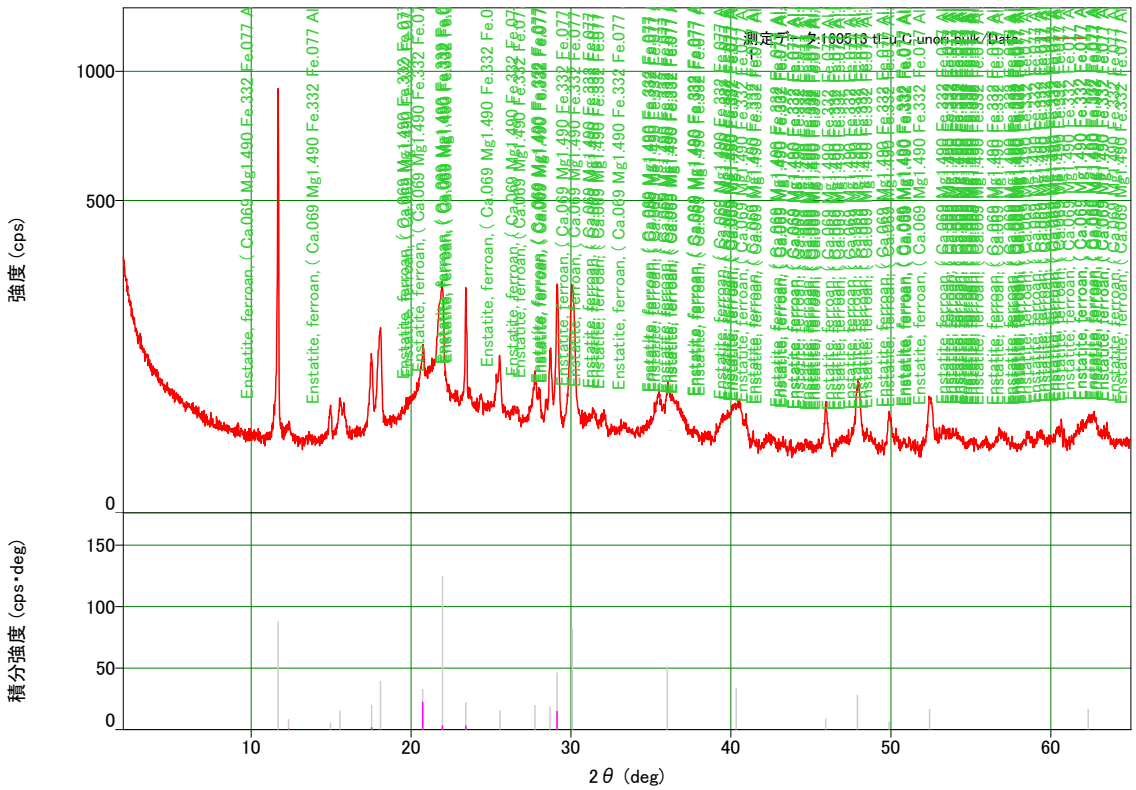

Appendix 3-2: XRD results in Chapter 1 (Coase fraction sieved into 250μm-1mm)

定性分析結果

基本情報

解析日	2016/05/18 22:54:04		
試料名	Gf-0 1-250 unori (Gfl-0 のサンプル)	測定日	2016/05/16 04:22:06
ファイル名	0160515 Gf-0 1-250 unori.raw	測定者	User1
コメント	Ouchi slow		

同定された結晶相

結晶相名	化学式	FOM	相の登録手法	DB カード番号
Cristobalite low	Si O2	0.657	ICDD (PDF-2/Release	01-076-0936
Alunite, sodian	(K0.72 Na0.28) Al3	1.050	ICDD (PDF-2/Release	01-077-8327
Quartz, syn	Si O2	1.284	ICDD (PDF-2/Release	00-046-1045
Rutile, syn	Ti O2	1.149	ICDD (PDF-2/Release	01-073-2224
INTERMEDIATE	NA AL SI3 O8	0.905	JICST	2595
Magnetite, titanian,	Fe ((Fe1.904	2.739	ICDD (PDF-2/Release	01-077-8398
Albite (heat-treated)	Na (Al Si3 O8)	1.045	ICDD (PDF-2/Release	01-089-6425
Kaolinite	Al2 O3 ・2 Si O2 ・2	1.884	ICDD (PDF-2/Release	00-003-0052
cristobalite-α high	Si O2	2.641	ICDD (PDF-2/Release	01-071-6245
Plagioclase	Ca0.63 Na0.37	1.789	ICDD (PDF-2/Release	01-083-1367
Tridymite M low	Si O2	0.711	ICDD (PDF-2/Release	01-076-0894
Anatase, syn	Ti O2	2.615	ICDD (PDF-2/Release	01-070-7348

結晶相データパターン

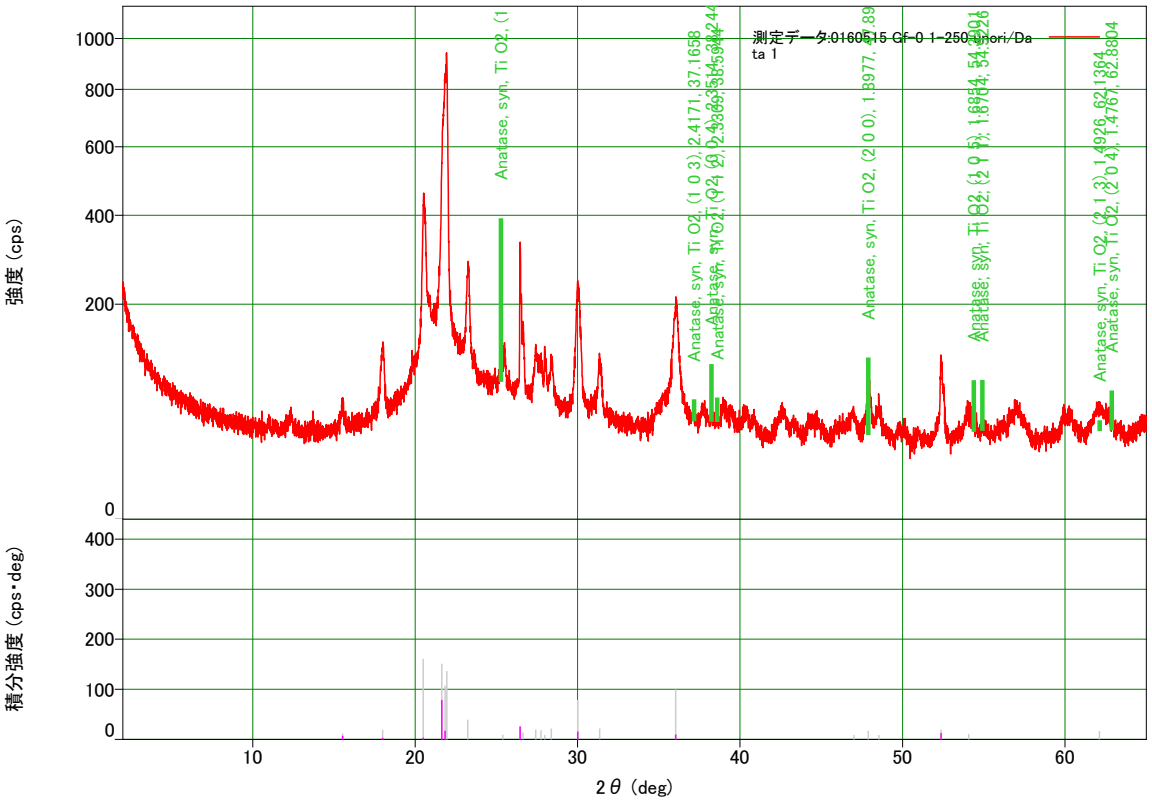

定性分析結果

基本情報

解析日	2016/05/18 17:57:39		
試料名	Gf-1 1-250 unori (Gfl-1 のサンプル)	測定日	2016/05/16 00:09:21
ファイル名	0160515 Gf-1 1-250 unori.raw	測定者	User1
コメント	Ouchi slow		

同定された結晶相

結晶相名	化学式	FOM	相の登録手法	DB カード番号
Plagioclase	Ca0.65 Na0.32	0.861	ICDD (PDF-2/Release	01-083-1368
Chlorite	(Mg , Fe)5 (Al , Si)5	3.103	ICDD (PDF-2/Release	00-002-0028
Kaolinite	Al4 (O H)8 (Si4	2.121	ICDD (PDF-2/Release	01-078-2110
Natroalunite	Na0.58 K0.42 Al3 (S	2.659	ICDD (PDF-2/Release	01-075-1685
Cristobalite, syn	Si O2	2.745	ICDD (PDF-2/Release	00-039-1425
Pyrophyllite	Al (Si2 O5) (O H)	1.889	ICDD (PDF-2/Release	01-083-1805
Alunite	(K0.805 Na0.132 (H2	3.235	ICDD (PDF-2/Release	01-075-9141
Quartz, low	Si O2	3.004	ICDD (PDF-2/Release	00-005-0490
Biotite-2M1	(K1.891 Na0.062)	3.111	ICDD (PDF-2/Release	01-076-6571
phlogopite	K Mg2.75 Si3.5 Al0.5	1.820	ICDD (PDF-2/Release	01-071-1885
Augite	(Mg0.9 Fe0.06 Al0.02	2.783	ICDD (PDF-2/Release	01-073-8529
Enstatite, syn	Mg (Ca0.031	3.141	ICDD (PDF-2/Release	01-072-7790

Olivine ある

結晶相データパターン

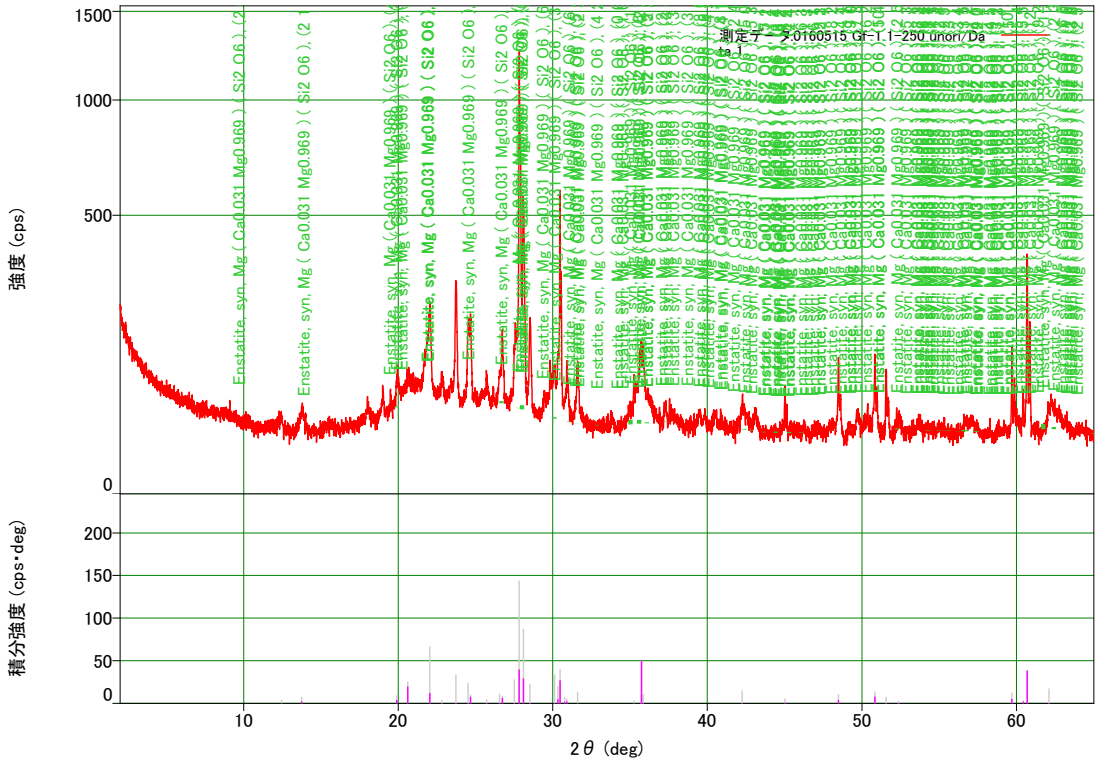

定性分析結果

基本情報

解析日	2016/05/18 19:03:29		
試料名	Gf-2 1-250 unori upper (Gfl-2 のサンプル)	測定日	2016/05/16 12:46:43
ファイル名	0160515 Gf-2 1-250 unori.raw	測定者	User1
コメント	Ouchi slow		

同定された結晶相

結晶相名	化学式	FOM	相の登録手法	DB カード番号
Anorthite, sodian,	(Ca , Na) (Si , Al)4	0.996	ICDD (PDF-2/Release	00-041-1481
Zirconolite-2M	Ca Zr Ti2 O7	1.627	ICDD (PDF-2/Release	00-034-0167
Albite, calcian,	(Na , Ca) Al (Si , Al)3	1.685	ICDD (PDF-2/Release	00-041-1480
Alunite	(K0.805 Na0.132 (H2	2.775	ICDD (PDF-2/Release	01-075-9141
Natroalunite	Na0.58 K0.42 Al3 (S	3.021	ICDD (PDF-2/Release	01-075-1685
Augite	(Mg0.86 Fe.1 Al0.03	2.837	ICDD (PDF-2/Release	01-073-8528
Enstatite, ferroan	(Mg , Fe) Si O3	3.378	ICDD (PDF-2/Release	00-019-0605
Quartz	Si O2	2.691	ICDD (PDF-2/Release	01-070-8054
Olivine, syn	Mg Fe (Si O4)	3.145	ICDD (PDF-2/Release	01-070-6488
Cristobalite	Si O2	3.172	ICDD (PDF-2/Release	00-002-0286
Tridymite	Si O2	2.862	ICDD (PDF-2/Release	01-071-0261
Sanidine, potassian,	(Na , K) (Si3 Al) O8	2.655	ICDD (PDF-2/Release	00-010-0357
iron diiron(III) oxide,	Fe3 O4	2.692	ICDD (PDF-2/Release	01-071-6339
Ilmenite, syn	Fe Ti O3	2.224	ICDD (PDF-2/Release	01-070-6274
Biotite-1M	(K0.95 Na0.03)	1.777	ICDD (PDF-2/Release	01-076-8344

結晶相ピークパターン

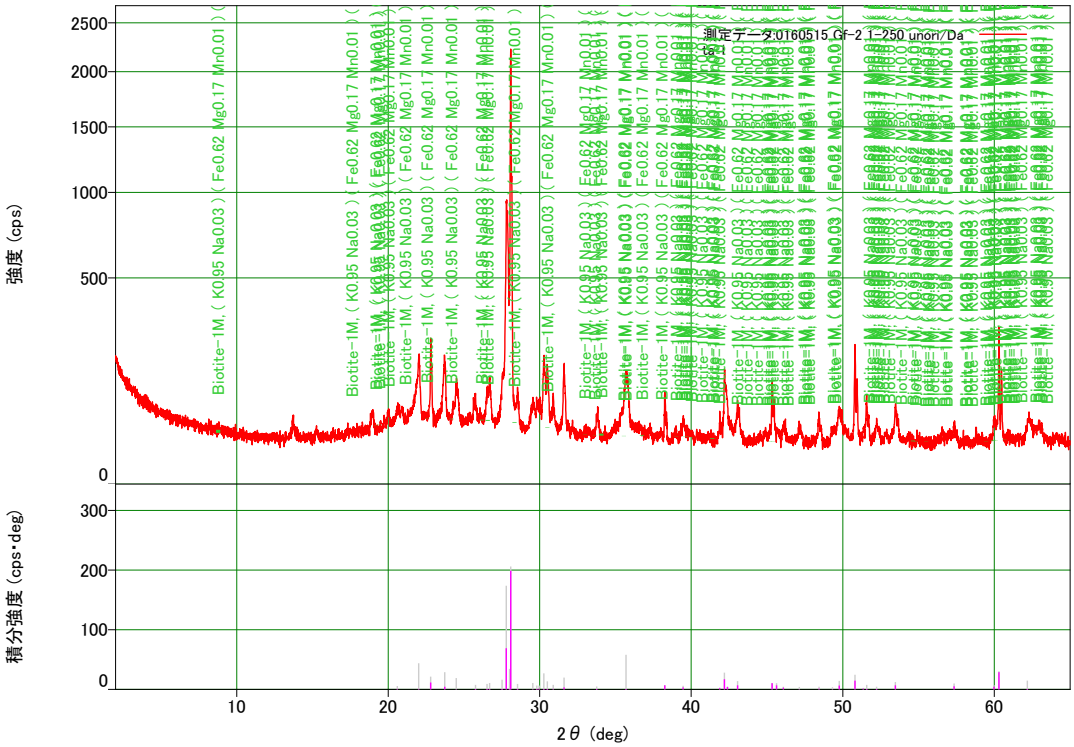

定性分析結果

基本情報

解析日	2016/05/18 19:06:31		
試料名	Gf tran 1-250 unori (Gfl-2 lower のサンプル)	測定日	2016/05/16 08:34:25
ファイル名	0160515 Gf transfer 1-250 unori.raw	測定者	User1
コメント	Ouchi slow		

同定された結晶相

結晶相名	化学式	FOM	相の登録手法	DB カード番号
Albite, syn	Na (Al Si3 O8)	1.268	ICDD (PDF-2/Release	01-071-1150
Augite	(Mg0.81 Fe0.16	1.104	ICDD (PDF-2/Release	01-073-8552
tridymite	Si O2	1.598	ICDD (PDF-2/Release	05-001-0058
Cristobalite, low	Si O2	1.426	ICDD (PDF-2/Release	01-071-3839
Anorthite	Ca (Al2 Si2 O8)	1.657	ICDD (PDF-2/Release	01-076-0948
Orthopyroxene	(Mg0.919 Fe0.071)	1.477	ICDD (PDF-2/Release	01-076-3322
Quartz, syn	Si O2	2.896	ICDD (PDF-2/Release	00-046-1045
Forsterite, ferroan	Mg1.784 Fe0.216 Si	3.296	ICDD (PDF-2/Release	01-083-1481
Natroalunite	Na0.58 K0.42 Al3 (S	2.878	ICDD (PDF-2/Release	01-075-1685
Alunite	(K0.805 Na0.132 (H2	2.932	ICDD (PDF-2/Release	01-075-9141
Plagioclase	Ca0.65 Na0.32	1.454	ICDD (PDF-2/Release	01-083-1368
Magnetite, titanian	Fe (Fe1.24 Ti0.61)	2.730	ICDD (PDF-2/Release	01-071-6447
Fayalite (Olivine)	(Fe0.94 Mg0.06)2 Si	3.354	ICDD (PDF-2/Release	00-007-0164
Ilmenite (Mg,Si-	Mg (Si O3)	3.348	ICDD (PDF-2/Release	01-082-1644
Fluor-phlogopite, 1M	K Mg3 (Si3 Al O10)	1.391	ICDD (PDF-2/Release	00-010-0494
Kaolinite	Al4 (O H)8 (Si4	3.113	ICDD (PDF-2/Release	01-078-2110
Sanidine, syn	K (Si1.2 Fe0.5 Al0.3)	3.006	ICDD (PDF-2/Release	01-072-3540

結晶相データパターン

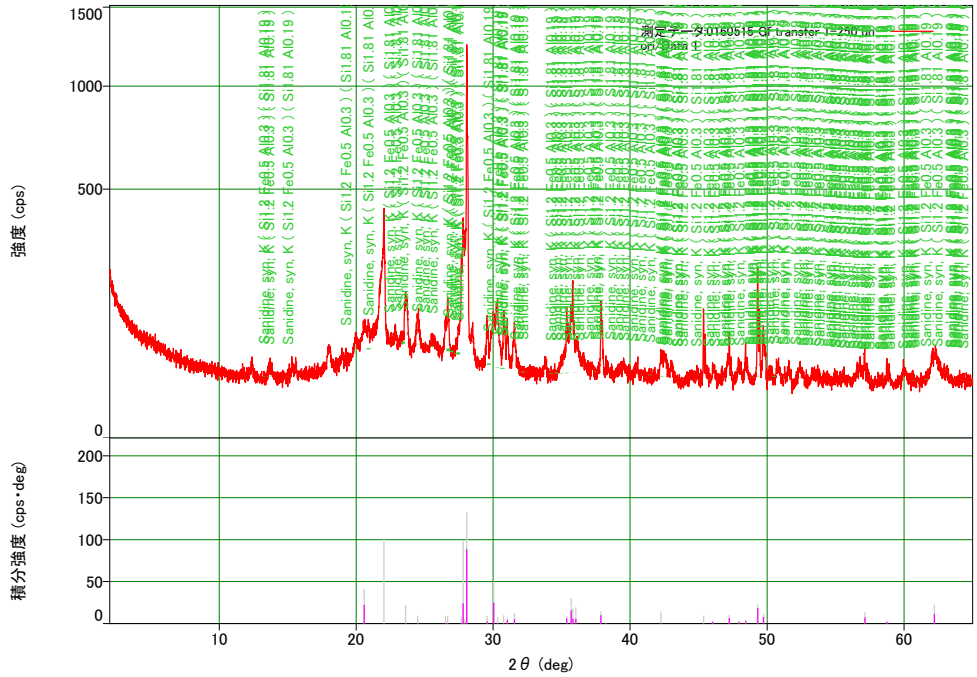

定性分析結果

基本情報

解析日	2016/05/18 19:32:49		
試料名	0160515 TL-A coarse	測定日	2016/05/15 10:15:17
ファイル名	0160515 TL-A 1-250 unori.raw	測定者	User1
コメント	Ouchi slow		

同定された結晶相

結晶相名	化学式	FOM	相の登録手法	DB カード番号
Cristobalite, syn	Si O2	0.860	ICDD (PDF-2/Release	00-011-0695
Alunite, syn	K Al3 (S O4)2 (O	0.700	ICDD (PDF-2/Release	00-047-1885
Albite, calcian	(Na0.84 Ca0.16)	0.700	ICDD (PDF-2/Release	01-076-0927
Natroalunite	Na0.58 K0.42 Al3 (S	1.393	ICDD (PDF-2/Release	01-075-1685
Rutile, syn	Ti O2	1.848	ICDD (PDF-2/Release	01-076-0317
Pyrite, syn	Fe S2	1.990	ICDD (PDF-2/Release	01-075-6907
Magnetite, titanian	Fe (Fe1.24 Ti0.61)	1.049	ICDD (PDF-2/Release	01-071-6447
Augite	Ca (Mg , Fe) Si2 O6	1.757	ICDD (PDF-2/Release	00-024-0203
Enstatite, ferroan	(Mg0.92 Fe0.02	1.259	ICDD (PDF-2/Release	01-073-9812

結晶相データパターン

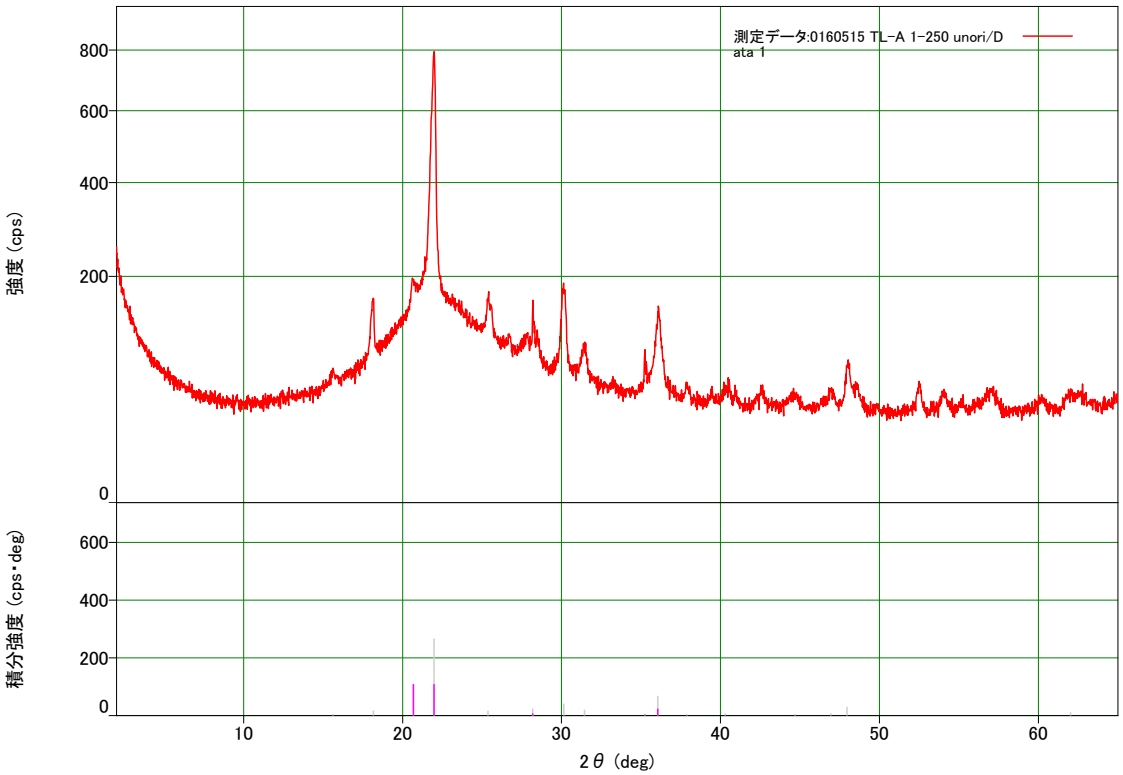

定性分析結果

基本情報

解析日	2016/05/18 19:48:40		
試料名	0160515 TL-B coarse	測定日	2016/05/15 14:27:39
ファイル名	0160515 TL-B 1-250 unori.raw	測定者	User1
コメント	Ouchi slow		

同定された結晶相

結晶相名	化学式	FOM	相の登録手法	DB カード番号
Cristobalite, syn	Si O2	0.704	ICDD (PDF-2/Release	00-011-0695
Natroalunite	Na Al3 (S O4)2 (O	0.863	ICDD (PDF-2/Release	00-014-0130
Anorthite, ordered	Ca Al2 Si2 O8	1.097	ICDD (PDF-2/Release	00-041-1486
Albite, syn	Na (Al Si3 O8)	1.439	ICDD (PDF-2/Release	01-071-1150
Magnetite, titanian,	Fe ((Fe1.902	1.566	ICDD (PDF-2/Release	01-077-8399
Pyrite	Fe S2	3.098	ICDD (PDF-2/Release	01-071-0053
Anhydrite	Ca (S O4)	1.326	ICDD (PDF-2/Release	01-086-2270
Anatase, syn	Ti O2	3.157	ICDD (PDF-2/Release	01-070-7348
Kaolinite	Al4 (O H)8 (Si4	2.963	ICDD (PDF-2/Release	01-078-2110
Chlorite	Mg2 Al3 (Si3 Al) O10	1.992	ICDD (PDF-2/Release	00-013-0003

結晶相データパターン

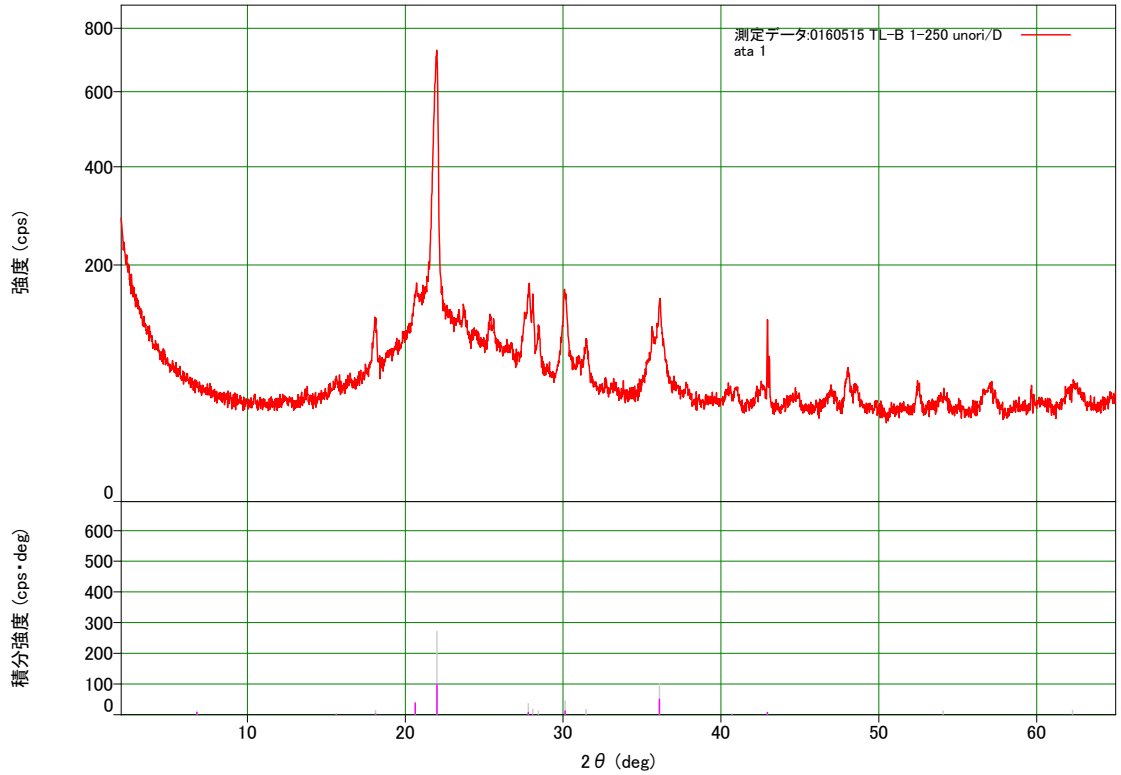

定性分析結果

基本情報

解析日	2016/05/18 22:11:41		
試料名	0160515 TL-C coarse	測定日	2016/05/15 18:39:59
ファイル名	0160515 TL-C 1-250 unori.raw	測定者	User1
コメント	Ouchi slow		

同定された結晶相

結晶相名	化学式	FOM	相の登録手法	DB カード番号
Diopside, potassian,	(Ca0.88 K0.12)	1.288	ICDD (PDF-2/Release	01-075-8702
Alunite, sodian	(K0.72 Na0.28) Al3	1.038	ICDD (PDF-2/Release	01-077-8327
Anorthite	Ca (Al2 Si2 O8)	0.874	ICDD (PDF-2/Release	01-070-0287
Cristobalite, syn	Si O2	1.522	ICDD (PDF-2/Release	01-074-9378
Opal-A	Si O2 ・x H2 O	1.467	ICDD (PDF-2/Release	00-038-0448
Kaolinite	Al4 (O H)8 (Si4	1.717	ICDD (PDF-2/Release	01-078-2110
Natroalunite	Na0.58 K0.42 Al3 (S	2.608	ICDD (PDF-2/Release	01-075-1685
Albite, syn	Na (Al Si3 O8)	0.703	ICDD (PDF-2/Release	01-071-1150
Tridymite, syn	Si O2	0.898	ICDD (PDF-2/Release	01-074-8988

結晶相データパターン

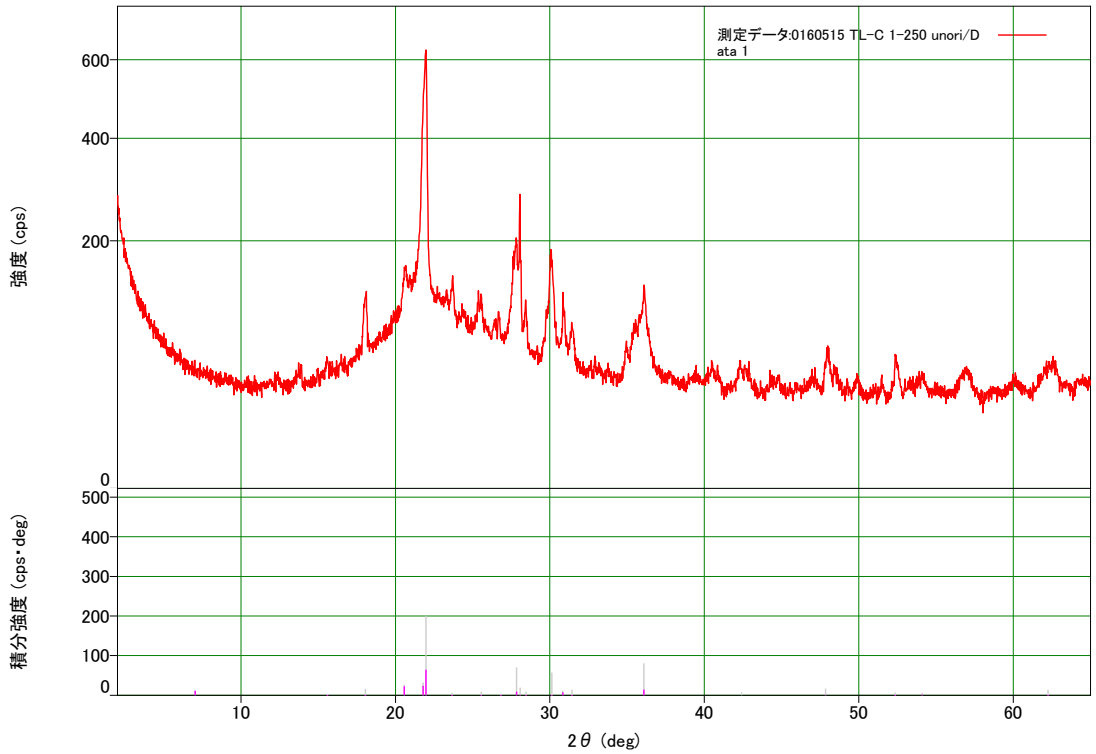

Appendix 4: List of described ash grains in Chapter 1

Abbreviations

Mineral name. Sil (Silica mineral): quartz, cristobalite, and tridymite, Sa: sanidine to anorthoclase, Pl: plagioclase, Aug: augite, Hd: hedenbergite, Pig: pigeonite, Sph: sphene, Opx: orthopyroxene, Ol: olivine, Mag: Magnetite, Ti Mag: titanomagnetite, Mca: mica mineral, Ilm: ilmenite, Rt: rutile or anatase, Chl: chlorite, Kl: kaolin group mineral, Alu: alunite, Anh: anhydrite, Jar: Jarosite, and Py: pyrite, Bar: barite.

Ash type. Silica: silica type (sil), Alunite: alunite type (sil+alu±kl), Kaolin mineral type (sil+kl), Volcanic: unaltered lava, pumice and scoria, and Holocrystalline: holocrystalline-equigranular rock.

Alteration degree. I: intensely altered, W: weakly altered, and Unaltered: not altered and fresh rock.

No.	Code	Colur	Texture	Mineral assemblage	Alteration	Ash type
1	Gfl0-001	Pale gray	Dissolution tex.	Sil-Rt-Py	I	Silica
2	Gfl0-002	Red. browm	Very fine grained and Collofrom tex	Sil-Alu-Kl-Rt-Mag	I	Alunite
3	Gfl0-003	Pale-Yellow. gray	Dissolution tex. Partly fine grained.	Sil-Alu-Kl-Rt-(Sa?)	W	Alunite
4	Gfl0-004	White	Infill tex	Sil-Alu	I	Alunite
5	Gfl0-005	Yellow. white	Psuedomorph tex, of volcanic rock	Sil-Alu-Kl-Rut	I	Alunite
6	Gfl0-006	Pale-Yellow. brown	Dissolution tex.	Sil-Ant-(Py)	I	Silica
7	Gfl0-007	Pale gray	Partlly remained porphyritic tex.	Sil-Alu-Py-Aug?	W	Alunite
8	Gfl0-008	Gray	Dissolution tex. Partly fine grained.	Sil-Pl?-Px?	W	Silica
9	Gfl0-009	Dark gray	Augite crystal fragment	Aug, Ti Mag-v.glass	Unaltered	volcanic
10	Gfl0-010	Pale gray	Partlly remained porphyritic tex.	Sil-Alu-Py-Mag-Pl-Sa?-Px	W	Alunite
11	Gfl0-011	Dark gray	Polas and glassy, partially altered.	Sil-Alu-Kl-v.glass	W	Alunite
12	Gfl0-012	Pale-Yellow. white	Dissolution tex.	Sil-Alu-Py-Rt-Mag-Sa?	W	Alunite
13	Gfl0-013	Gray	Dissolution tex.	Sil-Alu-Kl	I	Alunite
14	Gfl0-014	White	Dissolution tex.	Sil-Rt-Py	I	Silica
15	Gfl0-015	Brown	Very fine grained.	Sa?-Alu-Mag	I	Alunite?
16	Gfl0-016	White	Dissolution tex.	Sil-Alu-Kl-Rt-Pl-Bar	W	Alunite
17	Gfl0-017	Dark gray	Augite crystal fragment	Aug, Sil-Opx-Ti Mag-v.glass	W	Silica
18	Gfl0-018	Red. browm	Scoria, porphyritic tex. (hyaloohitic)	Pl-Aug-Opx-Mag-Ap	Unaltered	volcanic
19	Gfl0-019	Pale-Yellow. brown	Altered Pl fragment? Psuedomorph tex.	Sil-Alu-Kl-Pl-v. glass	W	Alunite
20	Gfl0-020	Dark gray	Equiglanular tex? Not comon	Sil-Alu-Kl?-Rt-Sa?	W	Alunite
21	Gfl1-001	White	Partlly remained equigranular tex.	Sil-Alu-Kl-Sa-Mag	W	Alunite
22	Gfl1-002	Pale-Yellow. white	Dissolution tex.	Sil-Rt	I	Silica
23	Gfl1-003	Yellow. white	Porphyritic tex and hyaloohitic tex.	Ph, Pl-Mag-Ti Mag-Aug-Opx, Gr, v.glass	Unaltered	volcanic
24	Gfl1-004	Dark gray	Crystal fragment (Px and Ti-Mag). Part of porphyritic tex?	Opx-Ti Mag-v.glass	Unaltered	volcanic
25	Gfl1-005	Transparent	Crystal fragment (Px). Part of porphyritic tex?	Opx-v.glass	Unaltered	volcanic
26	Gfl1-006	Dark gray	Crystal fragment (Pl). Part of porphyritic tex?	Pl-Ap-Ti Mag-v. glass	Unaltered	volcanic
27	Gfl1-007	Brown	Partlly remained porphyritic tex.	Sil-Kl-Pl-Opx-Ol-Mag-Ti-Mag	W	Kaolin
28	Gfl1-008	Yellow	Dissolution tex.	Sil-Rt	I	Silica
29	Gfl1-009	Brown	Partlly remained equigranular tex.	Sil-Pl-Sa-Il-Chl(very fine)	W	Silica?
30	Gfl1-010	Pale-Pink. white	Remained porphyritic tex. Partlly psuedomorph tex. of porphyritic	Sil-Kl-Pl-Sa-Mag-Ti Mag	W	Kaolin
31	Gfl1-011	Gray. Green	Crystal fragment (Pl). Part of porphyritic tex?	Pl, Opx-Pig-Ti Mag-v.glass	Unaltered	volcanic
32	Gfl1-012	Black	Crystal fragment (Pl). Part of porphyritic tex?	Pl, Ti Mag-v.glass	Unaltered	volcanic
33	Gfl1-013	Red. browm	Remaind porphyritic tex, of volcanic rock, partlly with colloform tex.	Ph, Opx-Aug, Gr, pl-v. glass, Altered: Sil-Kl	W	Kaolin
34	Gfl1-014	Dark brown	Remained porphyritic tex. (Scoria). Partly infilled with sil, alu, and kl	Sil-Alu-Kl-Pl-Opx-Ti Mag-v.glass	W	Alunite
35	Gfl1-015	White-translucent	Dissolution tex.	Sil-Alu-Kl?-Rt-Mag	I	Alunite
36	Gfl1-016	Gray-translucent	Partlly remained equigranular tex. with colloform tex.	Sil-Kl-Pl-Sa-Rt-Il-Mca	W	Kaolin
37	Gfl1-017	Dark gray	Crystal fragment (Px and Ti-Mag). Part of porphyritic tex?	Opx-Ti Mag-Ap-Py-v.glass	Unaltered	volcanic
38	Gfl1-018	White	Dissolution tex.	Sil-Alu-Rt	I	Alunite
39	Gfl1-019	Dark brown	Porphyritic tex.	Aug-Ti Mag-Opx-Pl-v.glass	Unaltered	volcanic
40	Gfl1-020	Yellow.brown-translucent	Dissolution tex. Vary fine grained	Sil-Alu-Rt	I	Alunite
41	Gfl1-021	Red. white	Partlly remained porphyritic tex? with psuedomorph tex	Sil-Alu-Kl-Rt-Mag-Sa-Pl	W	Alunite
42	Gfl1-022	White	Very fine grained	Sil-Kl-Mag?	I	Kaolin
43	Gfl1-023	Black	Aug phenocryst with scoria part (totally porphyritic tex)	Aug, pl-v. glass-(Si-Alu)	W	Alunite
44	Gfl1-024	White. gray	Very fine grained	Sil-Alu-Kl-Rt	I	Alunite
45	Gfl1-025	Pale. pink-gray	Remained equigranular tex.	Sil-Alu-Kl-Pl-Sa?	W	Alunite
46	Gfl1-026	Orange. white	Remained equigranular tex.	Sil-Alu-Kl-Pl-Sa?-Il	W	Alunite
47	Gfl1-027	Dark gray	Remained porphyritic tex. (Scoria). Partly infilled with sil, alu, and kl	Sil-Alu-Kl-Pl-Opx-Aug-Ti Mag-v.glass	W	Alunite
48	Gfl1-028	Pale-Yellow. white	Remained equigranular tex.??	Sil-Kl-Sa-Il	W	Kaolin
49	Gfl1-029	Dark gray	Crystal fragment (Pl). Part of porphyritic tex?	Pl-v.glass	Unaltered	volcanic
50	Gfl1-030	Yellow. white	Dissolution tex.	Sil-Alu-Rt	I	Alunite
51	Gfl1-031	Dark gray	Porphyritic tex. Poorly vesicular	Pl-Pig-Il or Ti Mag-v. glass	Unaltered	volcanic
52	Gfl1-032	Dark gray	Remained porphyritic tex. (Scoria). Partly infilled with sil, alu, and kl	Sil-Alu-Kl-Pl-Aug-Opx-Ti Mag-v.glass	W	Alunite
53	Gfl1-033	Dark gray	Crystal fragment (Px). Part of porphyritic tex?	Opx-v.glass	Unaltered	volcanic
54	Gfl1-034	Red. browm	Crystal fragment (Mag). Part of porphyritic tex?	Ti Mag-Ap-v.glass	Unaltered	volcanic
55	Gfl1-035	Black	Remained porphyritic tex. (Scoria). Partly infilled with sil, alu and kl	Pl-Aug-Ol-Mag-v. glass-(Sil-Alu-Kl)	W	Alunite
56	Gfl1-036	Black	Remained porphyritic tex. (Scoria). Partly infilled with sil and kl	Pl-Aug-Ol-Mag-v. glass-(Sil-Kl)	W	Kaolin
57	Gfl1-037	Pale-yellow	Partlly remained equigranular tex.	Sil-Alu-Kl-Pl-Sa-Il-Mca	W	Alunite
58	Gfl1-038	White	Psuedomorph tex. of volcanic rock.	Sil-Alu?-Kl-Mag	I	Alunite?
59	Gfl1-039	Black	Crystal fragment (Px). Part of porphyritic tex?	Aug, pl-Ti Mag-Ap-v.glass	Unaltered	volcanic
60	Gfl1-040	White	Dissolution tex. Vary fine grained	Sil-Alu-Kl-Py	I	Alunite
61	Gfl1-041	Yellow. brown	Dissolution tex. Vary fine grained. Partly psudomorph tex of volcanic rock.	Sil-Alu-Kl-Mag	I	Alunite
62	Gfl1-042	Gray	Partly remained equigranular tex.	Sil-Kl-Pl-Sa-	I	Kaolin
66	Gfl2 lower-001	Pale-Yellow. white	Partlly remained porphyritic tex. Partlly dissolution tex.	Sil-alu-v. glass (altered?)	W	Alunite
67	Gfl2 lower-002	Yellow. brown	Dissolution tex. Partly remained holocrystaline-equigranular tex.	Silica-Pl-Sa-Kl	W	Kaolin
68	Gfl2 lower-003	Dark gray	Partlly remained porphyritic tex.	Sil-Rt-Py-v.glass	W	Silica
69	Gfl2 lower-004	Red. browm	Pl fragment	Pl, Sil-Alu-Aug-Il	W	Alunite
70	Gfl2 lower-005	White	Partlly remained porphyritic tex. Mostly dissolution tex.	Sil-Sa?-Il-Py-Amp	W	Silica
71	Gfl2 lower-006	Gray	Porphyritic tex. (rock fragment)	Sil-Alu-Kl-Aug-Il-v. glass	W	Alunite
72	Gfl2 lower-007	Dark gray	Porphyritic tex. (rock fragment)	Opx-glass	Unaltered	Volcanic
73	Gfl2 lower-008	Gray	Porphyritic tex. and Interthertal tex. Pore is infilled with altered part.	Sil-Alu-Pl-Aug-Amp-Opx-Ol-v. glass	W	Alunite
74	Gfl2 lower-009	Pink. white	Dissolution tex.	Sil-Alu-Mag-Py	I	Alunite
75	Gfl2 lower-010	Pale gray	Dissolution tex.	Sil-Rt-Py	I	Silica
76	Gfl2 lower-011	White	Dissolution tex. Comb tex?	Sil-Rt-Py	I	Silica
77	Gfl2 lower-012	Yellow. gray	Porphyritic tex. and polas. Pore is infilled with altered part.	Sil-Alu-Kl-Pl-Ap-v. glass	W	Alunite
78	Gfl2 lower-013	White	Coarse alu and sil-kl network	Sil-Alu-Kl	I	Alunite
79	Gfl2 lower-014	Gray	Aug fragment.	Aug-Ap	Unaltered	volcanic
80	Gfl2 lower-015	Dark gray	Porphyritic tex. , polas, and glassy. (scoria). Hyaloohitic tex.	Pl-Opx-Il-Ap-v. glass	Unaltered	volcanic
81	Gfl2 lower-016	Pink. white	Porphyritic tex. , well crystalline. Intergranular tex?	Sil-Kl-Pl-Sa	W	Kaoin
82	Gfl2 lower-017	White	Psuedomorph tex, of volcanic rock	Sil-Alu-Kl	I	Alunite
83	Gfl2 lower-018	Gray	Holocrystalline, and equigranular tex.	Sil-Sa-Pl	Unaltered	Holocrystalline
84	Gfl2 lower-019	White	Partlly remained holocrystalline, and equigranular tex.	Sil-Kal-Sa-Pl	W	Kaolin
85	Gfl2 upper-001	Dark gray	Porphyritic tex. , polas, and glassy. (scoria). Hyaloohitic tex.	Ph: Ol, Gr: Aug-Ol	Unaltered	volcanic
86	Gfl2 upper-002	Dark gray	Porphyritic tex. , polas, and glassy. (scoria). Hyaloohitic tex.	Ph: Ol, Gr: Aug-Ol	Unaltered	volcanic
87	Gfl2 upper-003	Gray	Pl fragment. Zorning, core: Ab rich, rim: An rich	Pl, Opx-Mag-Il	Unaltered	volcanic
88	Gfl2 upper-004	White. gray	Fine grained and Polas.	Sil-Alu-Kl-Mag	I	Alunite
89	Gfl2 upper-005	Transparent	Pl fragment. Zorning, V. glass surrounded.	Pl, Aug-Ap-Py	Unaltered	volcanic
90	Gfl2 upper-006	White	Very fine grained.	Si-Al Si mineral-altered glass?	W	Silica
91	Gfl2 upper-007	Black	Opx fragment. V. glass surrounded.	Opx, Mag-Apa-v. glass	Unaltered	volcanic
92	Gfl2 upper-008	White. gray	Remained porphyritic tex. Partlly dissolution tex.	Sil-Alu?-Sa to Ano-Il-Mag-Py	W	Alunite
93	Gfl2 upper-009	Pale-Yellow. white	Holocrystalline, and equigranular tex.	Si-Sa to Ano-Al Si mineral-Il	W	Silica
94	Gfl2 upper-010	Yellow. white	Fine grained and partlly massive silica (dissolution tex.)	Sil-Kl-Il	I?	Kaoin
95	Gfl2 upper-011	White. gray	Porphyritic tex. , poorly polas, hyaloohitic tex.	Ph: Aug-Pl-Mag-Ol (inclusion), Gr: Pl-Opx- v. glass-Sa	Unaltered	volcanic
96	Gfl2 upper-012	White. gray	Porphyritic tex. , poorly polas, hyaloohitic tex. Fine grained	Ph: Pl-Aug-Amb, Gr: v. glass	Unaltered	volcanic
97	Gfl2 upper-013	Gray	Remained porphyritic tex. Partlly psuedomorph tex. of hyalopilitic tex. (Pumic	Sil-Pl-Opx-Al-Si mineral-Pl-v. glass	Unaltered	Holocrystalline
98	Gfl2 upper-014	Gray	Holocrystalline, and equigranular tex.	Sil(Qz?)-Sa-Pl-Il	Unaltered	Holocrystalline
99	Gfl2 upper-015	Gray	Porphyritic tex. Well crystallized. (Dacitic to Rhyolitic)	Ph: Pl-Aug-Opx-Sa, Gr: Pl-Sil(Qz?)	Unaltered	volcanic
100	Gfl2 upper-016	Pale-red. brown	Holocrystalline, and equigranular tex.	Sil-Al Si mineral-Mag-Rt	W?	Silica?
101	Gfl2 upper-017	White. gray	Psuedomorph tex, of volcanic rock, foliation?	Sil-Alu-Rt-Mag-Al Si mineral	I	Alunite
102	Gfl2 upper-018	White. orange	Remained porphyritic tex. Partlly psuedomorph tex. of volcanic rock	Sil-Alu-v. glass (altered?)	W	Alunite
103	Gfl2 upper-019	Gray	Porphyritic tex, and Hyaloohitic tex.	Ph: Pig-Opx-Pl, Gr:v. glass	Unaltered	volcanic
104	Gfl2 upper-020	Gray	Porphyritic tex, and Hyaloohitic tex.	Ph: Ol, Gr: Opx-Amb-Aug. glass	Unaltered	volcanic
105	Gfl2 upper-021	N.d.	Remained porphyritic tex. Partlly psuedomorph tex. of hyalopilitic tex. (Pumic	Sil-Alu?-Rut-Pl?	W	Alunite
106	Gfl2 upper-022	Dark gray	Porphyritic tex. , polas, and glassy. (scoria). Hyaloohitic tex.	Ph: Aug, Gr: Opx-Pl-Il-Ti Mag-v. glass	Unaltered	volcanic
107	Gfl2 upper-023	Dark gray	Porphyritic tex. , polas, and glassy. (scoria). Hyaloohitic tex.	Ph: Opx-Ol, Gr: Pl-Mag-v. glass	Unaltered	volcanic
108	Gfl2 upper-024	Dark gray	Porphyritic tex. , polas, and glassy. (scoria). Hyaloohitic tex.	Ph: Opx-Pl, Gr: Opx-Pl-v. glass	Unaltered	volcanic

No.	Code	Colur	Texture	Mineral assemblage	Alteration	Ash type
109	Unit A-001	Pale gray	Psuedomorph tex, of volcanic rock	Sil-Alu-Rut	I	Alunite
110	Unit A-002	Gray	Partlly remained porphyritic tex.	Sil-Alu-Pl-Aug-v. glass	W	Alunite
111	Unit A-003	Dark gray	Dissolution tex. Partly fine grained.	Sil-Rt-Py-(Alu?)	I	Alunite
112	Unit A-004	White. orange	Psuedomorph tex, of volcanic rock	Sil-Alu-(altered glass?)-Bar	W	Alunite
113	Unit A-005	Gray	Very fine grained.	Sil-Alu-Kl	I	Alunite
114	Unit A-006	Pale gray	Partlly remained porphyritic tex.	Sil-Pl-Opx-Ti Mag-v. glass	W	Silica
115	Unit A-007	Gray	Dissolution tex. Partly fine grained.	Sil-Rt-Py	I	Silica
116	Unit A-008	Gray	Partlly remained porphyritic tex.	Sil-Rt-Py-v.glass?(altered?)	W	Silica
117	Unit A-009	Pale brown	Psuedomorph tex, of volcanic rock	Sil-Rt-Py	I	Silica
118	Unit A-010	Pale gray	Very fine grained.	(Sil)-Alu(dominant)	I	Alunite
119	Unit A-011	Pale-Yellow. gray	Psuedomorph tex, of volcanic rock with colloform tex.	Sil-Alu-Rut	I	Alunite
120	Unit A-012	Dark gray	Aug fragment (little aletered)	Aug, Opx-Mag-Sil-v.glass?	W	Silica
121	Unit A-013	Yellow	Aggregate of alu with Jar netwaork	Sil(little)-Alu-Jar	I	Alunite
122	Unit A-014	Dark gray	Partlly remained porphyritic tex.	Sil-Aug?-v. glass?	W	Silica
123	Unit A-015	White. brown	Psuedomorph tex, of volcanic rock	Sil-Alu-Ti Oxide?	W	Alunite
124	Unit A-016	White. orange	Partlly remained porphyritic tex.	Sil-Alu-Kl?-Rt-Pl-Aug-Ap	W	Alunite
125	Unit B-001	Pale-Yellow. white	Fine grained and Polas.	Sil-Cpx(Hd)-Mag	W?	Silica?
126	Unit B-002	Pale-Yellow. brown	Partlly remained porphyritic tex.	(Sil)-Pl-Aug-Mag-Il-v.glass	W	Silica
127	Unit B-003	White	Psuedomorph tex, of volcanic rock	Sil	I	Silica
128	Unit B-004	Red. browm	Fine grained and Polas.	Sil-Mag-Anh-Px?	W	Silica
129	Unit B-005	Yellow	Very fine grained.	Sil-Alu-Rut	I	Alunite
130	Unit B-006	Pale-Yellow. gray	Partlly remained porphyritic tex.	Sil-Alu-Px?-Rt-Mag-Il-v. glass	W	Alunite
131	Unit B-007	Red. browm	Fine grained and Polas.	Sil-Alu-Mag-Il	I?	Alunite
132	Unit B-008	Pale gray	Fine grained and Polas.	Sil-Alu- Pl	W	Alunite
133	Unit B-009	Gray	Fine grained and Polas.	Sil-Sa?-v. glass	W?	Silica
134	Unit B-010	Pale-green-yellow, gray	Psuedomorph tex, of volcanic rock	Sil-Alu-Rt	I	Alunite
135	Unit B-011	White	Dissolution tex.	Sil-Opx-Rt	I	Silica
136	Unit B-012	Pale gray	Dissolution tex. ? with colloform tex.	Sil-Pl-Mag-Sph	W?	Silica
137	Unit B-013	Pale gray	Partlly remained porphyritic tex.	(Sil)-Pl-Aug-Ti Mag-v.glass	W	Silica
138	Unit B-014	Pale-Yellow. brown	Opx fragment with volcanic rock groundmass	Opx, Pl-Aug-Il	Unaltered	volcanic
139	Unit B-015	Gray	Altered Pl fragment? Psuedomorph tex.	Sil-Pl-Al Si mineral?	W	Silica
140	Unit B-016	Pale-Yellow. gray	Polas.	Sil-Sph	W?	Silica?
141	Unit C-001	White	Partlly remained porphyritic tex.	Sil-Pl-Rt-v. glass (altered)	W	Silica
142	Unit C-002	White. orange	Dissolution tex. Partly fine grained.	Si-Alu-Mag-Ti Mag	I?	Alunite
143	Unit C-003	White. orange	Partlly remained porphyritic tex. Partly infill tex.	Sil-Alu-Mag	I?	Alunite
144	Unit C-004	Pale gray	Dissolution tex.	Sil-Rt-Py	I	Silica
145	Unit C-005	Dark gray	Partlly remained porphyritic tex.	Sil-Pl-Aug-Pig-Il?-v. glass	W	Silica
146	Unit C-006	Pale gray	Dissolution tex. and psuedomorph tex, of volcanic rock	Sil-Rt-Py-Zr oxide?	I	Silica
147	Unit C-007	White	Psuedomorph tex, of volcanic rock	Sil-Alu-Rt	I	Alunite
148	Unit C-008	Yellow. brown	Polas and porphyritic tex. (littele altered: infill tex.)	Sil-Alu-Pl-Aug-Pig-Il?-v. glass	W	Alunite
149	Unit C-009	Pale-Yellow. white	Dissolution tex. Partly fine grained.	Sil-Alu	I	Alunite
150	Unit C-010	White	Partlly remained porphyritic tex. Mostly dissolution tex.	Sil-Alu-Px?-Mag?	W	Alunite
151	Unit C-011	Dark gray	Polas and porphyritic tex. (littele altered: infill tex.)	(Sil-Alu)-Pl-Aug-Mag-v. glass	W	Alunite
152	Unit C-012	Pale brown	Dissolution tex.	Sil-Py	I	Silica
153	Unit C-013	Gray	Very fine grained.	Sil-Alu-Kl-Rt	I	Alunite
154	Unit C-014	Gray	Porphyritic tex. (rock fragment)	Sil-v. glass (altered?)	W	Silica

Appendix 5: Collected sample list in Chapter 3

No.	Sample code	Occurrence	Geological unit	Locality	
				Latitude (N)	Longitude (E)
1	AZM180803001_1	Thin vulcanian fall deposit	AZ-OA(Yamamoto 2005)	37°72′130″	140°24′954″
2	AZM180803001_2	Lahar deposit (phreatic?)	AZ-OA(Yamamoto 2005)	37°72′130″	140°24′954″
3	AZM180803002_1	Blocky lava (upper, well fractured)	Issaikyo lava? (0.3Ma?)	37°72′130″	140°24′954″
4	AZM180803002_2	Blocky lava (lower, coherent, river bed)	Issaikyo lava? (0.3Ma?)	37°72′431″	140°24′344″
5	AZM180805001_1	Blockly lava	Early pleistcene lava? (0.3-0.7Ma), Higashi Azuma	37°71′731″	140°25′990″
6	AZM180805001_2	Blockly lava (Very weathered)	Early pleistcene lava? (0.3-0.7Ma), Higashi Azuma	37°71′731″	140°25′990″
7	AZM180805002_1	Blockly lava	Early pleistcene lava? (0.3-0.7Ma), Higashi Azuma	37°71′710″	140°26′030″
8	AZM180805002_2	Fall rock (part of columnar joint of blockly lava)	Early pleistcene lava? (0.3-0.7Ma), Higashi Azuma	37°71′710″	140°26′030″
9	AZM180805002_3	Aa lava (blocky-massive part)	Kofuji unit (Yamamoto 2005) (around 6ka)	37°71′710″	140°26′030″
10	AZM180805002_4	Aa lava (clinker like vesiculated part)	Kofuji unit (Yamamoto 2005) (around 6ka)	37°71′710″	140°26′030″
11	AZM180806001_1	Fall rock (weakly hydrothermally silicified rock)	OA? from OA crater?	37°72′529″	140°24′195″
12	AZM180908001_1	White ash matrix (clay size), fall ash deposit	OA main part (L1-1)	37°72′794″	140°26′197″
13	AZM180908001_2	Blueish grey ash matrix (clay size), fall ash deposit	OA uppermost (L1-2)	37°72′794″	140°26′197″
14	AZM180908001_3	White ash matrix (clay size), fall ash deposit	unknown? (L2)	37°72′794″	140°26′197″
15	AZM180908001_4	Blueish grey ash matrix (fine sand size), fall ash deposit	unknown? (L3)	37°72′794″	140°26′197″
16	AZM180908001_5	Dark blueish grey ash matrix (fine sand size), fall ash deposit	unknown? (L4)	37°72′794″	140°26′197″
17	AZM180908001_6	Dark grey ash (sorting well), fall ash deposit	unknown? (L5)	37°72′794″	140°26′197″
18	AZM180908001_7	Blueish grey ash matrix (fine sand size), fall ash deposit	unknown? (L6)	37°72′794″	140°26′197″
19	AZM180908001_8	Grey ash matrix (fine sand size), fall ash deposit	unknown? (L7) underllying white clay ash layer (Meiji eruption?) with thicness 10cm.	37°72′794″	140°26′197″
20	AZM180908002_1	Yellowish white ash matrix (fine sand size), fall ash deposit	inderectly underlying L1-1 with boundary of soil layer (sampled as -1: corrected name as La)	37°72′857″	140°26′341″
21	AZM180908002_2	Yellowish white ash matrix (fine sand size), fall ash deposit	(sampled as -2: corrected name as Lb)	37°72′857″	140°26′341″
22	AZM180908002_3	Redish ash matrix (fine sand size), pyroclastic density current deposit (surge?) (red)	(sampled as -4: corrected name as Ld1)	37°72′857″	140°26′341″
23	AZM180908002_4	Pale brownish grey ash matrix (fine sand size), pyroclastic density current deposit (surge?) (pale gray)	(sampled as -5: corrected name as Ld2)	37°72′857″	140°26′341″
24	AZM180908002_5	Brownish grey ash matrix (fine sand size), pyroclastic density current deposit (surge?) (grey)	(sampled as -6: corrected name as Ld3)	37°72′857″	140°26′341″
25	AZM180908002_6	Brown to grey ash matrix (fine sand size), fall deposit (well sorted)	Le	37°72′857″	140°26′341″
26	AZM180909001_1	Dark grey ash (sorting well), fall ash deposit	L5?	37°44′032″	140°15′539″
27	AZM180909001_2	Dark grey ash (sorting well), fall ash deposit	L6 or L7	37°44′032″	140°15′539″

Appendix 6-1: XRD results in Chapter 3 (Bulk ash samples)

定性分析結果

基本情報

解析日	2019/04/21 22:51:40		
試料名	Az180908001_1_OA1-1	測定日	2019/04/19 12:24:20
ファイル名	Az180908001_1_OA1-1.raw	測定者	User1
コメント	Ouchi slow		

同定された結晶相

結晶相名	化学式	FOM	相の登録手法	DB カード番号
Quartz, low	Si O2	0.801	ICDD (PDF-	00-005-0490
Augite	(Na0.09	1.481	ICDD (PDF-	01-071-1070
Alunite	K (Al3 (S O4)2	3.108	ICDD (PDF-	01-071-1776
Plagioclase	Ca0.63 Na0.37	2.968	ICDD (PDF-	01-083-1367
cristobalite-α high	Si O2	2.768	ICDD (PDF-	01-071-6242
Kaolinite-1A	Al2 (Si2 O5) (O	3.414	ICDD (PDF-	01-078-1996
Natroalunite	Na0.58 K0.42 Al3	3.098	ICDD (PDF-	01-075-1685
Enstatite, syn	Mg Si O3	3.144	ICDD (PDF-	00-019-0768
Montmorillonite	(Na , Ca)0.3 (Al ,	2.826	ICDD (PDF-	00-007-0051
Chlorite	Mg2 Al3 (Si3 Al)	3.218	ICDD (PDF-	00-013-0003
Jarosite,	(K , H3 O) Fe3 (S	2.646	ICDD (PDF-	00-036-0427
Natrojarosite, syn	Na Fe3 (S O4)2	2.752	ICDD (PDF-	00-036-0425
Albite, ordered	Na Al Si3 O8	1.822	ICDD (PDF-	00-009-0466
Halloysite-7A	Al2 Si2 O5 (O	1.674	ICDD (PDF-	00-003-0184
Anorthoclase, syn	Na0.71 K0.29 Al	1.340	ICDD (PDF-	00-010-0361
Tridymite	Si O2	3.558	ICDD (PDF-	01-071-0261

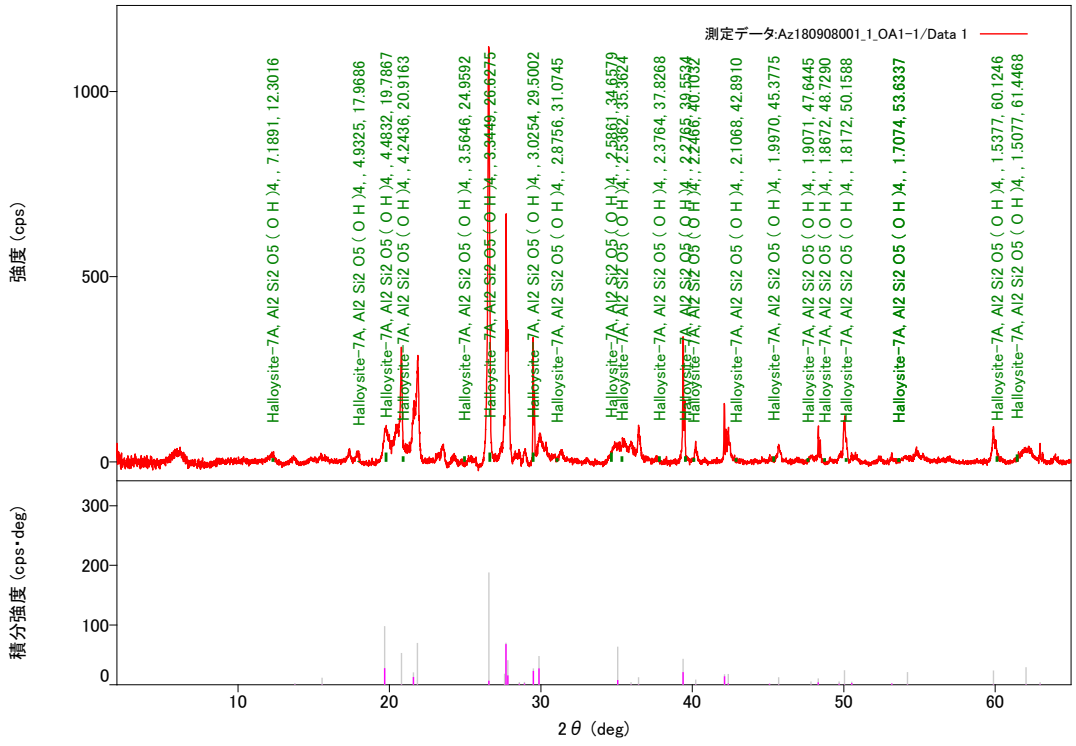

定性分析結果

基本情報

解析日	2019/04/21 22:54:26		
試料名	Az180908001_2_OA1-2	測定日	2019/04/19 16:37:06
ファイル名	Az180908001_2_OA1-2.raw	測定者	User1
コメント	Ouchi slow		

同定された結晶相

結晶相名	化学式	FOM	相の登録手法	DB カード番号
Augite	(Na0.09 Ca0.616)	1.819	ICDD (PDF-2/Release	01-071-1070
Enstatite, syn	Mg Si O3	3.167	ICDD (PDF-2/Release	00-019-0768
α-Si O2, quartz low	Si O2	0.659	ICDD (PDF-2/Release	01-078-1252
Montmorillonite-	Ca0.2 (Al , Mg)2 Si4	0.957	ICDD (PDF-2/Release	00-058-2008
Cristobalite, low	Si O2	1.071	ICDD (PDF-2/Release	01-071-3839
Dickite	Al2 (Si2 O5 (O H)4)	1.798	ICDD (PDF-2/Release	01-072-8193
Kaolinite-1A	Al2 (Si2 O5) (O H)4	1.787	ICDD (PDF-2/Release	01-078-1996
Halloysite-7A	Al2 Si2 O5 (O H)4	1.890	ICDD (PDF-2/Release	00-003-0184
Natroalunite	Na0.58 K0.42 Al3 (S	2.856	ICDD (PDF-2/Release	01-075-1685
Alunite	(K0.805 Na0.132 (H2	3.089	ICDD (PDF-2/Release	01-075-9141
Anorthoclase, syn	Na0.71 K0.29 Al Si3	1.710	ICDD (PDF-2/Release	00-010-0361
Orthoclase	(K0.94 Na0.06) (Al	3.115	ICDD (PDF-2/Release	01-076-0823
Sanidine, high, syn	K Al Si3 O8	2.968	ICDD (PDF-2/Release	00-010-0353

結晶相データパターン

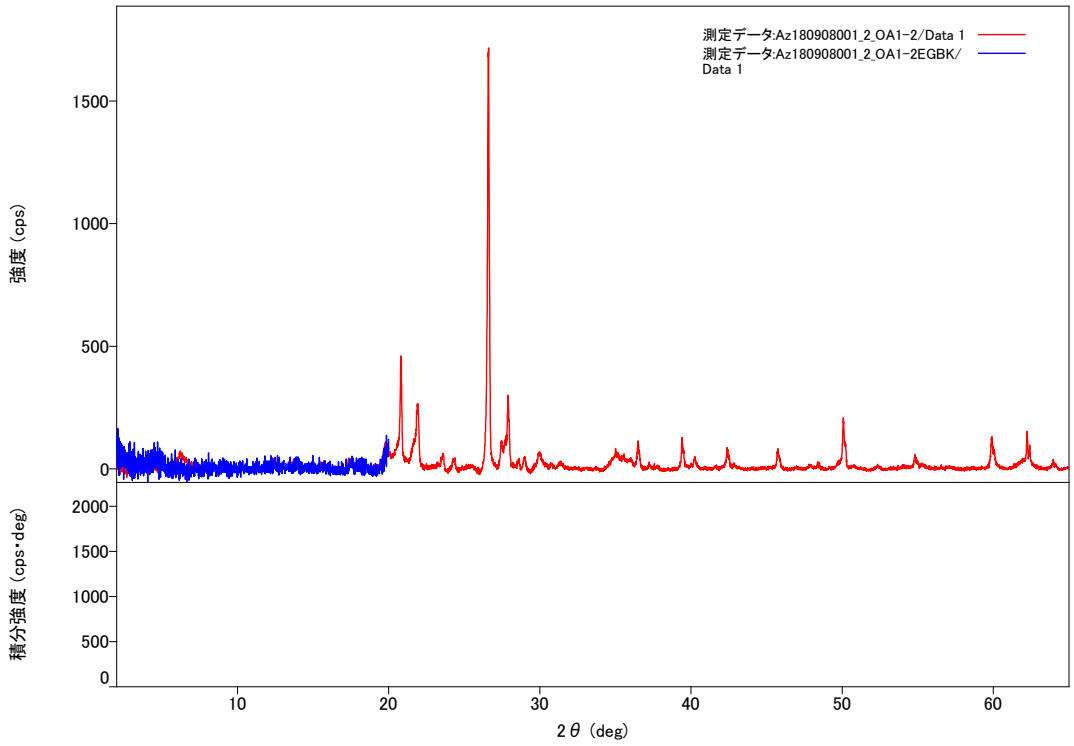

定性分析結果

基本情報

解析日	2019/04/21 22:55:50		
試料名	Az180908001_3_2	測定日	2019/04/19 21:01:43
ファイル名	Az180908001_3_2.raw	測定者	User1
コメント	Ouchi slow		

同定された結晶相

結晶相名	化学式	FOM	相の登録手法	DB カード番号
Orthopyroxene	(Mg0.924 Fe0.066)	0.577	ICDD (PDF-2/Release	01-076-3327
Cristobalite high	Si O2	0.440	ICDD (PDF-2/Release	01-076-0934
Albite, syn	Na (Al Si3 O8)	0.982	ICDD (PDF-2/Release	01-071-1150
Augite	(Na0.09 Ca0.616)	0.955	ICDD (PDF-2/Release	01-071-1070
Alunite	K (Al3 (S O4)2 (O	1.109	ICDD (PDF-2/Release	01-071-1776
Natroalunite	Na0.58 K0.42 Al3 (S	0.924	ICDD (PDF-2/Release	01-075-1685
Tridymite	Si O2	1.106	ICDD (PDF-2/Release	01-073-6613
Quartz	Si O2	0.427	ICDD (PDF-2/Release	01-074-1811
Dickite	Al2 (Si2 O5 (O H)4)	0.881	ICDD (PDF-2/Release	01-072-8193
Montmorillonite (Clay)	Na Mg Al Si O2 (O H)	0.760	ICDD (PDF-2/Release	00-002-0014
Kaolinite-1A	Al2 (Si2 O5) (O H)4	0.873	ICDD (PDF-2/Release	01-078-1996
Halloysite-7A	Al2 Si2 O5 (O H)4	1.056	ICDD (PDF-2/Release	00-003-0184
cristobalite-α high	Si O2	0.931	ICDD (PDF-2/Release	01-071-6245
Cristobalite low, syn	Si O2	0.935	ICDD (PDF-2/Release	01-077-1317

結晶相データパターン

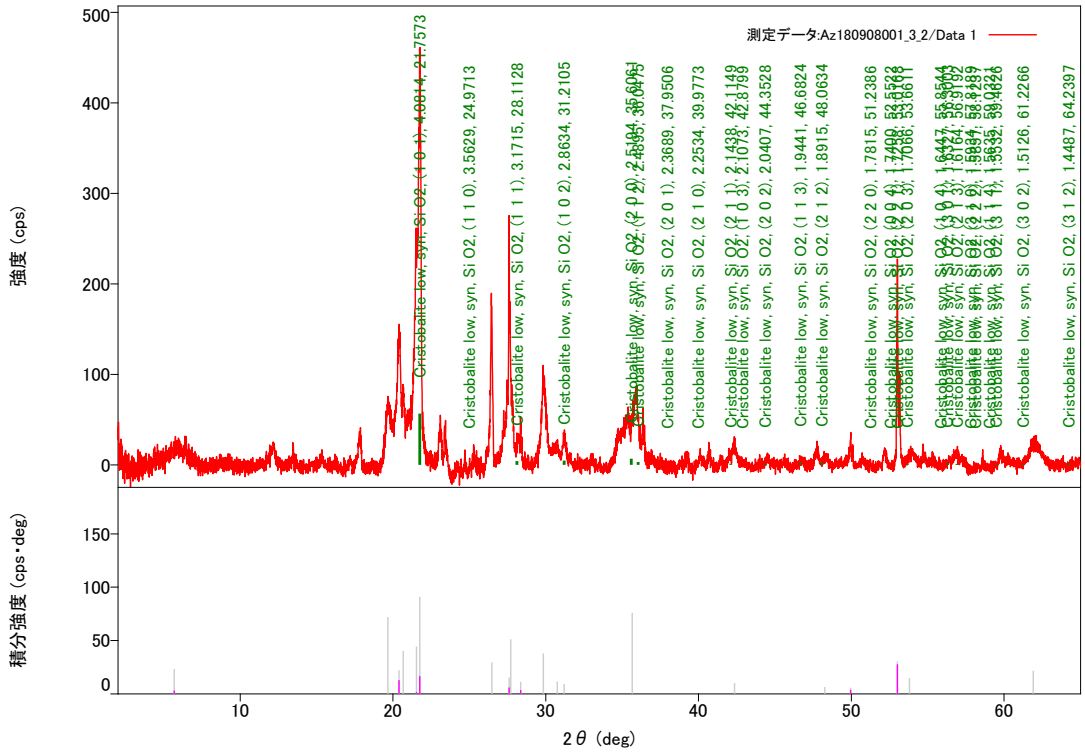

定性分析結果

基本情報

解析日	2019/04/21 22:57:53		
試料名	Az180908001_4_3	測定日	2019/04/20 01:14:29
ファイル名	Az180908001_4_3.raw	測定者	User1
コメント	Ouchi slow		

同定された結晶相

結晶相名	化学式	FOM	相の登録手法	DB カード番号
INTERMEDIATE	NA AL SI3 O8	1.255	JICST	2593
SILICON DIOXIDE,	SI O2	1.092	JICST	5946
Alunite	(K0.805 Na0.132 (H2	1.101	ICDD (PDF-2/Release	01-075-9141
Quartz, low	Si O2	1.201	ICDD (PDF-2/Release	00-005-0490
Kaolinite	Al4 (O H)8 (Si4	3.059	ICDD (PDF-2/Release	01-078-2110
Hornblende	Na0.9 K0.4 Ca1.6	2.936	ICDD (PDF-2/Release	01-071-1060
Kaolinite-1A	Al2 (Si2 O5) (O H)4	2.149	ICDD (PDF-2/Release	01-078-1996
Ferro-actinolite	Ca2 Fe5 Si8 O22 (O	3.061	ICDD (PDF-2/Release	00-023-0118
Augite	(Na0.09 Ca0.616)	2.019	ICDD (PDF-2/Release	01-071-1070
cristobalite-α high	Si O2	1.284	ICDD (PDF-2/Release	01-071-6242
Anorthite	Ca (Al2 Si2 O8)	2.350	ICDD (PDF-2/Release	01-075-1587
Actinolite	Ca1.68 Mg4.59	3.090	ICDD (PDF-2/Release	01-080-0521

結晶相データパターン

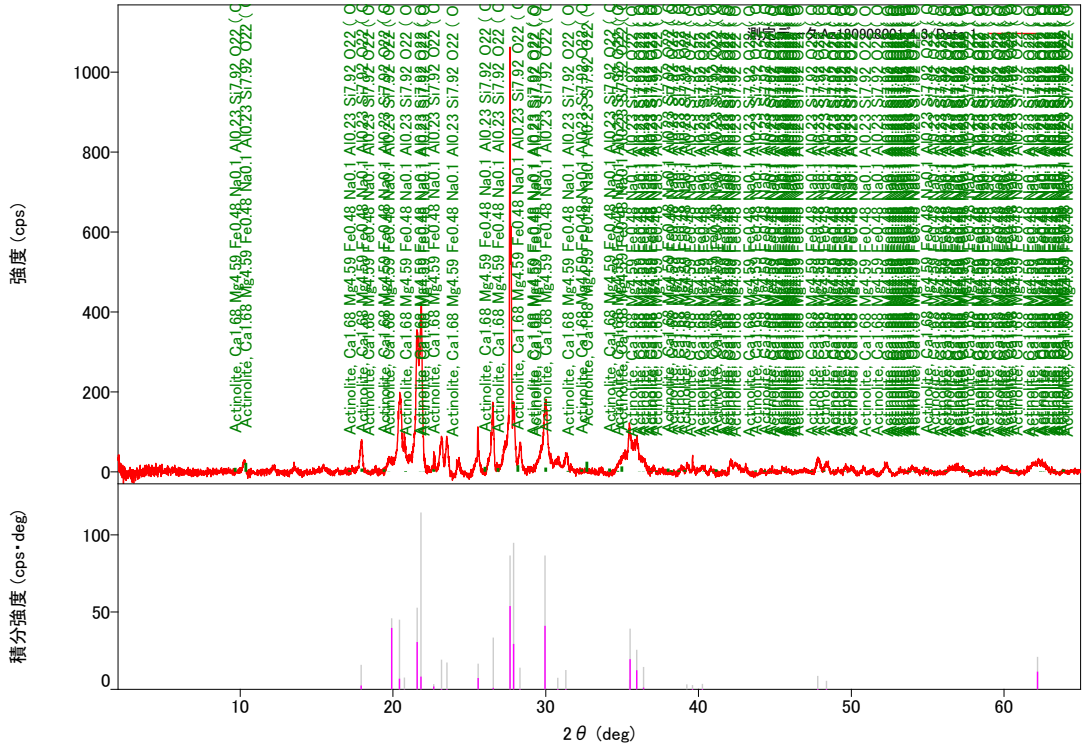

定性分析結果

基本情報

解析日	2019/04/21 22:59:01		
試料名	Az180908001_5_4	測定日	2019/04/20 10:08:45
ファイル名	Az180908001_5_4.raw	測定者	User1
コメント	Ouchi slow		

同定された結晶相

結晶相名	化学式	FOM	相の登録手法	DB カード番号
Plagioclase	Ca0.68 Na0.30	0.794	ICDD (PDF-2/Release	01-083-1372
Tridymite	Si O2	0.856	ICDD (PDF-2/Release	01-071-0261
Augite	(Na0.09 Ca0.616)	1.455	ICDD (PDF-2/Release	01-071-1070
Quartz, low	Si O2	1.465	ICDD (PDF-2/Release	00-005-0490
Enstatite, syn	Mg Si O3	1.638	ICDD (PDF-2/Release	00-019-0768
Sanidine, syn	K (Si1.2 Fe0.5 Al0.3)	1.961	ICDD (PDF-2/Release	01-072-3540
Anorthoclase, syn	Na0.71 K0.29 Al Si3	2.673	ICDD (PDF-2/Release	00-010-0361
Cristobalite, syn	Si O2	1.935	ICDD (PDF-2/Release	00-039-1425
Natroalunite	Na0.58 K0.42 Al3 (S	2.767	ICDD (PDF-2/Release	01-075-1685
Alunite	(K0.805 Na0.132 (H2	1.775	ICDD (PDF-2/Release	01-075-9141
Actinolite, heated	Mg , Ca , Fe , Na , Mn ,	2.757	ICDD (PDF-2/Release	01-089-5367
Hornblende	Na0.76 (Na0.46	2.037	ICDD (PDF-2/Release	01-080-3471
Kaolinite	Al4 (O H)8 (Si4	1.804	ICDD (PDF-2/Release	01-078-2110

結晶相データパターン

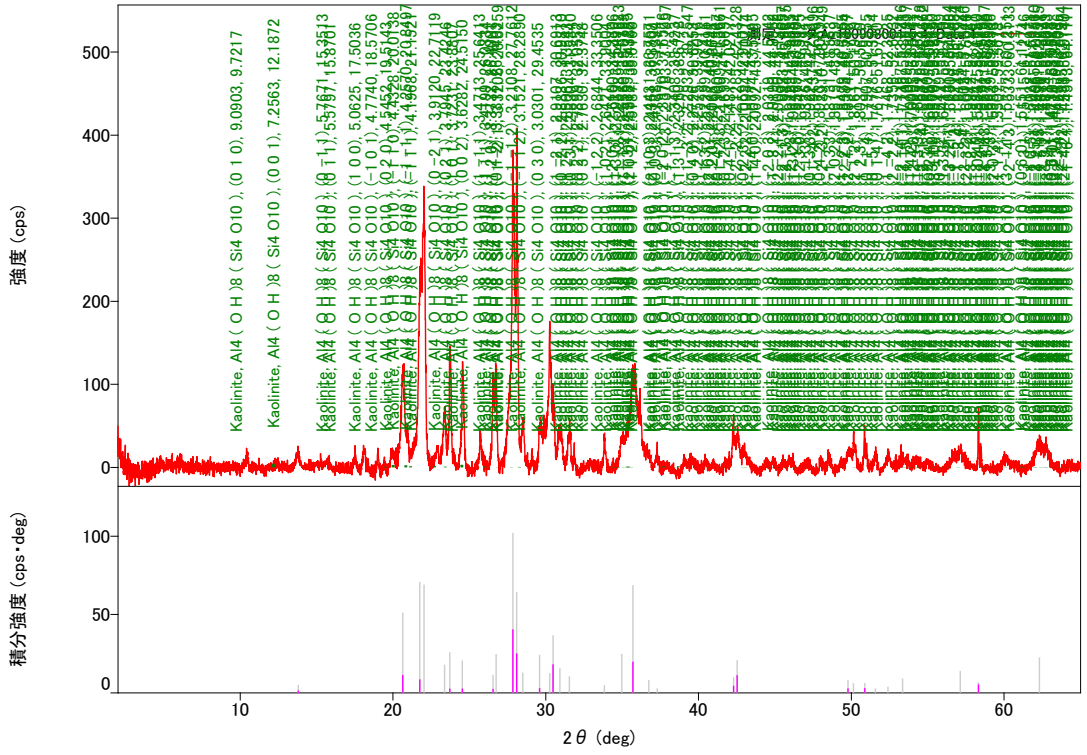

定性分析結果

基本情報

解析日	2019/04/21 22:59:44		
試料名	Az180908001_6_5.	測定日	2019/04/20 15:45:29
ファイル名	Az180908001_6_5.raw	測定者	User1
コメント	Ouchi slow		

同定された結晶相

結晶相名	化学式	FOM	相の登録手法	DB カード番号
Quartz	Si O2	0.789	ICDD (PDF-2/Release	01-074-1811
Cristobalite beta, syn	Si O2	1.146	ICDD (PDF-2/Release	01-077-8670
tridymite	Si O2	1.606	ICDD (PDF-2/Release	05-001-0058
Enstatite ferroan, syn,	(Fe0.115 Mg0.885)	1.396	ICDD (PDF-2/Release	01-083-0669
Augite	(Na0.09 Ca0.616)	1.661	ICDD (PDF-2/Release	01-071-1070
Alunite	(K0.805 Na0.132 (H2	3.050	ICDD (PDF-2/Release	01-075-9141
Natroalunite	Na0.58 K0.42 Al3 (S	3.465	ICDD (PDF-2/Release	01-075-1685
Sanidine	(K , Na) (Si3 Al) O8	1.569	ICDD (PDF-2/Release	00-019-1227
albite high, syn,	Na (Al Si3 O8)	1.873	ICDD (PDF-2/Release	01-071-1154
Kaolinite-1A	Al2 (Si2 O5) (O H)4	2.915	ICDD (PDF-2/Release	01-078-1996
Halloysite-7A	Al2 Si2 O5 (O H)4	3.076	ICDD (PDF-2/Release	00-003-0184
Montmorillonite	Mg O ・ Al2 O3 ・5 Si	3.044	ICDD (PDF-2/Release	00-003-0014

結晶相データパターン

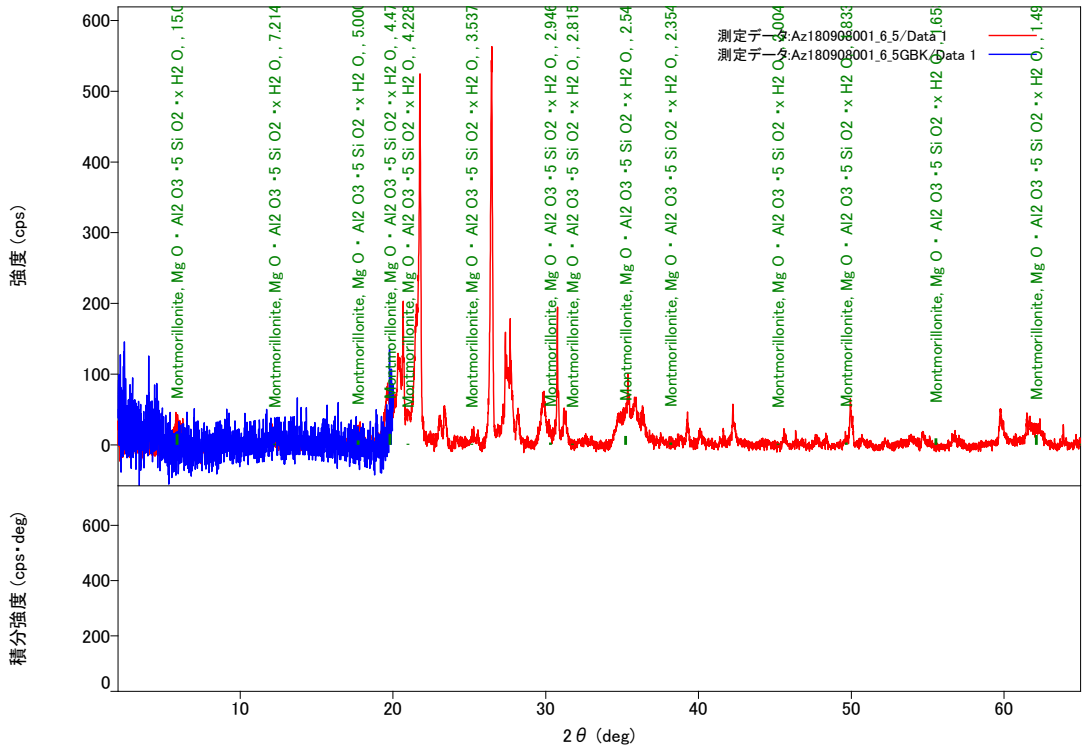

定性分析結果

基本情報

解析日	2019/04/21 23:00:29		
試料名	Az180908001_7_6	測定日	2019/04/20 19:58:14
ファイル名	Az180908001_7_6.raw	測定者	User1
コメント	Ouchi slow		

同定された結晶相

結晶相名	化学式	FOM	相の登録手法	DB カード番号
tridymite	Si O2	1.404	ICDD (PDF-2/Release	05-001-0058
anorthite high,	Ca (Al2 Si2 O8)	1.071	ICDD (PDF-2/Release	01-073-0265
SILICON DIOXIDE,	SI O2	1.099	JICST	7258
cristobalite-β high	Si O2	1.486	ICDD (PDF-2/Release	01-071-6246
Halloysite-7A	Al2 Si2 O5 (O H)4	2.019	ICDD (PDF-2/Release	00-003-0184
Kaolinite-1A	Al2 (Si2 O5) (O H)4	3.024	ICDD (PDF-2/Release	01-078-1996
Natroalunite	Na0.58 K0.42 Al3 (S	3.115	ICDD (PDF-2/Release	01-075-1685
Montmorillonite	Si3.74 Al2.03 Fe0.03	1.836	ICDD (PDF-2/Release	00-002-0009
Alunite	(K0.805 Na0.132 (H2	3.489	ICDD (PDF-2/Release	01-075-9141
Augite	(Na0.09 Ca0.616)	1.773	ICDD (PDF-2/Release	01-071-1070
Enstatite, syn	Mg Si O3	3.287	ICDD (PDF-2/Release	00-019-0768

結晶相データパターン

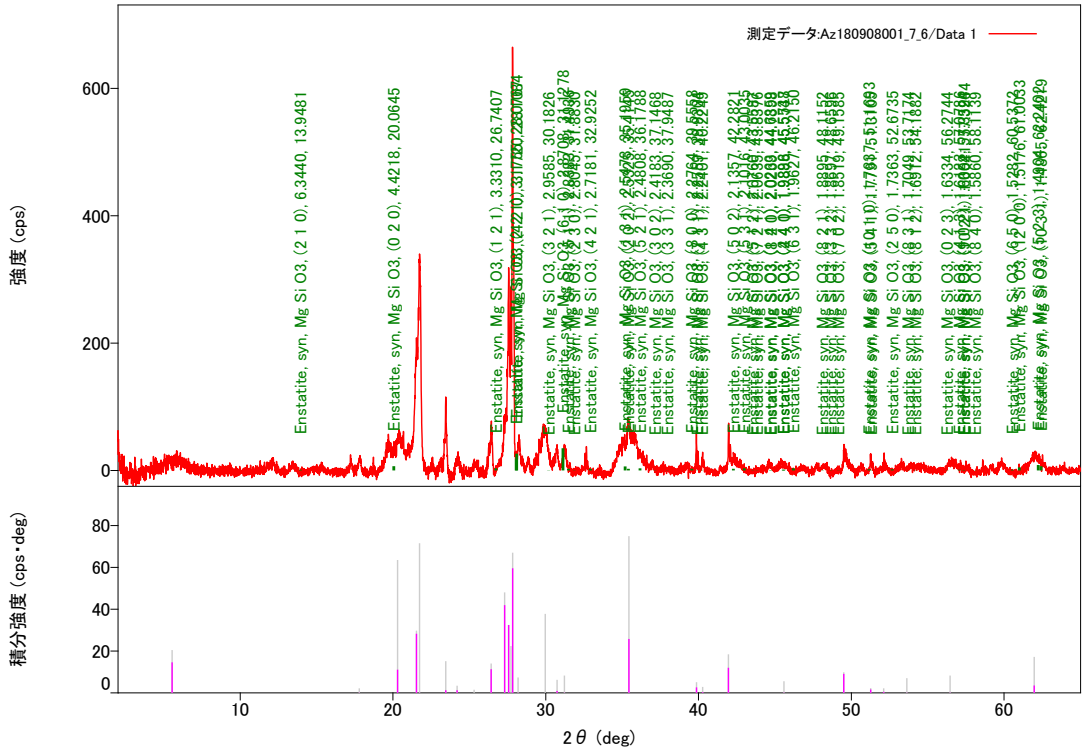

定性分析結果

基本情報

解析日	2019/04/21 23:01:27		
試料名	Az180908001_8_7	測定日	2019/04/21 00:10:34
ファイル名	Az180908001_8_7.raw	測定者	User1
コメント	Ouchi slow		

同定された結晶相

結晶相名	化学式	FOM	相の登録手法	DB カード番号
Quartz low, syn	Si O2	1.354	ICDD (PDF-2/Release	01-089-1961
Alunite	(K0.805 Na0.132 (H2	1.281	ICDD (PDF-2/Release	01-075-9141
Cristobalite, syn	Si O2	1.383	ICDD (PDF-2/Release	00-039-1425
Natroalunite	Na0.58 K0.42 Al3 (S	2.905	ICDD (PDF-2/Release	01-075-1685
Tridymite	Si O2	1.891	ICDD (PDF-2/Release	01-071-0261
Jarosite, hydronian	(K , H3 O) Fe3 (S	3.513	ICDD (PDF-2/Release	00-036-0427
Anorthoclase, syn	Na0.71 K0.29 Al Si3	1.486	ICDD (PDF-2/Release	00-010-0361
Albite	Na Al Si3 O8	1.630	ICDD (PDF-2/Release	00-001-0739
Sanidine, high, syn	K Al Si3 O8	2.993	ICDD (PDF-2/Release	00-010-0353
Halloysite-7A	Al2 Si2 O5 (O H)4	2.907	ICDD (PDF-2/Release	00-003-0184
Kaolinite-1A	Al2 (Si2 O5) (O H)4	3.074	ICDD (PDF-2/Release	01-078-1996
Enstatite, syn	Mg Si O3	1.831	ICDD (PDF-2/Release	00-019-0768
Augite	(Na0.09 Ca0.616)	2.859	ICDD (PDF-2/Release	01-071-1070

結晶相データパターン

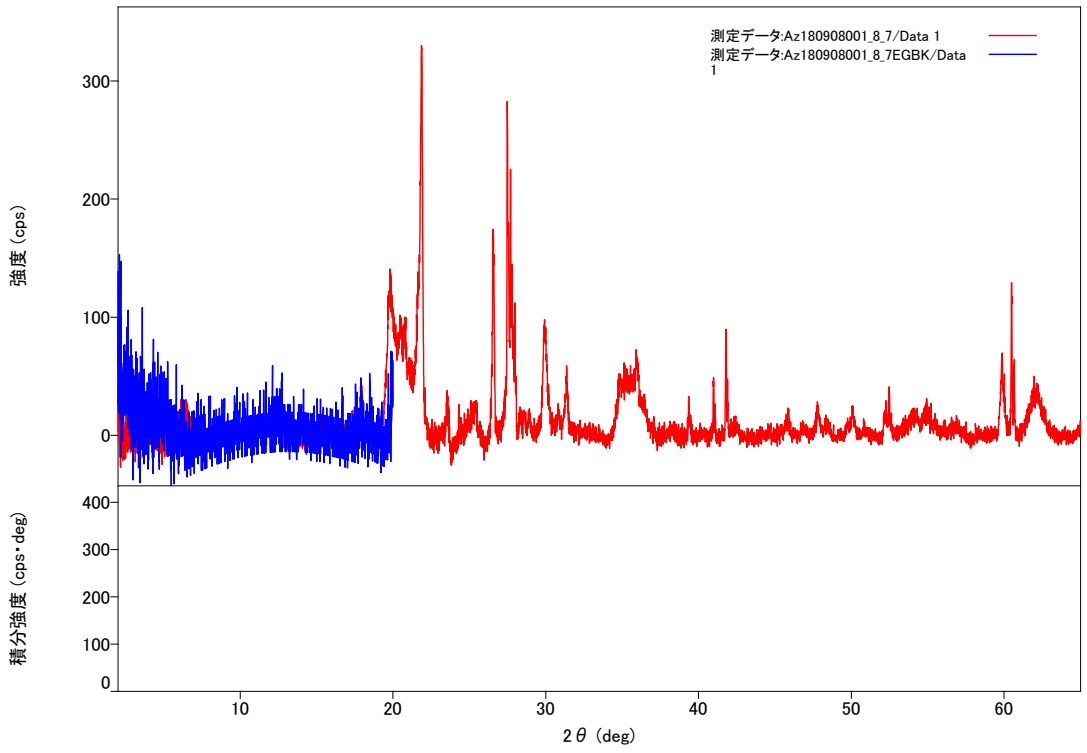

定性分析結果

基本情報

解析日	2019/04/21 23:02:04		
試料名	Az180908002_1_-1 (La)	測定日	2019/04/21 04:22:52
ファイル名	Az180908002_1_-1.raw	測定者	User1
コメント	Ouchi slow		

同定された結晶相

結晶相名	化学式	FOM	相の登録手法	DB カード番号
Quartz	Si O2	1.294	ICDD (PDF-2/Release	01-074-1811
tridymite 2H	Si O2	1.428	ICDD (PDF-2/Release	01-077-0126
Augite	(Na0.09 Ca0.616)	2.878	ICDD (PDF-2/Release	01-071-1070
Alunite	(K0.805 Na0.132 (H2	2.702	ICDD (PDF-2/Release	01-075-9141
albite high, syn,	Na (Al Si3 O8)	2.975	ICDD (PDF-2/Release	01-071-1154
Natroalunite	Na0.58 K0.42 Al3 (S	2.968	ICDD (PDF-2/Release	01-075-1685
Kaolinite-1A	Al2 (Si2 O5) (O H)4	1.858	ICDD (PDF-2/Release	01-078-1996
Montmorillonite, syn	Al2 O3 ・4 Si O2 ・x	3.007	ICDD (PDF-2/Release	00-003-0016
Halloysite-7A	Al2 Si2 O5 (O H)4	2.991	ICDD (PDF-2/Release	00-003-0184
Cristobalite low, syn	Si O2	2.775	ICDD (PDF-2/Release	01-077-1317

結晶相データパターン

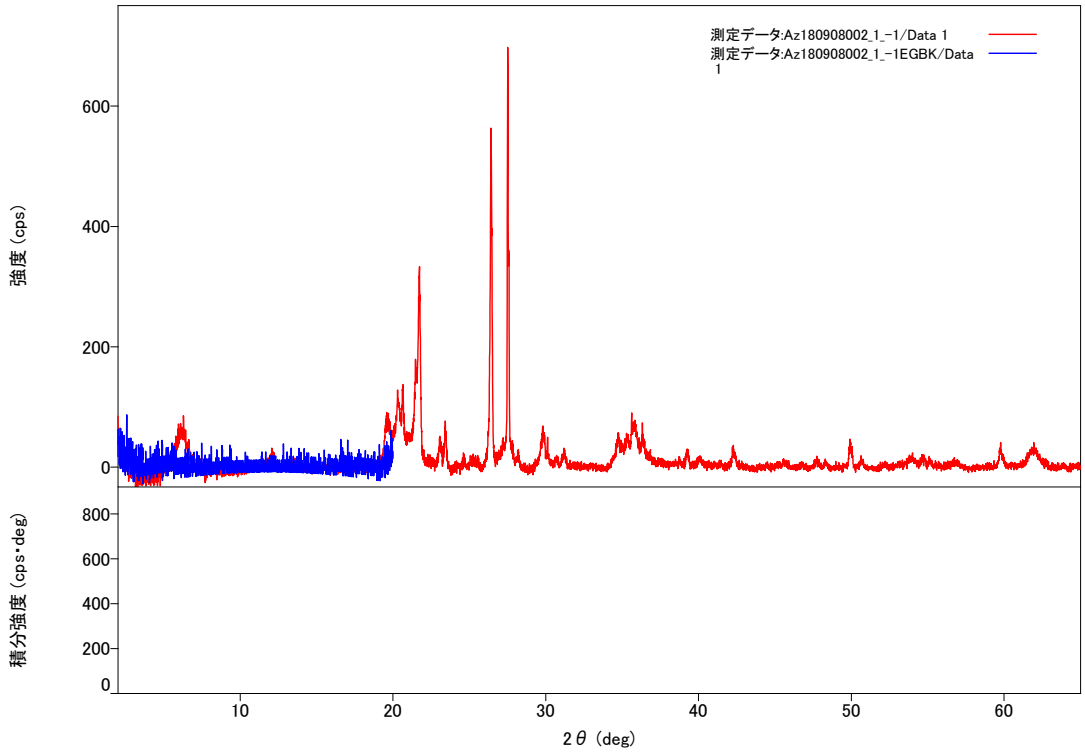

定性分析結果

基本情報

解析日	2019/04/21 23:02:41		
試料名	Az180908002_2_-2	測定日	2019/04/21 08:35:11
ファイル名	Az180908002_2_-2.raw	測定者	User1
コメント	Ouchi slow		

同定された結晶相

結晶相名	化学式	FOM	相の登録手法	DB カード番号
Quartz α, α-Si O2	Si O2	1.059	ICDD (PDF-2/Release	01-089-8937
cristobalite-α high	Si O2	0.835	ICDD (PDF-2/Release	01-071-6245
Tridymite	Si O2	1.536	ICDD (PDF-2/Release	01-071-0261
Alunite	(K0.805 Na0.132 (H2	2.897	ICDD (PDF-2/Release	01-075-9141
Augite	(Na0.09 Ca0.616)	2.957	ICDD (PDF-2/Release	01-071-1070
Plagioclase	Ca0.63 Na0.37	3.375	ICDD (PDF-2/Release	01-083-1367
Natroalunite	Na0.58 K0.42 Al3 (S	2.947	ICDD (PDF-2/Release	01-075-1685
Halloysite-7A	Al2 Si2 O5 (O H)4	2.976	ICDD (PDF-2/Release	00-003-0184
Kaolinite-1A	Al2 (Si2 O5) (O H)4	3.017	ICDD (PDF-2/Release	01-078-1996
Montmorillonite-14A	Na0.3 (Al , Mg)2 Si4	1.558	ICDD (PDF-2/Release	00-013-0259

結晶相データパターン

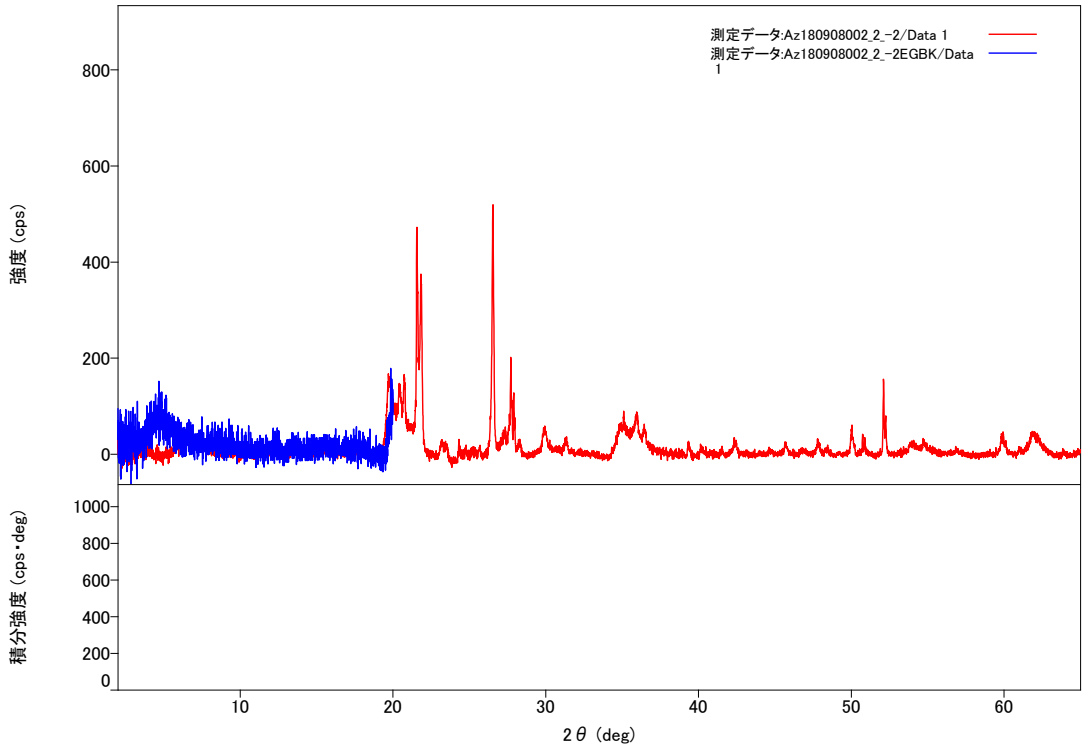

Appendix 6-2: XRD result in Chapter 3 (Fine fraction sieved into <250μm)

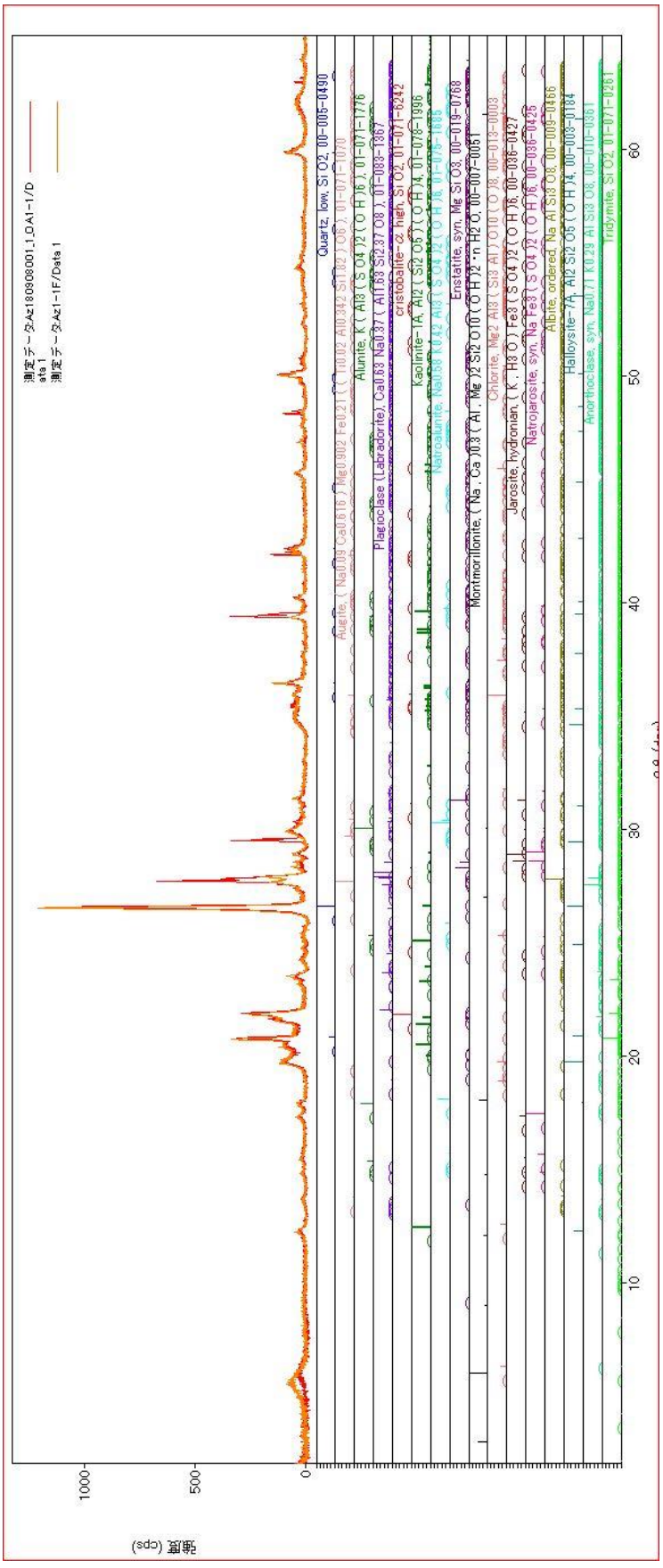
測定データ:Az180908001_1_DA1-1/D
sita1
測定データ:Az1-1F/Data 1
強度 (cps)
1000
500
0
10
20
30
40
50
60
Quartz, low, Si O2, 00-005-0490
Albite, K (Al3 (S O4)2 (O H)6), 01-071-1776
Plagioclase (Labradorite), Ca0.63 Na0.37 (Al1.63 Si2.37 O8), 01-083-1387
cristobalite-α, high, Si O2, 01-071-6242
Kaolinite-1A, Al2 (Si2 O5) (O H)4, 01-078-1996
Enstatite, syn, Mg Si O3, 00-019-0768
Montmorillonite, (Na, Ca)0.3 (Al, Mg)2 Si4 O10 (O H)2 · n H2 O, 00-007-0061
Jarosite, hydronian, (K, H3 O) Fe3 (S O4)2 (O H)6, 00-036-0427
Natrojarosite, syn, Na Fe3 (S O4)2 (O H)6, 00-036-0425
Albite, ordered, Na Al Si3 O8, 00-009-0466
Halloysite-7A, Al2 Si2 O5 (O H)4, 00-003-0784
Anorthoclase, syn, Na0.71 K0.29 Al Si3 O8, 00-010-0361
Tridymite, Si O2, 01-071-0261

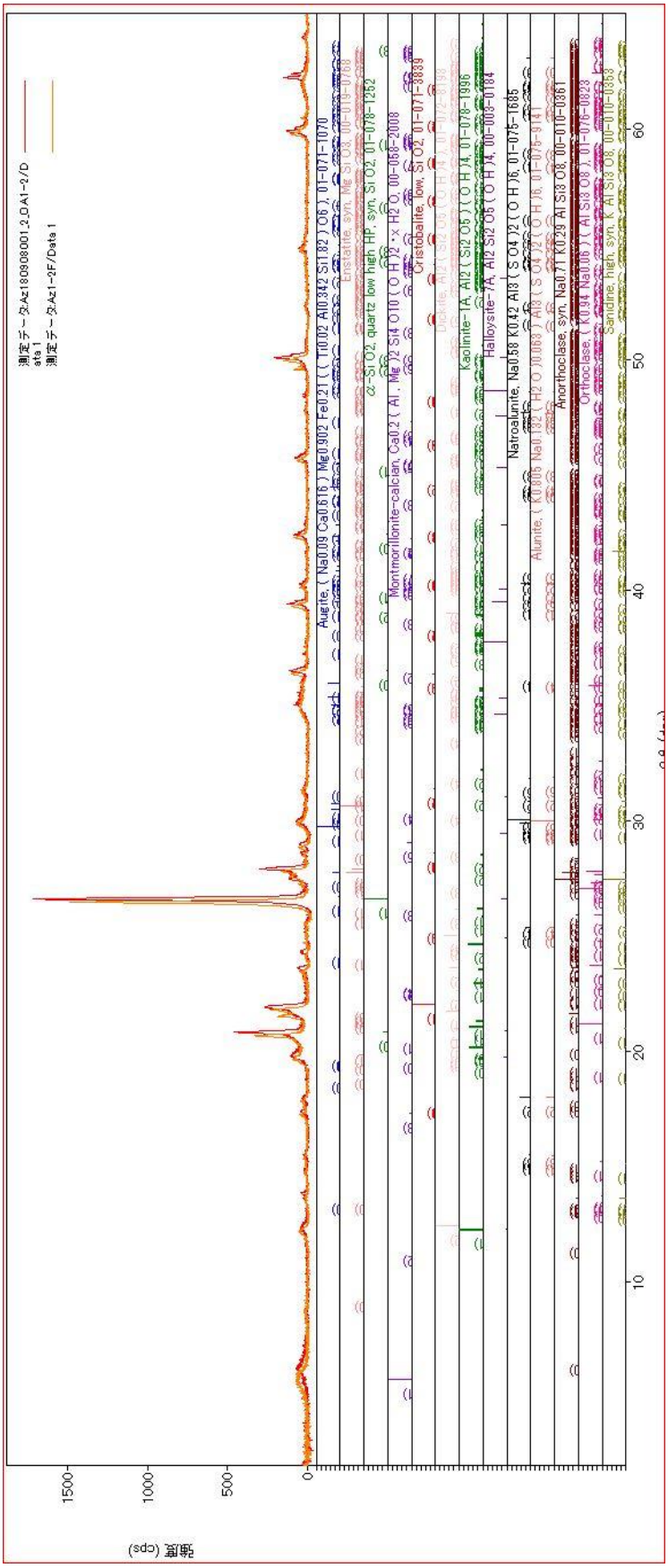
測定データ:Az180908001_2_0A1-2/Data 1
測定データ:Az1-2F/Data 1
強度 (cps)
1500
1000
500
0
10
20
30
40
50
60
Augite, (Na0.09 Ca0.616) Mg0.902 Fe0.21 ((Ti0.02 Al0.342 Si1.82) O6), 01-071-1070
Enstatite, syn, Mg Si O3, 00-019-0768
α-Si O2, quartz low high HP, syn, Si O2, 01-076-1252
Montmorillonite-calcian, Ca0.2 (Al, Mg)2 Si4 O10 (O H)2 ・x H2 O, 00-058-2008
Cristobalite, low, Si O2, 01-071-3839
Kaolinite-1A, Al2 (Si2 O5) (O H)4, 01-078-1996
Halloysite-7A, Al2 Si2 O5 (O H)4, 00-003-0184
Natroalunite, Na0.58 K0.42 Al3 (S O4)2 (O H)6, 01-075-1685
Alunite, (K0.805 Na0.192 (H2 O)0.063) Al3 (S O4)2 (O H)6, 01-076-9141
Anorthoclase, syn, Na0.71 K0.29 Al Si3 O8, 00-010-0361
Orthoclase, (K0.94 Na0.06) (Al Si3 O8), 01-076-0828
Sanidine, high, syn, K Al Si3 O8, 00-010-0363

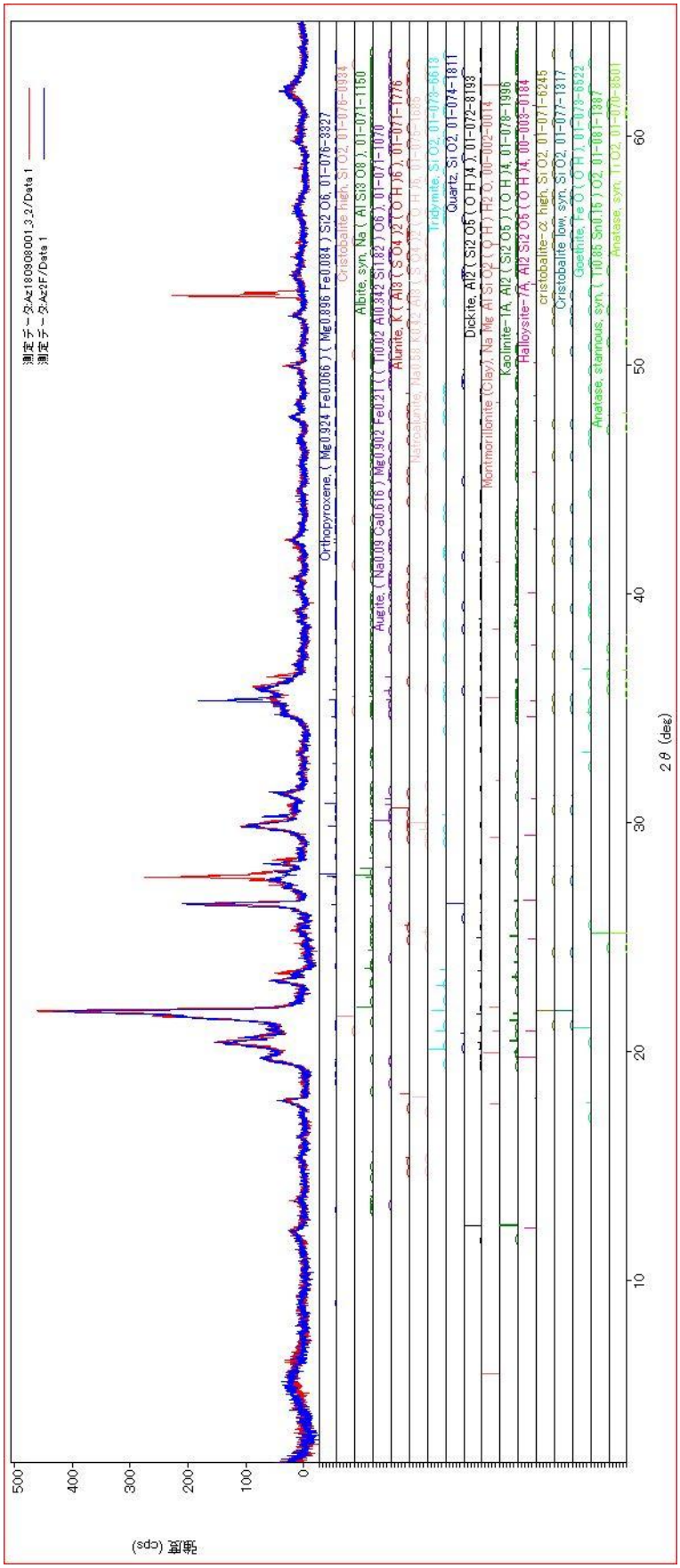
測定データ:Az180908001_3_2/Data 1
測定データ:Az2F/Data 1
Orthopyroxene, (Mg0.924 Fe0.066) (Mg0.896 Fe0.084) Si2 O6, 01-076-8327
Cristobalite high, Si O2, 01-076-0934
Albite, syn, Na (Al Si3 O8), 01-071-1150
Augite, (Na0.09 Ca0.616) Mg0.902 Fe0.21 (Ti0.02 Al0.342 Si1.82) O6), 01-071-1070
Alunite, K (Al3 (S O4)2 (O H)6), 01-071-1776
Nahcolite, Na H C O3, 01-070-1668
Tridymite, Si O2, 01-078-5613
Quartz, Si O2, 01-074-1811
Dickite, Al2 (Si2 O5 (O H)4), 01-072-8193
Montmorillonite (Clay), Na Mg Al Si O2 (O H)) H2 O, 00-002-0014
Kaolinite-1A, Al2 (Si2 O5) (O H)4, 01-078-1996
Halloysite-7A, Al2 Si2 O5 (O H)4, 00-003-0184
cristobalite-α high, Si O2, 01-071-6245
Cristobalite low, syn, Si O2, 01-077-1317
Goethite, Fe O (O H), 01-078-6522
Anatase, stannous, syn, (Ti0.85 Sn0.15) O2, 01-081-1387
Anatase, syn, Ti O2, 01-070-8501
強度 (cps)
2θ (deg)

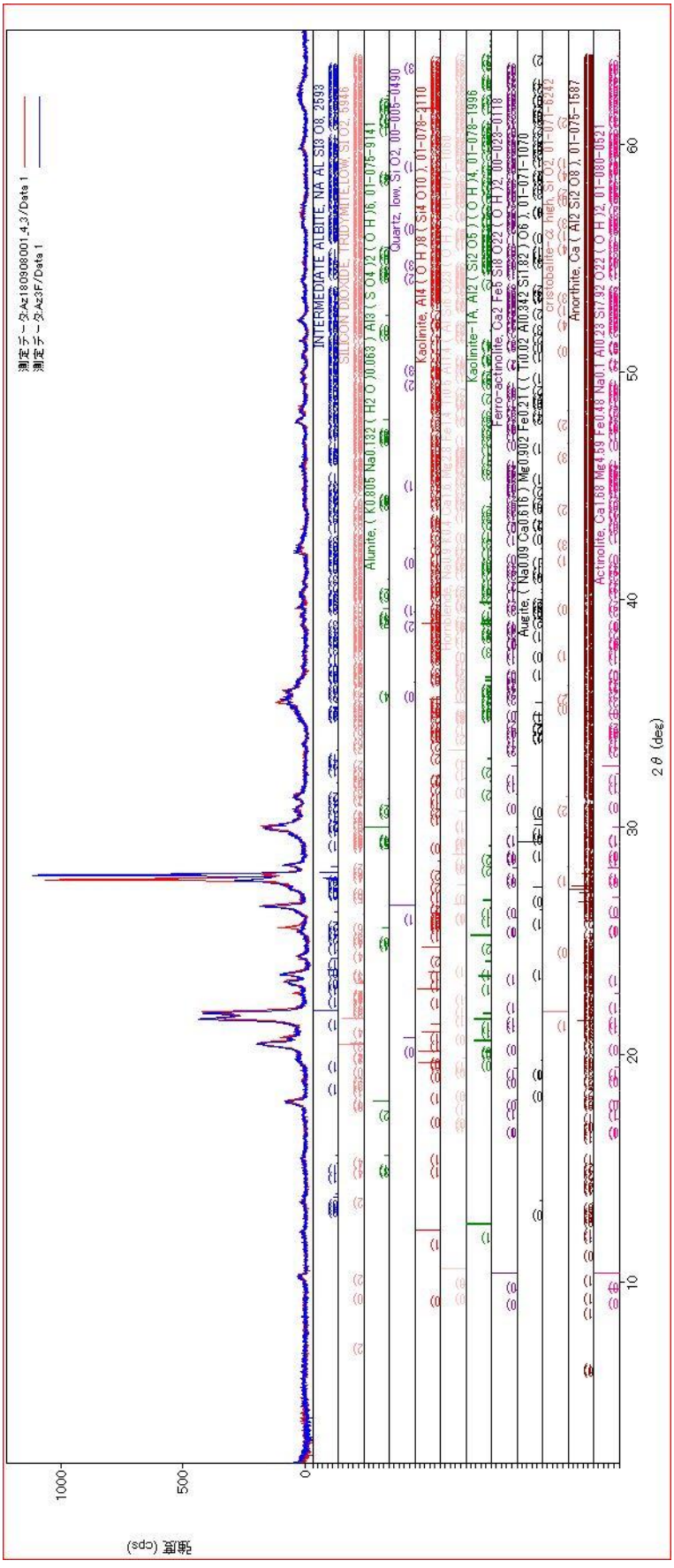
測定データ:Az180908001_4_3/Data 1
測定データ:Az3F/Data 1
INTERMEDIATE ALBITE, NA AL SI3 O8, 2593
Alunite, (K0.805 Na0.132 (H2 O)0.063) Al3 (S O4)2 (O H)6, 01-076-9141
Quartz, low, Si O2, 00-005-0490
Kaolinite, Al4 (O H)8 (Si4 O10), 01-078-2110
Kaolinite-1A, Al2 (Si2 O5) (O H)4, 01-078-1996
Ferro-actinolite, Ca2 Fe5 Si8 O22 (O H)2, 00-028-0118
Augite, (Na0.09 Ca0.616) Mg0.902 Fe0.21 ((Ti0.02 Al0.342 Si1.82) O6), 01-071-1070
cristobalite-α high, Si O2, 01-071-6242
Anorthite, Ca (Al2 Si2 O8), 01-075-1687
Actinolite, Ca1.68 Mg4.59 Fe0.48 Na0.1 Al0.29 Si7.92 O22 (O H)2, 01-080-0521
強度 (cps)
2θ (deg)

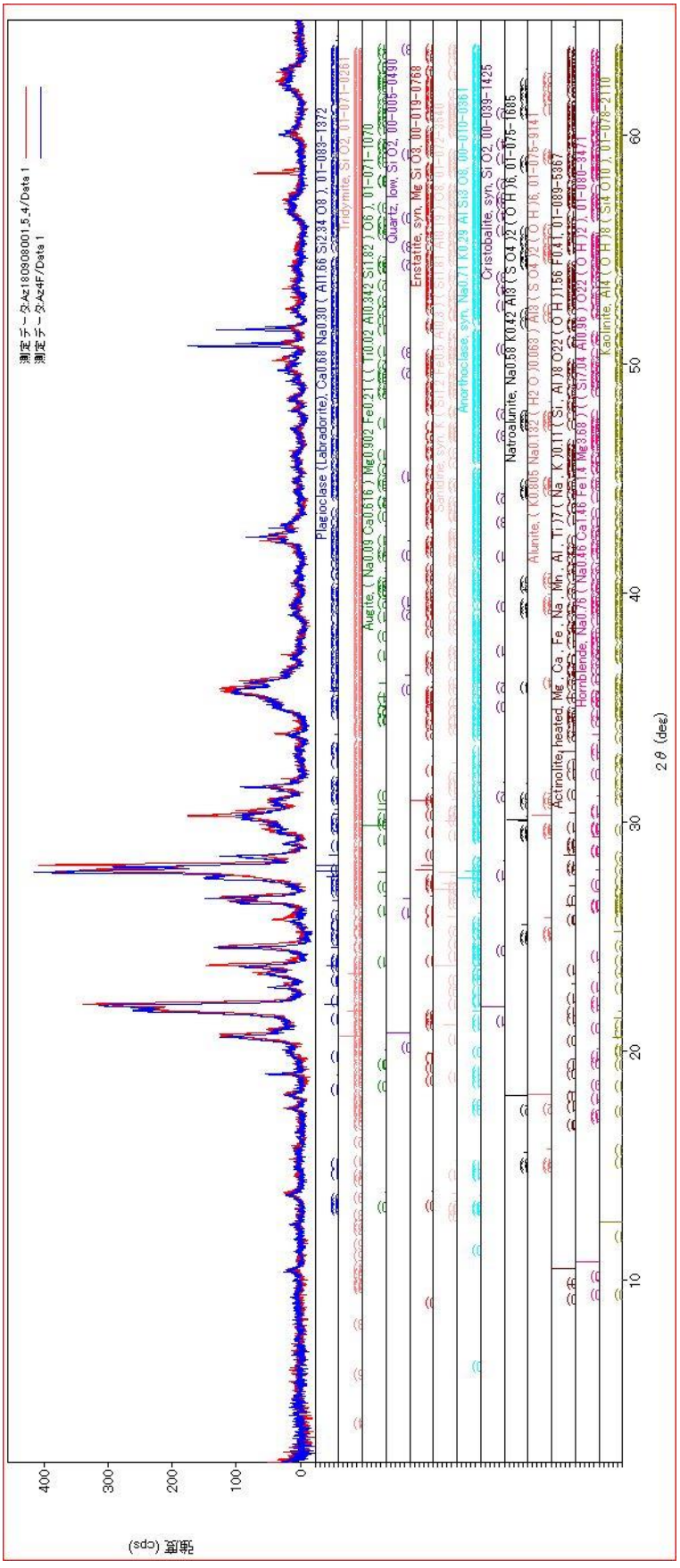
測定データ:Az180908001.5_4/Data 1
測定データ:Az4F/Data 1
Plagioclase (Labradorite), Ca0.68 Na0.30 (Al1.66 Si2.34 O8), 01-083-1372
Tridymite, Si O2, 01-071-0261
Augite, (Na0.09 Ca0.616) Mg0.902 Fe0.21 (Ti0.02 Al0.342 Si1.82) O6), 01-071-1070
Quartz, low, Si O2, 00-005-0490
Enstatite, syn, Mg Si O3, 00-019-0768
Anorthoclase, syn, Na0.71 K0.29 Al Si3 O8, 00-010-0361
Cristobalite, syn, Si O2, 00-039-1425
Natroalunite, Na0.58 K0.42 Al3 (S O4)2 (O H)6, 01-075-1605
Alunite, (K0.805 Na0.195) H2 O)0.063) Al3 (S O4)2 (O H)6, 01-076-1401
Actinolite, heated, Mg, Ca, Fe, Na, Mn, Al, Ti)7 (Si, Al)8 O22 (O H)1.86 F0.41, 01-089-6367
Hornblende, Na0.76 (Na0.46 Ca1.46 Fe1.4 Mg3.68) (Si7.04 Al0.96) O22 (O H)2), 01-080-8471
Kaolinite, Al4 (O H)8 (Si4 O10), 01-078-2110
強度 (cps)
2θ (deg)

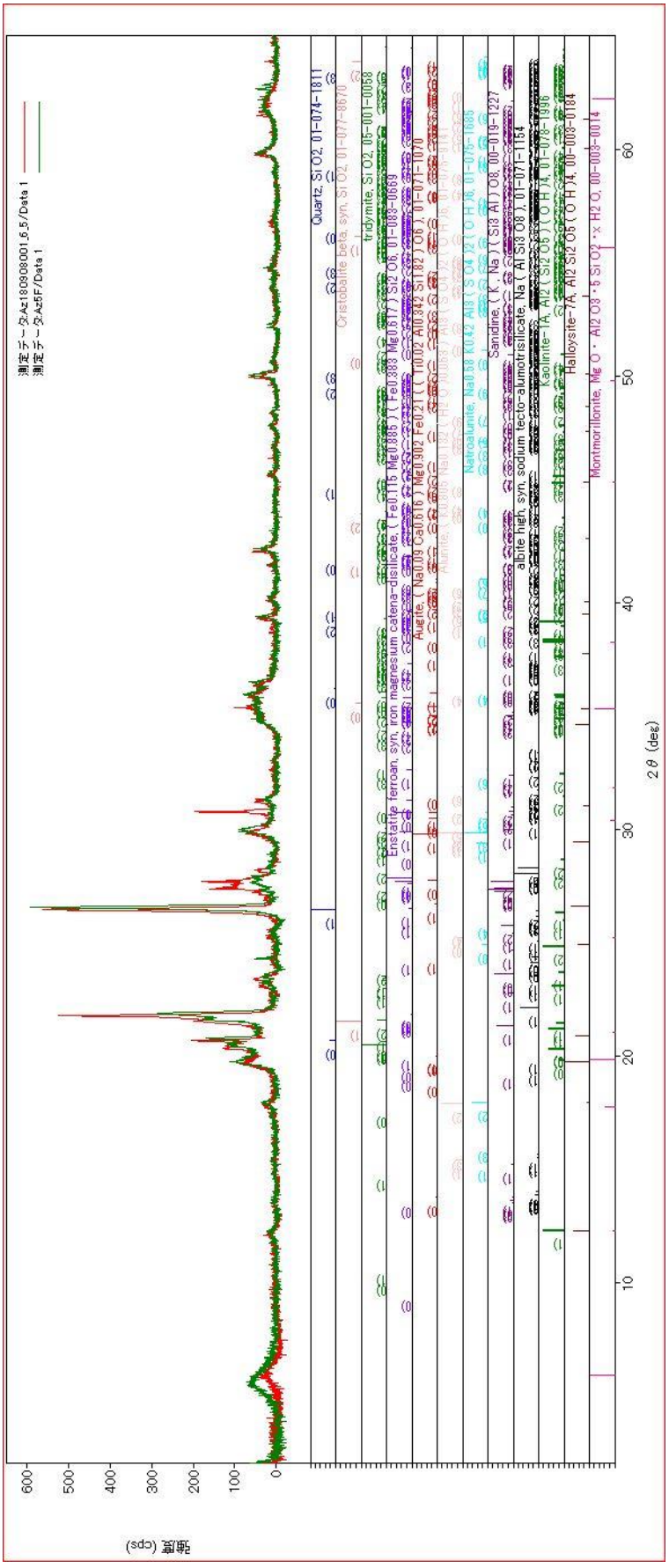
測定データ:Az180908001.6.5/Data 1
測定データ:Az5F/Data 1
Quartz, SiO2, 01-074-1811
Cristobalite beta, syn, SiO2, 01-077-0670
tridymite, SiO2, 05-001-0058
Enstatite ferroan, syn, iron magnesium catena-disilicate, (Fe0.115 Mg0.885) (Fe0.388 Mg0.817) Si2 O6, 01-083-0069
Augite, (Na0.09 Ca0.616) Mg0.902 Fe0.21 (Ti0.02 Al0.342 Si1.82 O6), 01-071-1070
Natroalunite, Na0.86 K0.42 Al3 (S O4)2 (O H)6, 01-076-1686
Sanidine, (K , Na) (Si3 Al) O8, 00-019-1227
albite high, syn, sodium tecto-alumotrisilicate, Na (Al Si3 O8), 01-071-1154
Kaolinite-1A, Al2 (Si2 O5) (O H)4, 01-078-1996
Halloysite-7A, Al2 Si2 O5 (O H)4, 00-003-0184
Montmorillonite, Mg O · Al2 O3 · 5 Si O2 · x H2 O, 00-003-0014
強度 (cps)
2θ (deg)

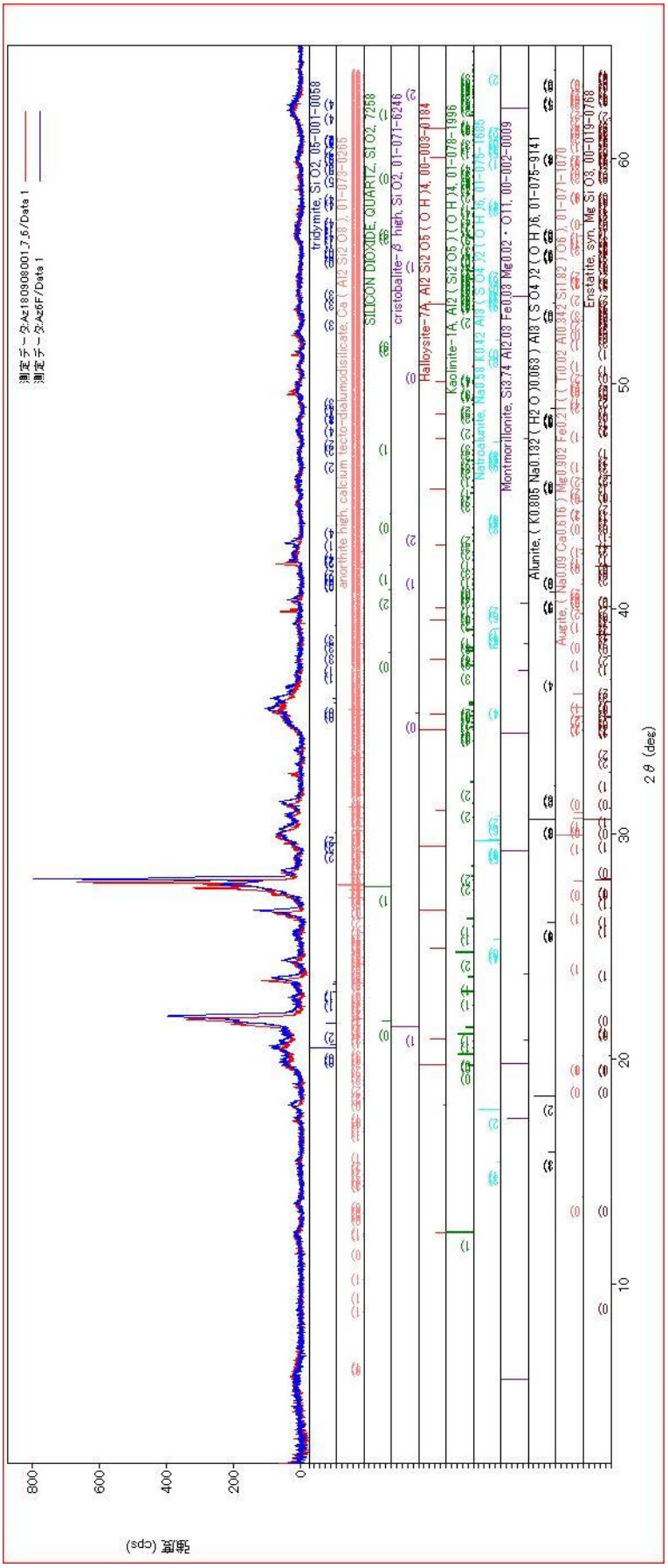
測定データ:Az180908001_7.6/Data 1
測定データ:Az6F/Data 1
tridymite, Si O2, 05-001-0058
SILICON DIOXIDE, QUARTZ, Si O2, 7258
cristobalite-β high, Si O2, 01-071-6246
Halloysite-7A, Al2 Si2 O5 (O H)4, 00-003-0184
Kaolinite-1A, Al2 (Si2 O5) (O H)4, 01-078-1996
Montmorillonite, Si3.74 Al2.03 Fe0.03 Mg0.02 - OTI, 00-002-0009
Alunite, (K0.805 Na0.182 (H2 O)0.063) Al3 (S O4)2 (O H)6, 01-076-9141
Augite, (Na0.09 Ca0.616) Mg0.902 Fe0.21 ((Ti0.02 Al0.342 Si1.82) O6), 01-071-1070
Enstatite, syn, Mg Si O3, 00-019-0768
強度 (cps)
2θ (deg)
0
200
400
600
800
10
20
30
40
50
60

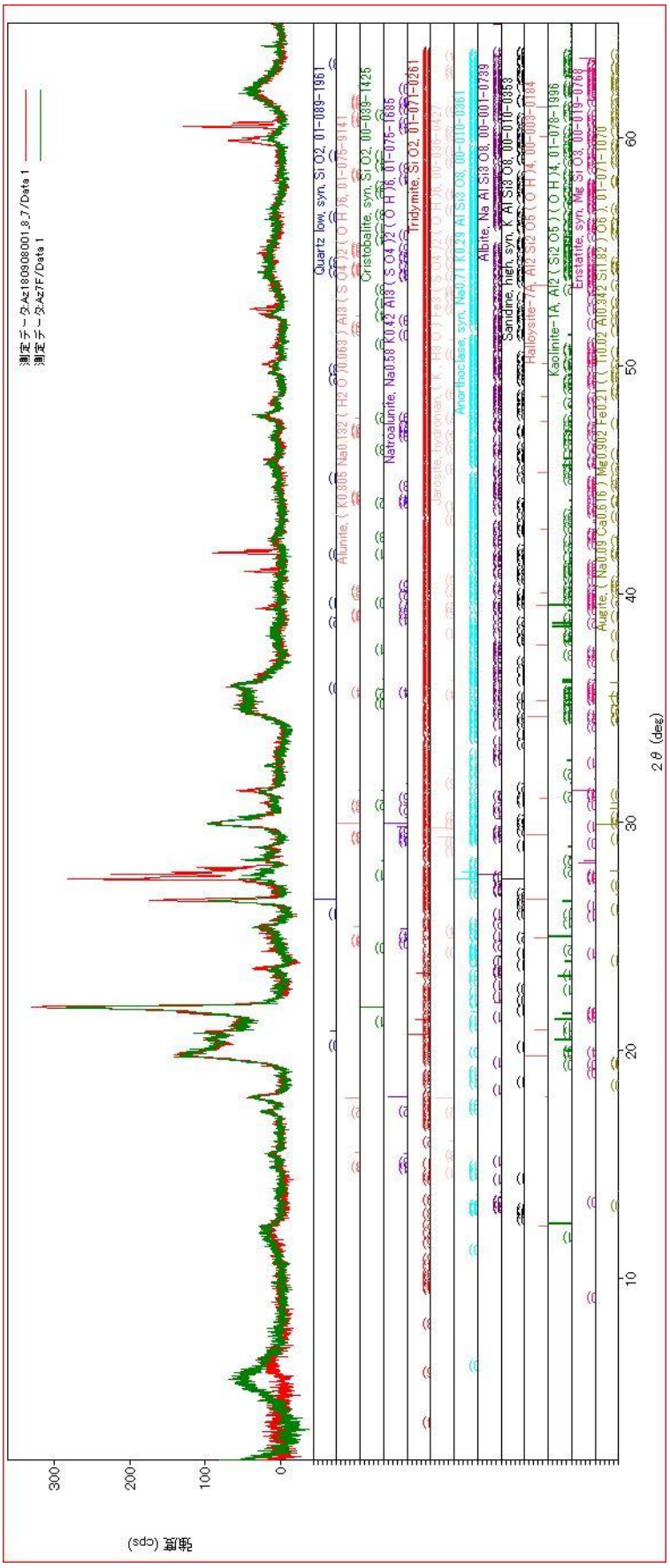
測定データAc180908001_8.7/Data 1
測定データAz7F/Data 1
Quartz low, syn, Si O2, 01-089-1961
Cristobalite, syn, Si O2, 00-039-1425
Natroalunite, Na0.58 K0.42 Al3 (S O4)2 (O H)6, 01-076-1685
Tridymite, Si O2, 01-071-0261
Albite, Na Al Si3 O8, 00-001-0739
Sanidine, high, syn, K Al Si3 O8, 00-010-0363
Halloysite-7A, Al2 Si2 O6 (O H)4, 00-029-0184
Kaolinite-1A, Al2 (Si2 O5) (O H)4, 01-078-1996
Enstatite, syn, Mg Si O3, 00-019-0768
強度 (cps)
2θ (deg)

Appendix 7: List of described ash grains in Chapter 3

*1: The characteristics are described for unaltered volcanic ash grains and unaltered part of weakly altered volcanic rock ash grain

*2: Intense: ash grains consisting only of altered minerals, Weak: ash grains consisting of unaltered ingenious rock part and altered part, Unaltered: ash grans consisting only of igneous minerals and fresh volcanic glass.

	sample code and grain no.	Descriptive name	Rock texture	Shape	Vesiculation*1	Crystallinity*1	SiO2% of glass (normalized)*1	Minral assemblage (phenocryst, groundmass or other)
1	L1-1_1	Pale grey (translucent) altered rock fragment	Infill tex by fine grained minerals	blocky				Pl-Coarse Si-Po?-Il-fine Si-Bi
2	L1-1_2	Pale yellowish grey altered volcanic rock fragment	Infill tex by fine grained minerals with holocrystalline volcanic tex	rounded	very poor (many voids by lack of crsytals?)	very well to holocrystalline	63	Pl+Alkali feld(An+Sa)+Sil+Altered glass+Il, Po(-smectite-illite)+very fine grained Sil+Alu
3	L1-1_3	Yellowish altered volcanic rock fragment	Infill tex by fine grained minerals with silicfied dissolution tex and holocrystalline volcanic tex.	elongated	very poor (many voids by lack of crsytals?)	very well to holocrystalline	too altered	Alkali feld, sil+pyrophyllite+veinlet alteration minerals (zircon-APS-goethite?)
4	L1-1_4	Pale yellowish grey altered volcanic rock fragment	Infill tex by fine grained minerals with pseudomorphs of holocrystalline volcanic tex	subrounded	very poor (many voids by lack of crsytals?)	very well to holocrystalline	70.64	Pl+Qtz+Opx, Pl+Sil+Alkali feld (Sa+Anto)+Aug+Ti-Mag, Sil+Kl+Fe-Ti ox (with APS), Sil+Kl+Alu with pure Ab and K-feldspar
5	L1-1_5	Yellowish brown altered volcanic rock fragment	Dissolution texture of massive silica with infill texture of fine grained minerals	blocky with cuspate surface	modelate (large pore may be the lack of phenocryst or microphenocryst)	well	too altered	Massive silica (with remained Pl and Aug cases), Pl+Opx+Alkali feld+rhyolitic glass (altered), sil, sil-alu-po, Ab+Illite+Chr+Epi?
6	L1-1_6	Yellowish brown altered rock fragment	Dissolution texture with pseudomorph by fine grained minerals	subrounded(vesiculated, irregular)	poor (many voids by lack of crsytals?)	well	too altered	Pl, Pl+Aug+Opx+Ti-Mag+Alkali feld (Sa)+rhyolitic glass, sil+kl+Alu+Fe-Ti oxide (with APS)
7	L1-1_7	Pale yellow grey altered rock fragment	Dissolution texture with pseudomorph by fine grained minerals and interthertal volcanic tex	blocky	n.d. (lack of phenocryst?)	very well	too altered	Pl+Aug+Opx+alkali feldspar (ant+Sa)+rhyolitic glass, sil+kl+alu(?very fine)
8	L1-1_8	Pale grey altered rock fragment	Infill tex by fine grained minerals with pseudomorphs of hypo]ocrystalline volcanic tex	blocky	n.d. (lack of phenocryst?)	n.d.,	too altered	Px+Alkali feld(Sa), sil+po+alu, Ab?
9	L1-1_9	Pale grey altered rock fragment	Dissolution texture of massive silica with infill texture of fine grained minerals	blocky	n.d. (porus and irregular shaped)	n.d.,	too altered	(Alkali feld?), sil+TiO2, Sil+po+alu(infill in vugs)
10	L1-1_10	Pale grey altered rock fragment	Dissolution texture with pseudomorph by fine grained minerals and holocrystalline volcanic tex	blocky	poor (many voids by lack of crsytals?)	very well to holocrystalline	too altered	Sil+Alkali feld (Sa), Sil+Kl (phenocryst and microphenocryst, groundmass crystals)
11	L1-1_11	Pale grey altered rock fragment	Dissolution texture of massive silica with infill texture of fine grained minerals	blocky	n.d.	n.d.,	n.d.	Remaind Pl, massive silica, sil+kl+alu+Fe-Ti oxide
12	L1-1_12	Redish volcanic rock fragment (andesitic)	porphyrytic hyalopillitic tex altered partly into disolution and infill tex of silica-kaolin minerals	rounded	poor (many voids by lack of crsytals?)	hypocrystalline	70.6	Opx+Aug, Pl+Alug+Opx+Ti Mag+rhyolitic glass
13	L1-1_13	Grey to redish volcanic altered rock fragment	Dissolution texture of massive silica with infill texture of fine grained minerals and sulfur-bearing minerals	blocky				Sa, silica, silica+Si-Al clay, Py, Baryte, K-feldspar
14	L1-1_14	Grey to redish volcanic altered rock fragment	Dissolution texture with pseudomorph by fine grained minerals, and remained hypocrystalline volcanic tex	blocky	Low	well crystalline	too altered	Il+Opx+Ti-Mag+Aug, Pl+Opx+Silica+altered rhyolitic glass, sil+kl
15	L1-1_15	Grey to redish volcanic altered rock fragment	Dissolution texture of massive silica	blocky				Sil+Ti Oxide
16	L1-1_16	Grey to redish volcanic altered rock fragment	Porphyritic tex: Hyaloohtic textute	blocky	Moderately	poorly crystalline	66.44	Opx+Aug, Pl+Aug+Opx+rhyolitic glass
17	L1-1_17	Grey to redish volcanic altered rock fragment	Dissolution texture with pseudomorph by fine grained minerals, and remained hypocrystalline volcanic tex	blocky	Low	well crystalline		Aug, Pl+Opx+Silica+Ti-Mag, Sil+Kl
18	L1-1_18	Grey to redish volcanic altered rock fragment	Precipitation of coarse silica and interstial fine minerals	blocky				Coarse s+ilica, sil+chl+alu+musc, Fe-Ti oxide+APS
19	L1-1_19	Grey to redish volcanic altered rock fragment	porphyrytic hyalopillitic to hyaloohitic tex altered partly into disolution and infill tex of fine grained minerals	blocky	n.d.	hypocrystaline		OpxTi-Mag, Pl, Sil+Kl+Alu+APS
20	L1-1_20	Grey to redish volcanic altered rock fragment	Massive fine grained minerals (psedomorphs and infill texture?)	blocky				Aug+Cr-spi, sil+kl+goe
21	L1-1_21	Grey to redish volcanic altered rock fragment	porphyrytic intertherthal tex altered partly into disolution and infill tex of silica-kaolin minerals	blocky	Low	well crystalline	75.35	Aug, Aug+Opx+Pl+Ti-Mag+Il+rhy glass
22	L1-1_22	Pale grey volcanic altered rock fragment	porphyrytic hyalopillitic tex altered partly[	blocky	Low	well crystalline	75.62	Pl, Pl+Alkali feldspar (Sa+Anot)+Ti-Mag+Il+Silica
23	L1-1_23	Pale grey altered rock fragment	porphyrytic hyalopillitic tex altered partly[	blocky	Low	well crystalline		Pl, Pl+Aug+Ti-Mag+Sil+Alkali feldspar (Sa)
24	L1-1_24	**Pale grey altered rock fragment**	**porphyrytic scoriaceous (hyalophtic to glassy) tex with infill tex of fine grained minerals**	**blocky with cuspate surface**	**high**	**very poorly crystalline**	**67**	**Opx+Ti-Mag+rhyolitic glass**
25	L1-1_25	Grey volcanic altered rock fragment	Dissolution texture with pseudomorph by fine grained minerals, and remained hyalopillitic volcanic tex	blocky	modelate	poorly crystalline	60 (glass)	no-fresh igneous minerals but altered glass there, sil, sil+alu, sil+kl+alu
26	L1-1_26	Grey volcanic altered rock fragment	Dissolution texture with pseudomorph by fine grained minerals, and remained hyaloophitic volcanic tex	blocky	modelate	very poorly crystalline	n.d.	Opx+Pl, Opx+pl+rhyolitic glass, sikl+Po+Alu.
27	L1-1_27	Grey volcanic altered rock fragment	Dissolution texture with pseudomorph by fine grained minerals, and remained hyaloohitic volcanic tex	blocky	modelate	very poorly crystalline		Pl, aug+pl+rhyolitic glass, slil, silu+alu
28	L1-1_28	Grey volcanic altered rock fragment	Dissolution texture with pseudomorph by fine grained minerals, and remained hyaloohitic volcanic tex	blocky	modelate	very poorly crystalline		, pl+pig+aug+Ti-Mag+rhyolitic glass, sil, sil+alu+aps
29	L1-1_29	Brownish gray altered volcanic rock fragment	Dissolution texture with pseudomorph by fine grained minerals, and remained hyalopillitic volcanic tex	blocky	poor	well crystalline		rhyolitic glass, sil, sil+alu
30	L1-1_30	Whitish altered volcanic rock fragment	Dissolution texture with pseudomorph by fine grained minerals, and remained holocrystalline porphyritic volcanic tex	rounded	poor	holocrystalline		Pl, Pl+Alakali feldspar (Sa, Anot)+Sil+Ti opxide, Sil+Po
31	L1-1_31	Yellowish brown altered volcanic rock fragment	Agregate of residual silica, precipitation silica, igneous minerals and altered minerals, and their fragments	subrounded				Pl+Il+Au+Opx+Ti-Mag, residual silica, Ab bearing silica, K-feldspar+biotite, sil+po+alu
32	L1-2_1	Grey to redish volcanic rock	Partly remaind hyaloophitic texture and disolved into Si-Al clay+Sil+alu pseudomorphs with colloform clay-sil.	blocky	n.d.	poor		Aug+Opx, Aug+Opx+Pl+TiMag+dacitic to rhyolitic glass,
33	L1-2_2	Grey to redish volcanic rock	Partly remaind intertherthal porphyrtic texture and dissolved into si-Al clay+sil psuedomorph from px	blocky with cuspate surface	originally high?	modelate	64	Pl, Opx+Aug+Ti-Mag+P+andesitic to dacitic glass, sil+kl
34	L1-2_3	Grey to redish volcanic rock	Partly remaind intertherthal porphyrtic texture and dissolved into si-Al clay+sil psuedomorph from px	blocky	poor	modelate		Aug+Opx+Pl+Alkali feldspar (anot)+rhyolitic glass, sil+kl
35	L1-2_4	Grey to redish volcanic rock	Partly remaind hyalopillitic porphyrtic texture and dissolved into si-Al clay+sil psuedomorph from px	blocky	poor	modelate		Aug+Opx, Pl+altered glass, sil+Po
36	L1-2_5	Grey to redish volcanic rock	Partly remaind intertherthal porphyrtic texture and dissolved into si-Al clay+sil psuedomorph from px	blocky	poor	modelate	59	pl, Aug+Pl+Opx, Aug+Opx+Pl+rhyoritic glass (intertherthal and glanular)
37	L1-2_6	Grey to redish volcanic rock	holocrystalline interthertahal porphyritic texture	blocky	extreamly poor	holocrystalline	75	pl+opx+Ti-Mag, Alkali feld (sa, anot)+Pl+Aug+Ti-Mag
38	L1-2_7	Grey to redish volcanic rock	porphyritic texture??	blocky	poor	hopocrystalline		
39	L1-2_8	Grey to redish volcanic rock	porphyritic texture??	blocky	poor	hopocrystalline		
40	L1-2_9	Grey to redish volcanic rock	porphyritic texture??	blocky	poor	hopocrystalline		
41	L1-2_10	Grey to redish volcanic rock	porphyritic texture??	blocky	poor	hopocrystalline		
42	L1-2_11	Grey to redish volcanic rock	porphyritic texture??	blocky	poor	hopocrystalline		
43	L1-2_12	Pale grey to white volcanic rock	holocrystalline intersertal porphyritic texture partly substittuted into vermiculite	blocky polygonal shape by rupture and lack of phenocrysts	extreamly poor	holocrystalline	74	Pl+Altered Opx (vermiculite)+Mag, Pl+Epd+Vermiculitic cpx-opx?+Sa+Qtz
44	L1-2_13	Pale grey to white volcanic rock	holocrystalline intersertal porphyritic texture partly substittuted into illite-silica	subrounded surface	extreamly poor	holocrystalline		Qtz (up to 100μm), Pl+Sa+Anot+K-feld (mic)+Muc+TiO2+Biotite?, illite+sil

	sample code and grain no.	Descriptive name	Rock texture	Shape	Vesiculation*1	Crystallinity*1	SiO2% of glass (normalized)*1	Minral assemblage (phenocryst, groundmass or other)
45	L1-2_14	translucent Qtz fragment	partly altered into mica clay	blocky				
46	L1-2_15	Pale grey to white volcanic rock	hyaloohitic texture	blocky to irregular	poor	poor	74	Pl+Opx+Aug+Ti-Mag, Pig+Aug++Qtz+Ti-Mag+Rhy glass
47	L1-2_16	Grey to white volcanic rock	intertherthal porphyrtic texture partly dissolved into sil+kl		poor	modelate		Opx+Aug, Opx+Aug+Pl+Pig+Rhy glass, sil+kl
48	L1-2_17	Grey to pale red altered volcanic rock	holocrystalline intersertal porphyritic texture partly substittuted into fine-grained Sil+Po	blocky to irregular	poor	holocrystalline		Opx+Pl+Ti-Mag, Opx+Ti-Mag+Anot+Sa+Qtz, Sil+Po
49	L1-2_18	Pale grey to white altered volcanic rock	holocrystalline intertherthal porphyrtic texture partly dissolved into Sil+Po psuedomorph from px or pl	blocky to irregular	poor	holocrystalline		Sil+Po pseudomorph, Pl+Sa+Qtz+Anot, sil+po
50	L1-2_19	Grey to white volcanic rock?	hyaloohitic texture mostly replased by sil+po	subrounded surface	poor	poor	70	Qtz+Ti-Mag, Qtz+Ti-Mag+rhy glass, sil+po
51	L1-2_20	Grey Qtz fragment with apatite inclusion						
52	L1-2_21	Pl fragments						
53	L1-2_22	Redish partly altered volcanic rock	intertherthal porphyrtic texture partly dissolved into sil+kl	blocky polygonal shape by ruptured phenocrysts	poor	highly		Pl+Opx (Phenocryst), Alkali feld (sa)+Pl+Aug+Tl-Mag+Opx+Rhy glass (few), sil+kl alteration
54	L1-2_23	Brown grey partly altered volcanic rock	intertherthal to dyctytaxtic porphyrtic texture partly dissolved into sil+po as pseudomorph	blocky to irregular	poor	modelate		Pl+Opx+Aug, Pl+Aug+Tl-Mag+Opx+Pig+Rhy to dacitic glass (few), sil+pol alteration
55	L1-2_24	Yellowish brown grey partly altered volcanic rock	holocrystalline intersertal porphyritic texture partly substittuted into fine-grained Sil+Po as pseudomorph	blocky to irregular	poor	holocrystalline		Aug+Opx+, PL+Alkali feld (Sa)+Qtz+Ti-Mag+Il, sil+po+alu?
56	L1-2_25	Grey to white volcanic rock	holocrystalline intersertal porphyritic texture	blocky polygonal shape by ruptured phenocrysts	poor	holocrystalline		Pl+Opx (Phenocryst)+Aug, Alkali feld (sa)+Pl+Aug+Tl-Mag+Opx+Qtz
57	L1-2_26	Grey to white altered volcanic rock	holocrystalline intersertal porphyritic texture	blocky polygonal shape by ruptured phenocrysts	poor	holocrystalline		phenocryst is all altered, Alkali feld (sa)+Pl+Tl-Mag+Qtz
58	L1-2_27	Po altered Opx fragment						
59	L1-2_28	Brown grey partly altered volcanic rock	porphyritic texure almost altered into sil+kl aggregate and bright jarosite veins	blocky	n.d.	n.d.	n.d.	remained Pl phenocryst and pseudomorph, sil+kl+jarosite
60	L1-2_29	White altered rock	dissolusion texture of massive silica	blocky	n.d.	n.d.	n.d.	sil+py
61	L1-2_30	White altered rock	dissolusion texture of massive silica with pore filling alunite aggregate	blocky	n.d.	n.d.	n.d.	sil, alu+TiO2 mineral
62	L1-2_31	Opx fragment						
63	L1-2_32	Brown partly altered volcanic rock	intertherthal to dyctytaxtic porphyrtic texture partly altered into sil+po	blocky polygonal shape by ruptured phenocrysts	poor	highly		Opx (Phenocryst), Opx+aug+Timag, Alkali feld (sa)+Pl+Aug+Tl-Mag+Opx+Qtz+Rhy glass (few), sil+po alteration
64	L1-2_33	Yellowish grey partly altered volcanic rock	porphyritic texure almost altered into sil+kl aggregates	blocky	modelate?	n.d.	n.d.	remained Pl+Opx phenocryst and pseudomorph, sil+kl
65	L1-2_34	Yellowish grey partly altered volcanic rock	porphyritic texure almost altered into sil+kl aggregates	blocky	modelate?	n.d.	n.d.	remained Pl+Opx phenocryst and pseudomorph, sil+kl
66	L1-2_35	Redish partly altered volcanic rock	hyalophtic porphyrtic texture partly dissolved into sil+kl	blocky polygonal shape by ruptured phenocrysts	high	poor	n.d.	Pl+Opx (Phenocryst), Aug+Opx+Pl+timagm, Aug+Pl+Timag+Rhy glass (few), sil+kl alteration
67	L1-2_36	Pl fragments						
68	L1-2_37	Grey to pale red altered volcanic rock	holocrystalline intersertal porphyritic texture partly substittuted into fine-grained Sil+Po	blocky to irregular	poor	holocrystalline	n.d.	Opx+Pl+Ti-Mag, Opx+Ti-Mag+Anot+Sa+Qtz, Sil+Po
69	L1-2_38	Pale grey igneous rock?	holocrystalline equigranular	blocky	poor	holocrystalline	n.d.	Microcline+Albite+Sanidine+Pl+Biotite (granitic?)
70	L2_1	Partly altered brown grey scoriaceous volcanic rock	partly infill texture of sil+kl+alu to the scoriaceous hyaloophtic porphyrytic texture	irregular to cuspate	high	poor	60	Opx+Pl, Pl+Opx+Au+Pig+Apt+andesitic to rhyolitic glass, sil+kl+alu
71	L2_2	Brown grey partly altered volcanic rock	dyctyctaxitic to intersertal porphyrytic texture partly altered into sil+kl+alu aggregates (pseudomorph)	blocky	poor	modelate	65	Aug+Opx+Pl, Opx+Aug+Pl+rhyolitic glass, sil+kl+alu
72	L2_3	Brown grey partly altered volcanic rock	porphyrytic texture almostly altered into sil+kl aggregates (pseudomorph and colloform)	blocky	n.d.	n.d.	n.d.	Opx, Opx+Ti-Mag, ruptured pl+ px fragments and sil+kl
73	L2_4	Transparent rhyolitic glass shard		blocky to irregular	moderelate	no	75	rhyolitic glass (95wt%)
74	L2_5	Brown grey partly altered scoriaceous volcanic rock	partly infill texture of sil+kl+alu to the scoriaceous hyaloophtic porphyrytic texture	irregular to cuspate	high	extreamly poor	62	Pl+Aug+Qtz, pl+andesitic glass, sil+alu
75	L2_6	Translucent white altered rock	dissolution texture of massive silica with pore-filling pyrite	blocky	n.d.	n.d.	n.d.	Qtz?+Py
76	L2_7	Brown grey volcanic rock (weathered)	hyaloohtic porphyrytic texture with highly vesiculated (more crystalline than 1) (rhyolitic glass melt inclusion there)	irregular to cuspate	high	modelate	56	Microphenocrysitc, Ol+Pig+Aug, Pl+Aug+Pig+andesitic glass with (rhyolitic melt inclusion glass)
77	L2_8	Brown grey to grey altered rock	Aggregate of alunite crystals (infill texture??)	rounded	n.d.	n.d.	n.d.	Alu
78	L2_9	Translucent white altered rock	dissolution texture of massive silica with pore-filling TiO2 mineral	blocky	n.d.	n.d.	n.d.	Qtz?+TiO2 mineral
79	L2_10	altered Opx fragment with IL						
80	L2_11	Aug fragment with rhy melt inclusion						
81	L2_12	Light grey altered volcanic rock	hyaloohtic porphyrytic texture almostly altered into sil+kl aggregates (pseudomorph and colloform)	blocky	modelate	poor	80	Opx, Aug+Opx+Pl+rhy glass,
82	L2_13	Trancent Qtz fragment						
83	L2_14	Trancent Qtz fragment						
84	L2_15	Translucent white partly altered pumiceous volcanic rock	pumiceous glassy porphyrytic texture partly altered by sil+kl aggregates filling fractures	irregular to cuspate	modelate?	extreamly poor		Pl+Alkali feld (Sa)+rhyicolitic glass (mostly Sa but porphyrytic Pl glass also occurs)
85	L2_16	Translucent white altered rock	dissolution texture of massive silica with pore-filling TiO2 mineral, and microveinlet silica	blocky	n.d.	n.d.	n.d.	Qtz?+TiO2 mineral
86	L2_17	Translucent white altered rock	dissolution texture of massive silica with pore-filling TiO2 mineral, and microveinlet precipitation silica	blocky	n.d.	n.d.	n.d.	Qtz?+TiO2 mineral
87	L2_18	White igneous rock	holocrystalline porphyrytic texture	irregular to cuspate	high	holocrystalline		Qtz+Alkali feld (Sa)+Ti-Mag
88	L2_19	Opx fragment with IL						
89	L2_20	Brown grey partly altered volcanic rock	porphyrytic texture almostly altered into sil+kl aggregates (pseudomorph and colloform)	irregular to cuspate	n.d.	n.d.	n.d.	remained Opx and Il, Sil+Kl+
90	L2_21	Trancent Qtz fragment						
91	L2_22	White volcanic rock	holocrystalline equiglanular texture	blocky	modelate	holocrystalline		Alkali feld (Sa, micrl)+Pl(~Ab86)
92	L2_23	Trancent Qtz fragment						
93	L2_24	White altered rock	Precipitation silica and muscovite interstially filled with sil+ill fine crystal aggregate	blocky	n.d.	n.d.	n.d..	Qtz+Musc+TiO2 mineral, sil+Ill
94	L2_25	Brown grey partly altered volcanic rock	Holocrystalline intersertal porphyrytic texture altered into sil+kl aggregates (pseudomorph)	blocky with irregular surface	modelate	holocrystalline	58	Aug+Mag+Opx, Aug+Qtz+Alkali feld (Sa), sil+kl?
95	L2_26	Brown grey partly altered volcanic rock	Holocrystalline intersertal porphyrytic texture altered into sil+kl aggregates (pseudomorph)	irregular to cuspate	modelate	holocrystalline	n.d.	no remain phenocryst, Pl+Alkali feld (anothoclase, sa)+Qtz
96	L2_27	Brown grey partly altered volcanic rock	Holocrystalline intersertal porphyrytic texture altered into massive sil and sil+alu fine crystal aggregates	blocky	modelate	holocrystalline		Aug+Opx, Pl+Alkali feld (anothoclase, sa)+Qtz
97	L2_28	Translucent white altered rock	dissolution texture of massive silica with pore-filling Py and sil+kl aggregates	blocky	n.d.	n.d.	n.d.	Qtz?+Py, sil+kl
98	L2_29	Transparentrhyolitic glass shard with sil+alu alteration		blocky to irregular	moderelate	no	75	rhyolitic glass (95wt%)
99	L2_30	Brown grey partly altered volcanic rock	Porphyrytic texture almost substited by sil+kl+alu fine crystal aggregates	blocky to irregular	n.d.	n.d.	n.d.	pl+Qtz fragments
100	L2_31	Brown grey partly altered volcanic rock	Porphyrytic texture almost substited by sil+kl+alu fine crystal aggregates	blocky to irregular	n.d.	n.d.	n.d.	pl+Qtz fragments

	sample code and grain no.	Descriptive name	Rock texture	Shape	Vesiculation*1	Crystallinity*1	SiO2% of glass (normalized)*1	Minral assemblage (phenocryst, groundmass or other)	Alteration degree*2
101	L2_32	Trancent Pl phenocryst (DVR)	Pl phenocryst with vesiculated groundmass partly altered into Sil+Alu (APS?)	blocky to irregular	modelate?	poor			weakly altered
102	L2_33	Trancent Qtz fragment							
103	L2_34	Dark grey scoriaceous volcanic rock	dyctytaxtic to hialopillitic porphyrytic texture partly altered into Sil+Alu just filling vesicules	irregular to cuspate	high	high	57	, Pl+Aug+Opx+Andesitic glass, sil+alu	weakly altered
104	L2_35	Brown grey partly altered volcanic rock	hyaloohtic porphyrytic texture almostly altered into sil+kl aggregates (pseudomorph)	irregular to cuspate	n.d.	poor		, Pl+Opx remain, altered glass (rhyolitic?)	weakly altered
105	L2_36	Yellowish brown grey partly altered volcanic rock	porphyrytic texture almostly altered into sil+kl aggregates (pseudomorph)	irregular to cuspate	poor	high?		, Pl+Qtz+Alkali feld (Sa) remain	weakly altered
106	L2_37	Dark grey altered volcanic rock	hyaloohtic porphyrytic texture altered into sil+alu (pseudomorphic phenocryst)	irregular to cuspate	modelate?	poor	n.d.	, Pl+Opx+Ti-Mag+altered glass (dacitic?)	weakly altered
107	L2_38	Aug fragment							
108	L2_39	Transparent Qtz fragment							
109	L2_40	Brown grey scoriaceous volcanic rock	hyaloohtic (glassy?) porphyrytic texture	irregular to cuspate	high	poor	55	, Pl+Opx+Aug+Pig?+andesitic glass	unaltered?
110	L2_41	Brown grey altered scoriaceous volcanic rock	hyaloohtic (glassy?) porphyrytic texture	irregular to cuspate	high	poor		, Pl+Opx+Aug+andesitic glass	unaltered?
111	L3_1	Black volcanic rock	hyalophtic porphyrytic texture (scoriaceous?)	Irregular to cuspate	high	poor	64	Pl, Opx+Ti Mag+Pl+Pig?+rhy glass	unaltered
112	L3_2	Brown grey partly altered volcanic rock	intersertal porphyrytic texture almostly altered into sil+po aggregates (pseudomorph and colloform) with wethered jarosite or FeOH mineral vein	blocky	poor	high	n.d.	Remained Opx microphenocryst, Qtz+Il+altered rhy glass (or sa?), sil+po+jarosite or FeOH mineral	weakly altered
113	L3_3	White altered rock	dissolution texture of massive silica (pseudomorph) with pore-filling alunite or sil+alu aggregates	blocky	n.d.	n.d.	n.d.	Sil+Alu	Intensely
114	L3_4	White altered rock	dissolution texture of massive silica with pore-filling alunite or sil+alu aggregates	blocky	n.d.	n.d.	n.d.	Sil+Alu+TiO2 mineral	Intensely
115	L3_5	Redish brown to grey volcanic rock	holocrystalline intersertal porphyrytic texture	blocky	poor	holocrystalline	64	Opxl, Pl+Aug+Opx+Alkali feld (Sa and Anot)TiMag+Il+Qtz,	unaltered
116	L3_6	White altered Pl fragment	dissolution silicification and sil+alu alteration undergone from fluid-solid surface						weakly altered
117	L3_7	light greenish volcanic rock	hyalopillitic pophyrytic texute	blocky	poor	high	n.d.	Opx+Pl+Ti Mag, ,Opx+Aug+Pl+Ti-Mag+Qtz+rhy glass	unaltered
118	L3_8	Opx fragment with inclusions of Cu-Fe sulfide and pl							
119	L3_9	Opx phenocryst fragment with groundmass glass and altered by sil+alu							weakly altered
120	L3_10	White altered volcanic vrock	holocrystalline intersertal porphyrytic texture altered into sil+kl+alu aggregates (pseudomorph and colloform)	blocky	poor	holocrystalline	n.d.	Aug+Pl+Akali feld (Sa and Anot)+Qtz, sil+kl+alu	weakly altered
121	L3_11	Brown grey partly altered volcanic rock	holocrystalline intersertal porphyrytic texture almost altered into sil+kl+alu aggregates (pseudomorph and colloform) with wethered jarosite or FeOH crust	rounded	poor	holocrystalline	n.d.	Opx, Pl+Akali feld (Sa and Anot)+Qtz+Il+TiMAg, sil+kl+alu	weakly altered
122	L3_12	White translucent volcanic rock	hyalophtic porphyrytic texture	Irregular to cuspate	high	poor to modelate	70	Aug+Opx+Pl, Pl+Opx+Aug+Qtz+rhy glass	unaltered
123	L3_13	Light grey translucent partly altered volcanic rock	dyctytaxtic to intersertal porphyrytic texture almost altered into sil+kl+alu aggregates (pseudomorph and colloform)	blocky to irregular	poor	high	n.d.	, Opx+Pl+Mag+altered rhy glass, sil+kl+alu	weakly altered
124	L3_14	White translucent volcanic rock	hyalophtic porphyrytic texture	Irregular to cuspate	high	poor to modelate	63	Pl+Opx+Aug+Qtz+rhy glass	unaltered
125	L3_15	Grey altered volcanic rock	dyctytaxtic to intersertal porphyrytic texture completely altered into sil+kl+ aggregates (pseudomorph)	blocky	n.d.	n.d.	n.d.	Sil+kl+Il+Mag?	Intensely
126	L3_16	White translucent altered rock (glass?)	vesicular glass fragment with sil, sil+alu alteration	Irregular to cuspate	high	none	n.d.		weakly altered
127	L3_17	Light grey translucent volcanic rock	holocrystalline intersertal porphyrytic texture	blocky to irregular	high	holocrystalline	72	, Opx+Pl+Alkali feld (Sa and Anot)+Timag+Qtz	unaltered
128	L3_18	Pl fragment							
129	L3_19	White altered rock	dissolution texture of massive silica (pseudomorph) with pore-filling sil+kl aggregates	blocky	n.d.	n.d.	n.d.	sil, Sil+kl	Intensely
130	L3_20	Light grey translucent partly altered volcanic rock	intersertal porphyrytic texture almost altered into sil+po aggregates (pseudomorph)	blocky	poor	holocrystalline	n.d.	Pl, Opx+Ti Mag+Pl+Aug+Alkali feld (sa+anot)+Qtz	unaltered
131	L3_21	Pl fragment with sil+po alteration							weakly altered
132	L3_22	Light grey translucent volcanic rock	holocrystalline intersertal porphyrytic texture	blocky	poor	holocrystalline	76	Pl+Timag+Qtz, Opx+Ti Mag+Pl+Alkali feld (sa)+Qtz	unaltered
133	L3_23	Brown grey partly altered volcanic rock	hyaloophticl porphyrytic texture (glassy pumiceos?) almost altered into sil+po+alu aggregates (pseudomorph of phenocrysts and colloform in fractures)	blocky	poor	very poor	71	pseudomorph, pl+pig?+timag+il+rhy glass, sil+po+alu	weakly altered
134	L3_24	Pl phenocryst fragment							
135	L3_25	White altered rock	dissolution texture of massive silica (pseudomorph) with pore-filling alunite or sil+alu aggregates	rounded	n.d.	n.d.	n.d.	Sil+Alu+TiO2 mineral	Intensely
136	L3_26	Pl fragment with Opx inclusion							
137	L3_27	Grey altered volcanic rock	porphyrytic texture completely altered into sil(+alu) aggregates (pseudomorph and colloform amigdule)	blocky	n.d.	n.d.	n.d.	Sil+alu, almost silica	Intensely
138	L3_28	Cpx fragment with Il orTimag or rhy glass inclusions							
139	L3_29	Yellowish white altered rock	massive aggregate of fine grained sil+kl mixtures	rounded	n.d.	n.d.	n.d.	Sil+kl	Intensely
140	L3_30	Grey partly altered volcanic rock ?	equiglanular?	blocky to irregular	high	holocrystalline	n.d.	Pl+Akali feld (Sa)+Qtz+Spinel+Illite or amphibole (全然わからない)	?
141	L3_31	Grey partly altered volcanic rock	holocrystalline intersertal porphyrytic texture	blocky to irregular	poor	holocrystalline	73	Pl+Opx+Timag,	
142	L3_32	Black volcanic rock	hyalophtic porphyrytic texture (scoriaceous?)	Irregular to cuspate	high	poor	65	Ol+Aug+Opx, Opx+Timag+Aug+Pl+Qtz+rhy glass	unaltered
143	L3_33	silicified Cpx fragment with pore filling alunite sil aggregates							weakly altered
144	L3_34	Brown grey partly altered volcanic rock	porphyrytic texture almostly altered into sil+kl+vermiculite aggregates (pseudomorph and colloform) (weathered and hydrothermally altered scoriaceous)	Irregular to cuspate	high?	n.d.	n.d.	sil (massive silicified), sil+kl, vermiculite	Intensely
145	L3_35	Pl fragment							
146	L3_36	Light grey translucent volcanic rock	holocrystalline intersertal porphyrytic texture	blocky	poor	holocrystalline	76	Pl+Timag+Qtz, Opx+Ti Mag+Pl+Alkali feld (sa)+Qtz	unaltered
147	L4_1	Redish brown to grey volcanic rock	dyctytaxitic to intersertal porphyrytic texture	blocky	poor	high	62	Aug+Opx+Pl, Pl+Alkali feld (anort)+Aug+Ti Mag+rhy glass (sa)	unaltered?
148	L4_2	White altered volcanic rock	Well crystalline intersertal porphyrytic texture partly altered into sil+po+alu aggregates (pseudomorph from microphenocryst and colloform in vesicule)	blocky	modelate?	very high	n.d.	psudomophs, Pl+Sa+rhyolitic glass, sil+Po+alu	weakly altered
149	L4_3	Black partly altered volcanic rock	hyalophtic to hyalopilitic porphyrytic texture partly filled by sil+alu aggregates	blocky to irregular	moderelate	modelate	64	Opx, Aug+Opx+Pl, Aug+Opx+Pl+rhy glass (sa and anort), sil+alul	weakly altered
150	L4_4	light grey holocrystalline volcanic rock	Holocrystalline intersertal porphyrytic texture	blocky	poor?	holocrystalline	77	Pl+Qtz+Sa+Opx microphenocryst to groundmass	unaltered?
151	L4_5	Brown grey volcanic rock	hyalophtic to hyalopilitic porphyrytic texture	blocky	poor?	modelate	63	Pl, Aug+Opx, Aug+Pl+Alkali feld (anort?)+Opx+Pig?+rhy glass	unaltered?
152	L4_6	Black veicular volcanic rock	hyalopilitic porphyrytic texture (with ruptured Pl)	blocky to irregular	high	modelate	63	Pl, Aug+Opx+Pl+Pig+rhy glass	unaltered?
153	L4_7	Pl frgament							unaltered
154	L4_8	Black volcanic rock	dyctyctaxitic to intersertal porphyrytic texture	blocky	modelate	high	65	Aug+ Opx+Ol, Pl+Aug+Pig?+TiMag+rhy glass	unaltered
155	L4_9	Redish brown to grey partly altered volcanic rock	porphyrytic texture almostly altered into sil+kl+alu aggregates (pseudomorph and colloform) with wethered jarosite vein	blocky	n.d.	n.d.	n.d.	remained groundmass Opx+Aug+Pl+Qtz??, Sil+Kl+Alu and jarosite	weakly altered

	sample code and grain no.	Descriptive name	Rock texture	Shape	Vesiculation*1	Crystallinity*1	SiO2% of glass (normalized)*1	Minral assemblage (phenocryst, groundmass or other)	Alteration degree*2
156	L4_10	Brown grey volcanic rock	intersertal porphyrytic texture	blocky	poor	very high	56	Opx+Pl+Aug, Pl+Opx+Aug+rhy glass	unaltered?
157	L4_11	Translucent white altered rock	dissolution texture of massive silica with pore-filling alunite or sil+alu aggregate	blocky	(many vugs)	n.d.		sil+alu	Intensely
158	L4_12	Light grey altered volcanic rock	porphyrytic texture almostly altered into sil+kl aggregates (pseudomorph and colloform)	blocky	n.d.	n.d.	n.d.	sil+kl	weakly altered
159	L4_13	Light grey altered volcanic rock	porphyrytic texture almostly altered into sil+kl aggregates (pseudomorph and colloform)	blocky	n.d.	n.d.	n.d.	sil+kl+alu, altered glass?, ruotured pseudomorphic phenocryst	Intensely
160	L4_14	Black volcanic rock	intersertal porphyrytic texture	blocky	modelate	modelate	61	Aug+ Opx+Ol+Ti Mag (microphenocrystic), Opx+Aug+Pig?+Pl+dacitic glass	unaltered
161	L4_15	Black volcanic rock	hyalopillitic to intersertal porphyrytic texture	blocky	modelate	modelate	64	Pl+Aug, Opx+Aug+Pig?+Pl+rhy glass	unaltered
162	L4_16	Aug fragment (+Pl+Opx+small groundmass)							unaltered
163	L4_17	Brown grey volcanic rock (scoriaceous?)	porphyrytic texture almostly altered into sil+po+alu aggregates	Irregular to cuspate	high?	poor?	n.d.	remained Opx+Pl+Aug+rhy glass, sil+Po+alu aggregate	weakly altered
164	L4_18	Grey volcanic rock	dyctyctaxitic to intersertal porphyrytic texture	blocky	poor	high	68	Aug+Opx, Pl+Aug+Opx+TiMag+Qtz+rhy glass	unaltered
165	L4_19	Pale grey partly altered volcanic rock	holocrystalline intersertal porphyrytic texture partly filled by sil+alu aggregates	blocky	poor	holocrystalline	67	Aug+Opx+Pl, Pl+Aug+Opx+Alkali feld (Sa and Anot)TiMag+Il+Qtz, sil+alu aggregate	weakly altered
166	L4_20	Grey volcanic rock	holocrystalline intersertal porphyrytic texture	blocky	poor	holocrystalline	60	Aug+Opx+Pl, Pl+Aug+Opx+Alkali feld (Sa)+Mag+Il+Qtz	unaltered
167	L4_21	Pale grey volcanic rock	holocrystalline intersertal porphyrytic texture	blocky	poor	holocrystalline	71	Aug+Opx+Pl, Pl+Aug+Opx+Alkali feld (Sa)+Mag+Il+Qtz	unaltered
168	L4_22	Brown to grey partly altered volcanic rock	hyalopilitic to hyaloohtic texture almostly altered into pore filling sil+kl-vermiculite+alu aggregates (pseudomorph and colloform)	blocky to irregular	modelate	modelate	n.d.	Pl+Aug, Opx+Aug+Pig?+Pl+rhy glass, sil+kl+vermiculite+alu	weakly altered
169	L5_1	Brown grey partly altered volcanic rock	porphyrytic texture almost altered into sil+kl+alu aggregates (pseudomorph of phenocrysts and colloform in fractures)	blocky	n.d.	n.d.	n.d.	little of sanidine, sil+kl, alu (APS)	weakly altered
170	L5_2	Light grey altered rock	dissolution texture of massive silica (pseudomorph) with pore-filling alunite or sil+alu aggregates	blocky	n.d.	n.d.	n.d.	Sil+Alu	Intensely
171	L5_3	Grey partly altered volcanic rock ?	equiglanular?	blocky to irregular	high	holocrystalline?	58	Akali feld (Sa)+Spinel, sil+alu	?
172	L5_4	Pl phenocryst fragment with rhy glass melt inclusion							
173	L5_5	Brown grey partly altered volcanic rock	holocrystalline intersertal porphyrytic texture slightly altered into sil+kl aggregates	blocky	modelate	holocrystalline	66	Ruptured Pl+Opx+Timag, Qtz+Alkali feld (sa and anot)+Opx, sil+kl	weakly altered
174	L5_6	black volcanic rock	holocrystalline intersertal porphyrytic texture	blocky	modelate	holocrystalline	71	Opx+Aug, Qtz+Alkali feld (sa and anot)+Opx	unaltered
175	L5_7	Redish brown to grey partly altered volcanic rock	porphyrytic texture almost altered into sil+kl+alu aggregates (pseudomorph of phenocrysts and colloform in fractures)	blocky	n.d.	n.d.	n.d.	little of pl+aug, sil+kl	weakly altered
176	L5_8	Redish brown to grey partly altered volcanic rock	porphyrytic texture altered into sil+alu aggregates (pseudomorph of phenocrysts and colloform in fractures)	blocky	poor	n.d.	n.d.	Qtz+Alkali feld (sa and anot)+Opx, sil+alu	weakly altered
177	L5_9	White altered rock	holocrystalline intersertal porphyrytic texture altered into sil+kl+alu aggregates (pseudomorph of phenocrysts and colloform in fractures)	blocky	n.d.	n.d.	n.d.	Qtz+Alkali feld (sa and anot)+Il+Py, sil+kl	weakly altered
178	L5_10	Qtz fragment							
179	L5_11	Light grey partly altered volcanic rock	holocrystalline intersertal porphyrytic texture slightly altered into sil+kl aggregates	blocky	modelate	holocrystalline	n.d.	Pl, Pl+Opx+pl+alkali feld (sa and anot)	weakly altered
180	L5_12	Pl fragment							
181	L5_13	Aug phenocryst fragment with groundmass							
182	L5_14	Pl fragment							
183	L5_15	White altered rock	coase Qtz and sil+ill fine crystal aggregates	rounded	n.d.	n.d.	n.d.	Qtz, sil+ill+TiO2 mineral	Intensely
184	L5_16	Light grey altered rock	dissolution texture of massive silica alunite or sil+alu aggregates (pseudomorph)	blocky	n.d.	n.d.	n.d.	Sil+Alu+TiO2 mineeal	Intensely
185	L5_17	Light grey altered rock	dissolution texture of massive silica (weakly pseudomorphic tex)	blocky	n.d.	n.d.	n.d.	Sil	Intensely
186	L5_18	Translucent wewakly altered volcanic rock	hyaloophtic (scoriaceous) texture altered into sil+Po+alu aggregates (pseudomorph of phenocrysts and colloform in fractures)	Irregular to cuspate	high?	poor	n.d.	Opx, Pl+Timag+Aug+Opx+Qtz+dacitic glass, sil+po+alu	weakly altered
187	L5_19	Grey partly altered volcanic rock ?	Almost dissolution texture of massive silica with remained igneous minerals	blocky	n.d.	n.d.	n.d.	remained Opx+Timag (mag?)+sa?, sil	weakly altered
188	L5_20	Grey partly altered volcanic rock ?	porphyrytic texture almost altered into sil+kl+alu aggregates (pseudomorph of phenocrysts and colloform in fractures)	blocky	high?	n.d.	n.d.	remained Opx+Aug+Alkali feld (anot)+Qtz, sil+kl+alu	weakly altered
189	L5_21	White altered rock	dissolution texture of massive silica (weakly pseudomorphic tex)	blocky	n.d.	n.d.	n.d.	Sil+TiO2 mineral	Intensely
190	L5_22	White altered volcanic rock	hyaloophtic porphyrytic texture (pumiceous) with whole altered hydrous glass (wethered?)	blocky	modelate	poor	88	Pl+Qtz+TiO2 mineral+rhy glass, sil+alu	weakly altered
191	L5_23	Pl phenocryst fragment with Opx pheno and groundmass	holocrystalline intersertal porphyrytic texture	blocky	modelate	holocrystalline	59	Ruptured Pl+Opx, Qtz+Alkali feld (sa and anot)+Opx	unaltered
192	L5_24	Brown grey partly altered volcanic rock	porphyrytic texture almost altered into sil+po+alu massive aggregates	Irregular to cuspate	high?	n.d.	n.d.	Ruptured Pl+Opx+Timag+microcline, sil+po+alu	weakly altered
193	L5_25	black volcanic rock	intersertal porphyrytic texture	blocky	modelate	very high	74	Opx+Pl, Qtz+Alkali feld (sa)+Opx+Qtz+Aug+Timag+rhy glass	unaltered
194	L5_26	Light grey altered rock	alomost substitued by dissolution texture of massive silica (weakly pseudomorphic tex) with sil+kl	blocky	vuggy	n.d.	n.d.	Sil, little of sil+alu aggregate, remaind Opx, sil+kl	weakly altered
195	L5_27	Light grey altered rock	alomost substitued by dissolution texture of massive silica (weakly pseudomorphic tex)	blocky	vuggy	n.d.	n.d.	Sil, little of sil+alu aggregate, remaind Opx	weakly altered
196	L5_28	Qtz fragment							
197	L5_29	Pl fragment							
198	L5_30	black volcanic rock	hyalopillitic to intersertal porphyrytic texture	blocky	modelate	modelate	61	Opx, Opx+Pl+Timag+rhy glass	unaltered
199	L5_31	brown grey volcanic rock	hyalopillitic to intersertal porphyrytic texture	blocky to irregular	modelate	modelate	65	Opx+Aug+Pl+Timag+rhy glass	unaltered
200	L5_32	Light grey altered rock	alomost substitued by dissolution texture of massive silica (weakly pseudomorphic tex)	Irregular to cuspate	vuggy	n.d.	n.d.	Sil, remained il	Intensely
201	L5_33	Light grey altered rock	alomost substitued by dissolution texture of massive silica (weakly pseudomorphic tex) (originally scoreaceous or pumiceous?)	Irregular to cuspate	high?	n.d.	n.d.	Sil, little of sil+alu aggregate	Intensely
202	L5_34	Grey altered volcanic rock	socoriaceous (glassy) porphyritic texture almost altered into silicification (silica pseudomorph)	Irregular to cuspate	high	poor	n.d.	pl+aug+andesitic glass, sil	weakly altered
203	L5_35	Light grey partly altered volcanic rock	holocrystalline intersertal porphyrytic texture altered into sil+kl aggregates (pseudomorph of phenocrysts and colloform in fractures)	blocky	poor	holocrystalline	78	Qtz, Qtz+Allkali feld (anot and sa)+Mag+Timag, sil+kl	weakly altered
204	L5_36	Pl fragment with sil+kl alteration							
205	L5_37	Grey altered volcanic rock	socoriaceous (glassy) porphyritic texture almost altered into coase massive silica and sil+ill fine crystal aggregates	Irregular to cuspate	high	poor	n.d.	Opx+il remained, sil and sil+illite	weakly altered
206	L5_38	white altered rock	massive aggregate of fine grained sil+kl+alu mixtures	rounded	n.d.	n.d.	n.d.	Sil+kl+alu	Intensely
207	L5_39	Light grey partly altered volcanic rock	holocrystalline intersertal porphyrytic texture altered into sil+kl aggregates (pseudomorph of phenocrysts and colloform in fractures)	blocky	poor	holocrystalline	n.d.	Qtz, Qtz+Allkali feld (sa)+Il, sil+kl	weakly altered
208	L5_40	white altered rock	massive aggregate of fine grained sil+kl mixtures	rounded	n.d.	n.d.	n.d.	Sil+kl+TiO2	Intensely
209	L6_1	Brown grey partly altered volcanic rock	hyaloophtic to hyalopillitic porphyrytic texture altered into sil+kl+alu aggregates (pseudomorph of phenocrysts and colloform in fractures)	blocky	modelate	modelate	62	Opx+Pl+Aug, Pl+Aug+Opx+Pig+Timag+rhy glass, sil+kl	weakly altered
210	L6_2	Black volcanic rock	dyctytaxtic to intersertal porphyrytic texture	blocky to irregular	poor	high	64	Opx+Pl+Aug, Pl+Aug+Opx+Pig+Timag+Qtz+rhy glass	unaltered

	sample code and grain no.	Descriptive name	Rock texture	Shape	Vesiculation*1	Crystallinity*1	SiO2% of glass (normalized)*1	Minral assemblage (phenocryst, groundmass or other)	Alteration degree*2
211	L6_3	Pl fragment with two pyroxene inclusions							
212	L6_4	Dark brown volcanic rock	hyaloophtic to hyalopillitic porphyrytic texture	blocky	poor	modelate	63	Opx, Pl+Aug+Opx+Pig+Timag+rhy glass	unaltered
213	L6_5	Brown grey volcanic rock (translucent?)	hyaloophtic to hyalopillitic porphyrytic texture	blocky to irregular	poor	modelate	n.d.	Pl, Pl+Aug+Opx+Timag+rhy glass	unaltered
214	L6_6	Brown grey volcanic rock (translucent?)	hyaloophtic to hyalopillitic porphyrytic texture	blocky to irregular	modelate	modelate	62	Opx+Aug+Pl, Pl+Aug+Opx+Pig+Timag+rhy glass	unaltered
215	L6_7	Brown grey partly altered volcanic rock	porphyrytic texture altered into sil+kl+alu aggregates	irregular to cuspate?	modelate	modelate	n.d.	Ruptured Pl+Opx+rhy glass, sil+kl+alu	weakly altered
216	L6_8	Light grey altered volcanic rock	porphyrytic texture copletely altered into sil+kl+alu aggregates (pseudomoprhs of porphyrytic phenocrysts)	blocky	n.d.	n.d.	n.d.	sil, sil+kl+alu	Intensely
217	L6_9	Light grey partly altered volcanic rock	holocrystalline intersertal porphyrytic texture altered into sil+po aggregates (pseudomorph of phenocrysts and colloform in fractures)	blocky	poor	holocrystalline	66	Opx+Aug+Pl, Pl+Aug+Opx+Pig+Timag+alkali feld (sa)+Qtz, sil+po	weakly altered
218	L6_10	White altered rock	porphyrytic texture completely altered into sil+kl aggregates (pseudomorph and pore filling colloform, microveinlet) and massive silica	blocky	n.d.	n.d.	n.d.	sil, sil+kl	Intensely
219	L6_11	Pl fragment							
220	L6_12	Brown grey volcanic rock (translucent?)	hyaloophtic to hyalopillitic porphyrytic texture	blocky to irregular	high	poor	63	Opx+Aug, Pl+Aug+Opx+Plg+Timag+rhy glass	unaltered
221	L6_13	Brown grey volcanic rock (translucent?)	hyaloophtic to hyalopillitic porphyrytic texture	blocky to irregular	high		61	Opx+Aug, Pl+Aug+Opx+Pig+Timag+rhy glass	unaltered
222	L6_14	White altered rock	holocrystalline intersertal porphyrytic texture altered into sil+kl aggregates (pseudomorph of phenocrysts and colloform in fractures)	blocky	poor	holocrystalline	n.d.	Opx+Aug+Pl, Pl+Aug+Opx+Pig+Timag+alkali feld (sa and anot)+Qtz, sil+kl	weakly altered
223	L6_15	Light yellowish brown partly altered volcanic rock	porphyrytic texture altered into sil+kl+alu aggregates	blocky to irregular	n.d.	n.d.	n.d.	Ruptured Pl, sil+kl+alu	weakly altered
224	L6_16	Dark brown volcanic rock	hyaloophtic to hyalopillitic porphyrytic texture	blocky	modelate	modelate	62	Opx+Aug+pl, Pl+Opx+Pig+Timag+rhy glass	unaltered
225	L6_17	Light grey altered rock	dissolution texture of massive silica	blocky	vuggy?	n.d.	n.d.	Sil+py	Intensely
226	L6_18	Brown grey volcanic rock (translucent)	glassy scoriaceous porhyrytic texture (scoria fragment)	blocky to irregular	very high	very poor	(53, amost Pl)	Pl, Pl+opx+rhy glass	unaltered
227	L6_19	Qtz fragment with alunite and APS, sil+kl inclusion							
228	L6_20	Brown grey partly altered volcanic rock	holocrystalline intersertal porphyrytic texture altered into sil+kl aggregates (pseudomorph of phenocrysts and colloform in fractures)	blocky	n.d.	holocrystalline	n.d.	Pl, Pl+Aug+Timag+alkali feld (sa and anot)+Qtz, sil+kl+alu	weakly altered
229	L6_21	Brown grey partly altered volcanic rock (translucent)	scoriaceous (hyaloophtic to glassy) porhyrytic texture (scoria fragment) with pore filling sil+kl+alu aggregate	blocky to irregular	high	very poor	58	Aug+Opx, Aug+Opx+Pl+rhy glass, sil+kl+alu	weakly altered
230	L6_22	White altered rock	porphyrytic texture completely altered into sil+kl aggregates (pseudomorph of phenocrysts and colloform in fractures)	blocky to irregular	n.d.	n.,d	n.d.	sil+kl+TiO2 mineal	Intensely
231	L6_23	Brown grey volcanic rock (translucent)	scoreaceous (hyaloophtic to glassy) porhyrytic texture (scoria fragment)	blocky to irregular	high	very poor	61	Aug+Opx, Aug+Opx+Pl+Tima g + rhy glass,	unaltered
232	L6_24	light brown grey partly altered volcanic rock	glassy pumiceous? porhyrytic texture (pumice fragment) with pore filling sil+kl+alu aggregate and itself pseudomorohs	blocky to irregular	modelate	very poor	n.d.	altered rhy glass?, sil+kl	weakly altered
233	L6_25	Light brown grey volcanic rock	glassy porhyrytic texture (scoria fragment)	blocky	modelate	very poor	62	Opx+pl, Opx+Pl+Tima g + rhy glass,	unaltered
234	L6_26	Trancent glassy volcanic rock	glassy scoriaceous porhyrytic texture (scoria fragment)	blocky to irregular	modelate?	very poor	(53, amost Pl)	Pl, Pl+opx+rhy glass	unaltered
235	L6_27	Pl fragment							
236	L6_28	White altered rock	holocrystalline intersertal porphyrytic texture altered	blocky	poor	holocrystalline	77	Pl, Pl+imag+alkali feld (sa and anot)+Qtz	weakly altered
237	L6_29	Light grey altered rock	dissolution texture of massive silica	blocky	vuggy?	n.d.	n.d.	Sil	Intensely
238	L6_30	Brown grey volcanic rock (translucent)	scoreaceous (hyaloophtic to glassy) porhyrytic texture (scoria fragment)	irregular to cuspate?	high	very poor	62	, Aug+Opx+Pl+Tima g + rhy glass,	unaltered
239	L6_31	White altered rock	sil+kl+alu aggregates (colloform in fractures)	blocky to irregular	n.d.	n.,d	n.d.	sil+kl+alu+TiO2 mineal	Intensely
240	L6_32	Brown grey partly altered volcanic rock (translucent)	hyaloophtic porhyrytic texture with pore filling sil+kl+alu aggregate	blocky	modelate?	poor	61	Aug+Opx+pl Opx+Pig+Pl+chalcopy?+Timag+rhy glass, sil+kl+alu	weakly altered
241	L7_1	pl fragment							
242	L7_2	pl fragment							
243	L7_3	yellowish white altered volcanic rock	holocrystalline porphyrytic texture almost altered into sil+ver+alu aggregates	blocky to irregular	n.d.	holocrystalline?	n.d.	pl+sa, sil+ver+alu+TiO2+FeOH mineral	weakly altered
244	L7_4	yellowish white altered volcanic rock	holocrystalline intersertal porphyrytic texture altered into sil+kl aggregates (pseudomorph of phenocrysts and colloform in fractures)	blocky	poor	holocrystalline?	n.d..	pseudomorph phenocryst, Opx+il+sa, sil+kl+(ver?)	weakly altered
245	L7_5	pl fragment with sil+kl alteration (dissolusion?)							weakly altered
246	L7_6	yellowish white altered rock	massive aggregates of sil+kl+alu fine-grained crystal mixtures (coloform infill texture)	blocky	porus?	n.d.	n.d.	sil+kl+alu (APS)+mag?	intensely
247	L7_7	yellowish brown altered rock	massive aggregates of sil+kl fine-grained crystal mixtures (coloform infill texture) (partly pseudomorphic porhyrytic tex?)	blocky	porus?	n.d.	n.d.	sil+kl+alu (APS)+TiO2 mineral	intensely
248	L7_8	yellowish brown altered rock	massive aggregates of sil+po fine-grained crystal mixtures (coloform infill texture) (partly pseudomorphic vesicular porhyrytic tex?)	blocky	high?	n.d.	n.d.	sil+po+alu+FeOH	intensely
249	L7_9	yellowish brown altered rock	massive aggregates of sil+kl fine-grained crystal mixtures (coloform to microveinlet infill texture) (partly pseudomorphic vesicular porhyrytic tex?)	irregular to cuspate	high?	n.d.	n.d.	sil+kl+alu+Il?	intensely
250	L7_10	white altered rock	dissolution texture of massive silica with pore filing alunite	blocky	n.d.	n,d,	n.d.	sil, alu	intensely
251	L7_11	pl fragment							
252	L7_12	pl fragment with fine grained silica (precipitation in fracture)							
253	L7_13	Opx phenocryst fragment with sil+alu altered groundmass							
254	L7_14	Pl fragment with sil+kl alteration							
255	L7_15	Grey partly altered volcanic rock	scoriaceous (glassy) porphyrytic texture altered into sil+kl aggregates (pseudomorph of phenocrysts and colloform pore filling vesicles)	irregular to cuspate	high?	very poor	63	opx+rhy glass, sil+kl	weakly altered
256	L7_16	pl fragment							
257	L7_17	opxfragment							
258	L7_18	pl fragment							
259	L7_19	Opx fragment							
260	L7_20	pl fragment							
261	L7_21	brownish partly altered volcanic rock	porphyrytic texture almost altered into sil+ill aggregates	blocky	n.d.	n.d.	n.d.	Opx phenocryst remained, sil+illite	
262	L7_22	pl fragment							
263	L7_23	Grey partly altered volcanic rock	pumiceous (glassy) porphyrytic texture altered into sil+kl aggregates (pseudomorph of phenocrysts and colloform pore filling vesicles)	irregular to cuspate	very high	very poor	n.d.	rhy glass, sil+alu+po	weakly altered
264	L7_24	yellowish white altered rock	massive aggregates of sil+kl fine-grained crystal mixtures (coloform to microveinlet infill texture) (partly pseudomorphic vesicular porhyrytic tex?)	blocky	porus?	n.d.	n.d.	sil+kl+alu+mag?	weakly altered
265	L7_25	Brown volcanic rock	hyaloophtic to hyalopilitic porphyrytic texture	blocky	poor	high	62	Opx+Pl Pl+Aug+Opx+Pig+Timag+Qtz+rhy glass	unaltered

	sample code and grain no.	Descriptive name	Rock texture	Shape	Vesiculation*1	Crystallinity*1	SiO2% of glass (normalized)*1	Minral assemblage (phenocryst, groundmass or other)	Alteration degree*2
266	L7_26	Brown grey volcanic rock	holocrystalline intersertal porphyrytic texture altered into sil+kl aggregates (pseudomorph of phenocrysts and colloform in fractures)	blocky	poor	holocrystalline	75	Opx+Pl Alkali feld (sa)+Pl+Aug+Opx+Timag+Qtz, sil+kl	unaltered
267	L7_27	Grey volcanic rock	hyaloophtic porphyrytic texture	blocky to irregular	high	poor	64	opx+il, pl+opx+aug+rhy glass	unaltered
268	L7_28	white altered rock	dissolution texture of massive silica with fine grained silica crystal aggregates	blocky to irregular	vuggy?	n,d,	n.d.	sil+TiO2 mineral	intensely
269	L7_29	yellowish white altered rock	massive aggregates of sil+kl fine-grained crystal mixtures (coloform infill texture)	blocky	porus?	n.d.	n.d.	sil+kl	intensely
270	L7_30	Grey partly altered volcanic rock	hyalopillitic porphyrytic texture altered into sil+kl+alu aggregates (pseudomorph of phenocrysts-groundmass, colloform pore filling vesicles)	irregular to cuspate	very high	modelate	n.d.	rhy glass+groundmass microlite (too small), sil+alu+kl	weakly altered
271	L7_31	white altered volcanic rock	porphyrytic texture altered into sil+kl aggregates (pseudomorph of phenocrysts and colloform in fractures)	blocky to irregular	n.d.	n,d,	n.d.	remaind Opx+rhy glass, sil+kl	weakly altered
272	L7_32	Qtz fragment							
273	L7_33	pl fragment							
274	L7_34	pl fragment with vein silica alteration							
275	L7_35	yellowish white altered rock	massive aggregates of sil+kl fine-grained crystal mixtures (coloform infill texture) (partly pseudomorphic porhyrytic tex?)	blocky	porus?	n.d.	n.d.	remained Opx+il, sil+kl	weakly altered

Appendix 8: Counted ash grains under binocular stereoscopic microscope in Chapter 3

	DVR	VVR	CF	MAS	PAVR
L7 (n=756)	64	6	40	274	372
L6 (n=435)	219	6	13	63	134
L5 (n=700)	312	26	4	128	230
L4 (n=571)	344	54	0	28	145
L3 (n=771)	385	5	26	156	199
L2 (n=714)	208	2	7	151	346
L1-2 (n=753)	231	1	49	314	158
L1-1 (n=782)	98	1	24	239	420

Appendix 9: Weathered scoria or scoria fragments under binocular stereoscopic microscope in Chapter 4